U.PORTO

DOUTORAMENTO EM CIÊNCIAS FARMACÊUTICAS

FARMACOLOGIA E FARMACOTERAPIA

NeuroD3S – Dual-Drug Delivery System based on cell-penetrating peptides and nanoparticles for application in biomedicine

Sara Silva

D

2022



NeuroD3S – Dual-Drug Delivery System based on cell-penetrating peptides and nanoparticles for application in biomedicine

Sara Cristina Pinto Silva

Doctoral Thesis in Pharmaceutical Sciences – Pharmacology and Pharmacotherapy Specialty (240 ECTS credits) submitted to the Faculty of Pharmacy of the University of Porto

Supervisor: Professor Nuno Vale (PhD), Faculty of Medicine, University of Porto, Portugal

Co-Supervisors: Professor António Almeida (PhD), Faculty of Pharmacy, University of Lisbon, Portugal and Professor Jorge Gonçalves (PhD), Faculty of Pharmacy, University of Porto, Portugal

Porto, Portugal May 2020

THIS THESIS IS PUBLICLY SUPPLIED ON CONDITION THAT ANYONE WHO CONSULTS IT IS UNDERSTOOD TO RECOGNISE THAT ITS COPYRIGHT RESTS WITH ITS AUTHOR AND THAT NO QUOTATION FROM THE THESIS AND NO INFORMATION DERIVED FROM IT MAY BE PUBLISHED WITHOUT PROPER ACKNOWLEDGMENT

This Doctoral Thesis was supported financially by the Foundation for Science and Technology (FCT, Portugal) and PhD Programme in Medicines and Pharmaceutical Innovation (i3DU) through the research grant [PD/BD/135458/2017].



The experimental work presented in this Doctoral Thesis was performed in the Department of Pharmacology, in the Faculty of Pharmacy, University of Porto, Portugal; in the Department of Pharmacy, Pharmacology and Health Technologies, the Faculty of Pharmacy, University of Lisbon, Portugal; and in the Department of Community Medicine, Information and Health Decision Sciences, Faculty of Medicine, University of Porto, Portugal.









To my Parents,

Cristina Silva and Fernando Silva,

for everything.

Acknowledgements

First and foremost, I thank my parents, Fernando and Cristina for their rock-solid unconditional support since the beginning of everything, also big acknowledgement to my godmother and godfather Josefina and José to always been there for me no matter what and I hold a deep respect to the rest of my family that contribute with love and understanding every time.

I am very grateful for my Supervisor, Professor Doutor Nuno Vale (PhD), for all the scientific guidance, consideration, and availability, trusting me and for having provided me all the conditions to perform this Thesis.

I would also like to express my deepest gratitude to my Co-Supervisor, Professor Doutor António Almeida for the enthusiastic co-supervision of my work, acceptance and guidance in all parts of the work developed in this Thesis. I will always be grateful for the opportunity to work in his laboratory and for always making me feel like I was home.

I am also thankful to for the incredible Doutor Lídia Gonçalves and Doutor Joana Marto, from Institute for Medicines & Pharmaceutical Sciences (iMed.ULisboa) of the Faculty of Pharmacy of the University of Lisbon for all the knowledge shared, acceptance, guidance and for the kind works in the right moments and the most needed hugs at the time.

I would like to thank my lab colleagues: Diana, Salomé and Abigail. For providing me with the best working environment I could ever wish for. For all the joint effort to do a better work. For all the moments extra work I will always keep close to my heart.

I also want to Acknowledgement the Portuguese National Funding Agency for Science and Technology (FCT) and PhD Programme in Medicines and Pharmaceutical Innovation (i3DU) for the financial support through the research grant [PD/BD/135458/2017].

I am also thankful to the Laboratory of Pharmacology of the Faculty of Pharmacy of the University of Porto and all its staff and collaborators for the help, support, and consideration. Special thanks to the Professor Doutor Jorge Gonçalves for the support and appreciation and to Céu and Mónica for everything.

I would like to express my gratitude to the Serviço de Gestão Académica e Expediente of the Faculty of Pharmacy of the University of Porto, special to Andrea Gouveia for all the guidance and problem resolution.

I am also thankful to the CENTESIS and the department of experimental biology of the Faculty of Medicine, of the University of Porto and Department of Anatomy of the Centro Hospitalar São João for providing all the conditions to perform the last experiments of this Thesis.

I am very grateful to all my friends that remind me every time to fight for my dreams and be happy. I'm eternally grateful to Rita, Marina, Isa, Lau, Dias, Romana, Joana, Ana, Mónica, Sérgio and André.

I must express my thankfulness to my second family that always support me and didn't let me give up. To Paula, Victor, Susana, Bruno, Mia, Ema, Emilia, Zé.

I would also like to express my deepest gratitude to my boyfriend and best friend Rafael for all the time he did not giving up on me, for all the care and unconditional love. For every-time I only saw black, and he guide me to the light. Thank you for the anticipated vow: in sickness and in health.

Abstract

The present Thesis addresses the current drug limitations and drawbacks in pharmacological treatment with the use of traditional therapies, and nanoparticulate strategy to overcome and enhance drug delivery in such disorders. Till today, the treatment of heterogeneous diseases, such as neurodegenerative diseases and cancer, is based on therapies that sometimes are ineffective and present several side effects. So, in order to overcome these limitations and increase pharmacological bioavailability, the use of nanoparticles (NP) as delivery vehicles has showed promising results in research. Several studies demonstrated an increase of drug delivery efficiency, reduction of side effects and improvement of the pharmacokinetic profile. There are different types of NP that, depending on their composition, can be classified: as organic, hybrid or inorganic and can adopt different structures (tubes, polymeric fibers, etc.). Furthermore, NP can be functionalized with different molecules, to decrease their peripheral metabolism, potentiate delivery to the site of interest and improve their therapeutic efficiency. The incorporation of cell-penetrating peptides (CPP) in NP has been widely tested and received a lot of interest. CPP are characterized to be relatively small, having between 6 to 30 amino acids and able to penetrate biological barriers and cell membranes without compromise them. Over the past few years, CPPs have demonstrated a variety of new cellular functions that go beyond their ability to penetrate cells. Taking this in consideration, the main goal of this Thesis was to develop a dual delivery system, with lipid NP and CPP, in order to potentiate the delivery of specific drugs, such as: rasagiline (RAS), tranylcypromine (TCP) and tacrine (TAC).

In a first phase of the work, the CPP used was the Model amphipathic peptide (MAP) and it was synthetized through manual peptide synthesis. Subsequently, some modifications were made, with the coupling of drugs (RAS, TCP and TAC) to the peptide chain, resulting in three different conjugates: RAS-MAP, TCP-MAP and TAC-MAP. The results of the analyzes performed indicated that all peptides were successfully synthesized and showed a purification greater than 92%.

In a second phase, the preparation of lipid NP (NLC) was carried out with an initial optimization protocol to achieve the final formulation. Several compounds, physical-chemical parameters, purification methods and cellular toxicity were evaluated, to obtain the best formulation. From this extensive analysis, it was determined that the NLC formulation (CT25) composed of 75% Compritol® ATO 888, 25% Transcutol® HP with 3% polysorbate 80 (T80) resulted in higher encapsulation efficiency and lower cellular toxicity.

In a third phase, NLC CT25 was prepared, and the previously synthesized conjugates (RAS-MAP, TCP-MAP and TAC-MAP) were encapsulated. Then, the formulations were subjected to an extensive physicochemical characterization and their toxicity in two cell lines (neuroblastoma SH-SY5Y and colon carcinoma Caco-2) was determined. The initial results showed that administration of peptide conjugates alone (RAS-MAP, TCP-MAP and TAC-MAP) promote significant antiproliferative activity at low concentrations in the SH-SY5Y and MCF-7 cell lines. Furthermore, it was further demonstrated, in other assay, that encapsulation of the respective conjugates in NLC CT25 led to an increase in antiproliferative activity in the SH-SY5Y and Caco-2 cell lines. Resulting in a decrease in IC_{50} values, when compared to the administration of the conjugates alone.

Considering the results obtained regarding the extensive antiproliferative activity of the compounds in cancer cell lines, an alternative strategy was tested in the fourth phase of the thesis, with the adsorption of different peptides onto the NLC CT25 surface. First, considering the lytic activity presented by MAP, neuropeptide Y (NPY) was chosen and added to the assay as an alternative non lytic peptide with interesting activity. Several studies show that NPY has great therapeutic potential in neurodegenerative diseases, due to the it's neuroprotection ability. An adsorption method was established to conduct this experiment and the results obtained, through the evaluation of the zeta potential, indicate that the compounds (Lys(N_3)-MAP, TAC-MAP and NPY) have a strong interaction with the surface of the NLC.

In the last Chapter of the Thesis, and reviewing the promising results of MAP, a preliminary in-silico study of the interaction of the MAP peptide with the neuronal membrane receptor of NPY is presented. The in-silico analysis showed promising results, indicating a strong interaction of MAP with the membrane receptor, with values similar to those obtained for NPY and the reference antagonist UR-ML299.

In conclusion, the work conducted on this Thesis demonstrated that the development of an NLC delivery system functionalized with CPP might enhance drug therapeutic efficacy at low concentrations. Furthermore, it allowed the identification of new functions of MAP and its conjugates, with high antiproliferative activity and, possibly, interaction with a neuronal receptor.

Keywords: Nanoparticles; Cell-penetrating peptides; Model amphipathic peptide; Neurodegenerative diseases; Cancer; Neuropeptide Y; Drug repurposing.

Resumo

O projeto que conduziu à redação desta tese pretendeu expor as diversas dificuldades e limitações existentes no tratamento farmacológico com o uso de terapêuticas tradicionais. Atualmente, o tratamento de doenças heterogéneas, como doenças neurodegenerativas e oncológicas, baseia-se em terapêuticas, por vezes, ineficazes e com efeitos secundários graves. De forma a colmatar essas limitações e aumentar a biodisponibilidade farmacológica, o uso de nanopartículas como veículos de entrega tem demonstrado resultados promissores. Diversos estudos têm demonstrado um aumento na eficiência da entrega de fármacos, redução dos efeitos secundários e aperfeiçoamento do perfil farmacocinético. Existem diferentes tipos de nanopartículas que, consoante a sua composição, podem ser classificadas como orgânicas, híbridas ou inorgânicas e apresentar diferentes estruturas (tubos, fibras poliméricas, etc.). Para além disso, podem ser funcionalizadas com diversas moléculas, de forma a diminuir a sua metabolização periférica, potenciar a entrega no local de interesse e melhorar a sua eficiência terapêutica. Uma funcionalização promissora tem sido a utilização de péptidos penetradores celulares (CPP). Estes péptidos são relativamente pequenos, possuindo entre 6 a 30 aminoácidos, sendo capazes de penetrar barreiras biológicas e membranas celulares. Ao longo dos últimos anos, os CPP têm demonstrado uma variedade de novas funções celulares, que vão para além da sua capacidade em penetrar células.

Tendo isto em consideração, o objetivo principal desta tese foi a criação de um duplo sistema de entrega, através da utilização de nanopartículas lipídicas e CPP, com o intuito de aumentar a entrega de fármacos específicos, nomeadamente a rasagilina (RAS), tranilcipromina (TCP) e tacrina (TAC).

Numa primeira fase do trabalho, o CPP utilizado, o Model amphipathic peptide (MAP), foi obtido através de síntese peptídica manual. Posteriormente, algumas modificações foram efetuadas, com o acoplamento dos fármacos (RAS, TCP e TAC) à cadeia peptídica, resultando em três conjugados diferentes: RAS-MAP, TCP-MAP e TAC-MAP. Os resultados das análises realizadas indicaram que todos os péptidos foram sintetizados com sucesso e apresentaram uma purificação superior a 90%.

Numa segunda fase, a preparação de nanopartículas lipídicas (NLC) foi realizada através de uma otimização inicial da formulação final. Diversos compostos, parâmetros físico-químicos, metodologias de purificação e toxicidade celular foram avaliados, de forma a obter a melhor formulação. Desta análise extensiva, determinou-se que a formulação NLC

(CT25) composta por 75% de Compritol® ATO 888, 25% de Transcutol® HP e 3% de polisorbato 80 resultou numa maior eficiência de encapsulamento e menor toxicidade celular.

Numa terceira fase, procedeu-se à preparação de NLC CT25 e encapsulação dos conjugados previamente sintetizados (RAS-MAP, TCP-MAP e TAC-MAP). Posteriormente, as formulações preparadas foram submetidas a uma extensa caracterização físico-química e foi determinada a sua toxicidade em duas linhas celulares: neuroblastoma SH-SY5Y e cólon Caco-2.

Os resultados dos ensaios efetuados demonstraram que os conjugados peptídicos (RAS-MAP, TCP-MAP e TAC-MAP) apresentavam uma atividade antiproliferativa significativa nas linhas celulares SH-SY5Y e MCF-7, a baixas concentrações. Mais ainda se demonstrou que a encapsulação dos respetivos conjugados nas NLC CT25 levou ao aumento acrescido da atividade antiproliferativa nas linhas celulares SH-SY5Y e Caco-2, resultando na diminuição da IC_{50}, quando comparada com a administração dos conjugados sozinhos.

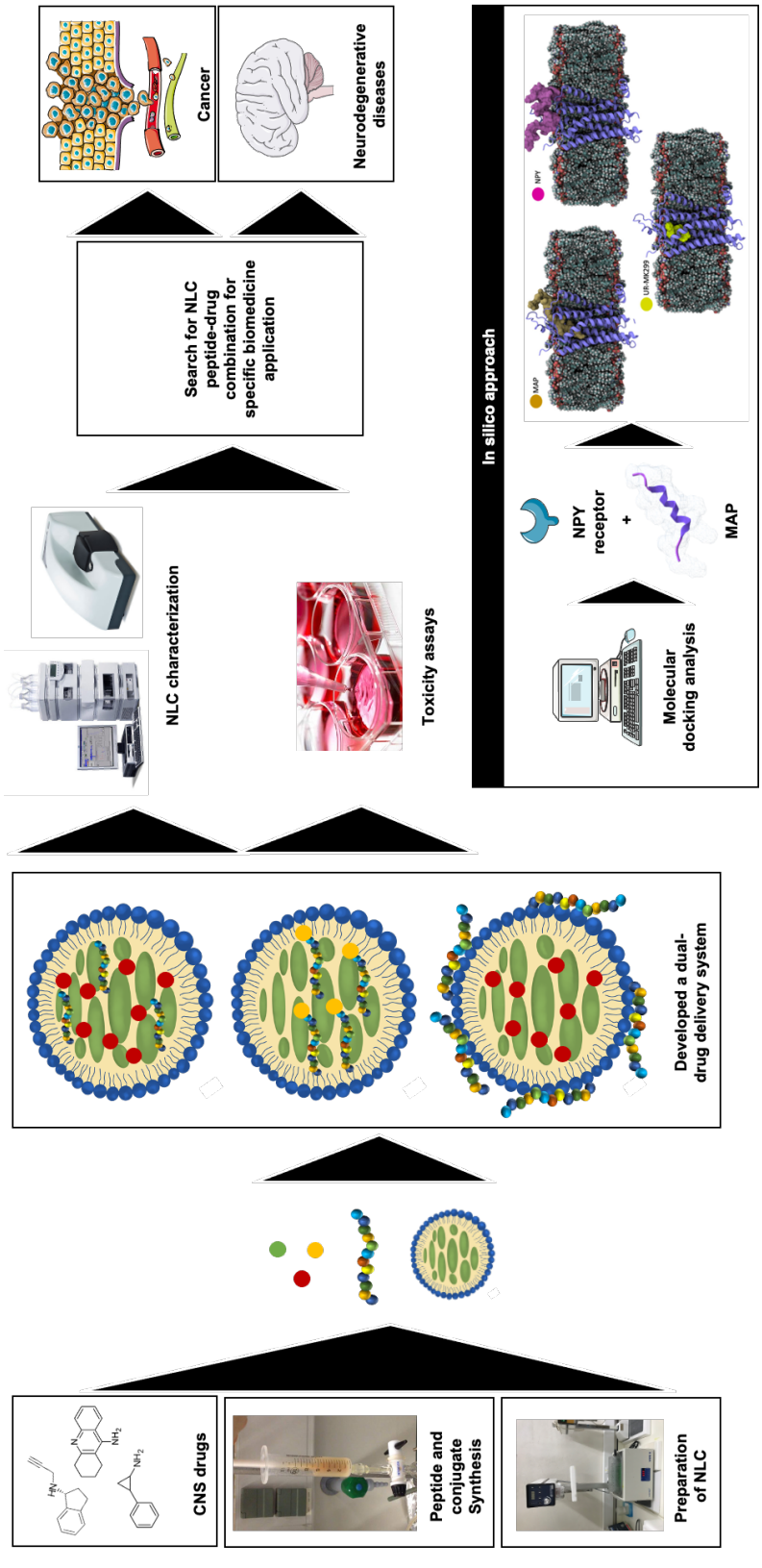
Tendo em consideração os resultados obtidos, relativamente à extensa atividade antiproliferativa dos compostos em linhas celulares cancerígenas, foi testada uma estratégia alternativa na quarta fase da tese, com a adsorção dos compostos peptídicos à superfície das NLC CT25. Numa primeira instância, tendo em conta a atividade apresentada pelo MAP e o interesse do tratamento biomédico diversificado, foi adicionado aos ensaios um péptido alternativo ao MAP, o neuropéptido Y. Diversos estudos demonstram que neuropéptido Y tem grande potencialidade terapêutica em doenças neurodegenerativas, devido à sua atividade neuronal protetora. Os resultados obtidos através da avaliação do potencial zeta da interação dos compostos (Lys(N3)-MAP, TAC-MAP e Neuropéptido Y) com a superfície das NLC indicaram a existência de uma forte interação de todos os compostos testados.

No último capítulo da tese, e revendo os resultados promissores do MAP, é apresentado um estudo preliminar in silico da interação do péptido MAP com o recetor de membrana neuronal do neuropéptido Y. A análise in silico demonstrou resultados promissores, indicando uma forte interação do MAP com o recetor de membrana, tendo-se obtido valores semelhantes aos obtidos para o Neuropéptido Y e para o antagonista de referência UR-ML299.

Com o trabalho efetuado no âmbito desta tese, pode-se concluir que o desenvolvimento de um sistema de entrega de NLC, funcionalizadas com CPP, potencia a eficácia terapêutica, em baixas concentrações. Para além disso, permitiu a identificação de novas funções do MAP e seus conjugados, com elevada atividade antiproliferativa e, possivelmente, interação com um recetor neuronal.

Palavras-Chave: Nanopartículas; Péptidos penetradores celulares; MAP; Doenças neurodegenerativas; Cancro; Neuropéptido Y; terapêutica farmacológica.

Graphical abstract



Thesis Overview

This Thesis aimed to develop a new dual modified nanoparticle system to delivery both peptides and CNS drugs, explore the possible applications and evaluate its toxicity. Therefore, the following five specific objectives were established.

Regarding the first part of the Thesis, Chapter 1 exhibits brief narrative review of the MAP and CNS drugs used in this Thesis and peptide synthesis conducted to generate MAP and respective conjugates. In Chapter 2 provides the sequential phase procedure of nanoparticle formulation and development to obtain an optimized NLC formulation. This topic is further explored with introduction of a peptide and peptide-drug conjugate in the NLC formulation in Chapter 3 by providing a state-of-the-art review concerning the use of nanoparticle systems modified with CPP in different areas of biomedicine. In addition, the experimental part of Chapter 3 was divided into 2 phases regarding MAPs own activity towards cancer and NLC formulation toxicity and safety against two cancer cell lines.

Regarding the second part of the Thesis, Chapter 4 offers a new alternative NLC modification with adsorption of MAP and MAP derivates or NPY on the surface. In Chapter 5 describes the computational approach of MAP possible interaction with receptors present in neuronal cells.

Table of Contents

Acknowledgements 14

Abstract 17

Resumo 19

Graphical abstract 23

Thesis Overview 24

Table of Contents 26

List of Figures 33

Chapter 1 33

Chapter 2 34

Chapter 3 37

Chapter 4 41

Chapter 5 43

Supplementary Information 43

List of tables 48

Abbreviations 50

Chapter 1 55

Peptide Synthesis 57

1.1 Introduction 57

1.1.1. Cell-penetrating peptides 57

1.1.2. Mechanisms of entrance inside cells 58

1.1.3. CPP for delivery cargos 61

1.1.4. Model amphipathic peptide 63

1.1.5. MAP conjugation and activity 64

1.1.6. Central nervous System drugs 66

1.1.6.1. Tacrine 67

1.1.6.2. Rasagiline 69

1.1.6.3. Tranylcypromine 71

1.1.7. Solid Phase Peptide Synthesis (SPPS) 71

1.2. Overview 73

1.3. Materials and methods 73

1.3.1. Materials 73

1.3.2. Methods 73

1.3.2.1. General Peptides Synthesis Procedure 73

1.3.2.2. General Peptides Analysis Procedure 74

1.4. Results 75
1.4.1. MAP 75
1.4.2. Lys(N_3)-MAP 77
1.4.3. RAS-MAP 78
1.4.4. TAC-MAP 80
1.4.5. TCP-MAP 82
1.5. Discussion 85
1.6. References 85
Chapter 2 *103*
Development of Nanoparticles *103*
2.1. Introduction 103
2.2. Overview 105
2.3. Materials and Methods 105
2.3.1. Materials 105
2.3.2. SLN/NLC preparation optimization 106
2.3.2.1. SLN preparation 106
2.3.2.2. Lipid solubility 106
2.3.2.3. NLC preparation 107
2.3.2.4. NLC purification 107
2.3.3. Chromatographic Instruments and Conditions 108
2.3.4. Characterization of NLC 108
2.3.4.1. Particle Size and Surface Change 108
2.3.4.2. Encapsulation Efficiency 108
2.3.5. *In Vitro* Drug Release 109
2.3.5.1. Drug Release from pH 7.4 109
2.3.5.2. TAC Release in Human Plasma 109
2.3.6. Stablish a primary neuronal cell culture 109
2.3.6.1. Poly-D-lysine coating of culture dishes 109
2.3.6.2. Isolation of neurons 110
2.3.7. *In vitro* cell viability studies 110
2.3.7.1. MTT assay 110
2.3.7.2. SRB Assay 111
2.3.7.3. Cell Morphology Visualization 111
2.3.8. Statistical Analysis 111
2.4. Results 112
PHASE 1 112
2.4.1. SLN/NLC optimization method 112
2.4.1.1. SLN characterization 112
2.4.1.2. SLN toxicity against Caco-2 cell line 113
PHASE 2 114
2.4.2. NLC optimization method 114
2.4.3. Lipid solubility 115
2.4.4. Toxicity of surfactant in Caco-2 cell line 116

2.4.5. NLC preparation, purification, and characterization 118
2.4.5.1. Drug Calibration Curve 118
2.4.5.2. Encapsulation efficiency 119
2.4.6. Preliminary Toxicity assays Caco-2 120
PHASE 3 122
2.4.7. NLC optimization method 122
2.4.7.1. NLC characterization 123
2.4.7.2. Stability in solution storage at 4 °C 126
2.4.7.3. Pharmaceutical release in PBS and Plasma 126
2.4.8. Toxicity assays in SH-SY5Y cells 127
2.4.8.1. MTT Assay 127
2.4.8.2. SRB Assay 129
2.4.8.3. SH-SY5Y Morphology Visualization and cell count 130
2.4.9. Toxicity assays in Caco-2 cell line 132
2.4.9.1. MTT assay 132
2.4.9.2. SRB assay 133
2.4.9.3. Caco-2 Morphology Visualization and cell count 134
2.5. Discussion and conclusion 137
2.6. References 138
Chapter 3 143
Nanoparticles conjugation of with 143
CPP and CNS drugs 143
3.1. Introduction 143
3.1.1. Neurodegenerative diseases 144
3.1.1.1. Alzheimer Disease 144
3.1.1.2. Parkinson Disease 147
3.1.1.3. CPP and NPs in CNS 151
3.1.2. Cancer 152
3.1.2.1. CPPs and NPs in Cancer 152
3.2. Overview 156
3.3. Material and Methods 156
3.3.1. Materials 156
3.3.2. Preparation of NLC 157
3.3.3. Characterization of NLC 157
3.3.3.1. Particle size and surface charge 157
3.3.3.2. Encapsulation efficiency 157
3.3.4. *In vitro* cell viability studies 158
3.3.4.1. MTT assay 158
3.3.4.2. SRB assay 159
3.3.4.3. Cell morphology visualization 160
3.3.5. Analysis of Drug Interactions 160
3.3.6. Statistical analysis 160
3.4. Results 160

PHASE 1 **160**
3.4.1. Toxicity of TAC and Its MAP Conjugate to MCF-7 and SH-SY5Y Cells 160
3.4.2. Determination of IC_{50} and Cell Count Analysis of TAC, MAP, and TAC-MAP against MCF-7. 162
3.4.3. Morphological Changes Caused by TAC, MAP, and TAC-MAP on MCF-7 Cells 163
3.4.4. Drug Interactions between TAC and MAP in the Conjugate 166
3.4.5. Discussion 166

PHASE 2 **167**
3.4.6. NLC formulation and characterization 167
3.4.7. *In vitro* cytotoxicity assays against Caco-2 cell line 169
3.4.7.1. Toxicity of MAP, Lys(N_3)-MAP and drug-MAP conjugate 169
3.4.7.2. Toxicity of NLC loaded with TCP, Lys(N_3)-MAP and TCP-MAP 172
3.4.7.3. Toxicity of NLC loaded with RAS, Lys(N_3)-MAP and RAS-MAP 175
3.4.7.4. Toxicity of NLC loaded with TAC, Lys(N_3)-MAP and TAC-MAP 178
3.4.8. *In vitro* cytotoxicity assays against SH-SY5Y 181
3.4.8.1. Toxicity of MAP, Lys(N_3)-MAP and drug-MAP conjugates. 181
3.4.8.2. Toxicity of NLC loaded with TCP, Lys(N_3)-MAP and TCP-MAP. 184
3.4.8.3. Toxicity of NLC loaded with RAS, Lys(N_3)-MAP and RAS-MAP 187
3.4.8.4. Toxicity of NLC loaded with TAC, Lys(N_3)-MAP and TAC-MAP 189
3.4.9. Discussion 192

3.5. References **195**

Chapter 4 ***207***

Nanoparticle surface Functionalization ***207***

4.1. Introduction **207**

4.2. Overview **209**

4.3. Materials and Methods **209**
4.3.1. Materials 209
4.3.2. Nanoparticle Preparation 210
4.3.3. Peptide and Peptide Conjugate Adsorption Method 210
4.3.4. Nanoparticle Size and Surface Charge 210
4.3.5. Statistical Analysis 211

4.4. Results **211**
4.4.1. CPP and CPP/Drug Complex Adsorption onto NLC Surface 211
4.4.1.1. Influence of Different Lys(N_3)-MAP Concentrations 211
4.4.1.2. Influence of Lys(N_3)-MAP Adsorbed into Drug Loaded NLC 213
4.4.1.3. Influence of Different TAC-MAP Concentrations 214
4.4.1.4. Influence of CT25 B Amount on TAC-MAP Adsorption 214
4.4.1.5. Influence of Incubation Medium H_2O vs. PBS on Peptide Adsorption 215
4.4.1.6. Neuropeptide Y Adsorption onto NLC Surface 216

4.5. Discussion **217**

4.6. References **220**

Chapter 5 ***227***

Preliminary In-Silico approach 227

5.1. Introduction 227

5.2. Overview 228

5.3. Methods 228

5.3.1. Receptor Molecular Docking Assays 228

5.3.1.1. Model Preparation for Human Neuropeptide Y Y1 Receptor 228

5.3.1.2. Preparation of MAP and NPY 228

5.3.2. Docking 229

5.4. Results and Discussion 229

5.4.1. Receptor Molecular Docking Assays 229

5.5. Discussion 233

5.6. References 234

Conclusions and Future Perspectives 239

Supplementary Information 243

CHAPTER 1 243

PEPTIDE SYNTHESIS 243

1.1. RAS-MAP 243

1.2. Pra-MAP 244

1.3. TAC-MAP 245

1.4. TCP-MAP 249

CHAPTER 2 252

Nanoparticles optimization 252

2.1. Stablish a primary neuronal cell culture 252

2.1.1. Protocol design 252

2.1.2. Isolation of neurons - Results 254

2.2. Toxicity assays SH-SY5Y 256

2.1.2. Cell Morphology Visualization 256

CHAPTER 3 259

Nanoparticles couple with CPP and CNS drugs 259

3.1. Encapsulation efficiency – Results 259

3.1.1. Ultraviolet-visible (UV-Vis) spectroscopy 259

3.1.2. Fluorescamine Protocol optimization 260

3.2. *In vitro* cytotoxicity assays against Caco-2 cell line 262

3.3. *In vitro* cytotoxicity assays against SH-SY5Y 268

List of Publications 275

First author: Sara Silva _____ **275**

Co-author _____ **276**

List of Figures

Chapter 1

Figure 1.1 - Schematic representation of different types of peptides available and its different activities. In depth representation of Cell-penetrating Peptides as delivery molecules and potential other interactions. 62

Figure 1.2 - Different representations of MAP. A – Structure sequence of MAP (ChemDraw 19.0); B – 3 D representation of MAP sequence (ChemBio 3D ultra); C – Secondary conformation of α-helix structure of MAP (3D data retrieved from CPP database (CPPsite 2.0) and analyzed by (ChemBio 3D ultra). 64

Figure 1.3 - CNS drugs molecular structure. 67

Figure 1.4 - General scheme of SPPS. X=O,NH; AA= amino acid; PG=protecting group; TPG=temporary group; P – resin (scheme retrieved from reference (146)) . 72

Figure 1.5 - Chromatogram of the product of the manual synthesis of the MAP, acquired with a HPLC system, with a C18 column, using ACN in water with 0.05% TFA as eluent, in gradient mode (0 – 100%), for 30 minutes, at a flow of 1 mL/min and detection at λ = 220 nm. 76

Figure 1.6 - Mass spectrum (LC-ESI/Orbitrap MS, positive mode) of the peptide MAP. 76

Figure 1.7 - Chromatogram of the product of the manual synthesis of Lys(N_3)MAP, acquired with a HPLC system, with a C18 column, using ACN in water with 0.05% TFA as eluent, in gradient mode (0 – 100%), for 30 minutes, at a flow of 1 mL/min and detection at λ = 220 nm. 77

Figure 1.8 - Mass spectrum (LC-ESI/Orbitrap MS, positive mode) of the Lys(N_3)-MAP (manual synthesis). 77

Figure 1.9 - Representation of the methodology applied for the synthesis of the RAS-MAP conjugate. 78

Figure 1.10 - Chromatogram of the product of the manual synthesis of Ras-MAP, acquired with a HPLC system, with a C18 column, using ACN in water with 0.05% TFA as eluent, in gradient mode (0 – 100%), for 30 minutes, at a flow of 1 mL/min and detection at λ = 220 nm. 79

Figure 1.11 - Mass spectrum (LC-ESI/Orbitrap MS, positive mode) of the conjugate Ras-MAP. 79

Figure 1.12 - Representation of the methodology applied for the synthesis of the TAC-MAP conjugate by SPPS. TAC-MAP was obtained with a good resolution and high level of

purity (99.6%). Data for preparation and characterization are in Supplementary Material. 81
Figure 1.13 - Chromatogram of the product of the manual synthesis of TAC-MAP, acquired with a HPLC system, with a C18 column, using ACN in water with 0.05% TFA as eluent, in gradient mode (0 – 100%), for 30 minutes, at a flow of 1 mL/min and detection at λ = 220 nm. 82
Figure 1.14 - Mass spectrum (LC-ESI/Orbitrap MS, positive mode) of the conjugate TAC-MAP. 82
Figure 1.15 - Representation of the methodology applied for the synthesis of the TCP-MAP conjugate. 83
Figure 1.16 - Chromatogram of the product of the manual synthesis of TCP-MAP, acquired with a HPLC system, with a C18 column, using ACN in water with 0.05% TFA as eluent, in gradient mode (0 – 100%), for 30 minutes, at a flow of 1 mL/min and detection at λ = 220 nm. 83
Figure 1.17 - Mass spectrum (LC-ESI/Orbitrap MS, positive mode) of the peptide TCP-MAP. 84

Chapter 2

Figure 2.1 - Schematic representation of different types of nanoparticles (NPs) divided into organic, hybrid and inorganic categories. 105
Figure 2.2 - Purification method implemented in Phase 3 of this thesis using Sephadex columns. 108
Figure 2.3 - Schematic representation of Phase 1 of optimization method to prepare nanoparticles SLN. 112
Figure 2.4 - DLS analysis particle size distribution of SLN – C (Yellow) and SLN – P (Orange). 113
Figure 2.5 - Relative cell viability of Caco-2 cell line measured by the MTT reduction after 2 and 4 h incubation. Treatment with free SLN – C and SLN - P at 1 % concentration. Results are expressed as mean SD (n = 3). Statistical analysis between the control group and other groups was performed using one-way ANOVA with Dunnet's post hoc test (* $p < 0.05$, ** $p < 0.01$). 114
Figure 2.6 - Schematic representation of Phase 2 of optimization method to prepared NLC. 115
Figure 2.7 - Preliminary surfactant toxicity against Caco-2 cell line. Treatment with Transcutol® HP (TE) and T80 at different concentrations and at different incubations time.

Statistical analysis between the control group and other groups was performed using one-way ANOVA with Dunnet's post hoc test (**** p < 0.0001). 118
Figure 2.8 - Calibration curve for TAC, obtained by plotting the absorbance of the drug in the function of its concentration in water solvent. 118
Figure 2.9 - Calibration curve for RAS, obtained by plotting the absorbance of the drug in the function of its concentration in water solvent. 119
Figure 2.10 - Calibration curve for TCP, obtained by plotting the absorbance of the drug in the function of its concentration in water solvent. 119
Figure 2.11 - Relative cell viability of Caco-2 cell line measured by the MTT reduction after 24 h incubation. Treatment with free TAC, blank NLC and NLC loaded with TAC (10 μM). Results are expressed as mean SEM (n = 4). Statistical analysis between the control group and other groups was performed using two-way ANOVA with Dunnet's post hoc test (** p <0.01; *** p <0.001; **** p <0.0001). 121
Figure 2.12 - Relative cell viability of Caco-2 cell line measured by the MTT reduction after 24 h incubation. Treatment with free RAS, blank NLC and NLC loaded with RAS (10 μM). Results are expressed as mean SEM (n = 4). Statistical analysis between the control group and other groups was performed using two-way ANOVA with Dunnet's post hoc test (** p <0.01). 121
Figure 2.13 - Relative cell viability of Caco-2 cell line measured by the MTT reduction after 24 h incubation. Treatment with free TCP, blank NLC and NLC loaded with TCP (10 μM). Results are expressed as mean SEM (n = 4). Statistical analysis between the control group and other groups was performed using two-way ANOVA with Dunnet's post hoc test (* p <0.05; ** p <0.01). 122
Figure 2.14 - Schematic representation of Phase 3 about optimization method for NLC nanoparticles. 123
Figure 2.15 - DLS analysis particle size distribution NLC Blank and drug loaded NLC. (blue) TAC, (orange) RAS and (green) TCP. 126
Figure 2.16 - Stability of encapsulated TAC in the formulations after 144 days in storage at 4 °C. 126
Figure 2.17 - Release profiles of TAC from Compritol® 888 ATO NLC in PBS, pH 7.4 and plasma 127
Figure 2.18 - Relative cell viability of SH-SY5Y cell line measured by the MTT reduction after 24 h incubation. Treatment with free TAC, blank NLC and NLC loaded with TAC (1–100 μM). Results are expressed as mean SD (n = 2). Statistical analysis between the control group and other groups was performed using two-way ANOVA with Dunnet's post hoc test (* p < 0.05; ** p <0.01; *** p <0.001; **** p <0.0001). 128

Figure 2.19 - Relative cell viability of SH-SY5Y cell line measured by the MTT reduction after 24 h incubation. Treatment with free TAC, blank NLC and NLC loaded with TAC (1–25 μM). Results are expressed as mean SD (n = 4). Statistical analysis between the control group and other groups was performed using two-way ANOVA with Dunnet's post hoc test (* p < 0.05; ** p <0.01; *** p <0.001; **** p <0.0001). 129
Figure 2.20 - Relative cell viability of SH-SY5Y cell line measured by the SRB reduction after 24 h incubation. Treatment with free TAC, blank NLC and NLC loaded with TAC (1–25 μM). Results are expressed as mean SEM (n = 4). Statistical analysis between the control group and other groups was performed using two-way ANOVA with Dunnet's post hoc test (*** p <0.001). 130
Figure 2.21 - Microscope cellular visualization through Lionheart FX of treatment with free TAC, different blank NLC formulations (CT20 B, CT25 B and CT30 B) and different NLC formulations loaded with TAC on SH-SY5Y cell line at a concentration of 10 μM. 131
Figure 2.22 - Cell count through Lionheart FX treatment with free TAC, blank NLC and NLC loaded with TAC (1–25 μM) for 24 h incubation. (** p <0.01; *** p <0.001; **** p <0.0001) 131
Figure 2.23 - Microscope cellular visualization through Lionheart FX (20x) of treatment with negative control (ultra-purified H_2O), positive control (10% DMSO), different blank NLC formulations (CT20 B, CT25 B and CT30 B) and different NLC formulations loaded with TAC on SH-SY5Y cell line at a concentration of 10, 20 and 25 μM. 132
Figure 2.24 - Relative cell viability of Caco-2 cell line measured by the MTT reduction after 24 h incubation. Treatment with free CNS drugs, blank NLC (CT25 B) and NLC loaded with drugs (1, 5 and 10 μM). Results are expressed as mean SD (n = 4). Statistical analysis between the control group and other groups was performed using two-way ANOVA with Dunnet's post hoc test (* p < 0.05; ** p <0.01; *** p <0.001; **** p <0.0001). 133
Figure 2.25 - Relative cell viability of Caco-2 cell line measured by the SRB reduction after 24 h incubation. Treatment with free CNS drugs, blank NLC (CT25 B) and NLC loaded with drugs (1, 5 and 10 μM). Results are expressed as mean SD (n = 4). Statistical analysis between the control group and other groups was performed using two-way ANOVA with Dunnet's post hoc test. 134
Figure 2.26 - Cell count through Lionheart FX treatment with free CNS drugs, blank NLC (CT25 B) and NLC loaded with CNS drugs (1, 5 and 10 μM) for 24 h incubation. Statistical analysis between the control group and other groups was performed using two-way ANOVA with Dunnet's post hoc test (* p <0.05; ** p <0.01). 135
Figure 2.27 - Microscope cellular visualization through Lionheart FX and Leica DFC350 FX of treatment with negative control (ultra-purified H_2O), positive control (10% DMSO),

free drugs, CT25 B and CT25 loaded with different CNS drugs on Caco-2 cell line at a concentration of 1, 5 and 10 μM. 137

Chapter 3

Figure 3.1 - Schematic representation of recent CPP-based strategies. This dual conjugation of CPP, nanoparticle and effector (cargo) can further potentiate the therapeutic effectiveness and enhance stability. 143
Figure 3.2 - An overview of the major hallmark events leading to AD such as amyloid hypothesis, Tau hyperphosphorylation, neuroinflammation, and excitotoxicity. Amyloid hypothesis begins with an imbalance between aβ production and clearance which leads to an increase of aβ production. Gradual accumulation of aβ leads to the formation of aβ oligomers followed by the formation of aβ plaque with direct impairment of neuronal, synaptic function (neurotoxicity), microglia and astrocyte activation with release of cytokines (neuro- inflammation), increase of reactive oxygen species (excitotoxicity), and induce Tau hyperphosphorylation. 145
Figure 3.3 - Overview of acetylcholinesterase inhibitors mechanisms of action and respective molecular structure of AD drugs referred in the present review; ACh, acetylcholine; AChE, acetylcholinesterase; ChTA, choline acetyltransferase; AcCoA, acetyl–ScoA (derived from mitochondria) 146
Figure 3.4 - Schematic representation of the major hallmark events leading to Parkinson's disease with the formation of Lewis bodies, ubiquitin proteosome system (UPS) dysfunction, neuroinflammation, and synaptic disruption with neurodegeneration. Endoplasmic reticulum (ER); alfa-synuclein (α-syn). 148
Figure 3.5 - The current Parkinson's disease treatment introduced to recently diagnosed patients. 149
Figure 3.6 - PD pharmacotherapy mechanism and sites of action. COMT: Catechol o-methyltransferase; MAO-B: mono-amide oxidase B. Aromatic L-amino acid decarboxylase (AADC); Catechol o-methyltransferase (COMT); mono-amide oxidase B (MAO-B); Dopamine receptors (DR); dihydroxyphenyl acetic acid (DOPAC). 150
Figure 3.7 - MCF-7 breast cancer and SH-SY5Y cell line cytotoxic effects of increasing concentrations of TAC, and TAC-MAP after a 24 h incubation. H_2O was used in control. Significant differences (ANOVA test, followed by the with Dunnett's post hoc test): * $p < 0.05$, ** $p < 0.01$, *** $p < 0.001$ and **** $p < 0.0001$ vs. Control. The values represent mean ± SEM (n = 3). 161

Figure 3.8 - Cell count through Lionheart FX treatment of MCF-7 and SH-SY5Y cell lines with TAC and TAC-MAP (1, 2.5, 5, and 10 μM) after 24h incubation (*n* = 1). 2.5. Determination of IC_{50} and cell count analysis of TAC, MAP, and TAC-MAP against MCF-7. 162

Figure 3.9 - Dose-response curves (from triplicates) of MCF-7 cells viability with increasing concentrations of MAP (left plot) and TAC-MAP (right plot). IC_{50} values thus determined are shown next to the respective curves. The values represent mean ± SD (n = 3). 163

Figure 3.10 - Cell count through Lionheart FX treatment of MCF-7 lines with TAC, MAP, and TAC-MAP (1-25 μM) after 24 h incubation (n = 1). 163

Figure 3.11 - Micrographs (Lionheart FX of phase-contrast images) obtained for MCF-7 cells after a 24 h period of incubation with TAC, MAP, and TAC-MAP conjugate at different concentrations. 165

Figure 3.12 - Dose-effect curves of TAC, MAP, and TAC-MAP estimated by the unified theory using CompuSyn software. The dose was plotted on the y-axis as a function of effect level (Fa) on the x-axis to assess each drug behavior. Doses below the red arrow indicate better activity of TAC-MAP conjugate than MAP and TAC alone. Experiments were conducted in triplicate (n = 3). 166

Figure 3.13 - Relative cell viability of Caco-2 cell line measured by the MTT reduction after 24 h incubation. Treatment with free MAP, Lys(N_3)-MAP, TAC-MAP, TCP-MAP and RAS-MAP (0.25 μM-10 μM). Results are expressed as mean ±SD (n = 3 or 6). Statistical analysis between the control groups was performed using two-way ANOVA with Tukey's multiple comparisons test (* p <0.05; *** p <0.001; **** p <0.0001). 169

Figure 3.14 - The effect of MAP and Lys(N_3)-MAP on Caco-2 cell line dose-response curve. Each point is the average of at least three independent experiments. 170

Figure 3.15 - Microscope cellular visualization through Lionheart FX and Leica DFC350 FX of treatment with negative control (ultra-purified H_2O), positive control (10% DMSO), free peptides and conjugates on Caco-2 cell line at a concentration of 0.25, 0.5, 1, 5 and 10 μM. 171

Figure 3.16 - Relative cell viability of Caco-2 cell line measured by the MTT reduction after 24h incubation. (A) represents NLC safety test with the treatment of free TCP, blank CT25 and TCP loaded CT25 (0.25-10 μM). (B) Represents differences in the cell viability of treatment with free TCP, TCP-MAP, blank CT25, TCP loaded CT25, MAP, TCP-MAP loaded CT25 (0.25-10 μM). (C) Represents co-administration of TCP and TCP-MAP with blank CT25 (1-10 μM). (D) Represents the data obtained from the encapsulation of Lys(N_3)-MAP and co-encapsulation of TCP and Lys(N_3)-MAP in the NLC compared to peptide conjugate. Results are expressed as mean ±SD (n = 4). Statistical analysis

between the groups was performed using two-way ANOVA with Tukey's multiple comparisons test (* p <0.05; ** p <0.01; *** p <0.001; **** p <0.0001). _____ 172
Figure 3.17 - The effect of TCP-MAP, CT25TCP-MAP, CT25 Lys(N_3)-MAP and CT25 TCP + Lys(N_3)-MAP on Caco-2 cell line dose-response curve. Each point is the average of at least three independent experiments._____ 173
Figure 3.18 - Microscope cellular visualization through Leica DFC350 FX of treatment with negative control (ultra-purified H_2O), positive control (10% DMSO), free drug and NLC loaded formulations on Caco-2 cell line at a concentration of 0.25, 0.5 and 1 μM. 174
Figure 3.19 - Relative cell viability of Caco-2 cell line measured by the MTT reduction after 24h incubation. (A) represents NLC safety test with the treatment of free RAS, blank CT25 and RAS loaded CT25 (0.25-10 μM). (B) Represents differences in the cell viability of treatment with free RAS, RAS-MAP, blank CT25, RAS loaded CT25, MAP, RAS-MAP loaded CT25 (0.25-10 μM). (C) Represents co-administration of RAS and RAS-MAP with blank CT25 (1-10 μM). (D) Represents the data obtained from the encapsulation of Lys(N_3)-MAP and co-encapsulation of RAS and Lys(N_3)-MAP in the NLC compared to peptide conjugate. Results are expressed as mean ±SD (n = 4 or 6). Statistical analysis between the groups was performed using two-way ANOVA with Tukey's multiple comparisons test (* p <0.05; ** p <0.01; *** p <0.001; **** p <0.0001). _____ 175
Figure 3.20 - The effect of RAS-MAP, CT25RAS-MAP, CT25 Lys(N_3)-MAP and CT25 RAS + Lys(N_3)-MAP on Caco-2 cell line dose-response curve. Each point is the average of at least three independent experiments._____ 176
Figure 3.21 - Microscope cellular visualization through Leica DFC350 FX of treatment with negative control (ultra-purified H_2O), positive control (10% DMSO), free drug and NLC loaded formulations on Caco-2 cell line at a concentration of 0.25, 0.5 and 1 μM. 177
Figure 3.22 - Relative cell viability of Caco-2 cell line measured by the MTT reduction after 24h incubation. (A) represents NLC safety test with the treatment of free TAC, blank CT25 and TAC loaded CT25 (0.25-10 μM). (B) Represents differences in the cell viability of treatment with free TAC, TAC-MAP, blank CT25, TAC loaded CT25, MAP, TAC-MAP loaded CT25 (0.25-10 μM). (C) Represents co-administration of TAC and TAC-MAP with blank CT25 (1-10 μM). (D) Represents the data obtained from the encapsulation of Lys(N_3)-MAP and co-encapsulation of TAC and Lys(N_3)-MAP in the NLC compared to peptide conjugate. Results are expressed as mean ±SD (n = 4). Statistical analysis between the groups was performed using two-way ANOVA with Tukey's multiple comparisons test (* p <0.05; ** p <0.01; *** p <0.001; **** p <0.0001). _____ 178
Figure 3.23 - The effect of TAC-MAP, CT25TAC-MAP, CT25 Lys(N_3)-MAP and CT25TAC + Lys(N_3)-MAP on Caco-2 cell line dose-response curve. Each point is the average of at least three independent experiments._____ 179

Figure 3.24 - Microscope cellular visualization through Lionheart FX and Leica DFC350 FX of treatment with negative control (ultra-purified H_2O), positive control (10% DMSO), free drug and NLC loaded formulations on Caco-2 cell line at a concentration of 0.25, 0.5, 1, 5 and 10 μM. 180
Figure 3.25 - Relative cell viability of SH-SY5Y cell line measured by the MTT reduction after 24 h incubation. Treatment with free MAP, Lys(N_3)-MAP, TAC-MAP, TCP-MAP and RAS-MAP (0,25 μM-10 μM). Results are expressed as mean ±SD (n = 3 or 6). Statistical analysis between the control groups was performed using two-way ANOVA with Tukey's multiple comparisons test (* p <0.05; *** p <0.001; **** p <0.0001). 181
Figure 3.26 - The effect of MAP SH-S5Y5 cell line dose-response curve. Each point is the average of at least three independent experiments. 182
Figure 3.27 - Microscope cellular visualization through Lionheart FX and Leica DFC350 FX of treatment with negative control (ultra-purified H_2O), positive control (10% DMSO), free peptides and conjugates on SH-SY5Y cell line at a concentration of 0.25, 0.5, 1, 5 and 10 μM 183
Figure 3.28 - Relative cell viability of SH-SY5Y cell line measured by the MTT reduction after 24 h incubation. (A) represents NLC safety test with the treatment of free TCP, blank CT25 and TCP loaded CT25 (0.25-10 μM). (B) Represents differences in the cell viability of treatment with free TCP, TCP-MAP, blank CT25, TCP loaded CT25, MAP, TCP-MAP loaded CT25 (0.25-10 μM). (C) Represents co-administration of TCP and TCP-MAP with blank CT25 (1-10 μM). (D) Represents the data obtained from the encapsulation of Lys(N_3)-MAP and co-encapsulation of TCP and Lys(N_3)-MAP in the NLC compared to peptide conjugate. Results are expressed as mean ±SD (n = 4). Statistical analysis between the groups was performed using two-way ANOVA with Tukey's multiple comparisons test (* p <0.05; ** p <0.01; **** p <0.0001). 184
Figure 3.29 - The effect of TCP-MAP, CT25TCP-MAP, CT25 Lys(N_3)-MAP and CT25 TCP + Lys(N_3)-MAP on SH-S5Y5 cell line dose-response curve. Each point is the average of at least three independent experiments. 185
Figure 3.30 - Microscope cellular visualization through Leica DFC350 FX of treatment with negative control (ultra-purified H_2O), positive control (10% DMSO), free drug and NLC loaded formulations on SH-SY5Y cell line at a concentration of 0.25, 0.5 and 1 μM. 186
Figure 3.31 - Relative cell viability of SH-SY5Y cell line measured by the MTT reduction after 24 h incubation. (A) represents NLC safety test with the treatment of free RAS, blank CT25 and RAS loaded CT25 (0.25-10 μM). (B) Represents differences in the cell viability of treatment with free RAS, RAS-MAP, blank CT25, RAS loaded CT25, MAP, RAS-MAP loaded CT25 (0.25-10 μM). (C) Represents co-administration of RAS and RAS-MAP with

blank CT25 (1-10 μM). (D) Represents the data obtained from the encapsulation of Lys(N_3)-MAP and co-encapsulation of RAS and Lys(N_3)-MAP in the NLC compared to peptide conjugate. Results are expressed as mean ±SD (n = 4). Statistical analysis between the groups was performed using two-way ANOVA with Tukey's multiple comparisons test (* p <0.05; ** p <0.01; *** p <0.001; **** p <0.0001). 187

Figure 3.32 - The effect of RAS-MAP, CT25RAS-MAP, CT25 Lys(N_3)-MAP and CT25 RAS + Lys(N_3)-MAP on SH-S5Y5 cell line dose-response curve. Each point is the average of at least three independent experiments. 188

Figure 3.33 - Microscope cellular visualization through Leica DFC350 FX of treatment with negative control (ultra-purified H_2O), positive control (10% DMSO), free drug and NLC loaded formulations on SH-SY5Y cell line at a concentration of 0.25, 0.5 and 1 μM. 189

Figure 3.34 - Relative cell viability of SH-SY5Y cell line measured by the MTT reduction after 24 h incubation. (A) represents NLC safety test with the treatment of free TAC, blank CT25 and TAC loaded CT25 (0.25-10 μM). (B) Represents differences in the cell viability of treatment with free TAC, TAC-MAP, blank CT25, TAC loaded CT25, MAP, TAC-MAP loaded CT25 (0.25-10 μM). (C) Represents co-administration of TAC and TAC-MAP with blank CT25 (1-10 μM). (D) Represents the data obtained from the encapsulation of Lys(N_3)-MAP and co-encapsulation of TAC and Lys(N_3)-MAP in the NLC compared to peptide conjugate. Results are expressed as mean ±SD (n = 4). Statistical analysis between the groups was performed using two-way ANOVA with Tukey's multiple comparisons test (* p <0.05; ** p <0.01; *** p <0.001; **** p <0.0001). 190

Figure 3.35 - The effect of TAC-MAP, CT25TAC-MAP, CT25 Lys(N_3)-MAP and CT25 TAC + Lys(N_3)-MAP on SH-S5Y5 cell line dose-response curve. Each point is the average of at least three independent experiments. 191

Figure 3.36 - Microscope cellular visualization through Lionheart FX and Leica DFC350 FX of treatment with negative control (H_2O), positive control (10% DMSO), free drug and NLC loaded formulations on SH-SY5Y cell line at a concentration of 0.25, 0.5, 1, 5 and 10 μM. 192

Chapter 4

Figure 4.1 - Graphical representation of adsorption method applied with the three peptides, NLCs, different concentrations, and medium conditions conducted in this project. 209

Figure 4.2 - Particle size, polydispersity index, and zeta potential of blank CT25 NLC before and after adsorption experiments with different peptide concentrations of Lys(N_3)-MAP at 37 °C with incubation in ultra-purified double distilled water (H_2O dd); mean ± SD, *n* = 3. Statistical analysis between the control groups was performed using two-way ANOVA with Tukey's multiple comparisons test (* $p < 0.05$; ** $p < 0.01$; **** $p < 0.0001$). 212

Figure 4.3 - Particle size, polydispersity index and zeta potential of CT25 B and drug load CT25 NLC before and after adsorption experiments with 0.8 mg/mL Lys(N_3)-MAP at 37 °C with incubation in H_2O dd; mean ± SD, n = 3. Statistical analysis between the control groups was performed using two-way ANOVA with Tukey's multiple comparisons test (* $p < 0.05$; **** $p < 0.0001$). 213

Figure 4.4 - Particle size, polydispersity index and zeta potential of blank CT25 NLC before and after adsorption experiments with different TAC-MAP concentrations at 37 °C with incubation in H_2O dd; mean ± SD, *n* = 3. Statistical analysis between the control groups was performed using two-way ANOVA with Tukey's multiple comparisons test (** $p < 0.01$; **** $p < 0.0001$). 214

Figure 4.5 - Particle size, polydispersity index and zeta potential of different initial amount of blank CT25 NLC before and after adsorption experiments with 0.5 mg/mL TAC-MAP at 37 °C with incubation in H_2O dd; mean ± SD, *n* = 3. Statistical analysis between the control groups was performed using two-way ANOVA with Tukey's multiple comparisons test (**** $p < 0.0001$). 215

Figure 4.6 - Particle size, polydispersity index, and zeta potential of blank CT25 NLC before and after adsorption experiments with 0.5 mg/mL Lys(N_3)-MAP and 0.5 mg/mL TAC-MAP at 37 °C with different incubation medium H_2O dd and PBS; mean ± SD, *n* = 3. Statistical analysis between the control groups was performed using two-way ANOVA with Tukey's multiple comparisons test (**** $p < 0.0001$). 216

Figure 4.7 - Particle size, polydispersity index, and zeta potential of CT25 B and drug load CT25 NLC before and after adsorption experiments with NPY at 37 °C with incubation in H_2O dd; mean ± SD, *n* = 3. Statistical analysis between the control groups was performed using two-way ANOVA with Tukey's multiple comparisons test (**** $p < 0.0001$). 216

Figure 4.8 - Schematic representation of three hypotheses occurring through the data obtain in this project to explain the differences on particle size and PDI observed. 218

Chapter 5

Figure 5.1 - Validation of the docking protocol by redocking UR-MK299 against NPY1R. In cyan, the conformation predicted from docking. In yellow the X-ray crystallography conformation. Slab-view representation, showing the plane of the interior binding pocket. 230

Figure 5.2 - Representation of the volume occupied by MAP, NPY and antagonist UR-MK299 when complexed with NPY1R, illustrating the different binding modes predicted for the two peptides and the one observed in the x-Ray of the complex formed with the antagonist molecule. 231

Figure 5.3 - Slab-view representation of the interaction of MAP and NPY with NPY1R, illustrating the most important interactions established. 232

Supplementary Information

Figure S1.1 - Schematic representation of conjugate Ras-MAP-resin formation through click reaction (CuAAC); Structure of Ras-MAP conjugate. 243

Figure S1.2 - Chromatogram of synthetic crude of Pra-MAP (**2**), acquired with a HPLC system, with a C18 column, using ACN and acidified water (0.05% TFA) as eluent, in gradient mode (0 – 100%), for 30 minutes, at a flow rate of 1 mL/min and detection at λ = 220 nm. 244

Figure S1.3 - MALDI-TOF mass spectrometry of synthetic crude of Pra-MAP 245

Figure S1. 4 - Schematic representation of synthesis of conjugate TAC-linker-Cl 245

Figure S1.5 - Mass spectrum (LC-ESI/Orbitrap MS, positive mode) of the TAC-linker-Cl. 246

Figure S1.6 - H NMR of TAC-linker-Cl. ^{1}H NMR (400 MHz, $CDCl_3$) δ(ppm) 8.52 (s, 1H), 8.00 (d, *J* = 8.4 Hz, 1H), 7.75 (d, *J* = 8.4 Hz, 1H), 7.67 – 7.57 (m, 1H), 7.51 – 7.41 (m, 1H), 4.34 (s, 2H), 3.13 (t, *J* = 6.5 Hz, 2H), 2.80 (t, *J* = 6.4 Hz, 2H), 2.01 – 1.90 (m, 2H), 1.89 – 1.81 (m, 2H). 246

Figure S1.7 - Schematic representation of conjugate TAC-linker-N_3 247

Figure S1.8 - Mass spectrum (LC-ESI/Orbitrap MS, positive mode) of TAC-linker-N_3. 247

Figure S1.9 - 1H NMR of TAC-linker-N_3. 1H NMR (400 MHz, CD3OD) δ(ppm) 7.92 (dd, J = 14.4, 8.4 Hz, 2H), 7.72 – 7.66 (m, 1H), 7.57 – 7.51 (m, 1H), 4.25 (s, 2H), 3.12 (t, J = 6.5 Hz, 2H), 2.84 (t, J = 6.5 Hz, 2H), 2.01 – 1.94 (m, 2H), 1.92 – 1.84 (m, 2H). 248

Figure S1.10 - ^{1}H NMR of TAC-linker-N_3. ^{13}C NMR (101 MHz, CD_3OD) δ 169.11 (C=O), 161.01 (C), 146.98 (C), 140.99 (C), 130.63 (CH), 129.61 (CH), 127.91 (CH), 127.54 (CH), 125.47 (CH), 123.85 (CH), 52.99 (CH_2), 34.08 (CH_2), 26.18 (CH_2), 23.43 (CH_2), 23.22 (CH_2). 248
Figure S1.11 - Schematic representation of conjugate TCP-linker-N_3. 249
Figure S1.12 - Mass spectrum (LC-ESI/Orbitrap MS, positive mode) of 2-TCP-linker-N_3. 250
Figure S1.13 - ^{1}H NMR (400 MHz, MeOD) δ(ppm) 7.27 – 7.23 (m, 2H), 7.17 – 7.13 (m, 2H), 3.85 (s, 2H), 2.87 (m, 1H), 2.09 – 2.05 (m, 1H), 1.23 – 1.19 (m, 2H). 250
Figure S1.14 - HMBC- ^{15}N (CD_3OD). 251
Figure S1.15 - NMR (101 MHz, MeOD) δ(ppm) 171.35 (C=O), 142.09 (C), 129.40 (2xCH), 127.34 (3xCH), 127.10 (CH_2), 52.89 (CH_2), 33.21 (CH), 25.16 (CH), 15.94 (CH_2). 251

Figure S2. 1 - Protocol implemented to establish and isolate a primary neuronal cell line. 253
Figure S2. 2 - Microscope images of identified neurons isolated from the experiment and protocol applied at different days *in vitro* (DIV). 255
Figure S2. 3 - Microscope images of possible astrocytes wrongly isolated from the experiment and protocol applied at different days *in vitro* (DIV). 255
Figure S2. 4 - Microscope images of cellular contamination and excess of tissue debris in the experiment conducted. 256
Figure S2. 5 - Microscope cellular visualization through Lionheart FX of treatment with negative control (ultra-purified H_2O), positive control (10% DMSO), free TAC, CT25 B and CT25 TAC on SH-SY5Y cell line at a concentration of 1-100 µM. 257
Figure S2. 6 - Microscope cellular visualization through Lionheart FX of treatment with negative control (ultra-purified H_2O), positive control (10% DMSO), different blank NLC formulations (CT20 B, CT25 B and CT30 B) and different NLC formulations loaded with TAC on SH-SY5Y cell line at a concentration of 1, 2.5, 5, 10, 20 and 25 µM. 258

Figure S3. 1 - Representation of the results obtain in the UV-Vis analysis. 259
Figure S3. 2 - Final protocol implemented to conduct Fluorescamine Assay. 260
Figure S3. 3 - Results obtain from Fluorescamine protocol optimization using Glycine as control. (A) determine the suitable pH needed to conduct the experiment. (B) concentration-dependent graphic; (C) Fluorescamine fluorescent decay at different time; (D) Fluorescamine RFU analysis with different volumes applied. 261

Figure S3. 4 - Representation of RFU values in crescent concentrations (μM) of Glycine through fluorescamine assay. 261
Figure S3. 5 - Relative cell viability of Caco-2 cell line measured by the SRB assay after 24 h incubation. Treatment with free MAP, Lys(N_3)-MAP, TAC-MAP, TCP-MAP and RAS-MAP (0.25 μM-10 μM). Results are expressed as mean ± SD (n = 3 or 6). Statistical analysis between the control groups was performed using two-way ANOVA with Tukey's multiple comparisons test (* p <0.05; ** p <0.01; *** p <0.001; **** p <0.0001). 262
Figure S3. 6 - Relative cell viability of Caco-2 cell line measured by the SRB assay after 24 h incubation. (A) represents NLC safety test with the treatment of free TCP, blank CT25 and TCP loaded CT25 (0.25-10 μM). (B) Represents differences in the cell viability of treatment with free TCP, TCP-MAP, blank CT25, TCP loaded CT25, MAP, TCP-MAP loaded CT25 (0.25-10 μM). (C) Represents co-administration of TCP and TCP-MAP with blank CT25 (1-10 μM). (D) Represents the data obtained from the encapsulation of Lys(N_3)-MAP and co-encapsulation of TCP and Lys(N_3)-MAP in the NLC compared to peptide conjugate. Results are expressed as mean ± SD (n = 4). Statistical analysis between the groups was performed using two-way ANOVA with Tukey's multiple comparisons test (* p <0.05; ** p <0.01; *** p <0.001; **** p <0.0001). 263
Figure S3. 7 - Relative cell viability of Caco-2 cell line measured by the SRB assay after 24 h incubation. (A) represents NLC safety test with the treatment of free RAS, blank CT25 and RAS loaded CT25 (0.25-10 μM). (B) Represents differences in the cell viability of treatment with free RAS, RAS-MAP, blank CT25, RAS loaded CT25, MAP, RAS-MAP loaded CT25 (0.25-10 μM). (C) Represents co-administration of RAS and RAS-MAP with blank CT25 (1-10 μM). (D) Represents the data obtained from the encapsulation of Lys(N_3)-MAP and co-encapsulation of RAS and Lys(N_3)-MAP in the NLC compared to peptide conjugate. Results are expressed as mean ± SD (n = 4). Statistical analysis between the groups was performed using two-way ANOVA with Tukey's multiple comparisons test (* p <0.05; ** p <0.01; *** p <0.001; **** p <0.0001). 264
Figure S3. 8 - Relative cell viability of Caco-2 cell line measured by the SRB assay after 24 h incubation. (A) represents NLC safety test with the treatment of free TAC, blank CT25 and TAC loaded CT25 (0.25-10 μM). (B) Represents differences in the cell viability of treatment with free TAC, TAC-MAP, blank CT25, TAC loaded CT25, MAP, TAC-MAP loaded CT25 (0.25-10 μM). (C) Represents co-administration of TAC and TAC-MAP with blank CT25 (1-10 μM). (D) Represents the data obtained from the encapsulation of Lys(N_3)-MAP and co-encapsulation of TAC and Lys(N_3)-MAP in the NLC compared to peptide conjugate. Results are expressed as mean ± SD (n = 4). Statistical analysis between the groups was performed using two-way ANOVA with Tukey's multiple comparisons test (* p <0.05; ** p <0.01; *** p <0.001; **** p <0.0001). 265

Figure S3. 9 - Microscope cellular visualization through Lionheart FX and Leica DFC350 FX of treatment with free drug and NLC loaded formulations on Caco-2 cell line at a concentration of 0.25, 0.5, 1, 5 and 10 μM. 266
Figure S3. 10 - Microscope cellular visualization through Lionheart FX and Leica DFC350 FX of treatment with free drug and NLC loaded formulations on Caco-2 cell line at a concentration of 1, 5 and 10 μM. 267
Figure S3. 11 - Relative cell viability of SH-SY5Y cell line measured by the SRB assay after 24 h incubation. Treatment with free MAP, Lys(N_3)-MAP, TAC-MAP, TCP-MAP and RAS-MAP (0.25 μM-10 μM). Results are expressed as mean ± SD (n = 3 or 6). Statistical analysis between the control groups was performed using two-way ANOVA with Tukey's multiple comparisons test (** p <0.01; **** p <0.0001). 268
Figure S3. 12 - Relative cell viability of SH-SY5Y cell line measured by the SRB assay after 24 h incubation. (A) represents NLC safety test with the treatment of free TCP, blank CT25 and TCP loaded CT25 (0.25-10 μM). (B) Represents differences in the cell viability of treatment with free TCP, TCP-MAP, blank CT25, TCP loaded CT25, MAP, TCP-MAP loaded CT25 (0.25-10 μM). (C) Represents co-administration of TCP and TCP-MAP with blank CT25 (1-10 μM). (D) Represents the data obtained from the encapsulation of Lys(N_3)-MAP and co-encapsulation of TCP and Lys(N_3)-MAP in the NLC compared to peptide conjugate. Results are expressed as mean ± SD (n = 4). Statistical analysis between the groups was performed using two-way ANOVA with Tukey's multiple comparisons test (* p <0.05; ** p <0.01; *** p <0.001; **** p <0.0001). 269
Figure S3. 13 - Relative cell viability of SH-SY5Y cell line measured by the SRB assay after 24 h incubation. (A) represents NLC safety test with the treatment of free RAS, blank CT25 and RAS loaded CT25 (0.25-10 μM). (B) Represents differences in the cell viability of treatment with free RAS, RAS-MAP, blank CT25, RAS loaded CT25, MAP, RAS-MAP loaded CT25 (0.25-10 μM). (C) Represents co-administration of RAS and RAS-MAP with blank CT25 (1-10 μM). (D) Represents the data obtained from the encapsulation of Lys(N_3)-MAP and co-encapsulation of RAS and Lys(N_3)-MAP in the NLC compared to peptide conjugate. Results are expressed as mean ± SD (n = 4). Statistical analysis between the groups was performed using two-way ANOVA with Tukey's multiple comparisons test (* p <0.05; ** p <0.01; **** p <0.0001). 270
Figure S3. 14 - Relative cell viability of SH-SY5Y cell line measured by the SRB assay after 24 h incubation. (A) represents NLC safety test with the treatment of free TAC, blank CT25 and TAC loaded CT25 (0.25-10 μM). (B) Represents differences in the cell viability of treatment with free TAC, TAC-MAP, blank CT25, TAC loaded CT25, MAP, TAC-MAP loaded CT25 (0.25-10 μM). (C) Represents co-administration of TAC and TAC-MAP with blank CT25 (1-10 μM). (D) Represents the data obtained from the encapsulation of

Lys(N_3)-MAP and co-encapsulation of TAC and Lys(N_3)-MAP in the NLC compared to peptide conjugate. Results are expressed as mean ± SD (n = 4). Statistical analysis between the groups was performed using two-way ANOVA with Tukey's multiple comparisons test (* p <0.05; ** p <0.01; **** p <0.0001). 271
Figure S3. 15 - Microscope cellular visualization through Lionheart FX and Leica DFC350 FX of treatment with free drug and NLC loaded formulations on SH-SY5Y cell line at a concentration of 0.25, 0.5, 1, 5 and 10 μM. 272
Figure S3. 16 - Microscope cellular visualization through Lionheart FX and Leica DFC350 FX of treatment with free drug and NLC loaded formulations on SH-SY5Y cell line at a concentration of 0.25, 0.5, 1, 5 and 10 μM. 273

List of tables

Table 1.1 - Structure representation and physical-chemical proprieties of peptides used in this Thesis. 84

Table 2.1 - Physicochemical properties of: empty nanostructured lipid carrier (SLN) (mean SD, n = 3).....113
Table 2.2 - Maximum solubilization concentration achieve for Transcutol® HP of TAC, TCP and RAS. 116
Table 2.3 - Physicochemical properties of: Phase 2 empty NLC, TAC-loaded NLC, RAS-loaded NLC and TCP-loaded NLC freshly prepared (mean SD, n = 2). 120
Table 2.4 - Physicochemical properties of: Phase 3 empty nanostructured lipid carrier (NLC), TAC-loaded NLC, RAS-loaded NLC and TCP-loaded NLC freshly prepared (mean SD, n = 2).....124

Table 3.1 - Physicochemical properties of all NLCs formulated freshly (mean SD, n = 4 or 6).....168

Table 4.1 - Resume data analysis from all the adsorption experiments conducted in this article. 212

Table 5.1 - Docking scores of UR-MK299, MAP and NPY on NPY1R.....231

Abbreviations

(DSPE)-PEG – distearoylphosphatidylethanolamine

AChE - Acetylcholinesterase

AChEI - Acetylcholinesterase inhibitors

ACN – Acetonitrile

ACPP - activable CPP

AD - Alzheimer's disease

AgNP - Silver NP

AuNP - Gold NP

aβ - Amyloid peptide

BBB – Blood brain barrier

CBD3 - Ca2+ channel binding domain 3

CNPs - Carbon- based NP

CNS - Central nervous system

CPPs – cell penetrating peptides

CSF - Cerebrospinal fluid

CuAAC - Copper(I)-catalyzed azide alkyne cycloaddition

DA – Dopamine

DCM – Dichloromethane

DL - Drug loading

DLS - Dynamic light scattering

DMF – Dimethylformamide

DMSO - Dimethyl sulfoxide

DOX – Doxorubicin

EE – Encapsulation efficiency

ESI-MS - Electrospray ionization mass spectrometry

FBS - Fetal bovine serum

Fmoc - 9 fluorenyl methoxycarbonyl

HBTU - Hexafluorophosphate benzotriazole tetramethyluronium

HPLC - high-performance liquid chromatography

HSH - high shear homogenization

IN – Intra-nasal

IV - Intra-venous

LC/MS - Liquid chromatography–mass spectrometry

MAO-B – Monoamide oxidase

MAP - Model amphipathic peptide

MeOH – Methanol

MMP - metalloproteinase

mPEG-PCL - Methoxypoly (ethylene glycol) /poly(caprolactone)

MTT - 3-(4,5-dimethyl-2-thiazolyl)-2,5-dipheny-2H-tetrazolium bromide

NLC - Nanostructure lipid carriers

NMDA - N-methyl-D-aspartate

NP – Nanoparticles

NPY - Neuropeptide Y

NPY1R - Neuropeptide Y receptor type 1

pAntp - Drosophila antennapedia homeobox sequence

PBCA - Poly(n-butylcyanoacrylate)

PBS - Phosphate buffer solution

PD – Parkinson disease

PEG - poly(ethylene glycol)

PEG-PCL - PEG-poly(ε-caprolactone)

PF68 - Pluronic F68

PI - Polydispersity index

RAS – Rasagiline

RR – arginine and arginine

Rt - Retention time

SERS - Surface-enhanced Raman spectroscopy

SLN - Solid lipid NPs

SPPS – Solid Phase Peptide Synthesis

SRB - Sulfarhodamine B sodium

T80 - Polysorbate 80

TAC – Tacrine

tBu - Tert-butyl

TCA - Trichloroacetic acid

TCP – tranylcypromine

TFA - Trifluoroacetic acid

TJ – Tight junctions

TPP - Sodium tripolyphosphate

UHPLC - Ultra-high-performance liquid chromatograph

ZP - Zeta potential

α-syn - Alpha-synuclein

Chapter 1
Peptide Synthesis

1.1 Introduction

1.1.1. Cell-penetrating peptides

The limited ability of current drugs to achieve penetration of the interior of the cell has contributed to their lack of biological action, decreased therapeutic efficacy and enhanced toxicity. These limitations have potentiated the development of alternative strategies, routes, vectors of delivery and administration methods. Over the last years, different cellular translocation techniques have been developed including physical methods—electroporation and microinjection; chemical methods—calcium phosphate; and viral vectors. However, these methods have been considered highly toxic to cells, thus, decreasing the cellular viability and potentiating viral recombination in the case of viral vectors (1). Ongoing research has discovered some protein transduction domains of peptides that are capable of translocating cell membrane efficiently without compromising their integrity (2). These are cell-penetrating peptides (CPPs), normally with a maximum length of 30 amino acid residues and are characterized by a high content of basic amino acid residues, resulting in an overall positive net charge. CPPs are advantageous over other translocation methods because they possess high cellular permeability rates, ability to translocate into a wide spectrum of cell types, large cargo capacity and low cell toxicity associated with no immunological response (3).

The first CPP, discovered in 1988, by Frankel and his team was HIV-Tat protein responsible for virus replication and considered a powerful transactivation factor of viral and cellular gene expression (4). HIV-Tat of 86 amino acid residues act as a viral growth factor and is taken up by the cells (4). Some years later, Vives and his team recognized the domain responsible for the rapid penetration of this peptide through plasma membrane—the truncated version of the HIV-Tat basic domain (5). In addition, Drosophila antennapedia homeobox sequence (pAntp) was reported as capable of entering nerve cells and accumulating in the nucleus (6). In 1994, Derossi and his team identified Penetratin, a 16-mer peptide derived from the C-terminal region of the third helix of the homeodomain of Antennapedia and capable of penetrating cells (7,8). The discovery of these two peptides with penetrating activities prompted more studies and the discovery of new CPPs. Over the next years, more CPPs were added to the list and nowadays a database has been built that

permits one to browse existing CPPs based on chemical modifications, category, cargo or peptide length (9) (Table 1).

CPP can be divided into different categories depending on the origin (protein-derived, synthetic, and chimeric CPP), conformation (linear or cyclic) and physicochemical properties (cationic, amphipathic and hydrophobic CPP) (10). The positive charge of cationic CPPs demonstrated strong electrostatic interactions with negative cytoplasmic membranes that leads to cellular internalization. These CPP sequence often present increased number of positively charged arginine's and contain more than five positively charge amino acids (11). There is few hydrophobic CPPs, still is sequence possess an increased number of non-polar residues (such as alanine, leucine, proline, valine and more) and a few charged amino acids. The most common CPPs discovered are the amphipathic CPPs, which contains both polar and non-polar amino acid regions and often adopt a secondary structure and bind to the membranes depending on the overall conditions (10,12).

1.1.2. Mechanisms of entrance inside cells

The exact mechanism of CPPs cell penetration still remains unknown (13). Over the years, some discrepancies between studies have generated controversial data. A variety of features and conditions are crucial to the efficiency of cellular translocation and mode of penetration, and influence the different outcomes observed, such as cargo, cell type, incubation time, sample handling (washing, fixation, delays), fluorophore, CPPs concentration, cell density, stage of cell cycle, read out (uptake distribution), etc (14–16). One of the first problems reported was the over-quantification of peptide uptake, and respective localization in the interior of the cell. The experimental fixation procedure, even when mild conditions were applied, lead to wrong statements about direct translocation for all the peptides (17). The cell sort flow cytometry presented another problem with overestimated uptake, since, at the time it was not possible to differentiate between membrane bound peptides and peptides in the interior of the cell without previous treatment with trypsin (17,18). Before 2003, direct penetration was considered the main route for CPPs penetration, until some authors assumed a possible misleading error found in the fixation protocol when comparing the results with those observed for living cells, which questioned the possibility of the existence of other types of endocytic mechanisms inherent to CPPs (18), and demanded an extra revaluation of the mechanism of CPPs penetration. Nowadays, many authors have investigated the mechanism of cell uptake and it has become clear that different pathways can be used by CPPs depending on the conditions

(19), and different effects on cellular membranes have been observed, such as curvature changes, alterations in membrane domain architecture, non-bilayer disorder, fusion of vesicles and/or lipid flip-flop processes (20). The different pathways can be divided into two groups: energy- independent direct penetration and energy-dependent endocytosis (21).

The process of direct penetration can be tested with the use of specific experimental conditions such as low temperature, ATP depletion and in the presence of endocytic inhibitors. The first step of uptake begins with initial electrostatic interactions between positively charged CPP and negatively charged membrane components such as the phospholipid bilayer, leading to the CPP entrance. For instances, CPP can penetrate cellular membrane through different model mechanisms such as transient pore formation or membrane destabilization (22,23).

The transient pore formation models are characterized by the formation of toroidal pores or barrel-stave pores on the cellular membrane. The barrel-stave model, described by Gazit and his team in 1994, is characterized by an initial interaction of CPP with cell membrane, which assume an amphipathic α-helix structure as the basic residues interact (24). Then, CPP inserts in the membrane and cluster together in a barrel-like structure in such a way that the hydrophobic region interacts with the lipid core and the hydrophilic region faces the interior of the transient pore (24).

The other two models responsible for membrane destabilization are the carpet-model and inverted micelle model. In 1992, Pouny and his team proposed the carpet-model, which stipulates that positively charged amphipathic CPPs bind to acid phospholipids head groups and dispose horizontally through the membrane surface in a “carpet-like” fashion (22). Further interactions of the hydrophobic region with the polar region of the membrane and positive charges directed towards the hydrophilic region consequently leads to destabilization of the cellular membrane and internalization of CPPs (22). The inverted micelle model was first described with pAntp CPP. Derossi and his team proposed that positively charged peptides interact with membranes dislocating negatively charge phospholipids to the site, inducing the formation of an inverted micelle and release of CPPs into the intracellular compartment (8).

Even though direct penetration was initially proposed as the main mechanism of CPPs internalization, later, in 2003, biophysical studies elucidated in detail the mechanisms of permeation of lipid bilayer and suggested that endocytosis could also represent the main entry route for many CPPs (15). Endocytosis comprises two distinct mechanisms of cell entry subdivided in two groups: (1) phagocytosis of large molecules are usually restricted

to specific types of cells responsible for the elimination of pathogens such as macrophages, monocytes and neutrophils; and (2) pinocytosis occurs in all cells. Focusing on pinocytosis, there are four different pathways: macropinocytosis, clatherin endocytosis, caveolae/lipid raft mediated endocytosis and Catherin and caveolae independent endocytosis ,which differ on the size of endosome, nature of the cargo and mechanism of vesicle formation (19,25). In order to study which mechanism is associated with CPPs entrance and escape from endosome to cytoplasm different experimental techniques and strategies can be applied.

To understand the specific mechanisms and involvement of certain proteins such as Catherin and caveolin, the experimental procedures that have been adopted used specific inhibitors such as amiloride (inhibits macropinocytosis) Dynasore, chlorpromazine and sucrose (Catherin dependent endocytosis), nystatin (caveolae-mediated) depletion of cholesterol (inhibits lipid raft endocytosis) and more (12,23,26–29).

Nonetheless, after endocytosis, CPPs or CPP-cargo conjugated are confined in endosomes and risk exposure to degradation from lysosomes. Thus, escaping from endosomes is a crucial step in order for them to reach their target site and execute their biological activity. The mechanism of endosomal escape is still poorly understood. However, some hypotheses have been presented. One hypothesis of endosomal escape is that it is determined by pH gradient, with vesicle maturation the pH decreases and promotes increased CPP interactions with membranes, and consequently, their release occurs (17). Another model proposes that positively charged CPPs, once inside the vesicle, interacts with negatively charged components of the endosomal membrane, which contributes to tightening the membrane, determines its disruption and the release of CPPs (30). A variety of agents have been designed to promote endosomal escape such as the lysosomotropic agent chloroquine (12), a classical antimalarial drug. Another approach is the introduction of histidine moieties in the CPP sequence ,which have a “proton sponge effect” and increase the osmotic pressure inside the endosome (31,32). Similar to this concept is the insertion of GALA, KLA and KALA sequences in the CPP sequence resulting in endosomal escape (33). A different strategy fused CPP with influenza virus sequence (dTat-HA2) and this enhanced macropinocytic escape (27,34). The work of Oba and his team added an unnatural amino acid (Lys) with a guanidinylethyl group in the side chain of amine to the arginine-rich peptide and the degree of protonation in the guanidinylethyl amine structure played a crucial role in endosome escape abilities (31).

1.1.3. CPP for delivery cargos

Since the discovery of the potential therapeutic approach of CPPs as safe and efficient delivery vectors, an increased number of studies have examined CPP-cargo transfection and modulation of cells and tissues both *in vitro* and *in vivo*. Different molecules such as peptides, proteins, drugs, antisense oligonucleotides, dyes, siRNAs have already been conjugated to CPPs and used in both research and therapeutic applications (1,32). The CPP-cargo conjugation has not only been widely studied but has also demonstrated interesting results so far in targeting different pathologies such as inflammation, ischemia, cardiovascular disease, psoriasis (35), their use as imaging agents (36–38), cancer and neurodegenerative diseases (39,40). Besides its therapeutic potential in oncologic conditions and neurologic disorders, the research focus is also on clarifying how CPPs can cross resistant tumor cells and be highly selective to the almost impermeable blood-brain barrier (BBB) (39,40). Another recent approach involving CPPs, is the possibility of delivering biopharmaceuticals through a non-invasive route. Some biopharmaceuticals are still administered through parental injection, which is associated with discomfort, pain and low patient compliance. The ideal administration route must be well tolerated and accepted among patients, preferably in oral dosage forms. Patients with chronic diseases require frequent injections and transition to oral forms of administration would increase the quality of life for millions of people. Nevertheless, successful oral delivery is still a big challenge, in part due to the inherent disadvantages of the gastro-intestinal tract that presents inter-individual and intra-individual variations, physical and biochemical barriers of intestinal mucosa, pH alterations and exposure to enzyme degradation. Potential oral use of CPPs has been presented in several research papers in order to facilitate and improve permeation of drugs and therapeutic proteins across intestinal epithelium (41). For this purpose, scientists have implemented different strategies for gene-targeted therapy with regulation of gene expression (36,42).

Although CPPs have been presented as useful and remarkable delivery tools, there are still some challenges to be addressed. Some of the barriers are associated with *in vivo* results such as poor bioavailability, low stability, lack of selectivity, reduced accuracy and short lifespan (16). The CPP incorporation of L-enantiomers instead of D-amino acid analogues and/or of unnatural amino acid enhances the stability and bioavailability of peptides in serum (43,44). Another successful approach is the cyclization of CPP structure (45). The enhancement of efficiency with cyclization of arginine-rich peptides has been demonstrated. The authors found maximal separation of guanidium groups by cyclization of the peptide

structure and enhanced their non-endocytic cellular uptake (46). The work of Gronewold and his team demonstrated that dimerization of CPP sC18 promoted increased cellular uptake (mainly direct penetration) and tumor cell selectivity, depending on the composition of target membrane (MCF-7 cancer cells) (47). Another important topic is the CPP's lack of selectivity, which can be addressed by the incorporation of sequences of targeting (40,48,49) to specific receptors (39) and the use of mRNA display technology to design tumor lineage-homing peptides (26). Furthermore, incorporation or conjugation of CPPs with complex structures such as nanoparticles (NP) (50,51), micelles (52) or liposomes (53) promotes stability, bioavailability and *in vivo* efficiency of CPPs.

The current research demonstrated a new side of CPP that can assume other cellular functions rather than be only a penetration delivery carrier but also present some intrinsic activity and interaction with important proteins, receptors and modified metabolic activity in cells (Figure 1.1) (54–58).

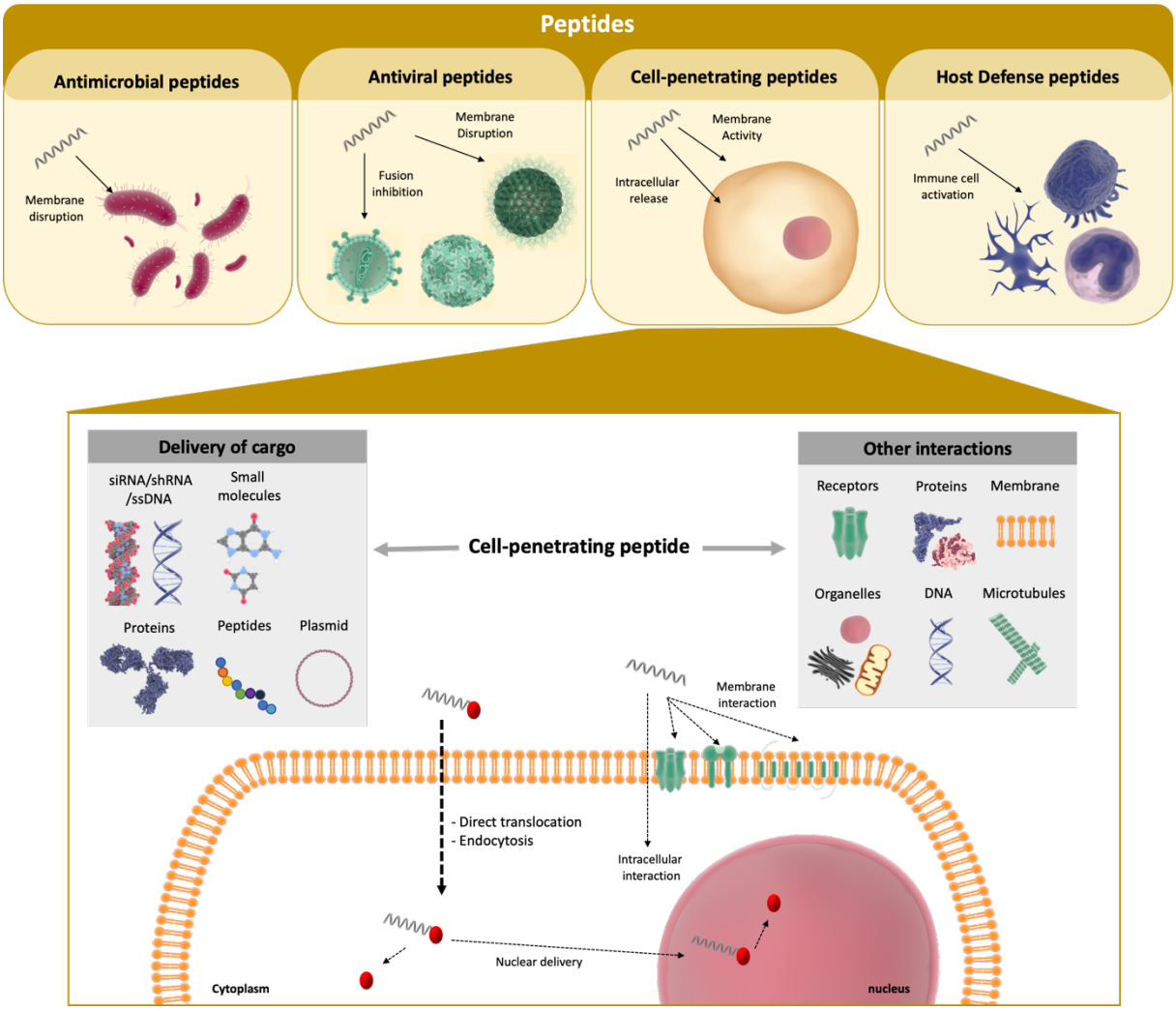


Figure 1.1 - Schematic representation of different types of peptides available and its different activities. In depth representation of CPP as delivery molecules and potential other interactions.

1.1.4. Model amphipathic peptide

One CPP that has demonstrated this possible dual functionality is the model amphipathic peptide (MAP – KLALKLALKALKAALKLA). The MAP is considered a secondary amphipathic CPP (59) and was first design by Steiner and his team to study interactions with lipidic interfaces (Figure 1.2) (60). Then in 2005, a pharmaceutical company, Nastech Pharmaceutical Company Inc., unaware of its existence, discovered a peptide PN159 with the same sequence as MAP, and demonstrated incredible cellular membrane interactions (61–63). The structure of MAP allows positioning of hydrophilic and hydrophobic residues on opposites sides, which, in the right conditions can adopt a stable α-helix structure, getting close to lipidic membrane in temperature between 25 and 55 °C (64), and even a β-structure with increase pressure and concentration (65,66). MAP is characterized by an overall positive net charge of 5 (67) and is very stable at physiological conditions associated with slow blood clearance (half-life above 72 h) on *in vivo* studies (68). The authors demonstrated that arginine and arginine bond (RR bond) could lead to degradation susceptibility of peptides, thus show that peptides not containing RR bonds demonstrated more stability that those with RR bond in the sequence (68). All these features allow MAP to possess strong cellular penetration in different cell types. Several studies have been conducted to understand and identified the crucial parts of its unique structure that enable its mechanism of cellular penetration and action. Initial studies indicated that amphipathic structure was crucial for its high interaction and penetration in cellular membranes. (64,69,70). Further ahead, new studies with different MAP derivates demonstrated that both amphipathic and non-amphipathic peptides were able to transgress cell membrane within few minutes (19,71–73). A study demonstrated that reduction of 4 amino acid residues in MAP, on both N (KLAL) and C terminal end (LKLA), resulted in a substantial reduction of cell uptake, showing that these 4 amino acids are crucial to α-helix to form. Moreover, it was also demonstrated that substitution of five lysins with glutamine residues lead to a reduced uptake and membrane toxicity (64,72), indicating that α-helix is a structural requirement of MAP to contribute to higher membrane interaction and higher cellular uptake. The MAP fluorescent pattern observed indicated that both non-endocytic and endocytic modes of cell uptake are involved due to cytosol and nucleus accumulation, accompanied by punctuate pattern around the nucleus (13,71,72,74). Another interaction observed was MAP had the ability to interact with cellular tight junctions (TJ) and modulate TJ to enhance systemic delivery (63). TJ are composed by three main proteins (occluding, claudins and junctional adhesion molecules) and are important for promoting integrity of cell barrier, and its dynamic structure regulates endocytic processes (63). In recent years, this

capability of MAP was further study by Bocsik and her team, and several experiments were conducted in order to understand which TJ-specific target was involved. The authors demonstrated that 10 μM for 1 h didn't cause significant change in metabolic activity of Caco-2 cell line or brain endothelial cells, and showed an increase molecular permeability through both barriers after MAP incubation (75).

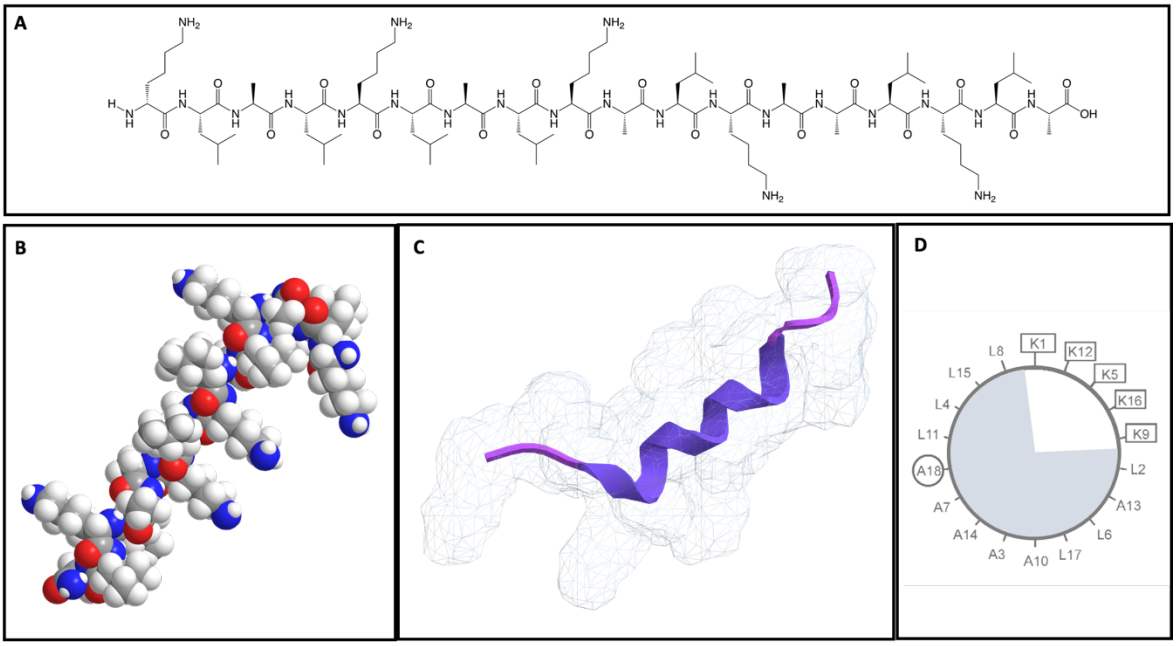


Figure 1.2 - Different representations of MAP. A – Structure sequence of MAP (ChemDraw 19.0); B – 3 D representation of MAP sequence (ChemBio 3D ultra); C – Secondary conformation of α-helix structure of MAP (3D data retrieved from CPP database (CPPsite 2.0) and analyzed by (ChemBio 3D ultra).

1.1.5. MAP conjugation and activity

The importance of new alternative delivery mechanisms is increasing as a consequence of current drug limitations, such as first-passage metabolism, secondary toxic effects, off target therapeutic effects, tumor resistance, solubility and biological barriers penetration. This general systemic distribution leads to the need for higher drug therapeutic concentrations to reach the target spot. In the ideal scenario, it will be possible to administer the minimal drug dosage required to have therapeutic activity only at the target site without compromising non-target organs, reducing side-effects and healthcare cost (77). However, this may also enable the delivery of different molecules that required a carrier to reach cells

such as antisense oligonucleotides, peptides, proteins, dyes, siRNAs, etc. (1). The use of CPPs as delivery molecules allows several advantages over conventional techniques.

Several articles demonstrated high cellular uptake of fluorescent dye covalently linked with MAP inside different cell lines (13,69,78–80). These studies were conducted to evaluate the mechanisms of cellular uptake used by MAP when interacting with cells. For instances, the results indicate that multiple processes of cellular uptake might be involved with MAP penetration (69), and at least 50 % uptake was found even with incubation temperatures below 0 °C on calf aortic endothelial cells (13).

Besides cellular delivery capabilities of MAP, other features and proprieties have been associated with this peptide. Kilk and his team, observed that MAP could potentially promote long-term effects on the metabolic profile in cells (57). Another particularity of MAP is the strong lytic capabilities at concentrations above 4 μM, and high aggregation propensity when close to lipidic membranes (81–83). The dual activity of MAP appears to promote cellular long-term effects and even promote cell death with increase of concentration. For instances, cytosolic metabolic alterations on CHO cells were observed with MAP treatment (57). Furthermore, appears that conjugation of MAP with other active compounds enhance its activity against different diseases in *in vitro* models, such as neurodegenerative and cancer. For example, in a study conducted by Vale and his team show that conjugation of RAS, a propargylamine of monoamide oxidase B (MAO-B), with MAP resulted on decrease the percentage of cells with alpha-synuclein (α-syn) inclusions at a lower concentration. The results suggested that both MAP and RAS could possibly interact with α-syn inhibiting its capability to form inclusions and induce a neuroprotective effect (84). Several α-helical peptides have demonstrated their activity as membrane permeate agents in host defense systems, and direct disruption or pore formation are the main mechanism of action present in these peptides. The moment that the membrane is compromise, electrochemical potential is lost and cellular cytoplasmic homeostasis dis-appears and cell death occurs. Still, the membrane perturbation energy depends not only the peptide used but also on the composition and nature of the lipid mixture present in the cell membranes. Different peptide behaviors will reflect on different pore sizes and insertion thresholds observed (85). It is important to mention that bacterial and tumor cell membrane share common features, such as: a negatively charged membrane and high transmembrane potentials (83). Tumor cells contain three to up seven times more phosphatidylserine than normal cells, and is located mainly in the outer leaflet, which results in a more negatively charged outer membrane. On the other hand, normal cells have more neutral membrane and low membrane potentials composed by phosphatidylcholine,

sphingomyelin, phosphatidylethanolamine, cholesterol and zwitterionic phospholipids. Phosphatidylserine is located exclusively in the inner leaflet of the membranes (86,87). All these different features can allow peptides to selectively interact more with tumor cell lines rather than normal cells (88). In a different work, the toxic activity was also observed by Moutal and his team, with treatment of MAP conjugate with Ca^{2+} channel binding domain 3 (CBD3) on cortical neuron cultures. The authors demonstrated that treatment with MAP-CBD3 lead to an increase influx of Ca^{2+} and nuclear targeting, consequently inhibiting the desired neuroprotection activity (58). Anti-bacterial activity was also assessed by Bocski and her team, demonstrating that MAP presented an antimicrobial effect at low concentrations against different ESKAPE pathogens (76). Moreover, targeted intracellular delivery is challenge strategy with the need for several molecules to be involved to work properly. Taking this in consideration, the use of CPP has demonstrated great potential in functionalizing nanoparticles which might allow to remedy several limitations present in each mechanism individually. Successful data have shown that conjugation can be beneficial to a new potential therapeutic approach against different diseases (89). In a study carried out by Zaro and her team, a pH-sensitive CPP nanoconstruct was constructed and compromise by a highly pH-sensitive co-oligopeptide sequence fused to MAP to prevent non-target internalization and disguise the cationic charge. The pH sensitivity was acquired by the incorporation of histidine residues that allowed the peptide to be internalized at pH 6 instead of pH 7.4 (90). The decrease of pH in extracellular media surrounding tumors was observed, and this strategy could allow a more targeted approach to tumors (91,92). The authors fused MAP with glutathione S-transferase protein and a 10-mer histidine moieties oligopeptide sequence. The results demonstrated a pH-dependent surface binding and internalization to cell membrane (90). These results demonstrated the potential use of this strategy in new therapeutic approaches, reducing the amount of drug use and increasing the therapeutic efficacy.

1.1.6. Central nervous System drugs

It takes around 10-15 years for a new drug to be developed, tested, and reach the pharmaceutical market. The costs of development are high, time-consuming, and around 90% of drugs results in clinical trial fail. For this, a new strategy has been explored to ensure a reduction of costs and a fast-testing track with the use of already-approved drugs with new therapeutic indications other than the original ones. Drug repurposing allows overcoming traditional new anti-cancer drug development limitations and the use of drugs already well characterized in terms of toxicity, side-effects, and dose efficacy. Taking this

in consideration this Thesis proposes the use of three already developed central nervous system (CNS) drugs that can be easily modified and linked with MAP and present interesting activity (Figure 1.3).

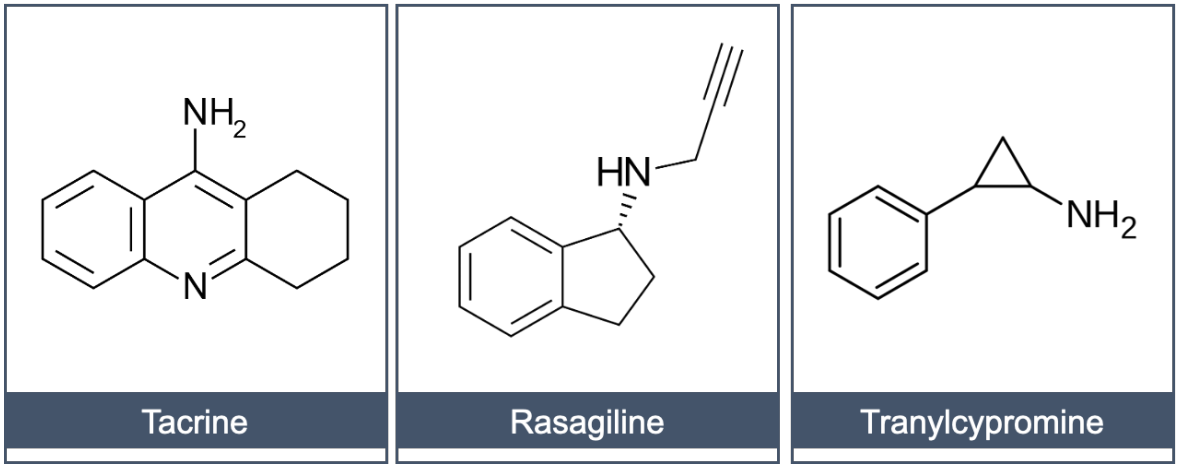


Figure 1.3 - CNS drugs molecular structure.

1.1.6.1. Tacrine

Tacrine (TAC)(Figure 1.3) is a competitive and reversible inhibitor of both acetylcholinesterase (AChE) and butylcholinesterase (93,94). TAC was first unsuccessfully investigated to be an antibacterial agent, but further studies revealed analeptic proprieties; therefore, it was used as a morphine antagonist to manage pain in terminal cancer patients. After that, TAC also demonstrated positive effects in patients with anticholinergic delirium so further studies were conducted to evaluate TAC interaction with the cholinergic system (95). In September of 1993, TAC was approved by the FDA for the treatment of Alzheimer's disease (AD), being the first approved treatment at the time (96,97). The mechanism of action of TAC relies on inhibition of AChE, leading to increased availability of acetylcholine associated with an enhancement on the muscarinic effect, improved memory and cognition of AD patients (94). However, in long-term treatments, TAC has demonstrated some undesired effects on AD patients such as gastrointestinal effects (nausea, vomiting), shivering and hepatoxicity with an increase of transaminases (98,99). In addition, pharmacokinetic studies showed that TAC has a short half-life time (around 2 h), low oral bioavailability (17%) and a high clearance rate from systemic circulation (100,101). Many efforts have been developed to overcome and reduce these side effects (102). So, the use of NP as delivery molecules has been used in many studies in order to diminish these limitations and permits a controlled release delivery (103,104). Nasal cavity route of drug

delivery has been explored and used by many researchers to target the central nervous system (CNS) (105). The major advantage of administrated drugs via nasal cavity is the ability to avoid first-pass effect and the BBB (106–108). For this, Jogani and his team developed a microemulsion delivery system to enhance nose-to-brain transport of TAC. This microemulsion formulation optimization consisted in addition of a mucoadhesive agent to prolong the contact time of the formulation in the nasal cavity and potentiate the absorption of TAC into the brain, reducing systemic distribution and major side effects. The authors demonstrated enhanced brain selectivity and accumulation on the intranasal (IN) administration than intra-venous (IV) administration of TAC. Moreover, intra-nasal (IN) administration resulted in faster memory regain of scopolamine-induced amnesic mice (107). Furthermore, Corace and his team developed a multifunctional liposome containing Toc and omega 3 fatty acid for IN administration of TAC (109). The results demonstrated enhancement in TAC permeability, high cellular uptake, and cytoprotective effects with the addition of Toc on liposomal composition (109). In another paper, Wilson and his team used a new strategy and developed a poly(n-butylcyanoacrylate) (PBCA) nanoparticle coated with T80 to deliver TAC and decrease its limitations. IV administration of the formulation demonstrated increase of 4.07-fold concentration of TAC in the mice brain when compared with free drug values (110). Then, two years later the same authors changed the main component of the NP for chitosan. Chitosan formulations have been widely used in nanotechnology due to its non-toxic effect, controllable polymer degradation and modulate drug release. In this paper, the authors explored chitosan with T80 coating as new delivery system for TAC. The physiochemical analysis demonstrated a particle size of 44 nm, mean zeta potential (ZP) of + 34.7 mV, and a drug loading capacity of 10.86%. However, biodistribution systemic results demonstrated similar amounts of TAC accumulation compared to the free drug, indicating that further modifications besides T80 coating are needed (111). Several studies continue the evaluation of different formulation methods to optimize chitosan NP formulations. For instances, Tamilselnan and his team also prepared a NP formulation with chitosan and sodium tripolyphosphate (TPP) loaded with TAC. The ionic gelation method was used to prepare the NP which differs from the method used by Wilson and his team (111). Different formulations were produced to assess the effect on NP physicochemical proprieties. Furthermore, *in vitro* cytotoxicity studies demonstrated that optimized formulation was safe at 10 and 100 µg/mL. In another article, chitosan-TPP NP were prepared also through modified ionic gelation method to optimize preparation process and encapsulate the TAC. The results demonstrated particle size of 88 nm, a ZP of + 37 mV, and an encapsulation efficiency of 65% (112). In another work, researchers used a different strategy with the use of magnetic TAC-loaded chitosan NP. They proposed that the use of magnetic compounds will lead to higher accumulation of desired drug in the target

region when subject to a magnetic field. The authors demonstrated that treatment with this technique prevented more efficiently behavior decline in AD-induced model of rats (113). PBCA NPs are efficient delivery carriers with target selectivity to the brain and rapid biodegradability. So, Eslami and his team. decided to conjugate PBCA and chitosan coated with T80 and developed a new delivery system taking into consideration the previously developed work by Wilson and his team (111,114,115). The authors used molecular simulations to evaluate if the formulations were successful in delivery of TAC and determined their compatibility of the polymers with TAC. Overall results showed that TAC in water media has higher compatibility with PBCA and chitosan NP (114). Pharmacokinetics limitations of TAC can be decreased with the use of NP. In this article, the authors were able to determine with very sensitivity the AChE activity and the amount of TAC in the solution which resulted in reduced activity of the enzyme to convert the subtract has expected. The group prepared polymeric NP consisting of methoxypoly (ethylene glycol) /poly(caprolactone) (mPEG-PCL) loaded with TAC. The results demonstrated that C-max values were increased 2.86-fold in the brain and decreased 1.78-fold on elimination rate when compared with plain drug (104). Nanotechnology can be used not only as delivery vector but also as biosensor in monitoring diseases, and one example of this strategy is with the use of carbon-based NP (CNPs), in particular fluorescent CNPs. Benitez-Martinez and his team developed a novel fluorescent sensor with nitrogen-doped graphene quantum dots and AChE for determination of TAC inhibition AChE values. In this article, the authors were able to successfully determine with very sensitivity the AChE activity and the inclusion of TAC in the solution demonstrated a reduced activity of the enzyme to convert the subtract has expected. This strategy allowed the detection of TAC in micro-molar range (4~20 μM) which could have an incredible potential to use this technique with other esterase family members (116).

1.1.6.2. Rasagiline

RAS is a highly selective propargylamine of MAO-B inhibitor that irreversibly inactivates the enzyme up to 95% (117) and is indicated for the symptomatic treatment of Parkinson disease (PD) (Figure 1.3). RAS present its antiparkinsonian activity by inhibiting oxidative breakdown of dopamine (DA) in the striatum which increase survival of dopaminergic neurons promoting neurite extension and increase density of varicosities (118,119) In addition pharmacokinetic studies demonstrated an oral bioavailability of 32% and half-life of around 3h. Different clinical studies reported the beneficial outcomes of RAS administration in both early and advance form of PD as adjuvant or alone. RAS treatment results in the improvement of motor performance and daily basis activities (120). TEMPO

and ADAGIO study administrated RAS in early forms of PD and demonstrated high efficacy and delay need for additional symptomatic antiparkinsonian drugs. In addition, LARGO and PRESTO study evaluated RAS treatment in advanced PD and demonstrated a decrease in motor fluctuations and improvement of non-motor symptoms (121). Over the years, several studies have demonstrated other beneficial effects of RAS on neuronal protection besides its MAO-B inhibition. The antiapoptotic effect could be associated with the synthesis of new proteins by upregulation of the expression of antiapoptotic pathways such as Bcl2 family (mitochondria function), protein kinase C-dependent mitogen activated protein kinase (122,123). Recently, it was reported that RAS can block the interaction between α-syn and TrkB receptor tyrosine kinase and rescue brain-derived neurotrophic factor pathway which is crucial for dopaminergic survival (124). Also, binding of α-syn to MAO-B increasing its enzymatic activity can be blocked by the use of RAS (125,126). However, a putative effect of RAS on α-syn aggregation has never been investigated. Even though MAO-B inhibitors present less effects, they also have less side-effects compared to treatments. Furthermore, several studies have demonstrated that another possible key feature of these compounds is their ability to act as neuroprotectants from oxidative stress (127,128). On the other hand, lipid-based NPs have been developed and demonstrated high biocompatibility and increased lipophilic or hydrophilic drug incorporation. One work demonstrated the incorporation of RAS in solid lipid NPs (SLNs) through a specific method of selection to ensure quickness, low waste, and low financial investment. An analytic hierarchy process was implemented, and RAS-loaded SLNs were prepared by a microemulsion technique that led to a yield of 83.6%. The average particle size was determined to be 248.7 nm, the ZP was around –35.5 mV, and the encapsulation efficiency (EE) of 86.6% (129). The further optimization of SLNs loaded with RAS was conducted using the microemulsion technique, and the effects of different formulations and processing parameters on physicochemical proprieties were evaluated (130). In another study conducted by the same group, the *in vitro* drug release of SLNs loaded with RAS was analyzed. The results demonstrated a biphasic release pattern with initial 20% release over 30 min and then a sustained release of up to 98.2% over 24 h (131). In addition, the stability analysis showed no aggregations or separation after six months in storage (132). To intravenously administer SLN, a size smaller than 1 μm and sterilization are required when preparing new NP formulations to ensure high quality physicochemical characterization and a high stability. In addition, to ensure that the selection of the sterilization technique does not affect the developed nano-formulation, several techniques such as heat, filtration, and y-irradiation are available. For instance, SLNs loaded with RAS were subjected to moist heat sterilization, and the results demonstrated no changes in particle size, ZP, and drug encapsulation efficiency (133). In the next article the authors showed the successful development of nanostructure lipid

carriers (NLCs) as delivery systems. The main composition of the NLCs was acetyl palmitate (solid lipid), squalene (liquid lipid), Myverol (lipophilic emulsifier), and Pluronic F68 (PF68) (emulsifier). In addition, the authors added different additives such as forestall, T80, and distearoylphosphatidylethanolamine (DSPE)-PEG to the formulation to optimize the nanodelivery system to target the brain. A particle size analysis showed a mean diameter of 396 nm of the basic NLC. The incorporation of T80 resulted in an enhanced particle size of 431 nm, and the incorporation of DSPE-PEG showed a smaller size of 372 nm. The use of T80 and DSPE-PEG by the authors ensure higher brain drug accumulation, and the *in vivo* administration of these NLCs showed a more efficient delivery to the brain when compared to the aqueous solution (134).

1.1.6.3. Tranylcypromine

TCP was first synthesized in 1948 as an amphetamine analogue. Later demonstrated a potent activity as a non-selective MAO inhibitor and increased brain catecholamines and serotonin (135,136) (Figure 1.3). Even though TCP present a potent anti-depressant activity, the clinical usage was limited to resistant depressions and atypical depressions (137,138) due to its side effects, tyramine rich food interactions and drug interactions. Some severe side-effects include hypertensive crisis and central serotonergic syndrome (136,138). In addition, pharmacokinetic studies have demonstrated an bioavailability of 50% and half-life of around 2 and half hours. Over the years, several studies have demonstrated that TCP can interact with other types of enzymes such as semicarbazide-sensitive amine oxidases, prostacyclin synthase, drug metabolizing enzymes and lysine specific demethylase 1 (excellent reviewed (139)). Lysine specific demethylase 1 overexpression in some cancers has demonstrated to be the possible link of TCP and TCP derivates and the anti-proliferation activity against cancer cell line (140). For instances, studies conducted with TCP demonstrated some anti-cancer activity against different breast cancer cell lines and neuroblastoma cell lines (141–143). However, this anticancer effect is not observed in other cancer cell lines such as human prostate cancer (LNCaP-LN3) cells (144).

1.1.7. Solid Phase Peptide Synthesis (SPPS)

SPPS methodology was first development by Merrifield in 1953 and showed a faster, simples and cheaper was to conduct peptide synthesis. The method relies on an insoluble solid support to construct the peptide sequence wanted. Then a reaction vessel is connected to a vacuum system which allows the removal of side products and excess of reagents and solvents through washing with Dichloromethane (DCM) and

Dimethylformamide (DMF) and filtration. The methodology starts with the coupling of an amino acid N α protected into the solid support (resin) then the remaining α-amino acids of the sequence are sequentially linked together through the formation of an amide bond. Each amino acid is coupled and the reactivity of the α-amino group is protected by a temporary protecting group (usually 9 fluorenyl methoxycarbonyl (Fmoc)) and the other reactive functional groups in the amino acid are blocked by tert-butyl (tBu). So, coupling of each amino acid results on a group of reactions with with activation of the carboxyl group through coupling agent and deprotection reactions with deprotection of the reactive alfa-amide group of the already linked amino acid. Another particularity is that sequence order of amino acids is assembled through Ct →Nt which is the opposite of biosynthetic route for peptides synthesis observed in nature. The elongation of peptide chain occurs through repetitive cycles of coupling reactions of protected amino acid and subsequent deprotection of the temporary protecting group (Figure 1.4)

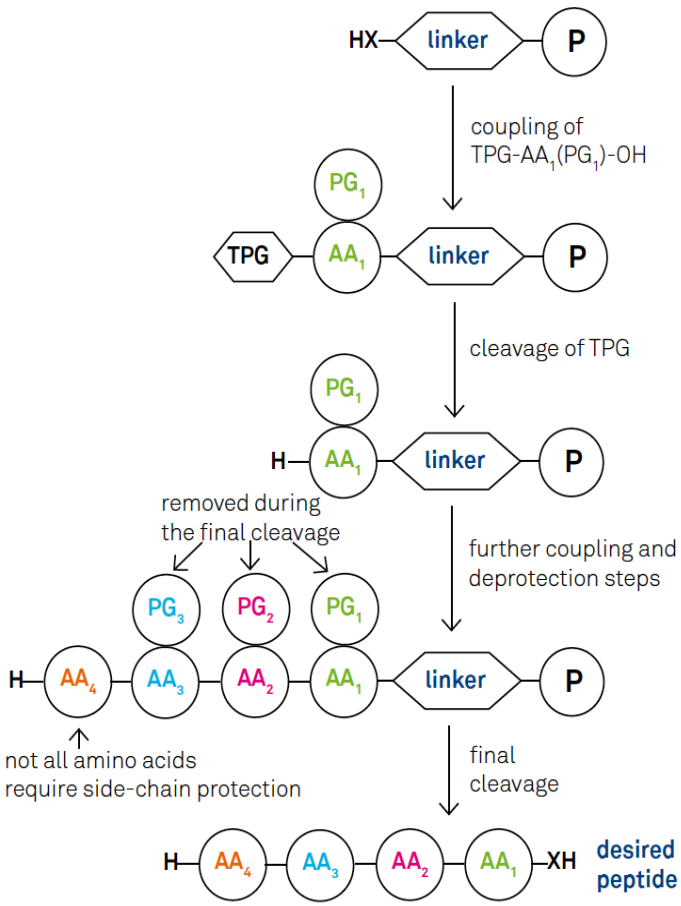


Figure 1.4 - General scheme of SPPS. X=O,NH; AA= amino acid; PG=protecting group; TPG=temporary group; P – resin (scheme retrieved from reference (146)) .

Once peptide sequence is completed, all permanent protected groups must be removed, and the peptide is cleaved from by chemical solution capable of breaking the bond with the solid support. Nowadays, this methodology can be automated such as Symphony X Multiplex Peptide Synthesizer, developed by Protein Technologies, Inc.©, which is a 24-channel peptide synthesizer that can run different sequences, scales and protocols on multiple reactors all at the same time, or run up to 12 reaction vessels with preactivation (145,146).

1.2. Overview

In this Chapter 1 is described the peptide and peptide-drug conjugate synthetizes through SPPS, respective purification and analysis procedure.

1.3. Materials and methods

1.3.1. Materials

In this work the reagents and solvents were acquired from Novabiochem (Fmoc-Rink Amide MBHA resin and Fmoc-amino acids), Sigma-Aldrich (coupling agents, piperidine, N, N-Diisopropylethylamine), Merck (trifluoroacetic acid (TFA), solvents). Peptides were characterized by mass spectrometry (LC/MS), on Finnigan Surveyor LCQ-DECA XP MAX. The purification step of peptides achieved by Reverse Phase Medium-Pressure Liquid Chromatography (RP-MPLC), using a C18 Vydac® 218TP stationary phase, by Grace Vydac. The purity of the peptides was determined by high-performance liquid chromatography (HPLC) on a Merck-Hitachi LaChrom Elite equipment, with a quaternary pump, automatic and thermostated by Peltier effect injector and a diode detector. A reverse phase Purospher star RP C-18 (octadecylsilane) column (125 x 4.0 mm), with a particle diameter of 5 µm, was used. The elution was performed with a variable gradient of acetonitrile (ACN) in water containing 0.05% TFA, at a 1 mL/min flow. The purified peptides were lyophilized in a BenchTop Pro 9L with omnitronics from SP Scientific (Department of Chemistry and Biochemistry of Faculty of Sciences of University of Porto).

1.3.2. Methods

1.3.2.1. General Peptides Synthesis Procedure

The peptide (C-terminal amide) was assembled by solid-phase peptide synthesis according to Fmoc/tBOc method and/or assisted with microwave energy, using a Liberty Microwave

Peptide Synthesizer. The resin was preconditioned for 15 min in DMF. The initial Fmoc deprotection step was carried out for 20 min using 20% piperidine in DMF. The C-terminal amino acid was then coupled to the deprotected Rink amide resin, using five molar equivalents (eq) of the Fmoc-protected amino acid in DMF, 5 eq of hexafluorophosphate benzotriazole tetramethyluronium (HBTU) in DMF, and 10 eq of N-ethyl-N,N-diisopropylamine; this coupling step was carried out for 1 h. The remaining amino acids were sequentially coupled in the C → N direction by means of similar deprotection and coupling cycles. With peptide assembled, the conjugation of RAS by click reaction was done. Briefly, the Pra-MAP and Lys(N_3)-MAP attached on the resin was linked with RAS, TAC and TCP by the copper(I)-catalyzed azide alkyne cycloaddition (CuAAC) using 1 eq. of RAS and TAC, 10 eq. DIEA, 10 eq. 2, 6-lutidine, 1 eq. NaAsc and 1 eq. CuBr in a solution of DMF and acetonitrile (ACN; 2:1, 3 mL) for 72 h. After this, the reaction chamber was washed with water, Methanol (MeOH), DMF and dichloromethane (3 times each). Following completion of the sequence's assembly, the peptides were released from the resin with concomitant removal of sidechain protecting groups, by a 3 h acidolysis at room temperature using a TFA-based cocktail containing thiol-free (TFA/H_2O/TIS 95:2.5:2.5 v/v/v). The synthesis crude was obtained by precipitation using tert-butylmethyl ether (<0 ◦C). Details for preparation of RAS-MAP, TAC-MAP TCP-MAP are in Supporting Information of this Thesis.

1.3.2.2. General Peptides Analysis Procedure

Peptide or conjugate analysis and purity degree were determined by HPLC, using a Hitachi-Merck Elite LaChrom system from Hitachi High-Technologies America (Schaum- burg, IL, USA) equipped with a quaternary pump, a thermostatted automated sampler, a diode-array detector, and a reverse phase C18 Nucleodur gravity column (Macherey-Nagel Inc., Bethlehem, PA, USA) with 5 µm particle size and the dimensions 4 mm ID × 125 mm. The samples were solubilized in aqueous acetic acid (10% *v/v*) and eluted over a gradient of 100% solvent A (100% H_2O with 0.05% (*v/v*) TFA) to reach 100% Solvent B (ACN with 0.05% (*v/v*) TFA) for 30 min, at a flow rate of 1 mL/min and detection at λ = 220 nm. Synthetic crudes were purified by a preparative HPLC system (LaPrep Sigma VWR, Pennsylvania, USA), equipped with a UV detector, a quaternary LPG pump injection with a fractionation valve pump, and a reverse-phase C18 column (250 × 25 mm ID with 5 µM pore size, Merck, Darmstadt, Germany). The mobile phase was a gradient elution of acidified H_2O (0.05% TFA)/ACN mixtures that are reported in the SI. Fractions containing the pure product (determined by HPLC) were pooled and freeze-dried. MS analysis was performed on an LTQ OrbitrapTM XL hybrid mass spectrometer (Thermo Fischer Scientific,

Bremen, Germany) controlled by LTQ Tune Plus 2.5.5 (Thermo Fischer Scientific, Bremen, Germany) and Xcalibur 2.1.0 (Thermo Fischer Scientific, Bremen, Germany). The electrospray ionization source settings were as follows: source voltage, 3.1 kV; the capillary temperature was 275 ◦C with a sheath gas flow rate at 40 and auxiliary gas flow rate at 10 (arbitrary unit as provided by the software settings). The capillary voltage was 36 V and the tube lens voltage 110 V. The direct electrospray ionization-ion trap mass spectrometry (ESI-IT MS) analysis was performed on a Finnigan Surveyor LCQ DECA XP MAX mass spectrometer from ThermoElectron Corporation (Waltham, MA, USA), and the LC-MS analysis was performed on the same equipment, coupled to a Finnigan Surveyor HPLC, equipped with a DAD Plus Detector, an Autosampler Plus, and an LC Pump Plus. MALDI-TOF/TOF matrix- assisted desorption/ionization mass spectrometry was performed using a Bruker Daltonics UltrafleXtreme (Bruker, MA, USA). MS data handling software (Xcalibur QualBrowser software, Thermo Fischer Scientific, Bremen, Germany) was used to obtain the confirmation of the synthetic peptides by their exact m/z value. All target products were obtained with correct mass spectral data and high chromatographic purity.

1.4. Results

1.4.1. MAP

Peptide MAP (KLALKLALKALKAALKLA-NH2) was synthesized through Fmoc/tBu SPPS methodologies, see supplementary information. After cleavage and purification of the crude product, as given in the supplementary information, the isolated peptide was analyzed by HPLC (Figure 1.5) and liquid chromatography–mass spectrometry (LC-MS, Figure 1.6). HPLC analysis showed a distinct peak [retention time (rt) = 14.7 min] corresponding to a purity degree of 100%. The exact and observed (base peak) molecular mass of MAP obtained by LC-MS were 1876.50 and 1877.32 Da, respectively, which confirmed the successful synthesis of the target peptide as its quasimolecular ion, [M + H]+. It was also possible to observe minor peaks corresponding to different protonation states of the peptide.

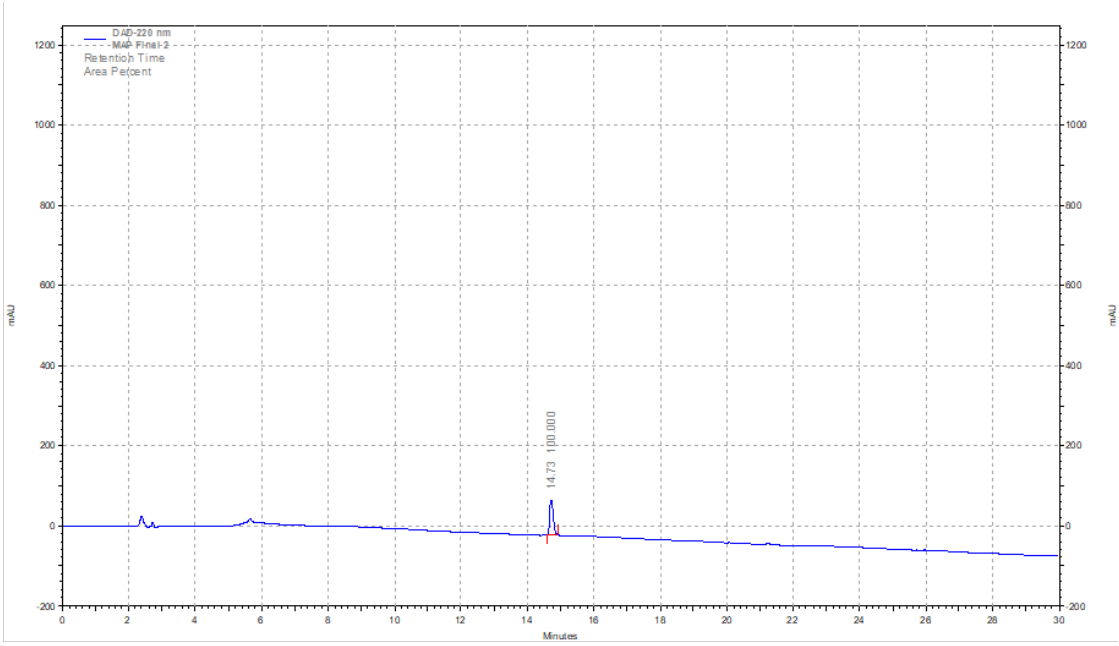


Figure 1.5 - Chromatogram of the product of the manual synthesis of the MAP, acquired with a HPLC system, with a C18 column, using ACN in water with 0.05% TFA as eluent, in gradient mode (0 – 100%), for 30 minutes, at a flow of 1 mL/min and detection at λ = 220 nm.

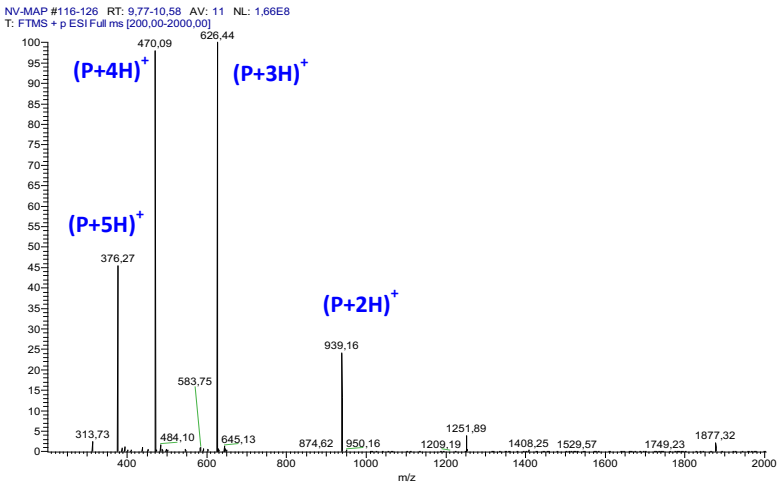


Figure 1.6 - Mass spectrum (LC-ESI/Orbitrap MS, positive mode) of the peptide MAP.

1.4.2. Lys(N_3)-MAP

Lys(N_3)-MAP was synthesized from MAP(-K), previously assembled by SPPS and the original peptide sequence (18 aa) was designed to incorporate an azide functionality (Fmoc-Lys(N_3)-OH) on the peptide's N-terminal. This modification allowed the conjugation other molecules. After cleavage and purification of the crude product, as given in the supplementary information, the isolated peptide was analyzed by HPLC (Figure 1.7) and LC-MS (Figure 1.8). HPLC analysis showed a distinct peak [retention time (rt) = 16.7 min] corresponding to a purity degree of 96.2%. More detail information presented in supplementary information.

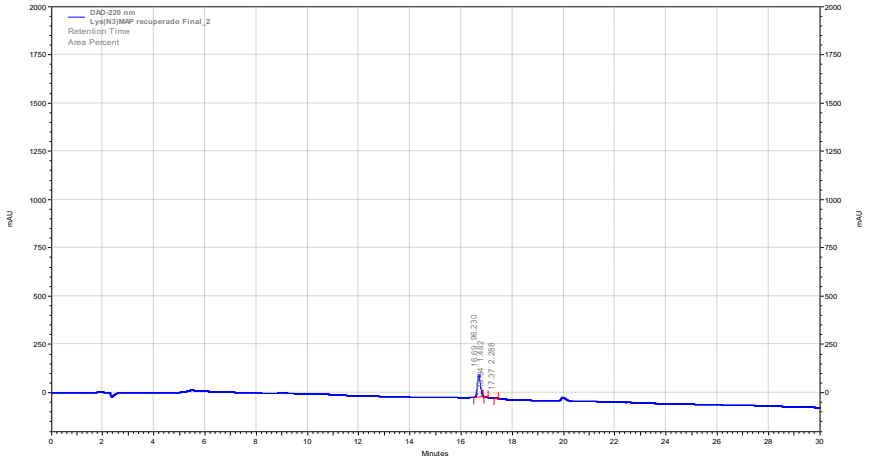


Figure 1.7 - Chromatogram of the product of the manual synthesis of Lys(N_3)-MAP, acquired with a HPLC system, with a C18 column, using ACN in water with 0.05% TFA as eluent, in gradient mode (0 – 100%), for 30 minutes, at a flow of 1 mL/min and detection at λ = 220 nm.

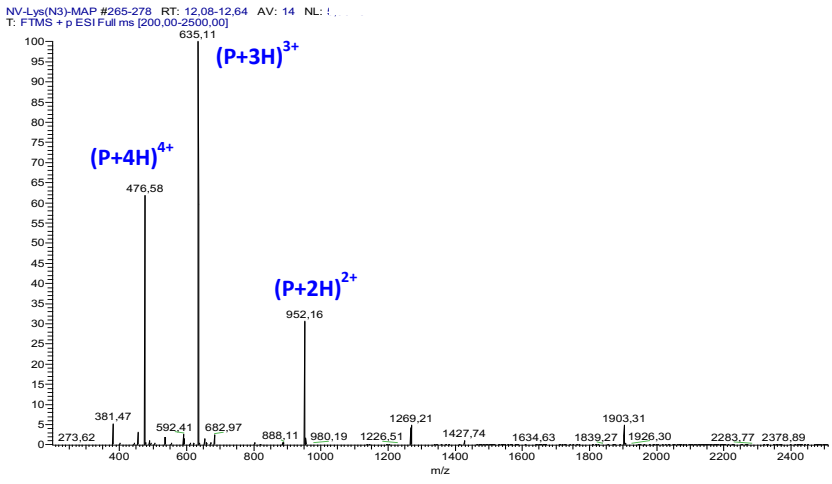


Figure 1.8 - Mass spectrum (LC-ESI/Orbitrap MS, positive mode) of the Lys(N_3)-MAP (manual synthesis).

1.4.3. RAS-MAP

RAS-MAP conjugate by SPPS. Lys(N_3)-MAP was synthesized from MAP(-K) (Figure 1.9 i)), previously assembled by SPPS and the original peptide sequence (18 AA) was designed to incorporate an azide functionality (Fmoc-Lys(N_3)-OH) on the peptide's N-terminal to permit the covalent linkage of RAS through a triazole linkage. Then, Lys(N_3)-MAP was covalently linked to RAS mesylate through a 1,3-dipolar cycloaddition reaction promoted by presence of copper(I) bromide, diisopropylethylamine, sodium ascorbate and 2,6-lutidine, for 24h at room temperature and, then, RAS-MAP was obtained with a good purification (Figure 1.9 ii)).

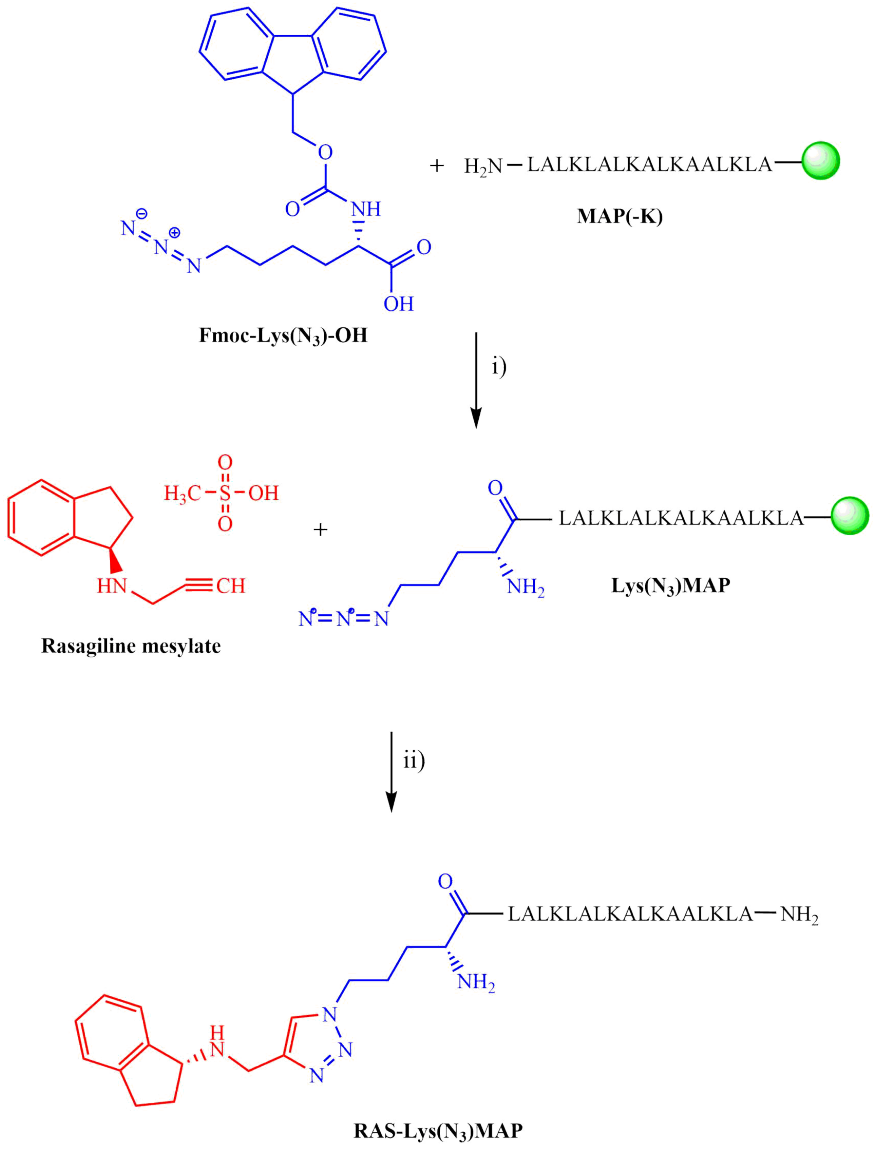


Figure 1.9 - Representation of the methodology applied for the synthesis of the RAS-MAP conjugate.

Consequently, the isolate peptide was analyzed and HPLC analysis showed a distinct peak [retention time (rt) = 15.43 min] corresponding to a purity degree of 93.4% (Figure 1.10). The exact and observed (base peak) molecular mass of MAP obtained by LC-MS confirmed the successful synthesis of the target peptide (Figure 1.11).

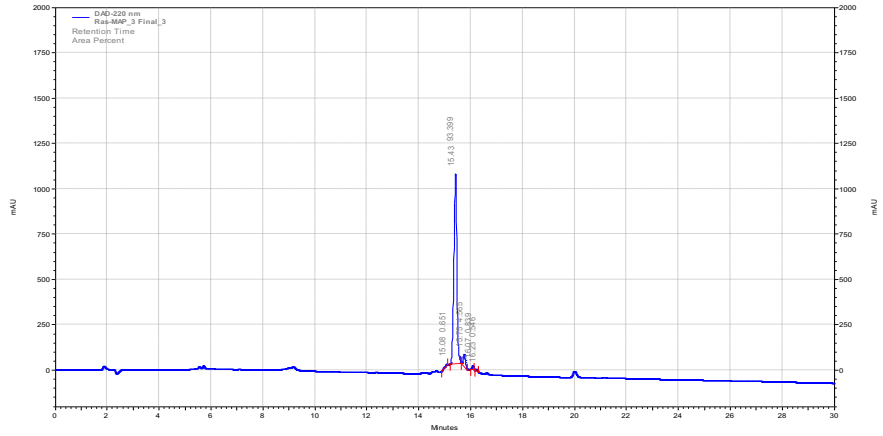


Figure 1.10 - Chromatogram of the product of the manual synthesis of Ras-MAP, acquired with a HPLC system, with a C18 column, using ACN in water with 0.05% TFA as eluent, in gradient mode (0 – 100%), for 30 minutes, at a flow of 1 mL/min and detection at λ = 220 nm.

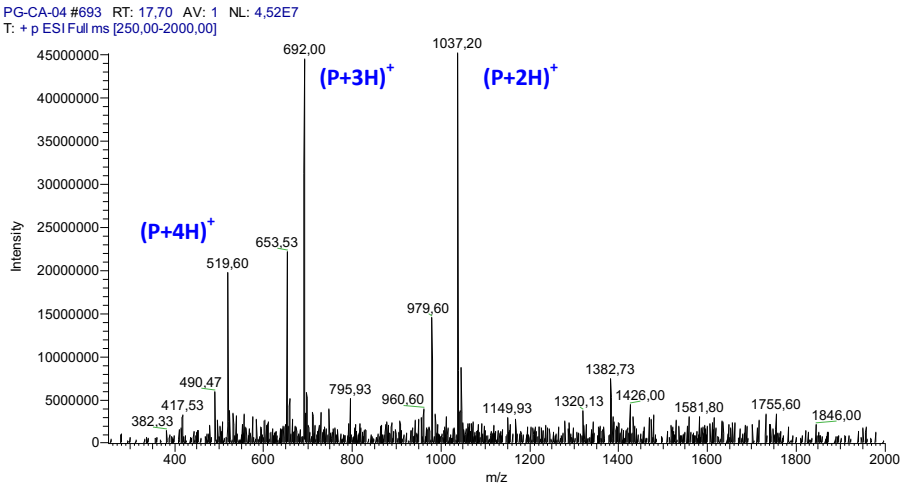


Figure 1.11 - Mass spectrum (LC-ESI/Orbitrap MS, positive mode) of the conjugate Ras-MAP.

1.4.4. TAC-MAP

TAC-MAP conjugation was achieved through one of the best known “click chemistry” reactions, the classical CuAAC or Huisgen’s 1,3-dipolar cycloaddition (Figure 1.12). CuAAC results in the chemoselective formation of a 1,2,3-triazole and can be carried out in either water or organic solvents under very mild conditions, while offering the possibility of being employed post-synthetically by use of purified units modified with alkynyl and azido functionalities, without need for additional protection of other functional groups. In this work, the CuAAC was promotedonresin, between an azide-modified derivative of TAC (1 in Figure 1.12) and the alkyne-modified version of MAP (Pra-MAP, 2 in Figure 1.12) in the presence of copper (I) bromide, diisopropylethylamine, sodium ascorbate and 2,6-lutidine, for 24 h at room temperature. Relevantly, the azide moiety could not be directly introduced in TAC through the reaction of its aniline group with azidoacetyl chloride, which was circumvented by first coupling chloroacetyl chloride onto TAC, followed by conversion of the terminal chlorine into azide upon reaction with sodium azide (Figure 1.12). After cleavage from the solid support and precipitation using tert-butylmethyl ether (<0 °C), the target TAC-MAP conjugate (3 in Figure 1.12) was purified on a preparative scale, under a suitable gradient of acidified H_2O (0.05% TFA) and ACN. The structure of the TAC derivative 1 was confirmed by electrospray ionization mass spectrometry (ESI-MS), 1H and 13C-NMR spectroscopy (see supplementary information), whereas the peptide-drug conjugate 3 was characterized by HPLC and LC-MS (Figure 1.13 and 1.14).

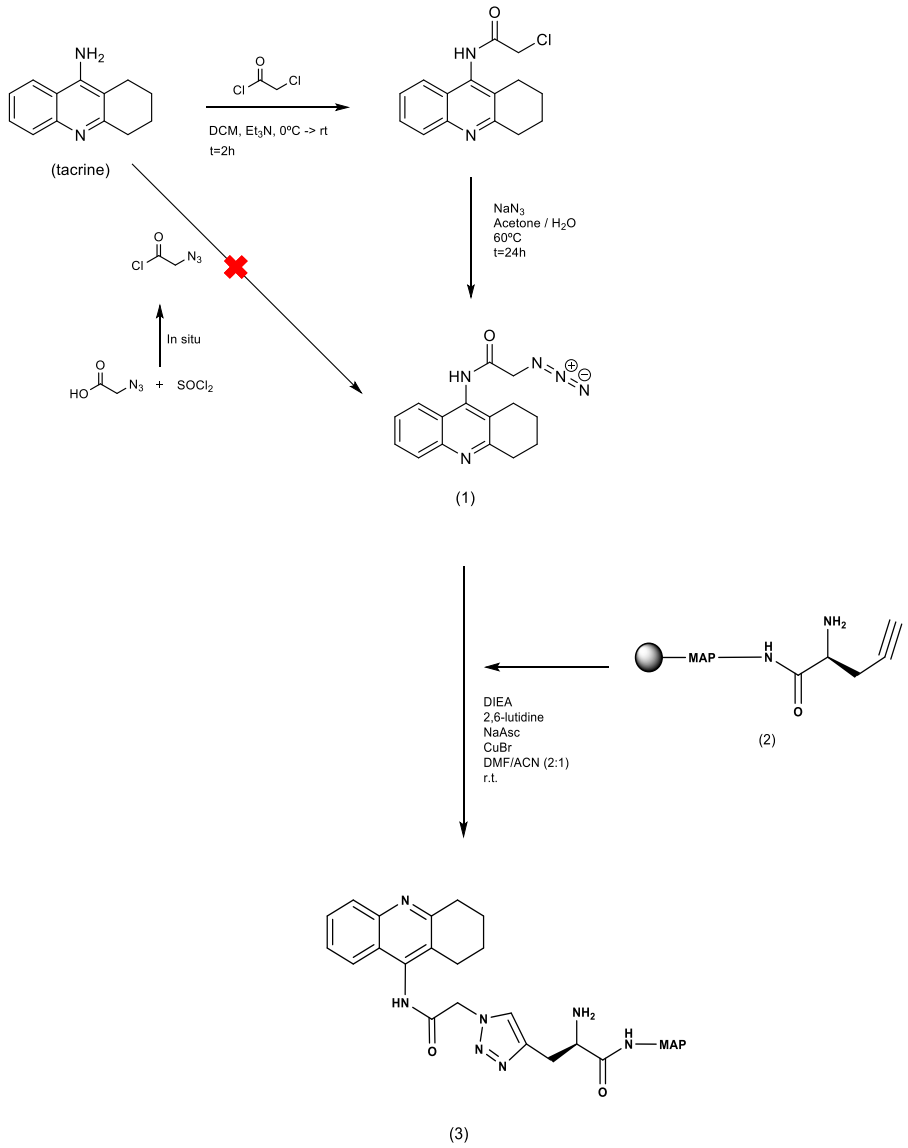


Figure 1.12 - Representation of the methodology applied for the synthesis of the TAC-MAP conjugate by SPPS. TAC-MAP was obtained with a good resolution and high level of purity (99.6%). Data for preparation and characterization are in Supplementary Material.

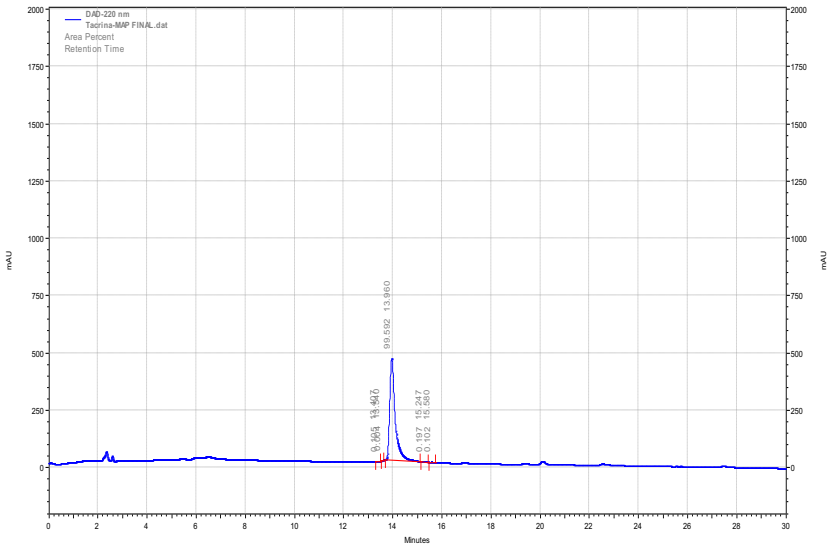


Figure 1.13 - Chromatogram of the product of the manual synthesis of TAC-MAP, acquired with a HPLC system, with a C18 column, using ACN in water with 0.05% TFA as eluent, in gradient mode (0 – 100%), for 30 minutes, at a flow of 1 mL/min and detection at λ = 220 nm.

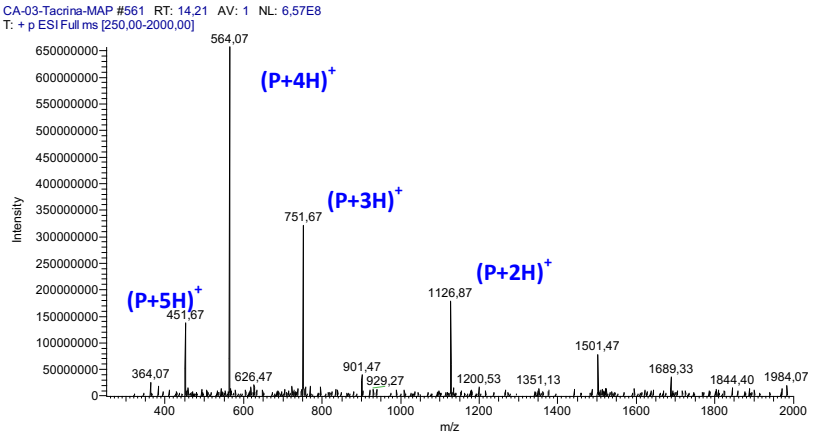


Figure 1.14 - Mass spectrum (LC-ESI/Orbitrap MS, positive mode) of the conjugate TAC-MAP.

1.4.5. TCP-MAP

Briefly, MAP was synthetized through Fmoc/tBu SPPS methodologies assisted with microwave energy, using a Liberty Microwave Peptide Synthesizer. Conjugation of TCP with MAP was achieved through “click chemistry” – a classical CuAAC reaction (Figure 1.15). Details for preparation of TCP-MAP are in Supporting Information (Synthesis of TCP-

linker-N_3, Synthesis of MAP and Synthesis of TCP-MAP). Whereas the peptide-drug conjugate was characterized by HPLC and LC-MS (Figure 1.16 and 1.17).

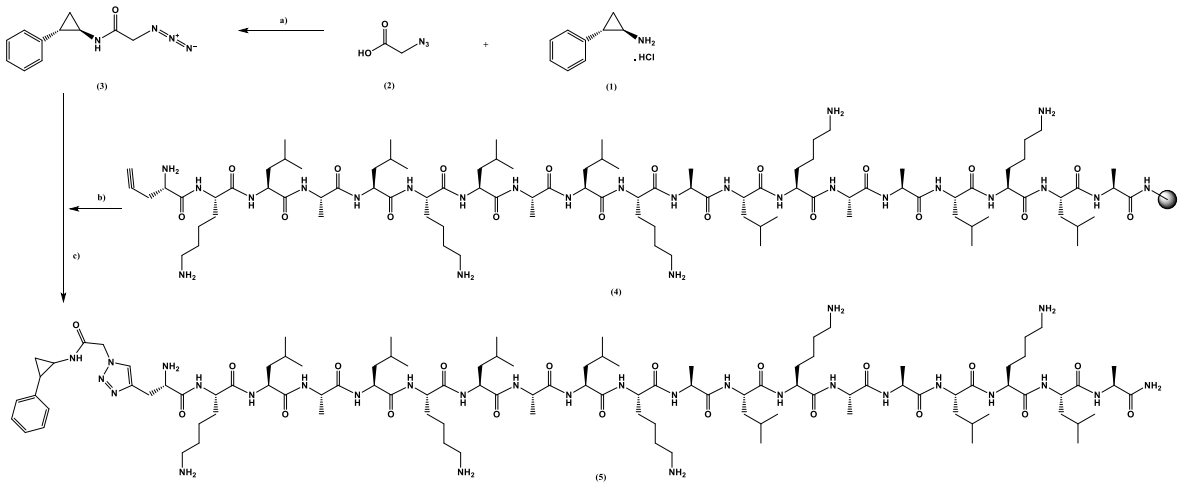


Figure 1.15 - Representation of the methodology applied for the synthesis of the TCP-MAP conjugate.

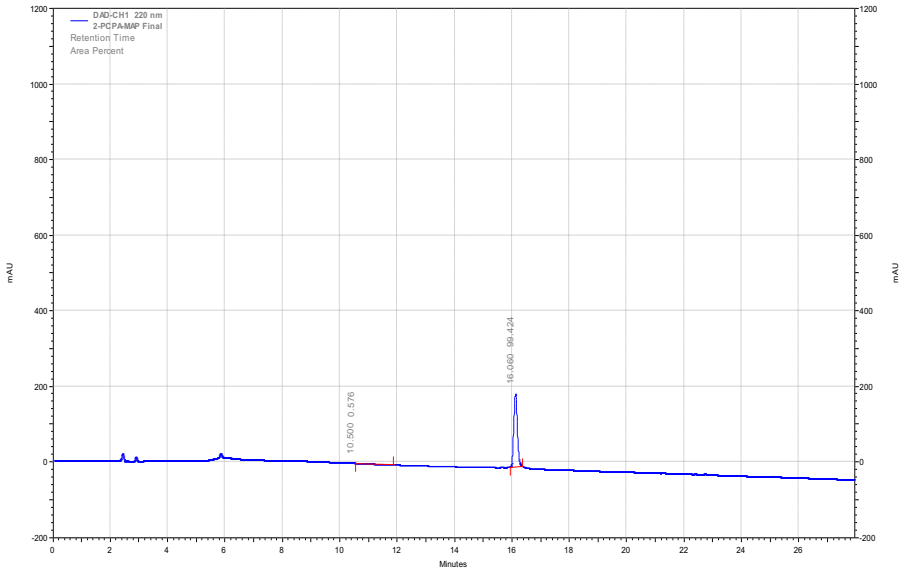


Figure 1.16 - Chromatogram of the product of the manual synthesis of TCP-MAP, acquired with a HPLC system, with a C18 column, using ACN in water with 0.05% TFA as eluent, in gradient mode (0 – 100%), for 30 minutes, at a flow of 1 mL/min and detection at λ = 220 nm.

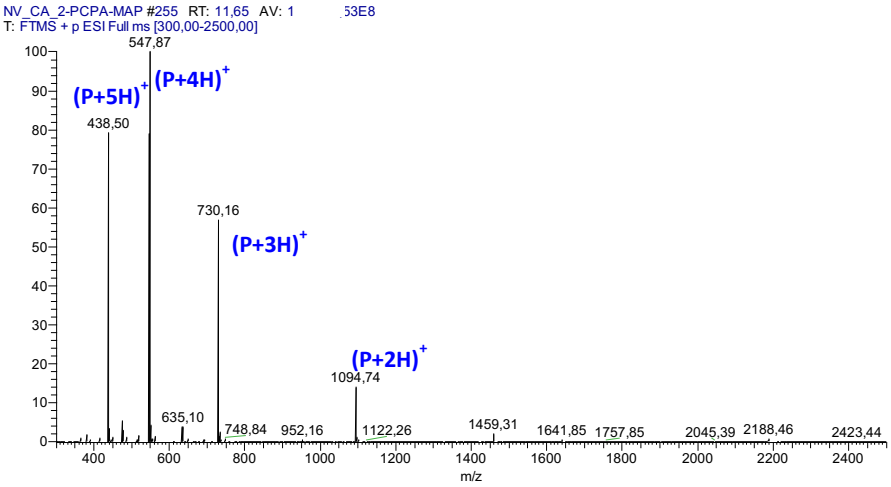
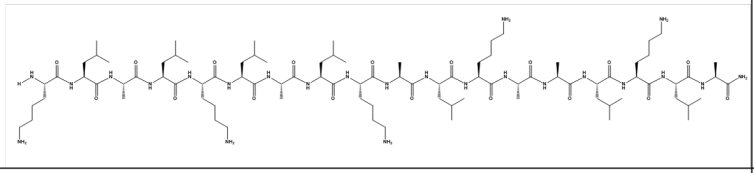
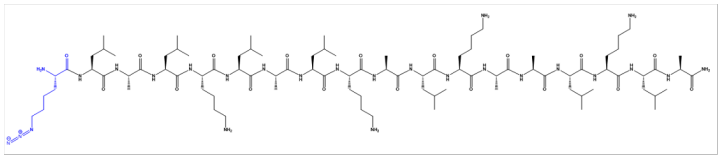
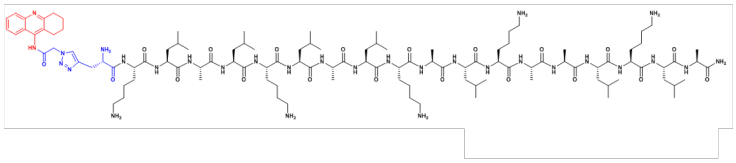
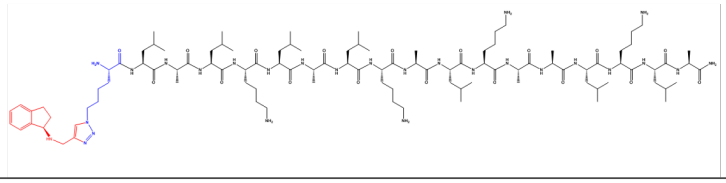
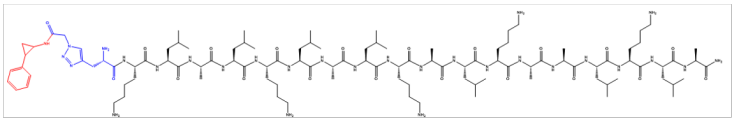


Figure 1.17 - Mass spectrum (LC-ESI/Orbitrap MS, positive mode) of the peptide TCP-MAP.

Table 1.1 - Structure representation and physical-chemical proprieties of peptides used in this Thesis.

Peptide	Structure	$MW_{exp.}$ /g.mol^{-1}	Purity (%)/HPLC
MAP		1876.50	100
Lys(N_3)-MAP		1902.50	96.2
TAC-MAP		2252.92	99.6
RAS-MAP		2072.40	93.4
TCP-MAP		2187.85	100

1.5. Discussion

Even though all the chemical reactions conducted were demanding the results observed indicate that all compounds were successful synthetized with good stability and high purification values (Table 1.1).

1.6. References

1. Zorko M, Langel U. Cell-penetrating peptides: mechanism and kinetics of cargo delivery. Adv Drug Deliv Rev [Internet]. 2005 Feb 28;57(4):529–45. Available from: https://linkinghub.elsevier.com/retrieve/pii/S0169409X04002674

2. Lundberg P, Langel U. A brief introduction to cell-penetrating peptides. J Mol Recognit [Internet]. 2003;16(5):227–33. Available from: http://www.ncbi.nlm.nih.gov/pubmed/14523933

3. Temsamani J, Vidal P, Temsamani J. The use of cell-penetrating peptides for drug delivery. Drug Discovery Today 2004 p. 1012–9. Available from: http://dx.doi.org/10.1016/j.peptides.2014.04.015

4. Frankel AD, Pabo CO, Frankel, A.D. and Pabo CO. Cellular uptake of the tat protein from human immunodeficiency virus. Cell. 1988;55(6):1189–93. Available from: https://linkinghub.elsevier.com/retrieve/pii/0092867488902632.

5. Vivès E, Brodin P, Lebleu B. A truncated HIV-1 Tat protein basic domain rapidly translocates through the plasma membrane and accumulates in the cell nucleus. J Biol Chem. 1997;272(25):16010–7.

6. Joliot A, Pernelle C, Deagostini-Bazin H, Prochiantz A. Antennapedia homeobox peptide regulates neural morphogenesis. Proc Natl Acad Sci [Internet]. 1991;88(5):1864–8. Available from: http://www.pnas.org/cgi/doi/10.1073/pnas.88.5.1864

7. Derossi D, Joliot AH, Chassaing G, Prochiantz A. The third helix of the Antennapedia homeodomain translocates through biological membranes. J Biol Chem. 1994;269(14):10444–50.

8. Derossi D, Calvet S, Trembleau A, Brunissen A, Chassaing G, Prochiantz A. Cell internalization of the third helix of the antennapedia homeodomain is receptor-independent. J Biol Chem. 1996;271(30):18188–93.

9. Gautam A, Singh H, Tyagi A, Chaudhary K, Kumar R, Kapoor P, et al. CPPsite: A curated database of cell penetrating peptides. Database. 2012;2012:1–7.

10. Xie J, Bi Y, Zhang H, Dong S, Teng L, Lee RJ, et al. Cell-Penetrating Peptides in Diagnosis and Treatment of Human Diseases: From Preclinical Research to Clinical Application. Front Pharmacol [Internet]. 2020 May 20;11:697. Available from: https://www.frontiersin.org/article/10.3389/fphar.2020.00697

11. Borrelli A, Tornesello AL, Tornesello ML, Buonaguro FM. Cell penetrating peptides as molecular carriers for anti-cancer agents. Molecules. 2018;23(2). Available from: http://www.ncbi.nlm.nih.gov/pubmed/29385037

12. Mäger I, Eiríksdóttir E, Langel K, EL Andaloussi S, Langel Ü. Assessing the uptake kinetics and internalization mechanisms of cell-penetrating peptides using a quenched fluorescence assay. Biochim Biophys Acta - Biomembr [Internet]. 2010;1798(3):338–43. Available from: http://dx.doi.org/10.1016/j.bbamem.2009.11.001

13. Oehlke J, Scheller A, Wiesner B, Krause E, Beyermann M, Klauschenz E, et al. Cellular uptake of an α-helical amphipathic model peptide with the potential to deliver polar compounds into the cell interior non-endocytically. Biochim Biophys Acta - Biomembr. 1998;1414(1–2):127–39.

14. Fotin-Mleczek M, Welte S, Mader O, Duchardt F, Fischer R, Hufnagel H, et al. Cationic cell-penetrating peptides interfere with TNF signalling by induction of TNF receptor internalization. J Cell Sci [Internet]. 2005 Aug 1;118(15):3339 LP – 3351. Available from: http://jcs.biologists.org/content/118/15/3339.abstract

15. Fischer R, Köhler K, Fotin-Mleczek M, Brock R. A Stepwise Dissection of the Intracellular Fate of Cationic Cell-penetrating Peptides. J Biol Chem. 2004;279(13):12625–35.

16. Reissmann S. Cell penetration: scope and limitations by the application of cell-penetrating peptides. J Pept Sci. 2014 Oct;20(10):760–84.

17. Melikov K, Chernomordik L V. Arginine-rich cell penetrating peptides: from endosomal uptake to nuclear delivery. Cell Mol Life Sci. 2005 Dec;62(23):2739–49. Available from: http://link.springer.com/10.1007/s00018-005-5293-y

18. Richard JP, Melikov K, Vives E, Ramos C, Verbeure B, Gait MJ, et al. Cell-penetrating peptides: A reevaluation of the mechanism of cellular uptake. J Biol

Chem. 2003;278(1):585–90. Available from: https://linkinghub.elsevier.com/retrieve/pii/S0021925819313080

19. Fischer R, Fotin-Mleczek M, Hufnagel H, Brock R. Break on through to the Other Side-Biophysics and Cell Biology Shed Light on Cell-Penetrating Peptides. ChemBioChem [Internet]. 2005 Dec 2;6(12):2126–42. Available from: https://onlinelibrary.wiley.com/doi/10.1002/cbic.200500044

20. Kauffman WB, Fuselier T, He J, Wimley WC. Mechanism Matters: A Taxonomy of Cell Penetrating Peptides. Vol. 40, Trends in Biochemical Sciences. 2015. p. 749–64. Available from: https://linkinghub.elsevier.com/retrieve/pii/S0968000415001887

21. Holm T, Langel Ü, El-Andaloussi S, Holm T, Langel U. Cell-Penetrating Peptides: Mechanisms and Applications. Curr Pharm Des [Internet]. 2005;11(28):3597–611. Available from: http://www.eurekaselect.com/openurl/content.php?genre=article&issn=1381-6128&volume=11&issue=28&spage=3597

22. Pouny Y, Rapaport D, Mor A, Nicolas P, Shai Y. Interaction of antimicrobial dermaseptin and its fluorescently labeled analogues with phospholipid membranes. Biochemistry. 1992;31(49):12416–23.

23. Jones SW, Christison R, Bundell K, Voyce CJ, Brockbank SMV, Newham P, et al. Characterisation of cell-penetrating peptide-mediated peptide delivery. Br J Pharmacol. 2005;145(8):1093–102.

24. Gazit E, Shai Y, Lee WJ, Brey PT. Mode of Action of the Antibacterial Cecropin B2: A Spectrofluorometric Study. Biochemistry. 1994;33(35):10681–92.

25. Guidotti G, Brambilla L, Rossi D. Cell-Penetrating Peptides: From Basic Research to Clinics. Trends Pharmacol Sci [Internet]. 2017;38(4):406–24. Available from: http://dx.doi.org/10.1016/j.tips.2017.01.003

26. Kondo E, Saito K, Tashiro Y, Kamide K, Uno S, Furuya T, et al. Tumour lineage-homing cell-penetrating peptides as anticancer molecular delivery systems. Nat Commun [Internet]. 2012;3:913–51. Available from: http://dx.doi.org/10.1038/ncomms1952

27. Kaplan IM, Wadia JS, Dowdy SF. Cationic TAT peptide transduction domain enters cells by macropinocytosis. J Control Release. 2005;102(1):247–53. Available from: https://linkinghub.elsevier.com/retrieve/pii/S0168365904004766

28. Lindgren ME, Hallbrink MM, Elmquist AM, Langel U, Hällbrink MM, Elmquist AM, et al. Passage of cell-penetrating peptides across a human epithelial cell layer *in vitro*. Biochem J [Internet]. 2004;377(Pt 1):69–76. Available from: http://www.ncbi.nlm.nih.gov/pubmed/12968950%5Cnhttp://www.pubmedcentral.nih.gov/articlerender.fcgi?artid=PMC1223834%5Cnhttp://www.pubmedcentral.nih.gov/articlerender.fcgi?artid=1223834&tool=pmcentrez&rendertype=abstract

29. Yamashita H, Kato T, Oba M, Misawa T, Hattori T, Ohoka N, et al. Development of a Cell-penetrating Peptide that Exhibits Responsive Changes in its Secondary Structure in the Cellular Environment. Sci Rep [Internet]. 2016;6(May):2–9. Available from: http://dx.doi.org/10.1038/srep33003

30. Hitz T, Iten R, Gardiner J, Namoto K, Walde P, Seebach D. Interaction of α-and β-oligoarginine-acids and amides with anionic lipid vesicles: A mechanistic and thermodynamic study. Biochemistry. 2006;

31. Oba M, Kato T, Furukawa K, Tanaka M. OPEN A Cell-Penetrating Peptide with a Guanidinylethyl Amine Structure Directed to Gene Delivery. Nat Publ Gr [Internet]. 2016;1–9. Available from: http://dx.doi.org/10.1038/srep19913

32. Snyder EL, Dowdy SF. Cell penetrating peptides in drug delivery. Pharmaceutical Research 2004 p. 389–93. Available from: http://link.springer.com/10.1023/B:PHAM.0000019289.61978.f5

33. Sakurai Y, Hatakeyama H, Sato Y, Akita H, Takayama K, Kobayashi S, et al. Endosomal escape and the knockdown efficiency of liposomal-siRNA by the fusogenic peptide shGALA. Biomaterials [Internet]. 2011;32(24):5733–42. Available from: http://dx.doi.org/10.1016/j.biomaterials.2011.04.047

34. Wadia JS, Stan R V., Dowdy SF. Transducible TAT-HA fusogenic peptide enhances escape of TAT-fusion proteins after lipid raft macropinocytosis. Nat Med. 2004;10(3):310–5. Available from: http://www.nature.com/articles/nm996

35. Richardson A, Muir L, Mousdell S, Sexton D, Jones S, Howl J, et al. Modulation of mitochondrial activity in HaCaT keratinocytes by the cell penetrating peptide Z-Gly-RGD(DPhe)-mitoparan. BMC Res Notes [Internet]. 2018;11(1):1–4. Available from: https://doi.org/10.1186/s13104-018-3192-1

36. De Figueiredo IR, Freire JM, Flores L, Veiga AS, Castanho MARB. Cell-penetrating peptides: A tool for effective delivery in gene-targeted therapies. IUBMB Life.

2014;66(3):182–94. Available from: https://onlinelibrary.wiley.com/doi/10.1002/iub.1257

37. Vasconcelos L, Pärn K, Langel Ü. Therapeutic potential of cell-penetrating peptides. Ther Deliv [Internet]. 2013;4(5):573–91. Available from: http://www.future-science.com/doi/10.4155/tde.13.22

38. Farkhani SM, Valizadeh A, Karami H, Mohammadi S, Sohrabi N, Badrzadeh F. Cell penetrating peptides: Efficient vectors for delivery of nanoparticles, nanocarriers, therapeutic and diagnostic molecules. Peptides [Internet]. 2014;57:78–94. Available from: http://dx.doi.org/10.1016/j.peptides.2014.04.015

39. Dubuc C, Savard M, Bovenzi V, Lessard A, Fortier A, Côté J, et al. Targeting intracellular B2 receptors using novel cell-penetrating antagonists to arrest growth and induce apoptosis in human triple-negative breast cancer. Oncotarget. 2018;9(11):9885–906. Available from: https://www.oncotarget.com/lookup/doi/10.18632/oncotarget.24009

40. Fu A, Zhang M, Gao F, Xu X, Chen Z. A Novel Peptide Delivers Plasmids across Blood-Brain Barrier into Neuronal Cells as a Single-Component Transfer Vector. PLoS One. 2013;8(3):1–9. Available from: https://dx.plos.org/10.1371/journal.pone.0059642

41. Kristensen M, Nielsen HM. Cell-penetrating peptides as tools to enhance non-injectable delivery of biopharmaceuticals. Vol. 4, Tissue Barriers. 2016. Available from: http://www.tandfonline.com/doi/full/10.1080/21688370.2016.1178369

42. Järver P, Langel Ü, Jarver P, Langel U, Järver P, Langel Ü. The use of cell-penetrating peptides as a tool for gene regulation. Drug Discov Today [Internet]. 2004 May;9(9):395–402. Available from: http://www.sciencedirect.com/science/article/pii/S1359644604030429

43. Oller-Salvia B, Sánchez-Navarro M, Ciudad S, Guiu M, Arranz-Gibert P, Garcia C, et al. MiniAp-4: A Venom-Inspired Peptidomimetic for Brain Delivery. Angew Chemie - Int Ed. 2016;55(2):572–5. Available from: https://onlinelibrary.wiley.com/doi/10.1002/anie.201508445

44. Regberg J, Srimanee A, Erlandsson M, Sillard R, Dobchev DA, Karelson M, et al. Rational design of a series of novel amphipathic cell-penetrating peptides. Int J Pharm [Internet]. 2014;464(1–2):111–6. Available from:

http://dx.doi.org/10.1016/j.ijpharm.2014.01.018

45. Malakoutikhah M, Pradesh R, Teixidó M, Giralt E. N-Methyl Phenylalanine-Rich peptides as highly versatile blood-brain barrier shuttles. J Med Chem. 2010;53(6):2354–63. Available from: https://pubs.acs.org/doi/10.1021/jm901654x

46. Lättig-Tünnemann G, Prinz M, Hoffmann D, Behlke J, Palm-Apergi C, Morano I, et al. Backbone rigidity and static presentation of guanidinium groups increases cellular uptake of arginine-rich cell-penetrating peptides. Nat Commun. 2011;2(1). Available from: http://www.nature.com/articles/ncomms1459

47. Gronewold A, Horn M, Ranđelović I, Tóvári J, Muñoz Vázquez S, Schomäcker K, et al. Characterization of a Cell-Penetrating Peptide with Potential Anticancer Activity. ChemMedChem. 2017;12(1):42–9. Available from: https://onlinelibrary.wiley.com/doi/10.1002/cmdc.201600498

48. Kumar P, Wu H, McBride JL, Jung KE, Hee Kim M, Davidson BL, et al. Transvascular delivery of small interfering RNA to the central nervous system. Nature. 2007;448(7149):39–43.

49. Sasaki-Hamada S, Funane T, Nakao Y, Sasaki R, Nagai M, Ueta Y, et al. Intranasal administration of neuromedin U derivatives containing cell-penetrating peptides and a penetration-accelerating sequence induced memory improvements in mice. Peptides [Internet]. 2018;99(September 2017):241–6. Available from: https://doi.org/10.1016/j.peptides.2017.10.010

50. Olson ES, Jiang T, Aguilera TA, Nguyen QT, Ellies LG, Scadeng M, et al. Activatable cell penetrating peptides linked to nanoparticles as dual probes for *in vivo* fluorescence and MR imaging of proteases. Proc Natl Acad Sci [Internet]. 2010;107(9):4311–6. Available from: http://www.pnas.org/cgi/doi/10.1073/pnas.0910283107

51. Jiang T, Zhang Z, Zhang Y, Lv H, Zhou J, Li C, et al. Dual-functional liposomes based on pH-responsive cell-penetrating peptide and hyaluronic acid for tumor-targeted anticancer drug delivery. Biomaterials [Internet]. 2012;33(36):9246–58. Available from: http://dx.doi.org/10.1016/j.biomaterials.2012.09.027

52. Kanazawa T, Morisaki K, Suzuki S, Takashima Y. Prolongation of life in rats with malignant glioma by intranasal siRNA/drug codelivery to the brain with cell-penetrating peptide-modified micelles. Mol Pharm. 2014;11(5):1471–8. Available

from: https://pubs.acs.org/doi/10.1021/mp400644e

53. Sharma G, Modgil A, Layek B, Arora K, Sun C, Law B, et al. Cell penetrating peptide tethered bi-ligand liposomes for delivery to brain *in vivo*: Biodistribution and transfection. J Control Release [Internet]. 2013;167(1):1–10. Available from: http://dx.doi.org/10.1016/j.jconrel.2013.01.016

54. Cameron A, Appel J, Houghten RA, Lindberg I. Polyarginines Are Potent Furin Inhibitors*. J Biol Chem [Internet]. 2000;275(47):36741–9. Available from: https://www.sciencedirect.com/science/article/pii/S0021925820885779

55. Kuo JS, Jan M, Lin Y-L, Lin C. Interactions between octaarginine and U-937 human macrophages: Global gene expression profiling, superoxide anion content, and cytokine production. J Control Release [Internet]. 2009;139(3):197–204. Available from: https://www.sciencedirect.com/science/article/pii/S0168365909004805

56. Ward B, Seal BL, Brophy CM, Panitch A. Design of a bioactive cell-penetrating peptide: when a transduction domain does more than transduce. J Pept Sci [Internet]. 2009 Sep;15(10):668–74. Available from: https://onlinelibrary.wiley.com/doi/10.1002/psc.1168

57. Kilk K, Mahlapuu R, Soomets U, Langel Ü. Analysis of *in vitro* toxicity of five cell-penetrating peptides by metabolic profiling. Toxicology [Internet]. 2009 Nov;265(3):87–95. Available from: https://linkinghub.elsevier.com/retrieve/pii/S0300483X09004892

58. Moutal A, François-Moutal L, Brittain JM, Khanna M, Khanna R. Differential neuroprotective potential of CRMP2 peptide aptamers conjugated to cationic, hydrophobic, and amphipathic cell penetrating peptides. Front Cell Neurosci [Internet]. 2015 Jan 26;8(JAN):1–15. Available from: http://journal.frontiersin.org/article/10.3389/fncel.2014.00471/abstract

59. Fernández-Carneado J, Kogan MJ, Pujals S, Giralt E. Amphipathic peptides and drug delivery. Biopolymers [Internet]. 2004;76(2):196–203. Available from: https://onlinelibrary.wiley.com/doi/10.1002/bip.10585

60. Steiner V, Schär M, Börnsen KO, Mutter M. Retention behaviour of a template-assembled synthetic protein and its amphiphilic building blocks on reversed-phase columns. J Chromatogr A. 1991 Nov 8;586(1):43–50.

61. Deli MA. Potential use of tight junction modulators to reversibly open membranous

barriers and improve drug delivery. Biochim Biophys Acta - Biomembr [Internet]. 2009 Apr;1788(4):892–910. Available from: http://dx.doi.org/10.1016/j.bbamem.2008.09.016

62. Chen S-C, Eiting K, Cui K, Leonard AK, Morris D, Li C-Y, et al. Therapeutic utility of a novel tight junction modulating peptide for enhancing intranasal drug delivery. J Pharm Sci [Internet]. 2006 Jun;95(6):1364–71. Available from: https://linkinghub.elsevier.com/retrieve/pii/S0022354916320226

63. Johnson PH, Quay SC. Advances in nasal drug delivery through tight junction technology. Expert Opin Drug Deliv [Internet]. 2005 Mar 12;2(2):281–98. Available from: https://www.tandfonline.com/doi/full/10.1517/17425247.2.2.281

64. Deshayes S, Morris MC, Divita G, Heitz F. Cell-penetrating peptides: tools for intracellular delivery of therapeutics. Cell Mol Life Sci [Internet]. 2005;62(16):1839–49. Available from: http://link.springer.com/10.1007/s00018-005-5109-0

65. Kerth A, Erbe A, Dathe M, Blume A. Infrared reflection absorption spectroscopy of amphipathic model peptides at the air/water interface. Biophys J. 2004;86(6):3750–8. Available from: https://linkinghub.elsevier.com/retrieve/pii/S000634950474415X

66. Janek K, Rothemund S, Gast K, Beyermann M, Zipper J, Fabian H, et al. Study of the Conformational Transition of Aβ(1−42) Using D-Amino Acid Replacement Analogues. Biochemistry [Internet]. 2001 May 1;40(18):5457–63. Available from: https://doi.org/10.1021/bi002005e

67. Oehlke J, Scheller A, Janek K, Wiesner B, Krause E, Beyermann M, et al. Rapid translocation of amphipathic βhelical and β-sheet-forming peptides through plasma membranes of endothelial cells. In: Peptide Science — Present and Future [Internet]. Dordrecht: Kluwer Academic Publishers; 2006. p. 782–3. Available from: http://link.springer.com/10.1007/0-306-46864-6_268

68. Sarko D, Beijer B, Boy RG, Nothelfer EM, Leotta K, Eisenhut M, et al. The pharmacokinetics of cell-penetrating peptides. Mol Pharm. 2010;7(6):2224–31. Available from: https://pubs.acs.org/doi/10.1021/mp100223d

69. Scheller A, Oehlke J, Wiesner B, Dathe M, Krause E, Beyermann M, et al. Structural requirements for cellular uptake of α-helical amphipathic peptides. J Pept Sci [Internet]. 1999 Apr;5(4):185–94. Available from: https://onlinelibrary.wiley.com/doi/10.1002/(SICI)1099-

1387(199904)5:4%3C185::AID-PSC184%3E3.0.CO;2-9

70. Oehlke J, Krause E, Wiesner B, Beyermann M, Bienert M. Extensive cellular uptake into endothelial cells of an amphipathic β-sheet forming peptide. FEBS Lett [Internet]. 1997 Sep 29;415(2):196–9. Available from: https://www.sciencedirect.com/science/article/pii/S001457939701123X

71. Oehlke J, Lorenz D, Wiesner B, Bienert M. Studies on the cellular uptake of substance P and lysine-rich, KLA-derived model peptides. J Mol Recognit [Internet]. 2005 Jan;18(1):50–9. Available from: https://onlinelibrary.wiley.com/doi/10.1002/jmr.691

72. Scheller A, Wiesner B, Melzig M, Bienert M, Oehlke J. Evidence for an amphipathicity independent cellular uptake of amphipathic cell-penetrating peptides. Eur J Biochem [Internet]. 2000 Oct;267(19):6043–50. Available from: http://doi.wiley.com/10.1046/j.1432-1327.2000.01681.x

73. Milletti F. Cell-penetrating peptides: classes, origin, and current landscape. Drug Discov Today [Internet]. 2012 Aug;17(15–16):850–60. Available from: http://dx.doi.org/10.1016/j.drudis.2012.03.002

74. Kenien R, Shen WC, Zaro JL. Vesicle-to-cytosol transport of disulfide-linked cargo mediated by an amphipathic cell-penetrating peptide. J Drug Target. 2012; Available from: http://www.tandfonline.com/doi/full/10.3109/1061186X.2012.719899

75. Bocsik A, Walter FR, Gyebrovszki A, Fülöp L, Blasig I, Dabrowski S, et al. Reversible Opening of Intercellular Junctions of Intestinal Epithelial and Brain Endothelial Cells with Tight Junction Modulator Peptides. J Pharm Sci. 2016;105(2):754–65. Available from: https://linkinghub.elsevier.com/retrieve/pii/S0022354915001331

76. Bocsik A, Gróf I, Kiss L, Ötvös F, Zsíros O, Daruka L, et al. Dual action of the PN159/KLAL/MAP peptide: Increase of drug penetration across caco-2 intestinal barrier model by modulation of tight junctions and plasma membrane permeability. Pharmaceutics. 2019;11(2). Available from: http://www.mdpi.com/1999-4923/11/2/73

77. Pierigè F, Serafini S, Rossi L, Magnani M. Cell-based drug delivery. Adv Drug Deliv Rev [Internet]. 2008;60(2):286–95. Available from: https://www.sciencedirect.com/science/article/pii/S0169409X07002505

78. Oehlke J, Wallukat G, Wolf Y, Ehrlich A, Wiesner B, Berger H, et al. Enhancement

of intracellular concentration and biological activity of PNA after conjugation with a cell-penetrating synthetic model peptide. Eur J Biochem. 2004;271(14):3043–9. Available from: https://onlinelibrary.wiley.com/doi/10.1111/j.1432-1033.2004.04236.x

79. Säälik P, Niinep A, Pae J, Hansen M, Lubenets D, Langel Ü, et al. Penetration without cells: Membrane translocation of cell-penetrating peptides in the model giant plasma membrane vesicles. J Control Release [Internet]. 2011;153(2):117–25. Available from: http://dx.doi.org/10.1016/j.jconrel.2011.03.011

80. Pae J, Säälik P, Liivamägi L, Lubenets D, Arukuusk P, Langel Ü, et al. Translocation of cell-penetrating peptides across the plasma membrane is controlled by cholesterol and microenvironment created by membranous proteins. J Control Release [Internet]. 2014;192:103–13. Available from: http://dx.doi.org/10.1016/j.jconrel.2014.07.002

81. Hällbrink M, Oehlke J, Papsdorf G, Bienert M. Uptake of cell-penetrating peptides is dependent on peptide-to-cell ratio rather than on peptide concentration. Biochim Biophys Acta - Biomembr. 2004;1667(2):222–8.

82. Wadhwani P, Bürck J, Strandberg E, Mink C, Afonin S, Ulrich AS. Using a Sterically Restrictive Amino Acid as a 19 F NMR label To Monitor and To Control Peptide Aggregation in Membranes. J Am Chem Soc [Internet]. 2008 Dec 10;130(49):16515–7. Available from: https://pubs.acs.org/doi/10.1021/ja804928q

83. Strandberg E, Tiltak D, Ieronimo M, Kanithasen N, Wadhwani P, Ulrich AS. Influence of C-terminal amidation on the antimicrobial and hemolytic activities of cationic α-helical peptides. Pure Appl Chem. 2007;79(4):717–28.

84. Vale N, Alves C, Sharma V, Lázaro DF, Silva S, Gomes P, et al. A new MAP-Rasagiline conjugate reduces α-synuclein inclusion formation in a cell model. Pharmacol Reports [Internet]. 2020 Apr 15;72(2):456–64. Available from: https://doi.org/10.1007/s43440-019-00032-x

85. Zemel A, Fattal DR, Ben-Shaul A. Energetics and Self-Assembly of Amphipathic Peptide Pores in Lipid Membranes. Biophys J [Internet]. 2003 Apr;84(4):2242–55. Available from: http://dx.doi.org/10.1016/S0006-3495(03)75030-9

86. Dathe M, Meyer J, Beyermann M, Maul B, Hoischen C, Bienert M. General aspects of peptide selectivity towards lipid bilayers and cell membranes studied by variation

of the structural parameters of amphipathic helical model peptides. Biochim Biophys Acta - Biomembr. 2002;1558(2):171–86.

87. Leuschner C, Hansel W. Membrane Disrupting Lytic Peptides for Cancer Treatments. Curr Pharm Des. 2005;10(19):2299–310. Available from: http://www.eurekaselect.com/openurl/content.php?genre=article&issn=1381-6128&volume=10&issue=19&spage=2299

88. Saar K, Lindgren M, Hansen M, Eiríksdóttir E, Jiang Y. Cell-penetrating peptides : A comparative membrane toxicity study. 2005;345:55–65. Available from: https://linkinghub.elsevier.com/retrieve/pii/S0003269705005439

89. Silva S, Almeida A, Vale N. Combination of Cell-Penetrating Peptides with Nanoparticles for Therapeutic Application: A Review. Biomolecules [Internet]. 2019 Jan 10;9(1):22. Available from: http://www.ncbi.nlm.nih.gov/pubmed/30634689

90. Zaro JL, Fei L, Shen W-C. Recombinant peptide constructs for targeted cell penetrating peptide-mediated delivery. J Control Release [Internet]. 2012 Mar;158(3):357–61. Available from: http://dx.doi.org/10.1016/j.jconrel.2012.01.039

91. Ward C, Meehan J, Gray ME, Murray AF, Argyle DJ, Kunkler IH, et al. The impact of tumour pH on cancer progression: strategies for clinical intervention. Explor Target Anti-tumor Ther [Internet]. 2020 Apr 9;1(2):71–100. Available from: https://www.explorationpub.com/Journals/etat/Article/10025

92. Pérez-Herrero E, Fernández-Medarde A. The reversed intra- and extracellular pH in tumors as a unified strategy to chemotherapeutic delivery using targeted nanocarriers. Acta Pharm Sin B [Internet]. 2021 Aug;11(8):2243–64. Available from: https://www.sciencedirect.com/science/article/pii/S2211383521000162

93. Shutske GM, Pierrat FA, Kapples KJ, Cornfeldt ML, Szewczak MR, Huger FP, et al. 9-Amino-1,2,3,4-tetrahydroacridin-1-ols. Synthesis and evaluation as potential Alzheimer's disease therapeutics. J Med Chem [Internet]. 1989 Aug;32(8):1805–13. Available from: https://pubs.acs.org/doi/abs/10.1021/jm00128a024

94. Crismon ML. Tacrine: First drug approved for alzheimer's disease. Ann Pharmacother. 1994;28(6):744–51.

95. Summers WK, Tachiki KH, Kling A. Tacrine in the Treatment of Alzheimer's Disease. Eur Neurol [Internet]. 1989;29(suppl 3(Suppl. 3):28–32. Available from: https://www.karger.com/DOI/10.1159/000116478

96. Tumiatti V, Minarini A, Bolognesi ML, Milelli A, Rosini M, Melchiorre C. Tacrine Derivatives and Alzheimers Disease. Curr Med Chem [Internet]. 2010 Jun 1;17(17):1825–38. Available from: http://www.eurekaselect.com/openurl/content.php?genre=article&issn=0929-8673&volume=17&issue=17&spage=1825

97. Summers WK. Tacrine, and Alzheimer's treatments. Journal of Alzheimer's Disease. 2006.

98. Summers WK, Majovski LV, Marsh GM, Tachiki K, Kling A. Oral Tetrahydroaminoacridine in Long-Term Treatment of Senile Dementia, Alzheimer Type. N Engl J Med. 1986; Available from: http://www.nejm.org/doi/abs/10.1056/NEJM198611133152001

99. Forsyth DR, Surmon DJ, Morgan RA, Wilcock GK. Clinical experience with and side-effects of tacrine hydrochloride in alzheimer's disease: A pilot study. Age Ageing. 1989;18(4):223–9. Available from: https://academic.oup.com/ageing/article-lookup/doi/10.1093/ageing/18.4.223

100. Forsyth DR, Wilcock GK, Morgan RA, Truman CA, Ford JM, Roberts CJC. Pharmacokinetics of tacrine hydrochloride in Alzheimer's disease. Clin Pharmacol Ther. 1989;46(6):634–41. Available from: http://doi.wiley.com/10.1038/clpt.1989.199

101. Tamilselvan N, Raghavan CV. Formulation and characterization of anti-alzheimer's drug loaded chitosan nanoparticles and its *In vitro* biological evaluation. J Young Pharm. 2015;7(1):28–35. Available from: http://www.jyoungpharm.org/article/736

102. Agrawal M, Saraf S, Saraf S, Antimisiaris SG, Chougule MB, Shoyele SA, et al. Nose-to-brain drug delivery: An update on clinical challenges and progress towards approval of anti-Alzheimer drugs. J Control Release [Internet]. 2018;281(May):139–77. Available from: https://doi.org/10.1016/j.jconrel.2018.05.011

103. J.-H. Lee, T. G. Park H-KC. Development of oral drug delivery system using floating microspheres. J Microencapsul [Internet]. 1999 Jan 29;16(6):715–29. Available from: http://www.tandfonline.com/doi/full/10.1080/026520499288663

104. Sathesh Kumar S, Felix Joe V. Pharmacokinetics of tacrine loaded MPEG-PCL polymeric nanoparticles. Res J Pharm Technol. 2017;10(1):135–40. Available from: http://www.indianjournals.com/ijor.aspx?target=ijor:rjpt&volume=10&issue=1&article=030

105. Erdő F, Bors LA, Farkas D, Bajza Á, Gizurarson S. Evaluation of intranasal delivery route of drug administration for brain targeting. Brain Res Bull. 2018;143(October):155–70. Available from: https://linkinghub.elsevier.com/retrieve/pii/S0361923018303678

106. Luppi B, Bigucci F, Corace G, Delucca A, Cerchiara T, Sorrenti M, et al. Albumin nanoparticles carrying cyclodextrins for nasal delivery of the anti-Alzheimer drug tacrine. Eur J Pharm Sci [Internet]. 2011;44(4):559–65. Available from: http://dx.doi.org/10.1016/j.ejps.2011.10.002

107. Jogani V V., Shah PJ, Mishra P, Mishra AK, Misra AR. Intranasal mucoadhesive microemulsion of tacrine to improve brain targeting. Alzheimer Dis Assoc Disord. 2008;22(2):116–24. Available from: https://journals.lww.com/00002093-200804000-00005

108. Saladini B, Bigucci F, Cerchiara T, Gallucci MC, Luppi B. Microparticles based on chitosan/pectin polyelectrolyte complexes for nasal delivery of tacrine hydrochloride. Drug Deliv Transl Res. 2013;3(1):33–41.

109. Corace G, Angeloni C, Malaguti M, Hrelia S, Stein PC, Brandl M, et al. Multifunctional liposomes for nasal delivery of the anti-Alzheimer drug tacrine hydrochloride. J Liposome Res. 2014;24(4):323–35. Available from: http://www.tandfonline.com/doi/full/10.3109/08982104.2014.899369

110. Wilson B, Samanta MK, Santhi K, Kumar KPS, Paramakrishnan N, Suresh B. Poly(n-butylcyanoacrylate) nanoparticles coated with polysorbate 80 for the targeted delivery of rivastigmine into the brain to treat Alzheimer's disease. Brain Res. 2008;1200:159–68. Available from: https://linkinghub.elsevier.com/retrieve/pii/S0006899308001406

111. Wilson B, Samanta MK, Santhi K, Kumar KPS, Ramasamy M, Suresh B. Chitosan nanoparticles as a new delivery system for the anti-Alzheimer drug tacrine. Nanomedicine Nanotechnology, Biol Med [Internet]. 2010;6(1):144–52. Available from: http://dx.doi.org/10.1016/j.nano.2009.04.001

112. Hassani S, Laouini A, Fessi H, Charcosset C. Preparation of chitosan-TPP nanoparticles using microengineered membranes - Effect of parameters and encapsulation of tacrine. Colloids Surfaces A Physicochem Eng Asp [Internet]. 2015;482:34–43. Available from: http://dx.doi.org/10.1016/j.colsurfa.2015.04.006

113. Hassanzadeh G, Fallahi Z, Khanmohammadi M, Elmizadeh H. Effect of Magnetic Tacrine-Loaded Chitosan Nanoparticles on Spatial Learning, Memory, Amyloid Precursor Protein and Seladin-1 Expression in the Hippocampus Of Streptozotocin-Exposed Rats. Int Clin Neurosci J. 2016;3(1):25–31.

114. Eslami M, Nikkhah SJ, Hashemianzadeh SM, Sajadi SAS. The compatibility of Tacrine molecule with poly(n-butylcyanoacrylate) and Chitosan as efficient carriers for drug delivery: A molecular dynamics study. Eur J Pharm Sci [Internet]. 2016;82:79–85. Available from: http://dx.doi.org/10.1016/j.ejps.2015.11.014

115. Wilson B, Samanta MK, Santhi K, Sampath Kumar KP, Ramasamy M, Suresh B. Significant delivery of tacrine into the brain using magnetic chitosan microparticles for treating Alzheimer's disease. J Neurosci Methods. 2009;177(2):427–33. Available from: https://linkinghub.elsevier.com/retrieve/pii/S016502700800650X

116. Benítez-Martínez S, Caballero-Díaz E, Valcárcel M. Development of a biosensing system for tacrine based on nitrogen-doped graphene quantum dots and acetylcholinesterase. Analyst. 2016;141(9):2688–95. Available from: http://xlink.rsc.org/?DOI=C6AN00357E

117. Vale N, Gomes P, A. Santos H. Metabolism of the Antituberculosis Drug Ethionamide [Internet]. Vol. 14, Current Drug Metabolism. 2013. p. 151–8. Available from: http://www.eurekaselect.com/article/47824

118. Vale N, Correia A, Silva S, Figueiredo P, Mäkilä E, Salonen J, et al. Preparation and biological evaluation of ethionamide-mesoporous silicon nanoparticles against Mycobacterium tuberculosis. Bioorganic Med Chem Lett. 2017;27(3). Available from: http://dx.doi.org/10.1016/j.bmcl.2016.12.060

119. Shahbazi M, Almeida P V, Mäkilä E, Correia A, Ferreira MP a, Kaasalainen M, et al. Poly(methyl vinyl ether- alt -maleic acid)-Functionalized Porous Silicon Nanoparticles for Enhanced Stability and Cellular Internalization. Macromol Rapid Commun [Internet]. 2014 Mar;35(6):624–9. Available from: https://onlinelibrary.wiley.com/doi/10.1002/marc.201300868

120. Shrestha N, Araújo F, Shahbazi M-A, Mäkilä E, Gomes MJ, Herranz-Blanco B, et al. Thiolation and Cell-Penetrating Peptide Surface Functionalization of Porous Silicon Nanoparticles for Oral Delivery of Insulin. Adv Funct Mater [Internet]. 2016 May;26(20):3405–16. Available from: https://onlinelibrary.wiley.com/doi/10.1002/adfm.201505252

121. Correia A, Shahbazi M-A, Mäkilä E, Almeida S, Salonen J, Hirvonen J, et al. Cyclodextrin-Modified Porous Silicon Nanoparticles for Efficient Sustained Drug Delivery and Proliferation Inhibition of Breast Cancer Cells. ACS Appl Mater Interfaces [Internet]. 2015 Oct 21;7(41):23197–204. Available from: https://doi.org/10.1021/acsami.5b07033

122. Youdim MBH. Rasagiline: An anti-Parkinson drug with neuroprotective activity. Expert Rev Neurother. 2003;3(6):737–49. Available from: http://www.tandfonline.com/doi/full/10.1586/14737175.3.6.737

123. Weinreb O, Amit T, Bar-Am O, Youdim MBH. Rasagiline: A novel anti-Parkinsonian monoamine oxidase-B inhibitor with neuroprotective activity. Prog Neurobiol [Internet]. 2010;92(3):330–44. Available from: http://dx.doi.org/10.1016/j.pneurobio.2010.06.008

124. Kang SS, Zhang Z, Liu X, Manfredsson FP, Benskey MJ, Cao X, et al. TrkB neurotrophic activities are blocked by α-synuclein, triggering dopaminergic cell death in Parkinson's disease. Proc Natl Acad Sci [Internet]. 2017;114(40):201713969. Available from: http://www.pnas.org/lookup/doi/10.1073/pnas.1713969114

125. Kang SS, Ahn EH, Zhang Z, Liu X, Manfredsson FP, Sandoval IM, et al. α-Synuclein stimulation of monoamine oxidase-B and legumain protease mediates the pathology of Parkinson's disease. EMBO J [Internet]. 2018;37(12):e98878. Available from: http://emboj.embopress.org/lookup/doi/10.15252/embj.201798878

126. Kakish J, Tavassoly O, Lee JS. Rasagiline, a suicide inhibitor of monoamine oxidases, binds reversibly to α-synuclein. ACS Chem Neurosci. 2015;6(2):347–55.

127. Ebadi M, Sharma S, Shavali S, El Refaey H. Neuroprotective actions of selegiline. J Neurosci Res. 2002;67(3):285–9.

128. Siddiqui MAA, Plosker GL. Rasagiline. Drugs Aging [Internet]. 2005;22(1):83–91. Available from: http://link.springer.com/10.2165/00002512-200522010-00006

129. Kunasekaran V, Krishnamoorthy K. Multi criteria decision making to select the best method for the preparation of solid lipid nanoparticles of rasagiline mesylate using analytic hierarchy process. J Adv Pharm Technol Res. 2014;5(3):115–21. Available from: http://www.japtr.org/text.asp?2014/5/3/115/137410

130. Kunasekaran V, Krishnamoorthy K. Experimental design for the optimization of nanoscale solid lipid particles containing Rasagiline mesylate. J Young Pharm.

2015;7(4):285–95. Available from: http://www.jyoungpharm.org/article/795

131. Kunasekaran V, Krishnamoorthy K. Kinetic modeling of Rasagiline mesylate from nanoscale solid lipid particles. Int J Pharm Pharm Sci. 2015;7(11):300–5.

132. Kunasekaran V, Krishnamoorthy K. Formulation and Evaluation of Nanoscale Solid Lipid Particles Containing a Hydrophilic Drug-Rasagiline Mesylate. J Appl Pharm Sci [Internet]. 2016;6(5):044–50. Available from: http://www.japsonline.com/abstract.php?article_id=1858

133. Kannan K, Viveksarathi K. Effect of the moist-heat sterilization on fabricated nanoscale solid lipid particles containing rasagiline mesylate. Int J Pharm Investig [Internet]. 2015;5(2):87. Available from: http://www.jpionline.org/index.php/ijpi/article/view/110

134. Hsu SH, Wen CJ, Al-Suwayeh SA, Chang HW, Yen TC, Fang JY. Physicochemical characterization and *in vivo* bioluminescence imaging of nanostructured lipid carriers for targeting the brain: Apomorphine as a model drug. Nanotechnology. 2010;21(40). Available from: https://iopscience.iop.org/article/10.1088/0957-4484/21/40/405101

135. Baker GB, Coutts RT, McKenna KF, Sherry-McKenna RL. Insights into the mechanisms of action of the MAO inhibitors phenelzine and tranylcypromine: a review. J Psychiatry Neurosci [Internet]. 1992 Nov;17(5):206–14. Available from: http://www.ncbi.nlm.nih.gov/pubmed/1362653

136. Atkinson RM, Ditman KS. Tranylcypromine: A review. Clin Pharmacol Ther [Internet]. 1965 Sep;6(5):631–55. Available from: http://doi.wiley.com/10.1002/cpt196565631

137. Himmelhoch JM, Fuchs CZ, Symons BJ. A Double-Blind Study of Tranylcypromine Treatment of Major Anergic Depression. J Nerv Ment Dis [Internet]. 1982 Oct;170(10):628–34. Available from: http://journals.lww.com/00005053-198210000-00007

138. Frieling H, Bleich S. Tranylcypromine. Eur Arch Psychiatry Clin Neurosci [Internet]. 2006 Aug;256(5):268–73. Available from: http://link.springer.com/10.1007/s00406-006-0660-8

139. Ulrich S, Ricken R, Adli M. Tranylcypromine in mind (Part I): Review of pharmacology. Eur Neuropsychopharmacol [Internet]. 2017 Aug;27(8):697–713. Available from: http://dx.doi.org/10.1016/j.euroneuro.2017.05.007

140. Duan Y-C, Ma Y-C, Qin W-P, Ding L-N, Zheng Y-C, Zhu Y-L, et al. Design and synthesis of tranylcypromine derivatives as novel LSD1/HDACs dual inhibitors for cancer treatment. Eur J Med Chem [Internet]. 2017 Nov;140:392–402. Available from: https://doi.org/10.1016/j.ejmech.2017.09.038

141. Lim S, Janzer A, Becker A, Zimmer A, Schüle R, Buettner R, et al. Lysine-specific demethylase 1 (LSD1) is highly expressed in ER-negative breast cancers and a biomarker predicting aggressive biology. Carcinogenesis [Internet]. 2010 Mar;31(3):512–20. Available from: https://academic.oup.com/carcin/article-lookup/doi/10.1093/carcin/bgp324

142. Schulte JH, Lim S, Schramm A, Friedrichs N, Koster J, Versteeg R, et al. Lysine-Specific Demethylase 1 Is Strongly Expressed in Poorly Differentiated Neuroblastoma: Implications for Therapy. Cancer Res [Internet]. 2009 Mar 1;69(5):2065–71. Available from: http://cancerres.aacrjournals.org/lookup/doi/10.1158/0008-5472.CAN-08-1735

143. Schmidt DMZ, McCafferty DG. trans -2-Phenylcyclopropylamine Is a Mechanism-Based Inactivator of the Histone Demethylase LSD1. Biochemistry [Internet]. 2007 Apr 1;46(14):4408–16. Available from: https://pubs.acs.org/doi/10.1021/bi0618621

144. Lee HT, Choi MR, Doh MS, Jung KH, Chai YG. Effects of the monoamine oxidase inhibitors pargyline and tranylcypromine on cellular proliferation in human prostate cancer cells. Oncol Rep [Internet]. 2013 Oct;30(4):1587–92. Available from: https://www.spandidos-publications.com/10.3892/or.2013.2635

145. Behrendt R, White P, Offer J. Advances in Fmoc solid-phase peptide synthesis. J Pept Sci. 2016;22(1):4–27. Available from: https://onlinelibrary.wiley.com/doi/10.1002/psc.2836

146. BACHEM. Solid Phase Solid Phase Peptide Synthesis. 2014;1–5

Chapter 2
Development of Nanoparticles

2.1. Introduction

The possibility of controlling drug delivery promoted the development of the “PEGlylaton concept” by Frank Davis who demonstrated that molecules with poly(ethylene glycol) (PEG) presented reduced immunogenicity (1) and could increase CPPs circularization time. Later, in 1965, Feynman introduced the nanotechnology concept with the discovery of the potentially therapeutic capabilities of liposomes in drug delivery (2). In 1970, Langer explored the abilities of non-degradable polymer matrices (polynyinilacetate) to deliver and release proteins (3). Through the years, several advances have been made in the field of nanostructures delivery systems. The definition of a NP is: “Nanoparticles may be defined as being submicronic (< 1uM) colloidal systems generally but not necessarily made of polymers’’ (4). Nanoparticles can be divided into three groups: organic (lipids, proteins or polymers); hybrid (nanofoams); and inorganic (metals or salts); and present a variety of structural forms such as polymeric nanoconstructs, nanomembranes, nanotubes, nanofibers and nanosized silicon drips (Figure 2.1) (5). Nanoparticles are able to mimic or alter biological processes and have been widely studied as potential delivery vectors to treat cancer, cardiovascular diseases, CNS disorders, infection diseases, imaging probes and more (2). Recent advances in nanotechnology demonstrated that NPs can facilitate effective drug delivery, improve bioavailability, decrease pharmacokinetic side-effects, decrease drug dosage, and increase target delivery to the brain against a wide range of diseases (2). NPs are versatile, nanosized colloidal systems and can be biodegradable or non-biodegradable depending on the nature of the polymer or material used. Nanotechnology-based alternatives were developed to address the current limitations of drugs. Depending on the type of material chosen, there are different ways to produce them and their final desired function or activity. For instance, the use of inorganic materials to produce nanosystems—metals or quantum dots, in particular—is usually applied to develop delivery imaging agents (6). On the other hand, the use of organic materials is linked to a higher biocompatibility and a low material toxicity (7). So, when developing NPs, it is critical to understand and determine their biological fate, toxicity, drug release capability, and stability. For example, NPs with a particle size of less than 5 nm are rapidly cleared by the renal system, NPs bigger than 200 nm accumulate in the spleen due to inter endothelial cell slits, and NPs between 2–5 μm in size tend to accumulate in the capillaries (8). For instance,

scientists used photon-correlation spectroscopy and dynamic light scattering to determine NP size, which is crucial to understanding the NP's biological fate, toxicity, drug release and stability (5). Another crucial analysis required is the surface properties of NP, such as hydrophobicity that influence their *in vivo* fate and ZP. The ZP (surface charge) reflects the electric potential of the NP, which is influenced by the composition and surrounding medium. ZP above ±30 mV shows NP stability in suspensions, reduced aggregation and can be used to determine where active material is encapsulated (9). An increasing number of studies have demonstrated that nanoparticles can enhance drug delivery through both conventional and unconventional administration routes, which is crucial to explore alternatives in progressively debilitating diseases. Among the most studied nanoparticulate systems, NLCs are attracting great scientific interest. In contrast to most polymeric nanoparticle systems, NLCs present a lower cytotoxic risk since their preparation avoids the use of organic solvents, still some sensitivity or irritation can arise from the amount of surfactant added (10). Moreover, when compared to the common solid lipid NP, NLCs are characterized by a less ordered structure which reflects on higher drug loading capacity and retention during storage. Another great advantage of this delivery system is the ability to functionalize through conjugation, grafting or coating with polymers and specific ligands (aptamer, peptides, antibodies and others) (11). Thus, the development of upgrade NPs leads to higher stability, improves targeting, increases circulation time and reduces undesired body distribution (11). Several studies have demonstrated the major advantages of using lipid-based nanoparticles for efficient target and delivery of different compounds against brain diseases (12,13). NLCs can be prepared with a variety of lipids and surfactants to achieve the optimal formulation. NLC have been use as a great alternative for SLN due to the use of liquid lipids in the formulation which enables the incorporation of higher drug loads and enhance encapsulation efficiency of the overall system (11). Another great advantage in that these types of nanoparticles systems is that they presented decreased toxicity risk due to organic solvent free preparation upon formulation. In addition, many research groups had demonstrated the potential use of these lipid based nanoparticles against several brain diseases (13–17). Nevertheless, several limitations have delayed NP usage in current therapeutics, mostly because of poor drug loading, rapid release, and lack of selectivity (18). The current limitations of NP have boosted the design of new alternatives conjugates. The field of NP-pharmacokinetics is the main area for obtaining maximal potential with efficient absorption and the right biodistribution (2). For that, NP optimization with surface modifications is required to design a more effective and successful therapeutic. Different possible modifications have been investigated for passive or active drug targeting (this subject is excellently reviewed for lipid NP by Gaspar and her team (2017) (11)). For example, coating NP with hydrophilic molecules, such as PEG,

polyoxamer, poloxamine and T80, is associated with prolonged circulation time and reduced phagocytosis. (11).

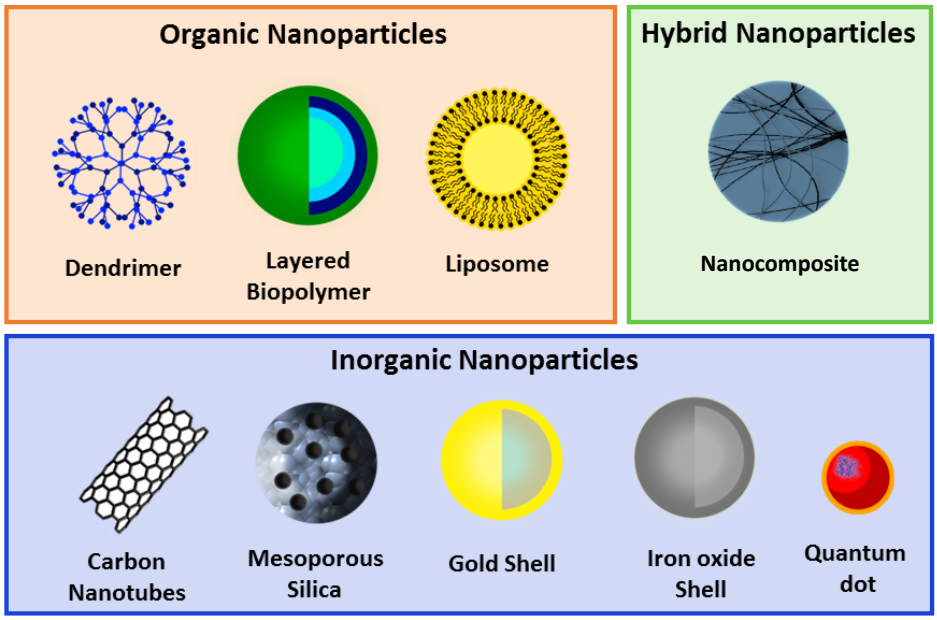


Figure 2.1 - Schematic representation of different types of nanoparticles (NPs) divided into organic, hybrid and inorganic categories.

2.2. Overview

Chapter 2 explores the development of NLC formulation used in this thesis and is divided into 3 Phases of optimization. The Phase 1 explore the solid lipids that could be used in the NP formulation. Phase 2 determines the introduction of liquid lipid to the formulation to ensure drug encapsulation into the NP core and preliminary toxicity assay. Finally, in Phase 3 a new purification method is implemented, and toxicity studies are conducted to evaluate the optimal formulation required.

2.3. Materials and Methods

2.3.1. Materials

TAC (9-amino-1,2,3,4-tetrahydroacridine hydrochloride hydrate), TCP ((±)-trans-2-Phenylcyclopropylamine) and RAS (N-Propargyl-1(R)-aminoindan methanesulfonate) were acquired from Sigma Aldrich (St Louis, MO, USA). Glyceryl dibehenate (Compritol® 888 ATO), Precirol® ATO 5) and diethylene glycol monoethyl ether (Transcutol® HP) was a kind

gift from Gattefossé (France). T80 was obtained from J. Vaz Pereira S.A. (Benavente, Portugal). The 3-(4,5-dimethyl-2-thiazolyl)-2,5-dipheny-2H-tetrazolium bromide (MTT), sulfarhodamine B sodium (SRB) and phosphate buffer solution (PBS—pH 7.4) were purchased from Sigma-Aldrich (St Louis, MO, USA). Caprylic/capric triglycerides (Miglyol® 812) were a gift from Sasol Olefins & Surfactants GmbH (Hamburg, Germany). Dimethyl sulfoxide (DMSO) was obtained from Merck. For the viability studies, neuroblastoma cell line (SH-SY5Y, ATCC® CRL-2266TM) and colorectal adenocarcinoma cell line (Caco-2, ATCC® HTB-37™) was used. Cell culture medium, papain and penicillin-streptomycin solution were acquired from Sigma-Aldrich and the rest of the cell culture supplies were acquired from Millipore Sigma. ACN of HPLC grade was obtained from Fisher Scientific (Fair Lawn, NJ, USA), and TFA obtain from Sigma-Aldrich (St Louis, MO, USA). Primary neuronal cell culture Poly-D-lysine, Hibernate A, Neurobasal and B27 supplement were acquire from Gibco Thermofisher. Optiprep was purchased from Stemcell, Germany.

2.3.2. SLN/NLC preparation optimization

2.3.2.1. SLN preparation

SLNs were prepared by hot high shear homogenization (HSH) method previously described (19). Briefly, the solid lipid consisting of 300 mg of Compritol® 888 ATO and Precirol® ATO 5 was melted at a temperature 10 °C above its melting point. A hot aqueous phase consisting of 3% T80 in 10 mL ultra-purified water was added to the lipid phase under high-shear homogenization at 12,3000 rpm for 10 min (Silverson SL2, UK), in a water bath to maintain the temperature. The SLN dispersion was finally allowed to cool in an ice bath with gentle stirring for 5 min. Each formulation was carried out in duplicates (n = 3). The final dispersion was sealed and stored at 4 °C until further use.

2.3.2.2. Lipid solubility

The solubility of TAC, TCP and RAS was first determined in Compritol® 888 ATO, Transcutol® HP and Mglyol. Briefly, the solid lipid Compritol® 888 ATO was melted at a temperature 10 °C above its melting point (80 °C), in a controlled temperature water bath, while the liquid lipids Miglyol® and Transcutol® HP were ready to use. Increasing amounts of TAC were successively added, with stirring, until saturation of the lipid was achieved. This occurred when excess of solid TAC, TCP and RAS persisted for more than 8 h. Each determination was carried out in triplicate (n = 3).

2.3.2.3. NLC preparation

TAC-loaded, RAS-Loaded and TCP-loaded NLCs were prepared using a modification of a hot HSH method previously described (19). Briefly, the solid lipid consisting of 300 mg of Compritol® 888 ATO was melted at a temperature 10 °C above its melting point. TAC, RAS, TCP was dissolved in the liquid lipid Transcutol® HP (at theoretical concentrations of 20%, 25% and 30%, *w*/*w*), which was added to the molten solid lipid. A hot aqueous phase consisting of 3% T80 in 10 mL ultra-purified water was added to the lipid phase under high-shear homogenization at 12,3000 rpm for 10 min (Silverson SL2, UK), in a water bath to maintain the temperature. The NLC dispersion was finally allowed to cool in an ice bath with gentle stirring for 5 min. Each formulation was carried out in duplicates (n = 2). The final dispersion was sealed and stored at 4 °C until further use.

2.3.2.4. NLC purification

Before NLC characterization and toxicity assays were conducted, all NLC formulations were purified through 2 methods. At first in phase 1 and phase 2, to separate free drug and surfactants in solution unassociated to the NLC, was used centrifugation method with Amicon ultra centrifugal filter units, ultra-15, molecular cutoff of 100 Kda (Sigma-Aldrich, Algés, Portugal). In the phase 3, protocol was change and NLC were purified on Sephadex G-25 medium pre-filled PD-10 columns (GE Healthcare life Science, UK) (Protocol represented in Figure 2.2).

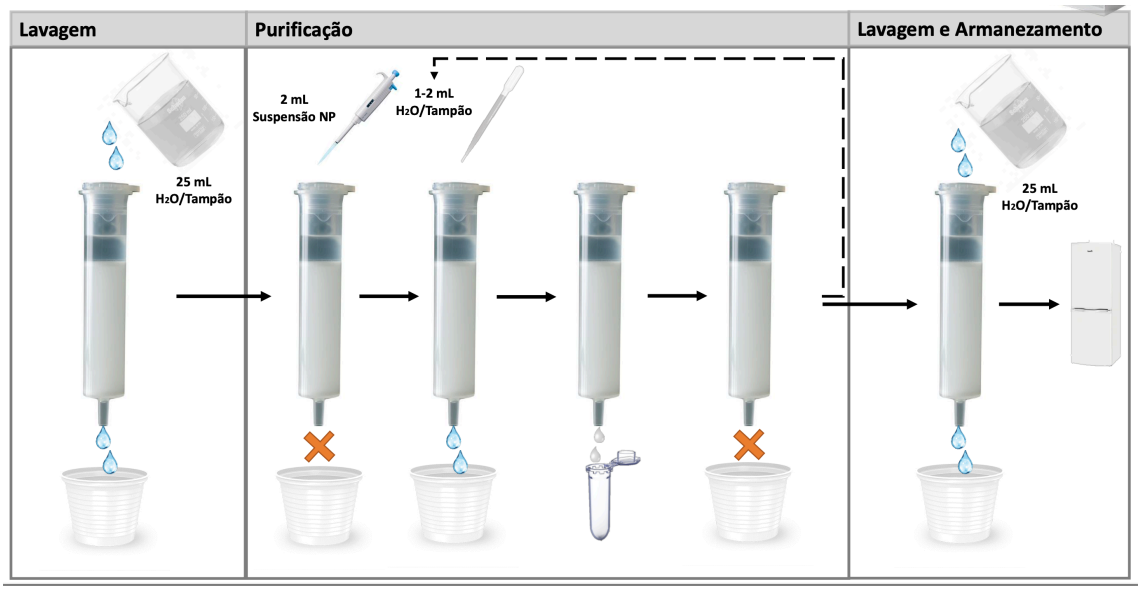


Figure 2.2 - Purification method implemented in Phase 3 of this thesis using Sephadex columns.

2.3.3. Chromatographic Instruments and Conditions

The ultra-high-performance liquid chromatograph (UHPLC) measurements was carried out using a VWR Hitachi Organizer (LaChrom Ultra, Tokyo, Japan), VWR Hitachi UV Detector L-24000U, VWR Hitachi Autosampler L-2200U, VWR Hitachi Pump L-2160U and VWR Hitachi Pump L-2160U. The mobile phase consisted of an aqueous phase (A) containing ultra-purified water and 0.05% (*v*/*v*) TFA and an organic phase (B), which was acetonitrile. Flow was set at 0.7 mL/min. A gradient method was used in which the mobile phase started as 80% A and 20% B and changed in a linear manner to 0% A and 100% B by 10 min. The analytical wavelengths used for the measurements of analyte peak areas applied for quantitative analysis were, 220 nm for UHPLC technique, 220 nm (RAS, TCP) and 243 nm (TAC).

2.3.4. Characterization of NLC

2.3.4.1. Particle Size and Surface Change

Particle size distribution was analyzed by dynamic light scattering (DLS) using Zetasizer Nano S (Malvern instruments, UK). For this, samples were placed in a specific cuvette and measurements were made at 25 ◦C. Results were expressed as average particle size and PI.

ZP was calculated through nanoparticle electrophoretic mobility (previously diluted with filtered purified water and placed in an appropriate), using a Zetasizer Nano Z (Malvern instruments, UK). For all measurements, at least three replicate samples were determined.

2.3.4.2. Encapsulation Efficiency

The EE and drug loading (DL) in the NLC formulations were determined using an indirect method. The free drug, i.e., unassociated to the NLC, was separated from the particles using centrifugation (Amicon ultra centrifugal filter units; ultra-15, MWCO 100 Kda, Sigma-Aldrich, Algés, Portugal). Briefly, 1 mL of the sample was kept in the upper chamber compartment of the ultra-centrifuge tube and centrifugated at 12,000 rpm for 15 min. The collected sample in the lower chamber was quantified using HPLC. Entrapment efficiency and drug loading were determined using the following equations:

$$Encapsulation\ efficiency\ (\%\ w/w) = \frac{(w1 - w2)}{w1} \times\ 100$$

$$Drug\ loading\ (\%\ w/w) = \frac{w1 - w2}{w3} \times 100$$

where w1 corresponds to amount of drug added in the NLCs, w2 is the amount of free drug and w3 is the amount of lipid.

2.3.5. *In Vitro* Drug Release

2.3.5.1. Drug Release from pH 7.4

Before release studies were performed, NLCs were desalted on Sephadex G-25 medium pre-filled PD-10 columns (GE Healthcare life Science, UK). The release of TAC, RAS and TCP was determined by incubating the nanoparticles in PBS (pH 7.4) with horizontal shaking at 37 ◦C. At suitable time intervals, each individual sample was centrifuged at 30,000× *g* for 30 min at 4 ◦C. The amount of TAC, RAS and TCP release was evaluated in the supernatants by HPLC, at 243 nm, 220nm and 220 nm, respectively.

2.3.5.2. TAC Release in Human Plasma

The purified NLCs were incubated in a solution of 80% human plasma with horizontal shaking for 48 h at 37 °C. At suitable time intervals, each individual sample was centrifuged 4 times at 13,000× *g* for 10 min at 10 °C. The amount of TAC and TAC-MAP release was evaluated in the supernatants by HPLC at 243 nm and 220 nm, respectively.

2.3.6. Stablish a primary neuronal cell culture

2.3.6.1. Poly-D-lysine coating of culture dishes

Plastic culture dishes were coated with Poly-D-Lysine prior to use. Briefly, each 35-mm plate was added 2 mL (50 µg/mL of poly-D-lysine) and was incubated for 1 hour at 37 °C. After incubation solution was aspirated, and the plates were washes three time with sterilized water and let them dry in the hood for 1 h cover with parafilm prior to use.

2.3.6.2. Isolation of neurons

The cells were isolated from mice brain cortex from 3-month wistar mice according to modified method described in (20,21) protocol is explained in detail in the supplementary information see section 2 (Figure S2.1). Briefly, after decapitation mice brain was removed and brain cortex was isolated with the use of sharp scissors the tissue was cutted into 0.5 mm slices. Then the pieces were incubated in shaking bath at 30 °C for 8 min in plating media (Hibernate 60 mL, B27 1,2 mL, 0,176 mL (Gln 0,5 mM)). After the incubation the tissue was transfer to a tube containing 1 mL of papain and incubated for further 30 min. Then the tissue was added to 2mL fresh plating media and gentle homogenized with fire-polish Pasteur pipette. The supernatant was collected and added to the top of optiprep density gradient and then centrifuge at 1900 rpm for 15 min at room temperature. Different phases appear (Figure 2.1), phase 3 was collected and diluted in 10 mL of plating media. Centrifugation was applied to form a cell pellet and the cells were plated in plastic dishes previously coated with poly-D-lysine. After incubation for around 1 h the medium was aspirated and replace with neurobasal supplemented with B27 the cells were let to grow and visualized in microscope (results obtain are mentioned in supplementary information – Figure S2.2, 2.3 and 2.4).

2.3.7. *In vitro* cell viability studies

The cytotoxicity of all NLC formulations against SH-SY5Y was assessed by MTT assay, SRB assay, microscope visualization and cell count.

2.3.7.1. MTT assay

For viability determination by the MTT assay, the cells were maintained in culture DMEM supplemented with 10% heat-inactivated fetal bovine serum (FBS) and 1% penicillin and streptomycin at 37 °C with controlled atmosphere of 5% CO_2. The day before the experiment, the cells were seeded in a sterile flat bottom 96-well plate at the density of 18,000 cells per well and incubated for 24 h. The medium was then replaced with increasing concentrations of free TAC, free TAC-MAP and drug loaded NLC. Cells were incubated for 24 h, in negative control cells incubated with culture media and sterilized water (5:1) and in positive control, DMSO 10% was added to promote the cell lyses.

After incubation, all media was removed and replaced with 100 μL of MTT solution (0.5 mg/mL). The cells were further incubated for 3 h. After incubation, 100 μL DMSO was added to dissolve the formazan crystals and the absorbance was measured at 570 nm in a microplate reader (Synergy HT, Biotech Instruments inc., USA). All experiments were performed in quadruplicates and the relative cell viability (%) was compared to control cells and was calculated using the following equation:

$$Cell\ viability\ (\%\ of\ sample) = \frac{Abs\ sample}{Abs\ control} \times 100$$

2.3.7.2. SRB Assay

Cytotoxicity of all formulations was also determined by SRB assay. Using the same conditions and methods described above for MTT assay, after treatment with all NLC formulations, the cells were fixed with 100 μL of ice cold 10% trichloroacetic acid (TCA) per well for 1 h at 4 °C. Then TCA was removed and allowed to dry before adding 100 μL of 0.4% SRB solution. After 1 h, the plates were then washed with running tap water and air dried. The incorporation dye was solubilized by the addition of 200 μL of 10 mM tris buffer per well. The absorbance was measured at 510 nm in a microplate reader. All experiments were performed in quadruplicates using the same equation mentioned above.

2.3.7.3. Cell Morphology Visualization

After the treatments, cell morphology, growth and cell count were assessed by contrast phase microscope Lionheart FX (Biotech, USA) with use of Gen5 software (Biotech, USA).

2.3.8. Statistical Analysis

Statistical analysis of the experimental data was performed using a one-way analysis of variance (one-way ANOVA) and differences between groups were tested by a one-way ANOVA with GraphPad Prism version 8.0 (GraphPad Software, San Diego, CA). Data were expressed as mean SD or 95% confidence interval. A $p<0.05$ value was considered significant. All data are shown as mean SD.

2.4. Results

PHASE 1

2.4.1. SLN/NLC optimization method

The phase 1 of this work consisted of the formulation of SLN testing two different solid lipid compositions (Compritol® 888 ATO and Precirol® ATO 5) with 3% of T80 as surfactant (SLN - C and SLN - P), then we characterized the SLN by DLS, introduced a purification step before testing in Caco-2 cell line (Figure 2.3).

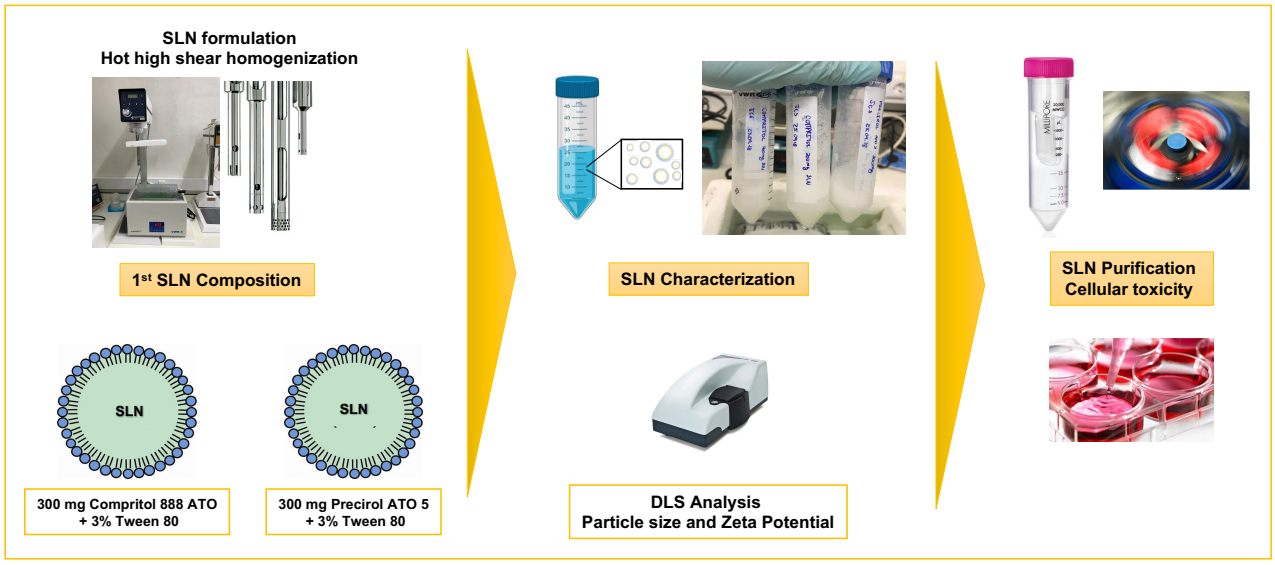


Figure 2.3 - Schematic representation of Phase 1 of optimization method to prepare nanoparticles SLN.

2.4.1.1. SLN characterization

The SLN presented a particle size distribution for SLN - C and SLN - P of 135.2 nm and 169.5 nm, respectively (Table 2.1 and Figure 2.4). PI of both formulation was below 0.3 and ZP analysis demonstrated negative values of -19 mV and -23 mV for SLN – C and SLN – P respectively (Table 2.1). Both PI and ZP values indicated that formulations are stable in solution, still SLN – C demonstrated a reduced particle size.

Table 2.1 - Physicochemical properties of: empty nanostructured lipid carrier (SLN) (mean SD, n = 3).

SLN	SLN Composition	PS (nm)	PI	ZP (mV)
SLN - C	Lipids: 300 mg C Surfactant: 3 % T80	135.2 ± 0.55	0.206 ± 0.020	-19 ± 0.32
SLN - P	Lipids: 300 mg P Surfactant: 3 % T80	169.5 ± 3.40	0.222 ± 0.009	-23 ± 0.55

Notes: C – Compritol® 888 ATO; P – Precirol® ATO 5; T80 – polisorbato 80; PS – Particle size; PI – Polydispersity Index; ZP – Zeta Potential;

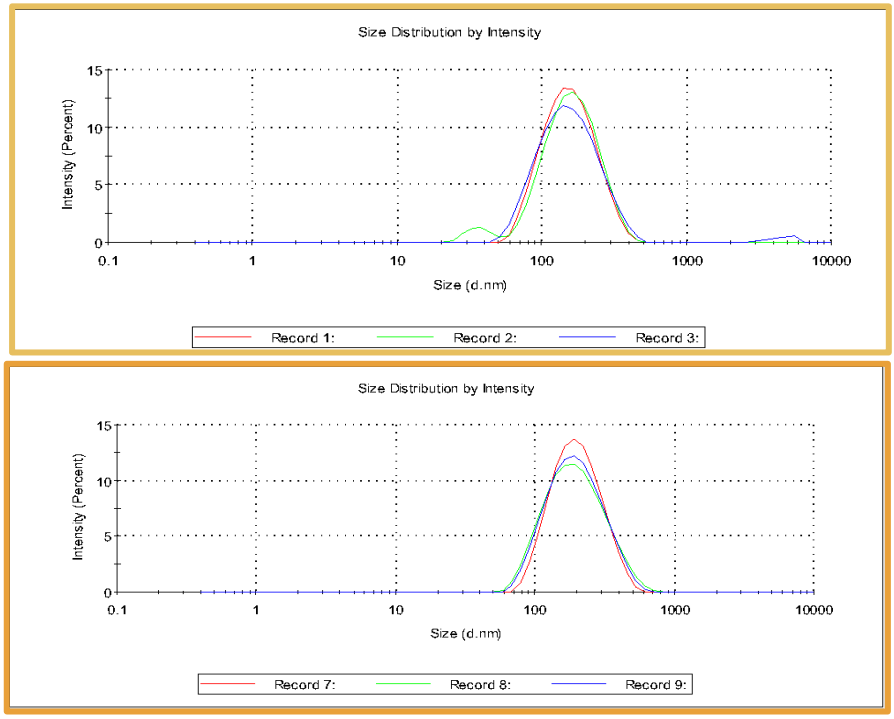


Figure 2.4 - DLS analysis particle size distribution of SLN – C (Yellow) and SLN – P (Orange).

2.4.1.2. SLN toxicity against Caco-2 cell line

In this work, SLN formulations were tested for a period of 2 and 4 h in a concentration of 1%. Results show that in SLN – C presented a significant decrease on cell viability after 2

and 4 h of incubation, The SLN – P only present a significant cell viability reduction after 4 h incubation time against Caco-2 cell line (Figure 2.5). The initial toxicity presented could be related to the T80 present in both SLN composition.

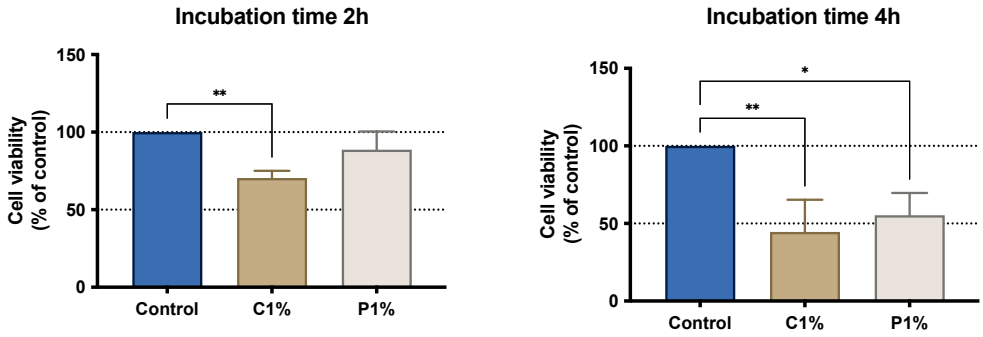


Figure 2.5 - Relative cell viability of Caco-2 cell line measured by the MTT reduction after 2 and 4 h incubation. Treatment with free SLN – C and SLN - P at 1 % concentration. Results are expressed as mean SD (n = 3). Statistical analysis between the control group and other groups was performed using one-way ANOVA with Dunnet's post hoc test (* $p < 0.05$, ** $p < 0.01$).

PHASE 2

2.4.2. NLC optimization method

In the phase 2 of this SLN optimization we had to change the initial SLN formulation due to poor drug solubility on the solid lipid used. For this we decided change form SLN to NLC formulation adding a liquid lipid to the formulation. For this we first conduct a solubility test to ensure that the drug's use in this work solubilized in liquid lipid and could be incorporated in the NLC core. After successful identified Transcutol® HP as the liquid lipid to be use, new NLC formulations were prepared, and full characterization and preliminary toxicity tests were conducted (Figure 2.6).

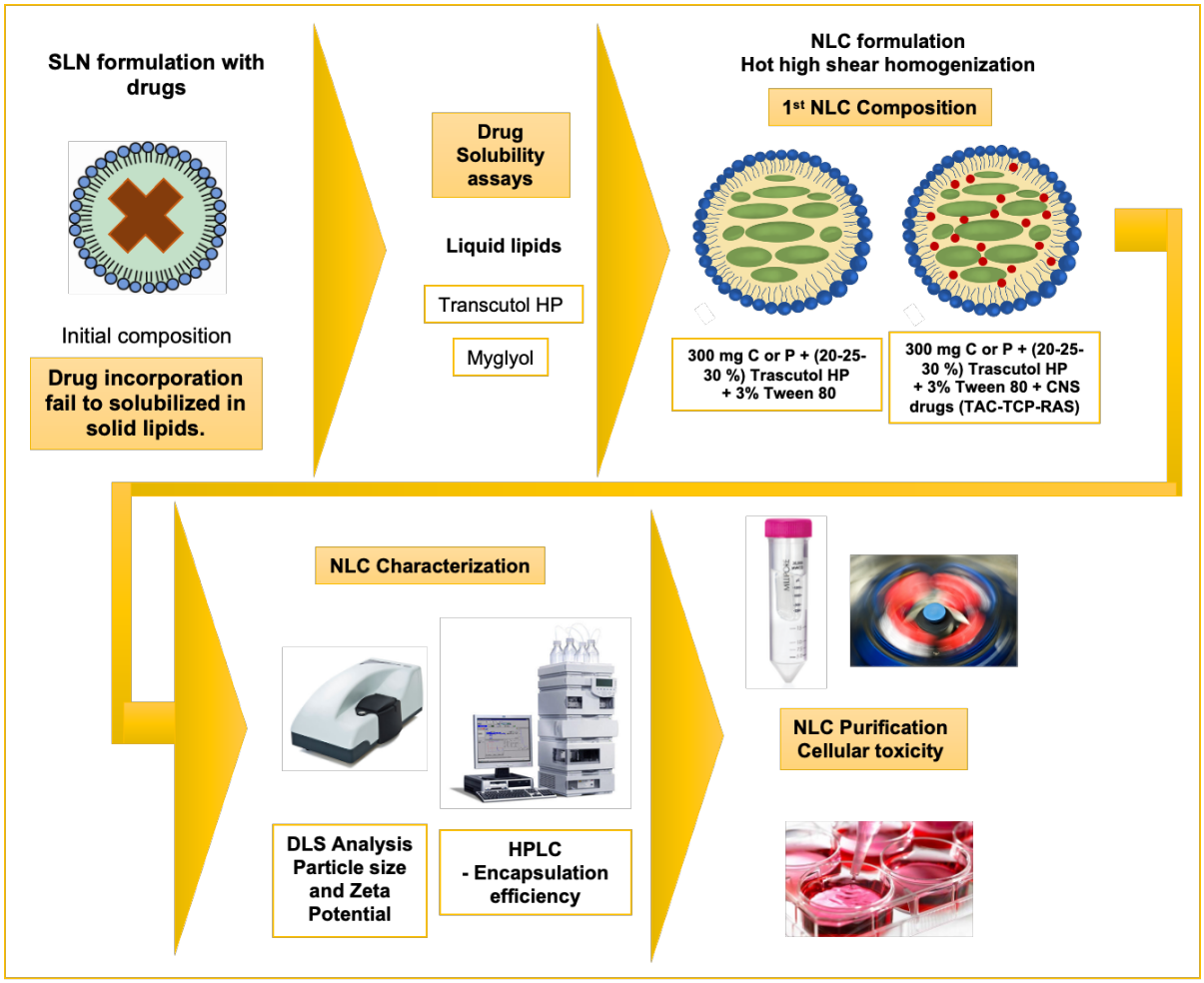


Figure 2.6 - Schematic representation of Phase 2 of optimization method to prepared NLC.

2.4.3. Lipid solubility

Preliminary solubility studies demonstrated that TAC, RAS and TCP had a maximum solubility level in liquid lipid Transcutol® HP when compared to the other lipid tested Myglyol and Compritol® 888 ATO. As showed in Table 2.2, TAC and TCP were able to be dissolved to a maximum of 25 mg/mL and RAS dissolved to a maximum 5 mg/mL.

Table 2.2 - Maximum solubilization concentration achieve for Transcutol® HP of TAC, TCP and RAS.

Drug	Weight measured (mg)	Transcutol® HP (mL)	Solvent – MeOH	Solubility concentration (mM)	Solubility Concentration(mg/mL)
TAC	12.5	0.5	n.d.	106.50	25
TCP	1	0.04	n.d.	147.36	25
RAS	5	1	n.d.	18.70	5

2.4.4. Toxicity of surfactant in Caco-2 cell line

In order to understand a possible toxicity associated with free surfactant present in solution of NLC formulation that could result on higher toxicity. We conducted a surfactant toxicity analysis of Transcutol® HP and T80 at different concentrations, combinations, and incubations times. The results demonstrated the significant toxicity levels promote on Caco-2 cell line even at 2 h incubation and total reduction on cell viability at 24 h incubation time, with exception of Transcutol® HP at 1 % (Figure 2.7). These results indicate that final NLC formulations preparation must be applied a purifying method to ensure almost none amount of residual surfactant in the solution remains in solution.

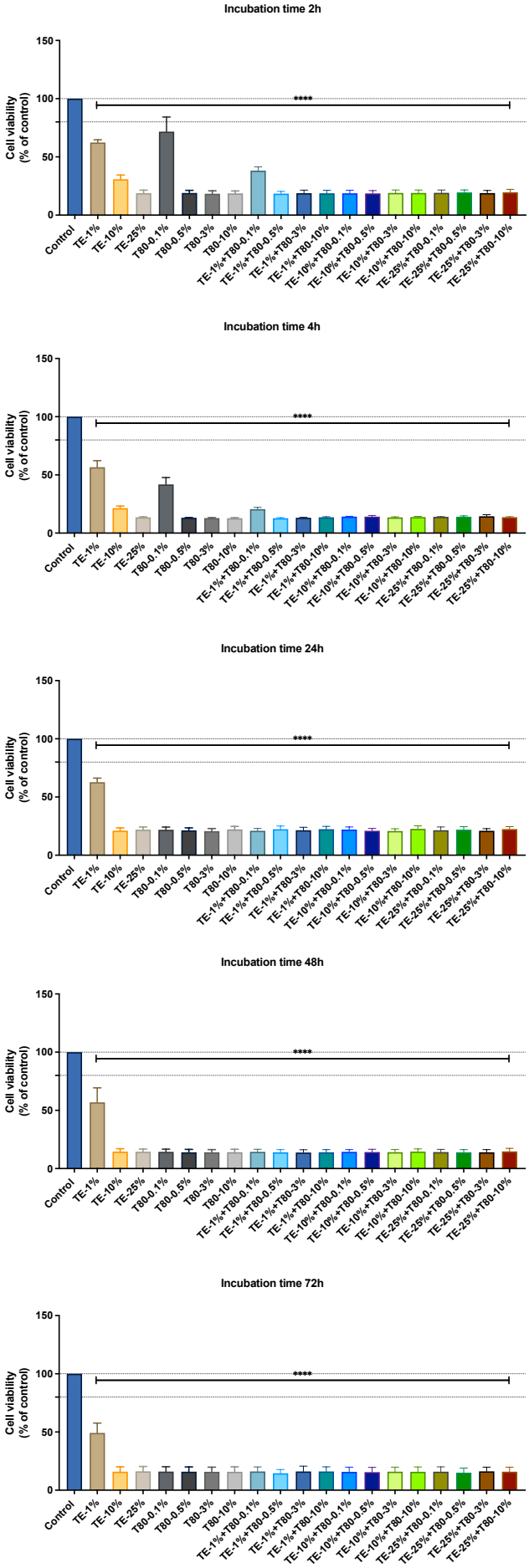

Incubation time 2h
Incubation time 4h
Incubation time 24h
Incubation time 48h
Incubation time 72h
Cell viability (% of control)
150
100
50
0
****
Control
TE-1%
TE-10%
TE-25%
T80-0.1%
T80-0.5%
T80-3%
T80-10%
TE-1%+T80-0.1%
TE-1%+T80-0.5%
TE-1%+T80-3%
TE-1%+T80-10%
TE-10%+T80-0.1%
TE-10%+T80-0.5%
TE-10%+T80-3%
TE-10%+T80-10%
TE-25%+T80-0.1%
TE-25%+T80-0.5%
TE-25%+T80-3%
TE-25%+T80-10%

Figure 2.7 - Preliminary surfactant toxicity against Caco-2 cell line. Treatment with Transcutol® HP (TE) and T80 at different concentrations and at different incubations time. Statistical analysis between the control group and other groups was performed using one-way ANOVA with Dunnet's post hoc test (**** $p < 0.0001$).

2.4.5. NLC preparation, purification, and characterization

2.4.5.1. Drug Calibration Curve

Calibration curves in the sample matrix were performed on 3 drugs in study. The equations of calibration curves and correlation coefficiency are express in Figure 2.8, 2.9 and 2.10. For the TAC quantification we obtain an equation: $y = 245406x + 699309$ with R^2 of 0.9982. For the RAS quantification we obtain an equation: $y = 26691x - 705990$ $R^2 = 0.9992$. For the TCP quantification we obtain an equation: $y = 8150.1x + 815584$ $R^2 = 0.999$.

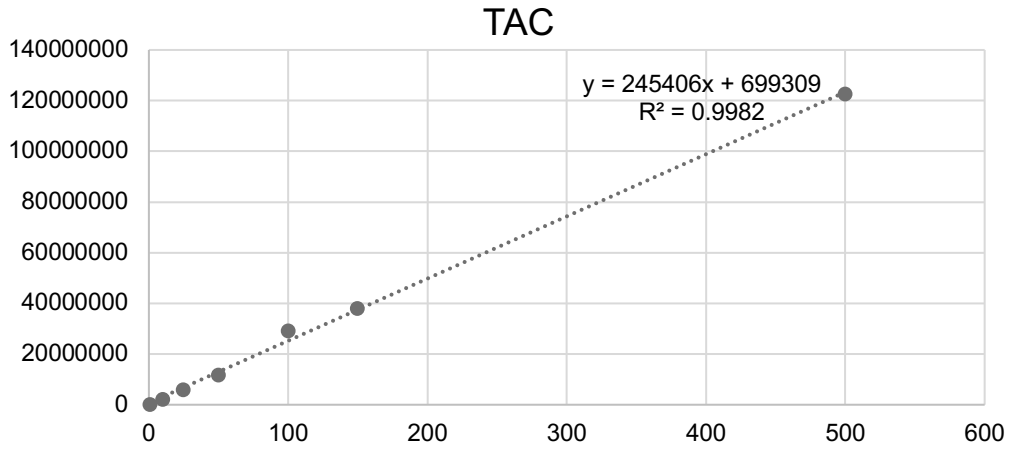


Figure 2.8 - Calibration curve for TAC, obtained by plotting the absorbance of the drug in the function of its concentration in water solvent.

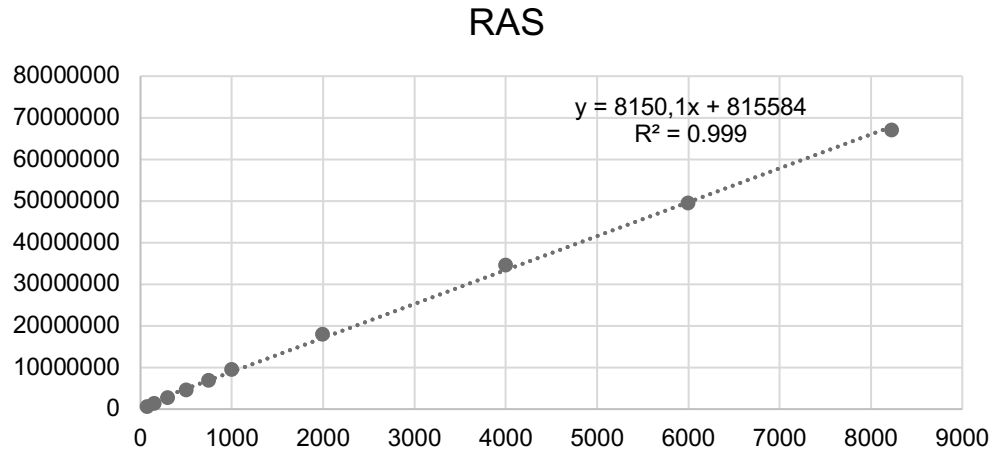


Figure 2.9 - Calibration curve for RAS, obtained by plotting the absorbance of the drug in the function of its concentration in water solvent.

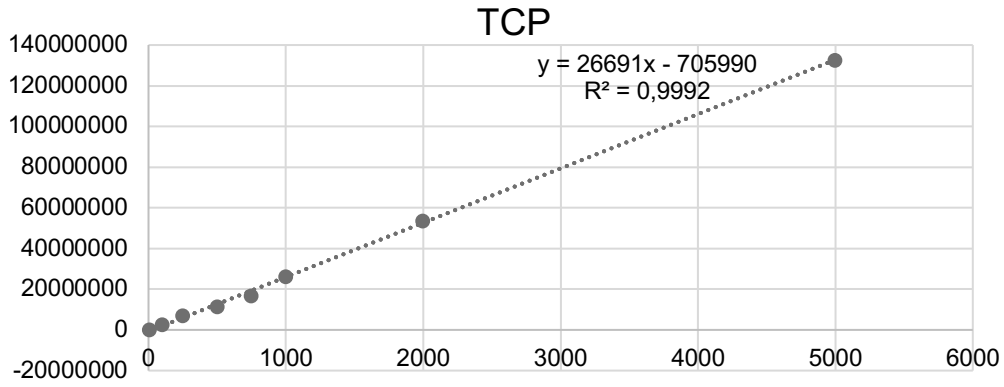


Figure 2.10 - Calibration curve for TCP, obtained by plotting the absorbance of the drug in the function of its concentration in water solvent.

2.4.5.2. Encapsulation efficiency

The EE determined for NLC-loaded with TAC was 63.9 %, 66.6 % and 58.5% for CT20 formulation, CT25 formulation and CT30 formulation, respectively (Table 2.3). In terms of RAS loading the EE were 39, 22.8 and 77.9 for CT20 formulation, CT25 formulation and CT30 formulation, respectively (Table 2.3). NLC loaded with TCP resulted on EE values of 38.1 % for CT20, 75.9 % for CT25 and 0 % for CT30 (Table 2.3).

Table 2.3 - Physicochemical properties of: Phase 2 empty NLC, TAC-loaded NLC, RAS-loaded NLC and TCP-loaded NLC freshly prepared (mean SD, n = 2).

NLC	NLC composition	PS (nm)	PI	ZP (mV)	EE %
CT20 B	Lipids: 80 % C and 20 % TE Surfactant: 3 % T80	136.8 ± 60.7	0.267 ± 0.059	-12.1 ± 2.8	n.d.
CT25 B	Lipids: 75 % C and 25 % TE Surfactant: 3 % T80	108.2 ± 30.1	0.255 ± 0.004	-12.1 ± 1.8	n.d.
CT30 B	Lipids: 70 % C and 30 % TE Surfactant: 3 % T80	72.0 ± 3.9	0.354 ± 0.044	-13.1 ± 2.2	n.d.
CT20TAC	Lipids: 80 % C and 20 % TE Surfactant: 3 % T80	82.9 ± 8.3	0.375 ± 0.044	-14.9 ± 1.8	63.9
CT25TAC	Lipids: 75 % C and 25 % TE Surfactant: 3 % T80	75.0 ± 8.3	0.385 ± 0.085	-13.2 ± 0.8	66.6
CT30TAC	Lipids: 70 % C and 30 % TE Surfactant: 3 % T80	162.1 ± 60.6	0.294 ± 0.034	-10.3 ± 2.1	58.5
CT20RAS	Lipids: 80 % C and 20 % TE Surfactant: 3 % T80	85.8 ± 2.4	0.269 ± 0.022	-13.9 ± 1.0	39.0
CT25RAS	Lipids: 75 % C and 25 % TE Surfactant: 3 % T80	107.8 ± 12.6	0.319 ± 0.094	-14.9 ± 0.9	22.8
CT30RAS	Lipids: 70 % C and 30 % TE Surfactant: 3 % T80	192.5 ± 13.8	0.393 ± 0.264	-12.4 ± 1.3	77.9
CT20TCP	Lipids: 80 % C and 20 % TE Surfactant: 3 % T80	175.7 ± 81.6	0.321 ± 0.070	-13.1 ± 2.8	38.1
CT25TCP	Lipids: 75 % C and 25 % TE Surfactant: 3 % T80	76.7 ± 4.2	0.360 ± 0.122	-13.3 ± 2.1	75.9
CT30TCP	Lipids: 70 % C and 30 % TE Surfactant: 3 % T80	124.8 ± 60.4	0.373 ± 0.154	-12.4 ± 2.1	0

2.4.6. Preliminary Toxicity assays Caco-2

Preliminary toxicity assays were conducted to evaluate the select the optimized NLC formulation based on the different levels of Transcutol® HP used. The first results demonstrated that after 2 h incubation NLC loaded with different drugs lead to a decrease on cell viability in all formulations tested (Figure 2.11, 2.12 and 2.13). After 4 h incubation cell viability was severe compromise independently of the percentage of the Transcutol® HP used (Figure 2.11, 2.12 and 2.13). However, as can see in the graphics obtain with this preliminary toxicity assay demonstrated a significant toxicity at all formulation of NLC after only 4 hours of incubation independently of the drug or formulation used. This could indicate

that there is a problem with the purification method and new protocol has to be implemented before taking more considerations with these results. As state before if the purification method is not well conducted small amount of surfactant in the solution could be crucial to enhance toxicity of the formulation in the cell culture.

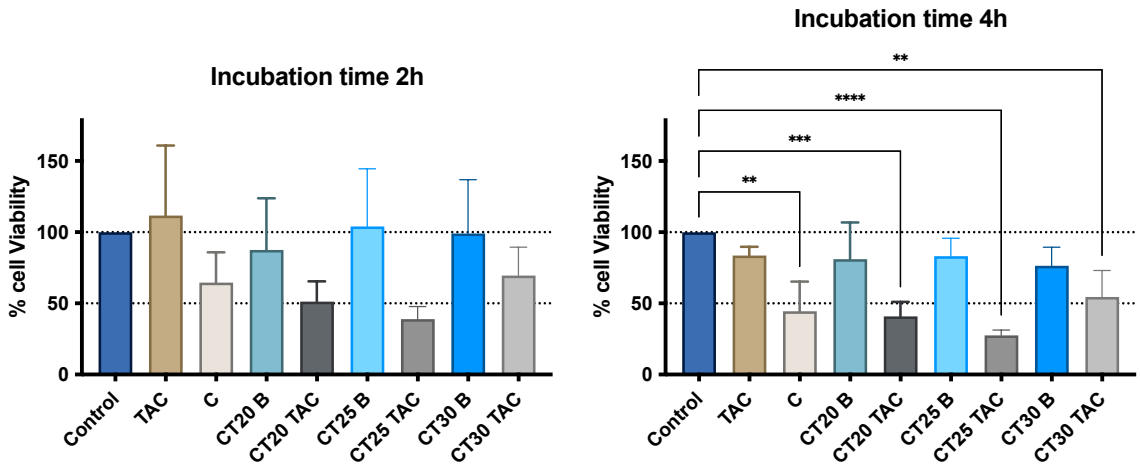


Figure 2.11 - Relative cell viability of Caco-2 cell line measured by the MTT reduction after 24 h incubation. Treatment with free TAC, blank NLC and NLC loaded with TAC (10 μM). Results are expressed as mean SEM (n = 4). Statistical analysis between the control group and other groups was performed using two-way ANOVA with Dunnet's post hoc test (** p <0.01; *** p <0.001; **** p <0.0001).

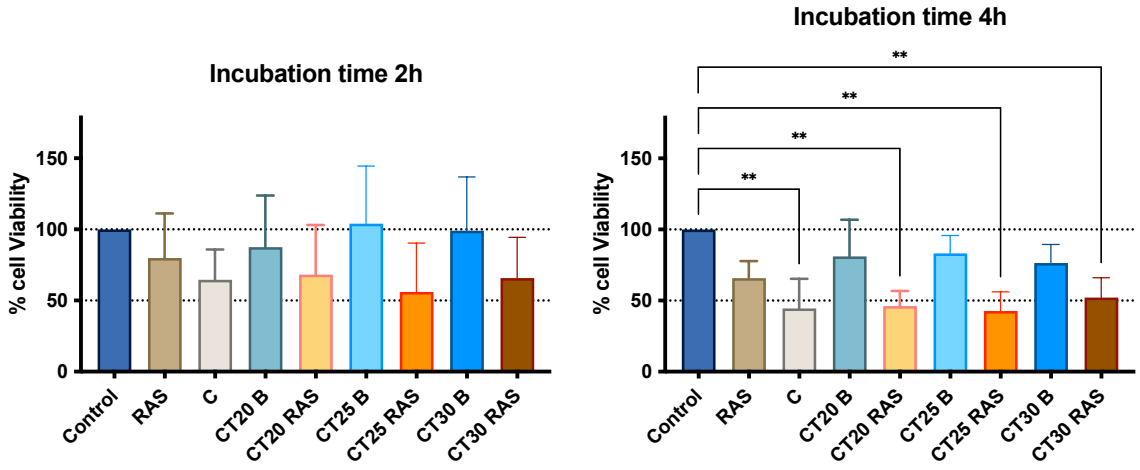


Figure 2.12 - Relative cell viability of Caco-2 cell line measured by the MTT reduction after 24 h incubation. Treatment with free RAS, blank NLC and NLC loaded with RAS (10 μM). Results are expressed as mean SEM (n = 4). Statistical analysis between the control group and other groups was performed using two-way ANOVA with Dunnet's post hoc test (** p <0.01).

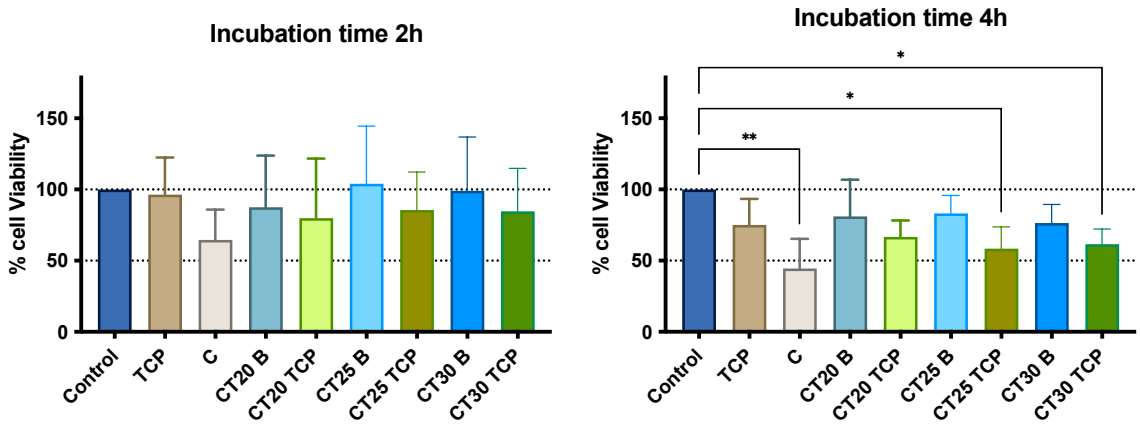


Figure 2.13 - Relative cell viability of Caco-2 cell line measured by the MTT reduction after 24 h incubation. Treatment with free TCP, blank NLC and NLC loaded with TCP (10 μM). Results are expressed as mean SEM (n = 4). Statistical analysis between the control group and other groups was performed using two-way ANOVA with Dunnet's post hoc test (* p <0.05; ** p <0.01).

PHASE 3

2.4.7. NLC optimization method

In the phase 3 of this NLC optimization we had to change the purification method due to significant toxicity observed against Caco-2 cell line with 4 h incubation period. So, in this phase we formulated new NLC with the same characteristics as stated before and conducted a different purification through Sephadex columns. After this we proceed to physical characterization and cellular toxicity assays (Figure 2.14).

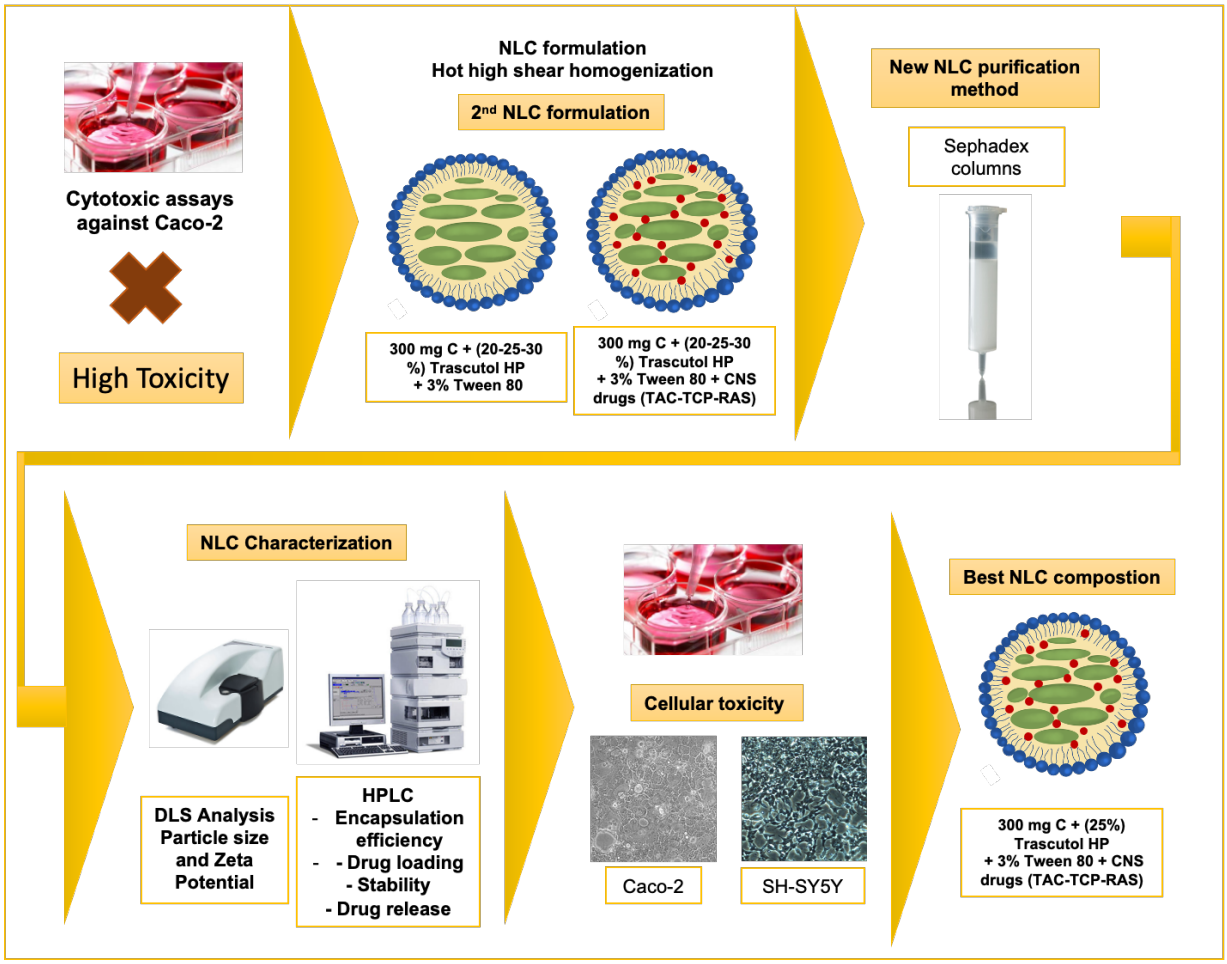


Figure 2.14 - Schematic representation of Phase 3 about optimization method for NLC nanoparticles.

2.4.7.1. NLC characterization

The former EE is also a crucial part in developed a delivery system, since higher levels of encapsulation are recommended and reflect on efficacy. The EE determined for NLC-loaded with TAC was 72.4%, 56.4% and 58.5% for CT20 formulation, CT25 formulation and CT30 formulation, respectively (Table 2.4). In terms of RAS loading the EE were 39, 75.2 and 77.9 for CT20 formulation, CT25 formulation and CT30 formulation, respectively (Table 2.4). NLC loaded with TCP resulted on EE values of 33.5% for CT20, 27 % for CT25 and 0 % for CT30 (Table 2.4). In addition, as you can see in Figure 2.15 NLC encapsulation with CNS didn't result on severe changes on particle size (Table 2.4). Additional cytotoxicity experiments were conducted to further optimize the formulations (see below).

Table 2.4 - Physicochemical properties of: Phase 3 empty nanostructured lipid carrier (NLC), TAC-loaded NLC, RAS-loaded NLC and TCP-loaded NLC freshly prepared (mean SD, n = 2).

NLC	NLC composition	PS (nm)	PI	ZP (mV)	EE %
CT20 B	Lipids: 80 % C and 20 % TE Surfactant: 3 % T80	136.8 ± 60.7	0.267 ± 0.059	-12.1 ± 2.8	n.d.
CT25 B	Lipids: 75 % C and 25 % TE Surfactant: 3 % T80	108.2 ± 30.1	0.255 ± 0.004	-12.1 ± 1.8	n.d.
CT30 B	Lipids: 70 % C and 30 % TE Surfactant: 3 % T80	72.0 ± 3.9	0.354 ± 0.044	-13.1 ± 2.2	n.d.
CT20TAC	Lipids: 80 % C and 20 % TE Surfactant: 3 % T80	82.9 ± 8.3	0.375 ± 0.044	-14.9 ± 1.8	72.4
CT25TAC	Lipids: 75 % C and 25 % TE Surfactant: 3 % T80	75.0 ± 8.3	0.385 ± 0.085	-13.2 ± 0.8	56.4
CT30TAC	Lipids: 70 % C and 30 % TE Surfactant: 3 % T80	162.1 ± 60.6	0.294 ± 0.034	-10.3 ± 2.1	58.5
CT20RAS	Lipids: 80 % C and 20 % TE Surfactant: 3 % T80	85.8 ± 2.4	0.269 ± 0.022	-13.9 ± 1.0	39.0
CT25RAS	Lipids: 75 % C and 25 % TE Surfactant: 3 % T80	107.8 ± 12.6	0.319 ± 0.094	-14.9 ± 0.9	75.2
CT30RAS	Lipids: 70 % C and 30 % TE Surfactant: 3 % T80	192.5 ± 13.8	0.393 ± 0.264	-12.4 ± 1.3	77.9
CT20TCP	Lipids: 80 % C and 20 % TE Surfactant: 3 % T80	175.7 ± 81.6	0.321 ± 0.070	-13.1 ± 2.8	33.5
CT25TCP	Lipids: 75 % C and 25 % TE Surfactant: 3 % T80	76.7 ± 4.2	0.360 ± 0.122	-13.3 ± 2.1	27.0
CT30TCP	Lipids: 70 % C and 30 % TE Surfactant: 3 % T80	124.8 ± 60.4	0.373 ± 0.154	-12.4 ± 2.1	0

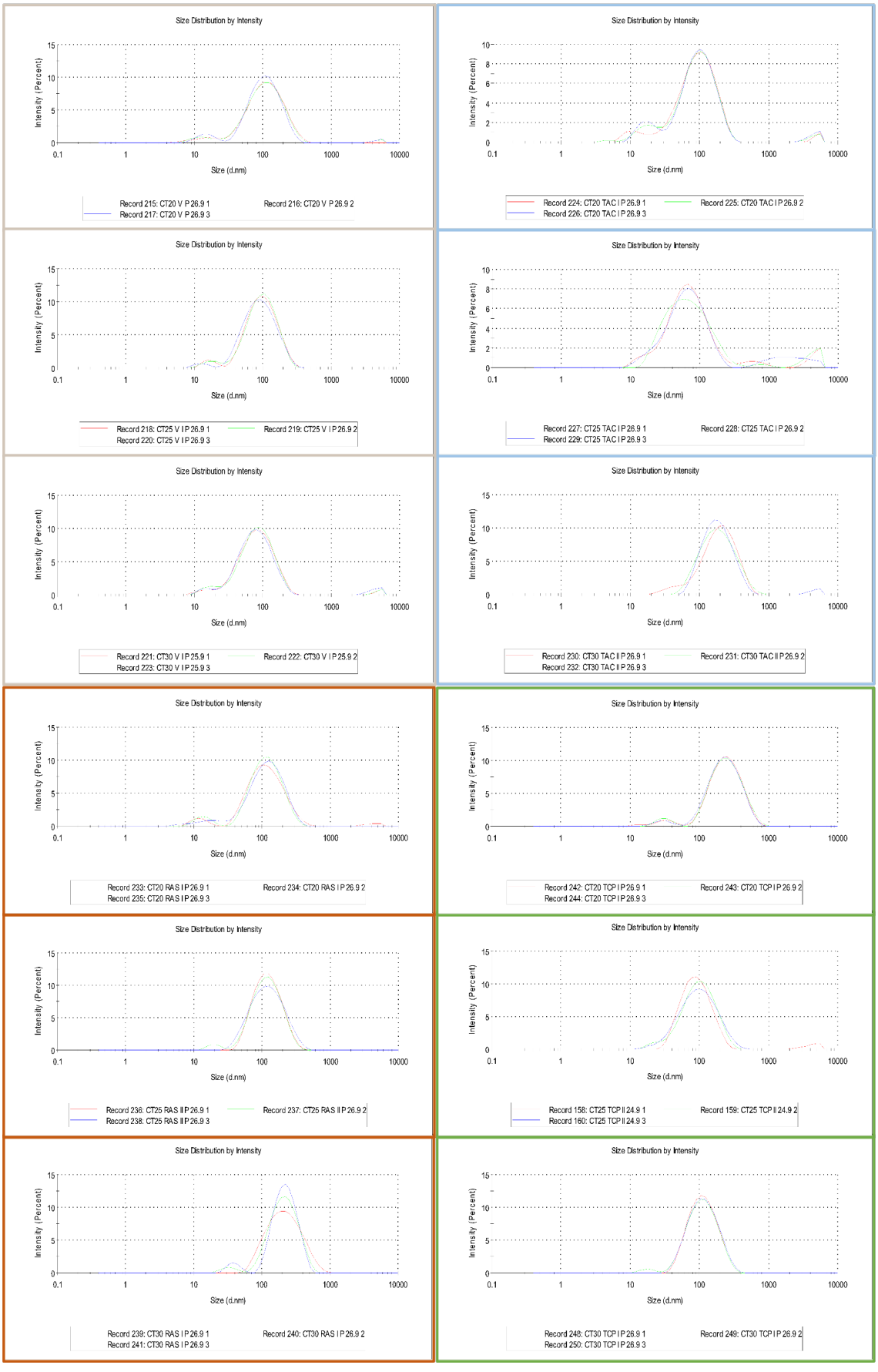

Size Distribution by Intensity
Intensity (Percent)
Size (d.nm)
Record 215: CT20 V P 26.9 1
Record 216: CT20 V P 26.9 2
Record 217: CT20 V P 26.9 3
Size Distribution by Intensity
Intensity (Percent)
Size (d.nm)
Record 224: CT20 TAC I P 26.9 1
Record 225: CT20 TAC I P 26.9 2
Record 226: CT20 TAC I P 26.9 3
Size Distribution by Intensity
Intensity (Percent)
Size (d.nm)
Record 218: CT25 V I P 26.9 1
Record 219: CT25 V I P 26.9 2
Record 220: CT25 V I P 26.9 3
Size Distribution by Intensity
Intensity (Percent)
Size (d.nm)
Record 227: CT25 TAC I P 26.9 1
Record 228: CT25 TAC I P 26.9 2
Record 229: CT25 TAC I P 26.9 3
Size Distribution by Intensity
Intensity (Percent)
Size (d.nm)
Record 221: CT30 V I P 25.9 1
Record 222: CT30 V I P 25.9 2
Record 223: CT30 V I P 25.9 3
Size Distribution by Intensity
Intensity (Percent)
Size (d.nm)
Record 230: CT30 TAC II P 26.9 1
Record 231: CT30 TAC II P 26.9 2
Record 232: CT30 TAC II P 26.9 3
Size Distribution by Intensity
Intensity (Percent)
Size (d.nm)
Record 233: CT20 RAS I P 26.9 1
Record 234: CT20 RAS I P 26.9 2
Record 235: CT20 RAS I P 26.9 3
Size Distribution by Intensity
Intensity (Percent)
Size (d.nm)
Record 242: CT20 TCP I P 26.9 1
Record 243: CT20 TCP I P 26.9 2
Record 244: CT20 TCP I P 26.9 3
Size Distribution by Intensity
Intensity (Percent)
Size (d.nm)
Record 236: CT25 RAS II P 26.9 1
Record 237: CT25 RAS II P 26.9 2
Record 238: CT25 RAS II P 26.9 3
Size Distribution by Intensity
Intensity (Percent)
Size (d.nm)
Record 158: CT25 TCP II 24.9 1
Record 159: CT25 TCP II 24.9 2
Record 160: CT25 TCP II 24.9 3
Size Distribution by Intensity
Intensity (Percent)
Size (d.nm)
Record 239: CT30 RAS I P 26.9 1
Record 240: CT30 RAS I P 26.9 2
Record 241: CT30 RAS I P 26.9 3
Size Distribution by Intensity
Intensity (Percent)
Size (d.nm)
Record 248: CT30 TCP I P 26.9 1
Record 249: CT30 TCP I P 26.9 2
Record 250: CT30 TCP I P 26.9 3

Figure 2.15 - DLS analysis particle size distribution NLC Blank and drug loaded NLC. (blue) TAC, (orange) RAS and (green) TCP.

2.4.7.2. Stability in solution storage at 4 ℃

NLC stability analysis was conducted up to 150 days to understand which formulation was more capable to retain the drug encapsulated inside NLC in solution during storage at 4 °C. The data demonstrated that both formulations at 20 % and 25 % were stable to retain encapsulation efficiency throughout time (Figure 2.16) except for NLC loaded with RAS (CT20RAS) that demonstrated a significant decrease and liberation of RAS to the solution after 110 days (Figure 2.16).

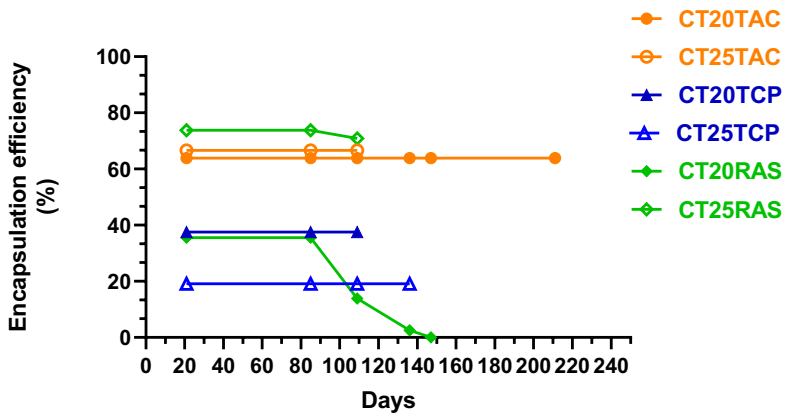


Figure 2.16 - Stability of encapsulated TAC in the formulations after 144 days in storage at 4 °C.

2.4.7.3. Pharmaceutical release in PBS and Plasma

Release studies were performed using PBS pH 7.4 and human plasma to take into consideration some parameters that should simulate *in vivo* conditions, such as pH and plasma components. In terms of pharmacokinetics, TAC presents some drawbacks, such as low bioavailability (17%) and a low half-life (2–3 h). Therefore, incorporation in NLC can help to overcome these limitations, while providing a slow rate of delivery. Release profiles were obtained for incubation in PBS pH 7.4 for up to 72 h, using sink conditions. After 24 h, almost 50.8% of TAC was released, 56.0% in 48 h and 60.7% in 72 h. The rapid initial release of TAC is possible due to the molecules of TAC present at the surface of the NLC. We can also observe that in the first 30 min there was an initial burst effect followed by a steady release up to 72 h, which can be attributed to the diffusion of TAC from the core of

the NLC (Figure 2.17). The results obtained with incubation in plasma were a release of 42.30% in 24 h incubation (Figure 2.17).

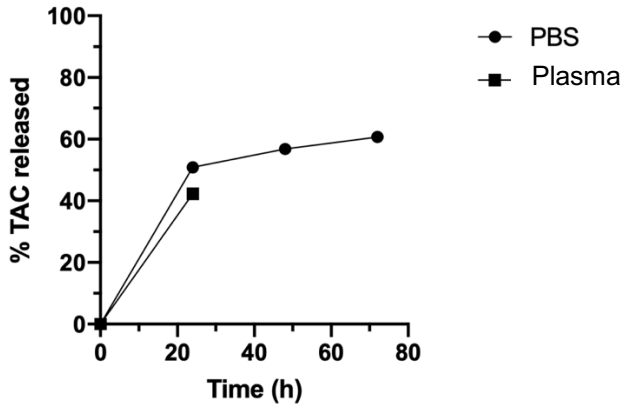


Figure 2.17 - Release profiles of TAC from Compritol® 888 ATO NLC in PBS, pH 7.4 and plasma

2.4.8. Toxicity assays in SH-SY5Y cells

In vitro cytotoxicity studies are important to validate the safety of the delivery system. With this purpose, toxicity was assessed by measuring the cell viability of the neuroblastoma cell line (SH-SY5Y), based on its ability to differentiate in a model of cholinergic neurons, treated with all formulations developed using the MTT and SRB assays.

2.4.8.1. MTT Assay

The MTT assay provides information about cell metabolism activity and is frequently used. The reduction of cellular metabolic activity has been used as an indicator of compromised cells. First, we conduct initial toxicity test with wide range of concentrations (1-100 μM). As seen in figure 2.18, the results indicate a concentration-dependent decrease on cell viability in all compounds tested. As expected, administration of free TAC at 100 μM resulted on a significant decrease on cell viability. Both NLC CT25 B and CT25TAC demonstrated significant toxicity activity against SH-SY5Y at concentration equal and above 25 μM (Figure 2.18).

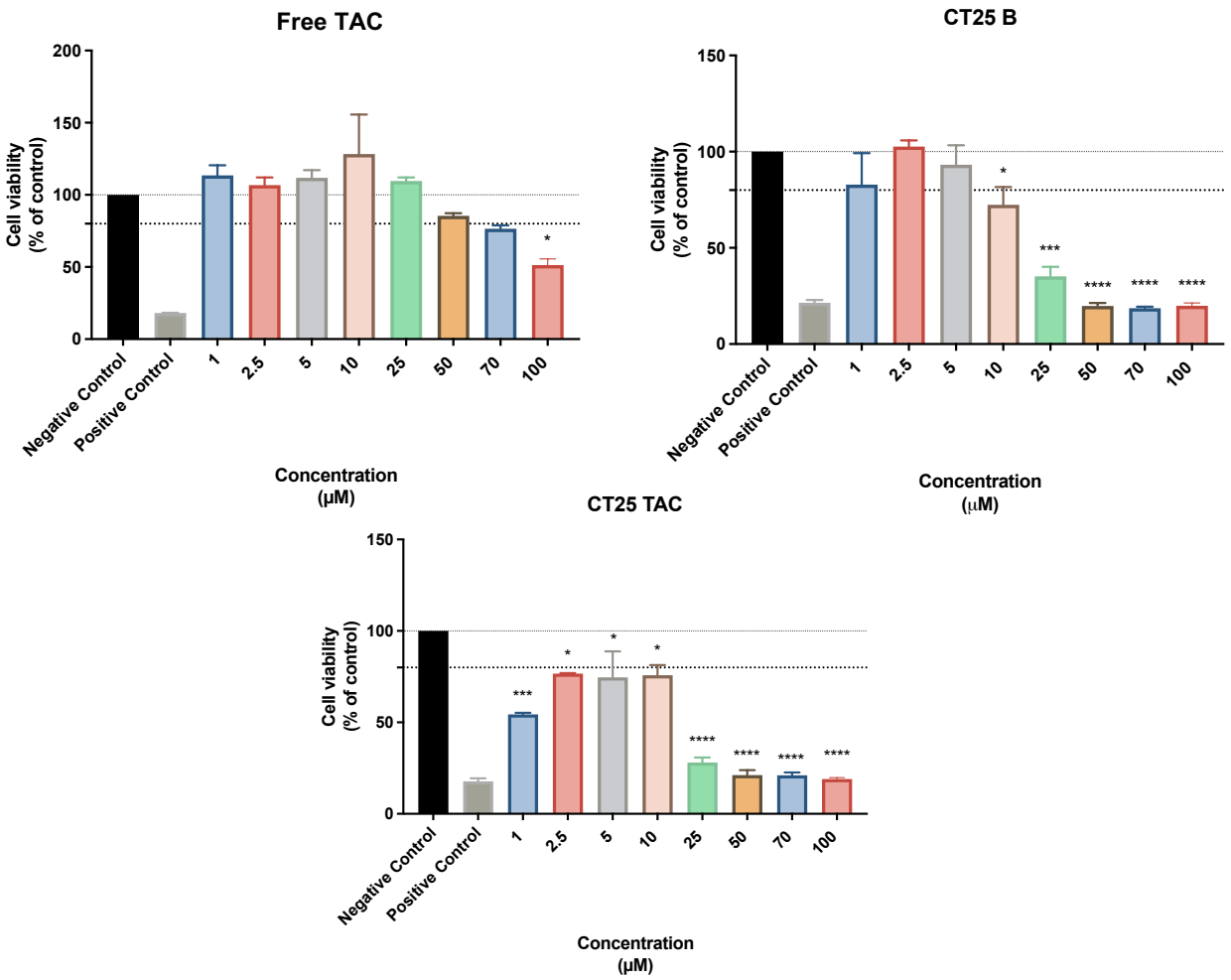


Figure 2.18 - Relative cell viability of SH-SY5Y cell line measured by the MTT reduction after 24 h incubation. Treatment with free TAC, blank NLC and NLC loaded with TAC (1–100 μM). Results are expressed as mean SD (n = 2). Statistical analysis between the control group and other groups was performed using two-way ANOVA with Dunnet's post hoc test (* $p < 0.05$; ** $p < 0.01$; *** $p < 0.001$; **** $p < 0.0001$).

Second part of this work, all formulations were tested for a period of 24 h in a concentration range of 1 μM to 25 μM. Results show that in CT25 formulations up to 20 μM, with or without TAC, no evidence of acute cytotoxicity was observed with an 80% of cell viability (Figure 2.19). The formulation of CT30 was relatively safe at 10 μM with a decrease in 20% of cell viability (Figure 2.19). On the other hand, CT20 formulations presented a high level of cytotoxicity in SH-SY5Y cells. One possible explanation for this result can be the higher PI, which may lead to a tendency to aggregate and increase toxicity. The slight decrease of

20% of cell viability was expected due to the use of T80 which is a surfactant considered to present some toxicity. The CT20 formulation showed to affect cell viability (Figure 2.19).

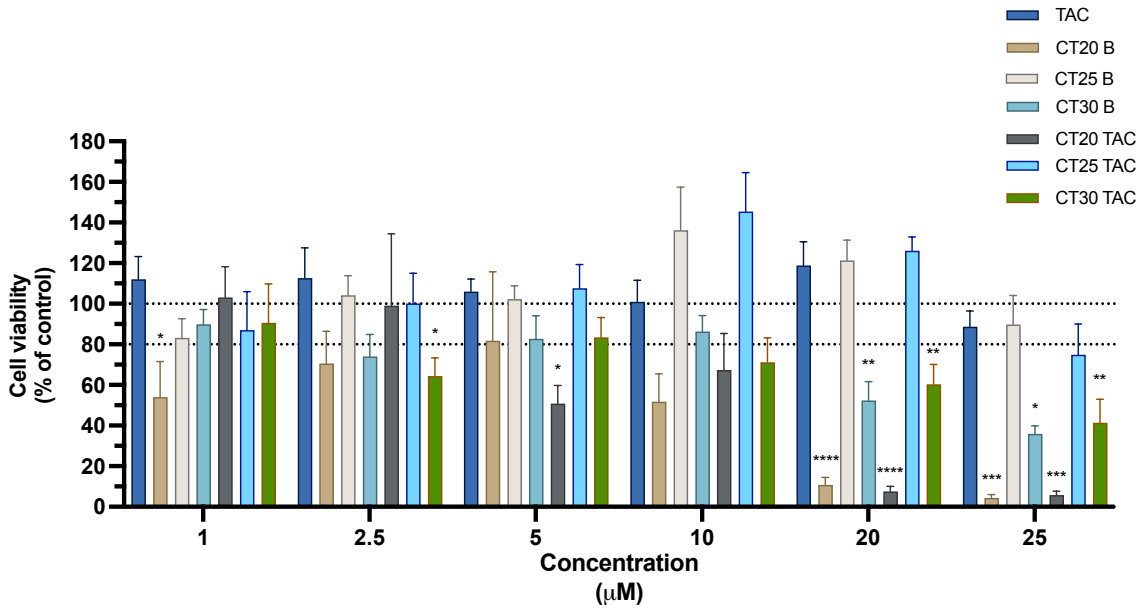


Figure 2.19 - Relative cell viability of SH-SY5Y cell line measured by the MTT reduction after 24 h incubation. Treatment with free TAC, blank NLC and NLC loaded with TAC (1–25 μM). Results are expressed as mean SD (n = 4). Statistical analysis between the control group and other groups was performed using two-way ANOVA with Dunnet's post hoc test (* $p < 0.05$; ** $p < 0.01$; *** $p < 0.001$; **** $p < 0.0001$).

2.4.8.2. SRB Assay

In addition, SRB assay was used to corroborate the MTT results, being a good indicator of cell density determination based on protein content. Unlike MTT, the SRB method does not allow distinguishing between viable and dead cells, but it can be used to detect cytotoxic effects of a drug. The SRB assay results obtained corroborate those from the MTT. Formulations CT25 and CT30 were not significantly cytotoxic in the same concentration range and CT20 formulations, either blank or TAC-loaded, were more toxic when compared to control (Figure 2.20).

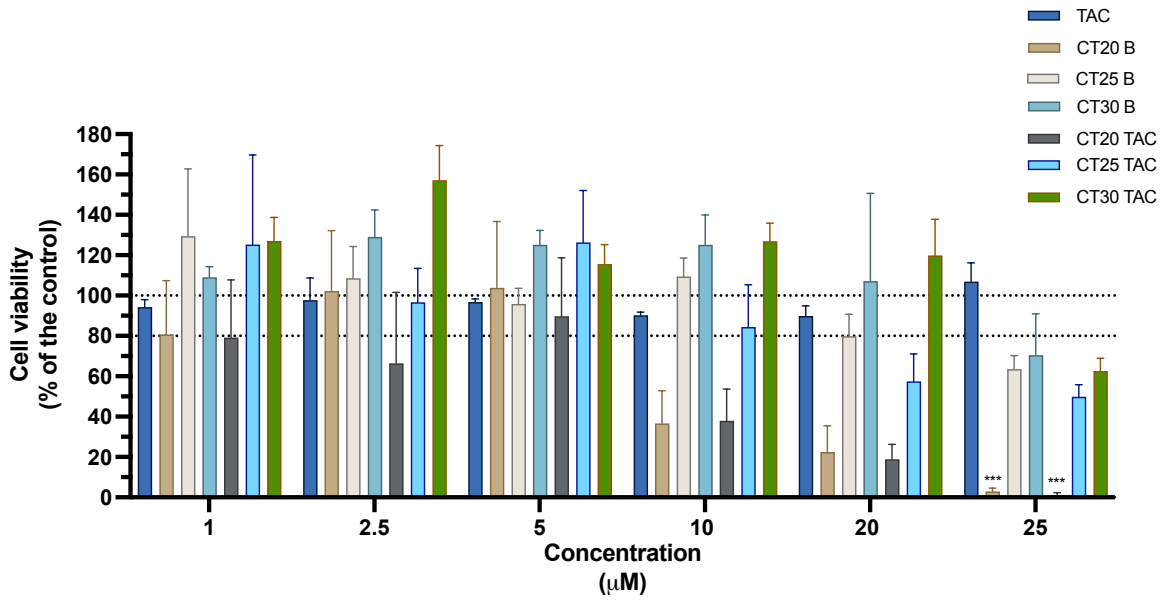


Figure 2.20 - Relative cell viability of SH-SY5Y cell line measured by the SRB reduction after 24 h incubation. Treatment with free TAC, blank NLC and NLC loaded with TAC (1–25 μM). Results are expressed as mean SEM (n = 4). Statistical analysis between the control group and other groups was performed using two-way ANOVA with Dunnet's post hoc test (*** p <0.001).

2.4.8.3. SH-SY5Y Morphology Visualization and cell count

The morphology of neuroblastoma SH-SY5Y cell line was evaluated after 24 h incubation with all formulations (see Supplementary Information Figure S2.5 and 2.6). This microscope cellular visualization was performed by Lionheart FX and its crucial to corroborate the data obtained with MTT and SRB assays. In the treatment with TAC, CT25 B, CT30 B, CT25TAC and CT30 TAC (10 μM), we can observe a small decrease of cell viability but no substantial cell morphology differences, thus supporting the *in vitro* cytotoxicity data (Figure 2.21). For instance, in the treatment with CT20 B and CT20TAC we observed an increase in cell number and small morphology differences which supports the *in vitro* cytotoxicity data (Figure 2.21). The cell count analysis corroborated with cell visualization and demonstrated that treatment with TAC and all NLC formulations did not affect the number of cells in culture up to 5 μM (Figure 2.22). Over 10 μM, the treatment with CT20 B, CT30 B, CT20TAC and CT30TAC resulted in a decrease of cell count (Figure 2.22). Moreover, taking a closer look on cell morphology changes with increase concentration levels in figure 2.23 shows clear loss of normal neuroblastoma morphology with decrease of cellular extensions at the concentration of 20 μM with the treatment of CT20 B, CT20TAC, CT30 B and CT30TAC. The treatment with CT25TAC have severe cell morphological changes with loss of cell projections and cellular rounding at 25 μM (Figure 2.23).

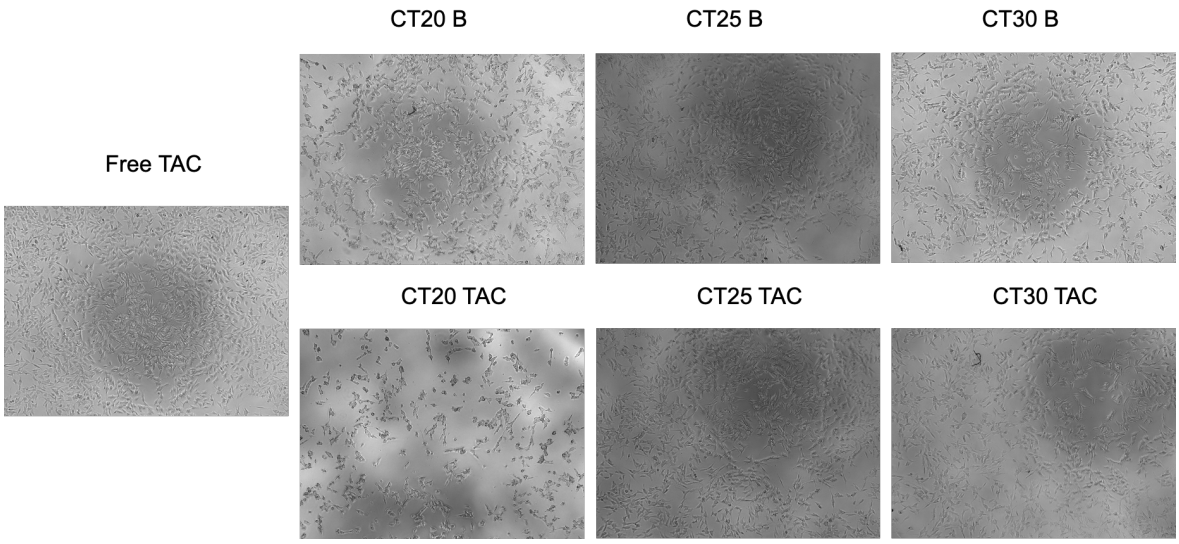


Figure 2.21 - Microscope cellular visualization through Lionheart FX of treatment with free TAC, different blank NLC formulations (CT20 B, CT25 B and CT30 B) and different NLC formulations loaded with TAC on SH-SY5Y cell line at a concentration of 10 µM.

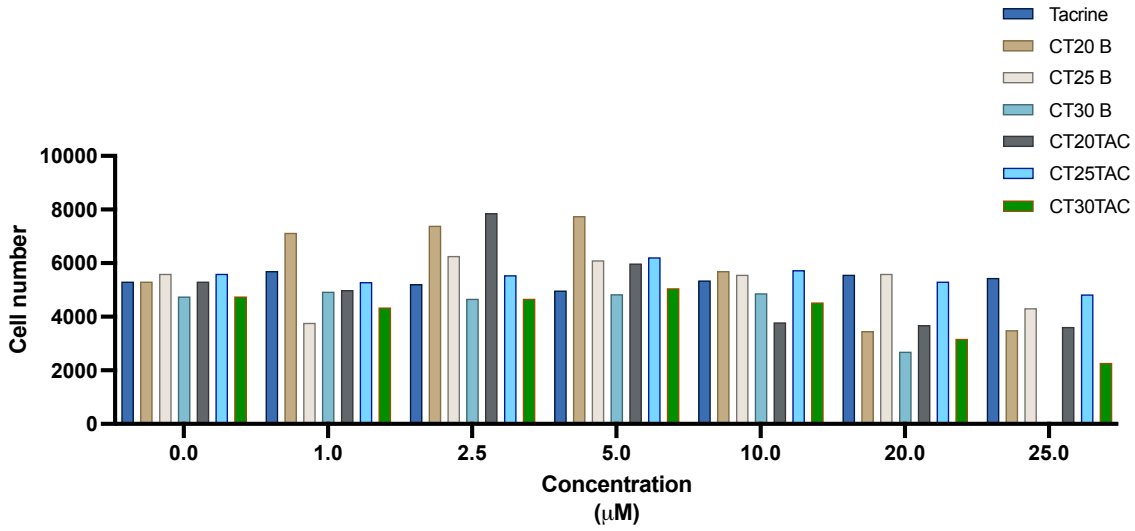


Figure 2.22 - Cell count through Lionheart FX treatment with free TAC, blank NLC and NLC loaded with TAC (1–25 µM) for 24 h incubation. (** p <0.01; *** p <0.001; **** p <0.0001)

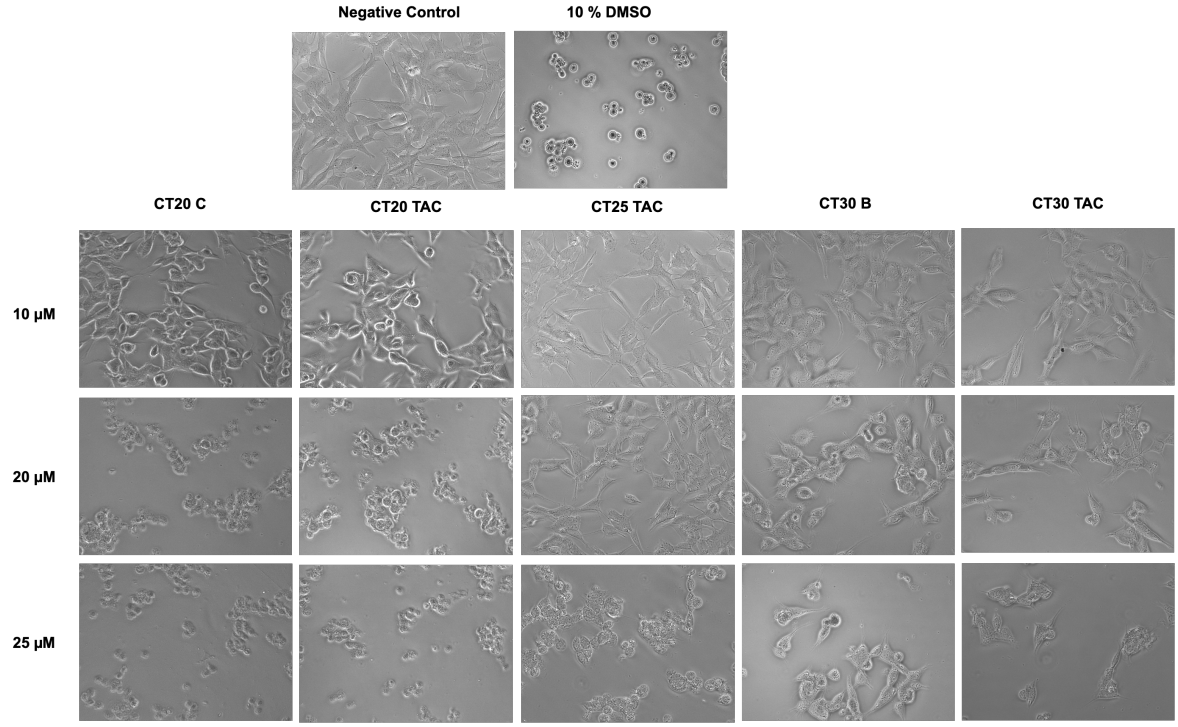


Figure 2.23 - Microscope cellular visualization through Lionheart FX (20x) of treatment with negative control (ultra-purified H_2O), positive control (10% DMSO), different blank NLC formulations (CT20 B, CT25 B and CT30 B) and different NLC formulations loaded with TAC on SH-SY5Y cell line at a concentration of 10, 20 and 25 µM.

2.4.9. Toxicity assays in Caco-2 cell line

The third part of this toxicity assays was to evaluate the most promising NLC formulations in other cell line, in this case Caco-2 cell line, and see if toxicity results are similar in the same formulations.

2.4.9.1. MTT assay

The results obtain from the MTT assay with reduced concentration analysis (1, 5 and 10 µM), expressed in Figure 2.24, show that treatment with NLC in CT25 formulations up to 5, with or without drugs, no evidence of acute cytotoxicity was observed with an 80% of cell viability. It's to point out that this cells in this experiment at 10 µM with treatment CT25 B resulted on a significant decrease on cell viability (Figure 2.24).

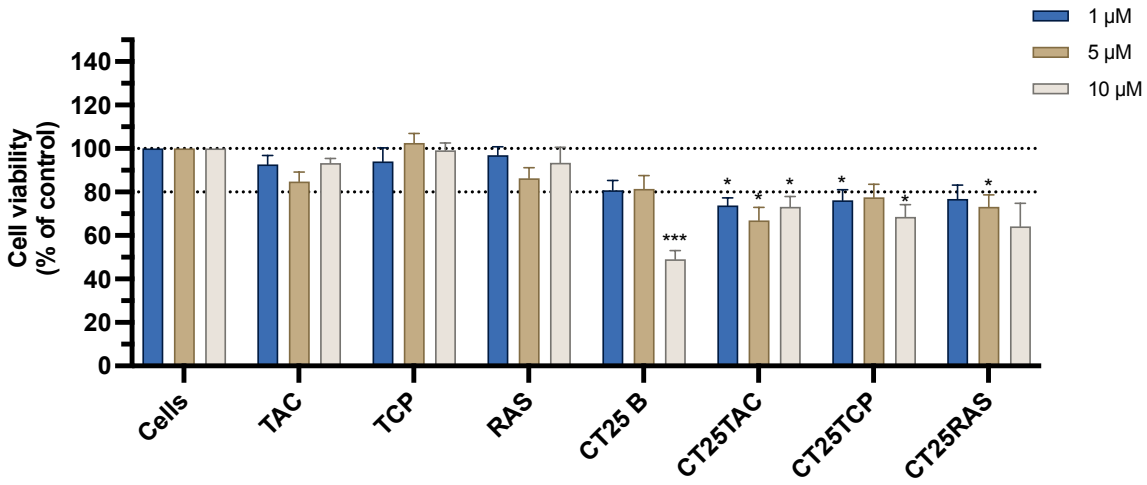


Figure 2.24 - Relative cell viability of Caco-2 cell line measured by the MTT reduction after 24 h incubation. Treatment with free CNS drugs, blank NLC (CT25 B) and NLC loaded with drugs (1, 5 and 10 µM). Results are expressed as mean SD (n = 4). Statistical analysis between the control group and other groups was performed using two-way ANOVA with Dunnet's post hoc test (* $p < 0.05$; ** $p < 0.01$; *** $p < 0.001$; **** $p < 0.0001$).

2.4.9.2. SRB assay

The results obtain from the MTT assay with reduced concentration analysis (1, 5 and 10 µM), expressed in Figure 2.25, show that treatment with all NLC formulations didn't result on a significant toxicity against Caco-2 cell line demonstrated an expected slight decrease on cell viability of 20 % (Figure 2.25).

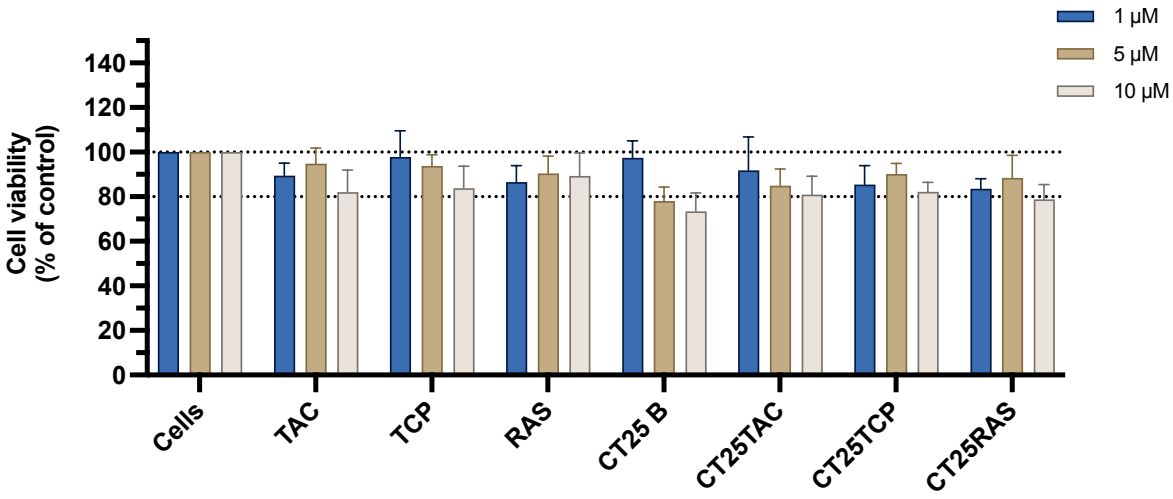


Figure 2.25 - Relative cell viability of Caco-2 cell line measured by the SRB reduction after 24 h incubation. Treatment with free CNS drugs, blank NLC (CT25 B) and NLC loaded with drugs (1, 5 and 10 µM). Results are expressed as mean SD (n = 4). Statistical analysis between the control group and other groups was performed using two-way ANOVA with Dunnet's post hoc test.

2.4.9.3. Caco-2 Morphology Visualization and cell count

The images retrieved from the experience from morphological visualization of Caco-2 cell line demonstrated no drastic changes with the treatment of CT25 drug loaded NLC for all concentrations tested (Figure 2.27). In addition, cell count analyses demonstrated significant decrease on cell number with the treatment of CT25 B, CT25TCP and CT25 RAS at concentration of 10 µM (Figure 2.26). Although, some degree of decrease is notice by the experiment, the cell count obtain couldn't assess all cells present in the well, thus create a more pronounced cell count decrease when compared to results obtain by MTT assay and SRB assay that take in consideration all cells plated in the well.

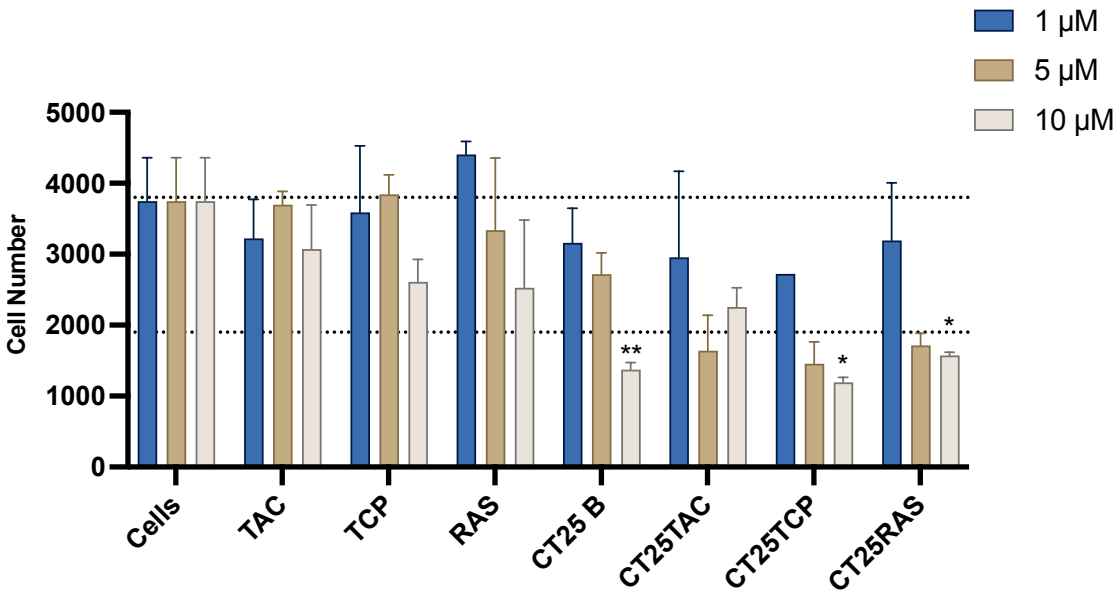


Figure 2.26 - Cell count through Lionheart FX treatment with free CNS drugs, blank NLC (CT25 B) and NLC loaded with CNS drugs (1, 5 and 10 µM) for 24 h incubation. Statistical analysis between the control group and other groups was performed using two-way ANOVA with Dunnet's post hoc test (* $p < 0.05$; ** $p < 0.01$).

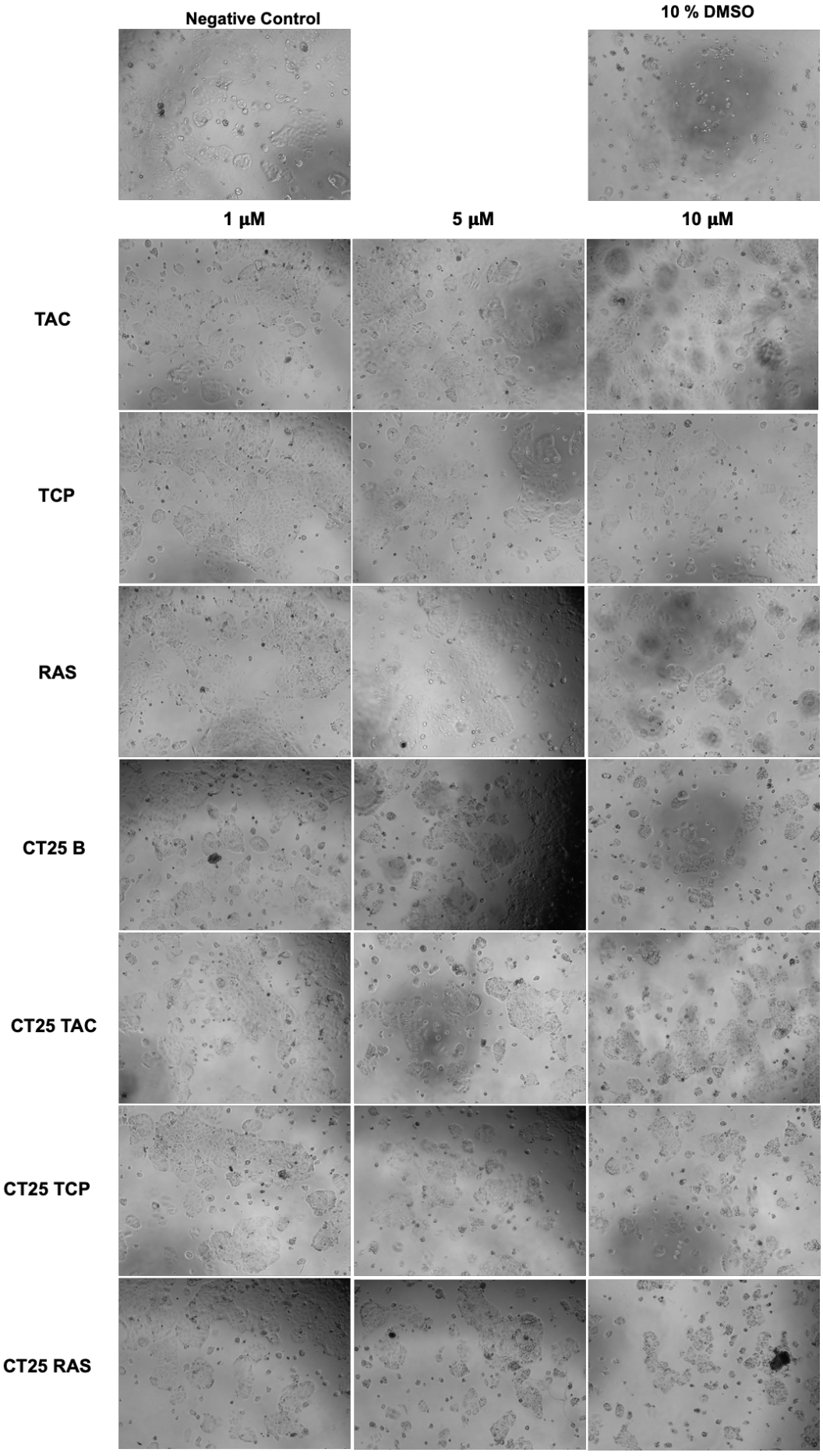

Negative Control
10 % DMSO
1 µM
5 µM
10 µM
TAC
TCP
RAS
CT25 B
CT25 TAC
CT25 TCP
CT25 RAS

Figure 2.27 - Microscope cellular visualization through Lionheart FX and Leica DFC350 FX of treatment with negative control (ultra-purified H_2O), positive control (10% DMSO), free drugs, CT25 B and CT25 loaded with different CNS drugs on Caco-2 cell line at a concentration of 1, 5 and 10 µM.

2.5. Discussion and conclusion

The overall sequential optimization protocol helped to choose formulations methods and selected the NLC formulation to continue the studies to evaluate it's activity. The initial idea was to conduct toxicity studies on a more adequate cell model with isolation of neurons from mice brain, however the protocol applied in our laboratory was difficult to achieve the amount off cell needed to conduct the experiments (see supplementary Information, Figures 2.2, 2.3 and 2.4) and a cell contamination was determinant to change and use another similar cell model. So, we conduct our toxicity assays first in neuroblastoma SH-SY5Y and then in Caco-2 cell lines. The results were helpful to determine first a change to the initial NPs formulation of SLN to NLC due to drug solubility upon formulation. Then noted that the initial purification method led to increase concentration of toxic surfactant in solution resulting on high cell toxicity. Then, after analyzing all the parameters such as encapsulation efficiency, particle size, NLC stability during storage and cell toxicity against both cell lines we concluded that NLC with 25 % of Transcutol® was acceptable to continue studies and conduct further modifications.

2.6. References

1. Davis FF. The origin of pegnology. Adv Drug Deliv Rev [Internet]. 2002;54(4):457–8. Available from: http://www.sciencedirect.com/science/article/pii/S0169409X02000212

2. Alonso M, Couvreur P. Chapter 1:Historical View of the Design and Development of Nanocarriers for Overcoming Biological Barriers. In 2012. Available from: http://dx.doi.org/10.1039/9781849735292-00003

3. LANGER R, FOLKMAN J. Polymers for the sustained release of proteins and other macromolecules. Nature [Internet]. 1976 Oct 28;263:797. Available from: http://dx.doi.org/10.1038/263797a0

4. Couvreur P, Barratt G, Fattal E, Vauthier C. Nanocapsule Technology: A Review. Crit Rev Ther Drug Carrier Syst [Internet]. 2002;19(2):99–134. Available from: http://www.dl.begellhouse.com/journals/3667c4ae6e8fd136,13237f906e958e8d,12624a520b8f6730.html

5. Singh R, Lillard JW. Nanoparticle-based targeted drug delivery. Exp Mol Pathol [Internet]. 2009 Jun;86(3):215–23. Available from: https://linkinghub.elsevier.com/retrieve/pii/S001448000800141X

6. Lewinski N, Colvin V, Drezek R. Cytotoxicity of nanopartides. Small. 2008;4(1):26–49. Available from: https://onlinelibrary.wiley.com/doi/10.1002/smll.200700595

7. Yohan D, Chithrani BD. Applications of nanoparticles in nanomedicine. J Biomed Nanotechnol. 2014;10(9):2371–92.

8. Blanco E, Shen H, Ferrari M. Principles of nanoparticle design for overcoming biological barriers to drug delivery. Nat Biotechnol [Internet]. 2015 Sep 1;33(9):941–51. Available from: http://www.nature.com/articles/nbt.3330

9. Gronewold A, Horn M, Ranđelović I, Tóvári J, Muñoz Vázquez S, Schomäcker K, et al. Characterization of a Cell-Penetrating Peptide with Potential Anticancer Activity. ChemMedChem. 2017;12(1):42–9. Available from: https://onlinelibrary.wiley.com/doi/10.1002/cmdc.201600498

10. Vu MN, Kelly HG, Wheatley AK, Peng S, Pilkington EH, Veldhuis NA, et al. Cellular Interactions of Liposomes and PISA Nanoparticles during Human Blood Flow in a

Microvascular Network. Small [Internet]. 2020 Aug 1;16(33):2002861. Available from: https://doi.org/10.1002/smll.202002861

11. Gaspar DP, Faria V, Quintas JP, Almeida AJ. Targeted Delivery of Lipid Nanoparticles by Means of Surface Chemical Modification. Curr Org Chem [Internet]. 2017 Nov 28;21(23):2360–75. Available from: http://www.eurekaselect.com/146869/article

12. Mohanta BC, Palei NN, Surendran V, Dinda SC, Rajangam J, Deb J, et al. Lipid Based Nanoparticles: Current Strategies for Brain Tumor Targeting. Curr Nanomater. 2019;4(2):84–100. Available from: http://www.eurekaselect.com/172075/article

13. Tapeinos C, Battaglini M, Ciofani G. Advances in the design of solid lipid nanoparticles and nanostructured lipid carriers for targeting brain diseases. J Control Release. 2017;264:306–32. Available from: http://dx.doi.org/10.1016/j.jconrel.2017.08.033

14. Chattopadhyay N, Zastre J, Wong HL, Wu XY, Bendayan R. Solid lipid nanoparticles enhance the delivery of the HIV protease inhibitor, atazanavir, by a human brain endothelial cell line. Pharm Res. 2008;25(10):2262–71. Available from: http://link.springer.com/10.1007/s11095-008-9615-2

15. Miranda A, Blanco-Prieto MJ, Sousa J, Pais A, Vitorino C. Breaching barriers in glioblastoma. Part II: Targeted drug delivery and lipid nanoparticles. Int J Pharm [Internet]. 2017;531(1):389–410. Available from: http://dx.doi.org/10.1016/j.ijpharm.2017.07.049

16. Gupta S, Kesarla R, Chotai N, Misra A, Omri A. Systematic approach for the formulation and optimization of solid lipid nanoparticles of efavirenz by high pressure homogenization using design of experiments for brain targeting and enhanced bioavailability. Biomed Res Int. 2017;2017. Available from: https://www.hindawi.com/journals/bmri/2017/5984014/

17. Loureiro JA, Andrade S, Duarte A, Neves AR, Queiroz JF, Nunes C, et al. Resveratrol and grape extract-loaded solid lipid nanoparticles for the treatment of Alzheimer's disease. Molecules. 2017;22(2):1–16. Available from: http://www.mdpi.com/1420-3049/22/2/277

18. Couvreur P. Nanoparticles in drug delivery: Past, present and future. Adv Drug Deliv Rev [Internet]. 2013;65(1):21–3. Available from:

http://dx.doi.org/10.1016/j.addr.2012.04.010

19. Gaspar DP, Faria V, Gonçalves LMD, Taboada P, Remuñán-López C, Almeida AJ. Rifabutin-loaded solid lipid nanoparticles for inhaled antitubercular therapy: Physicochemical and *in vitro* studies. Int J Pharm [Internet]. 2016 Jan;497(1–2):199–209. Available from: http://dx.doi.org/10.1016/j.ijpharm.2015.11.050

20. Brewer GJ, Torricelli JR. Isolation and culture of adult neurons and neurospheres. 2007;2(6):1490–8. Available from: http://www.nature.com/articles/nprot.2007.207

21. Kim HJ, Magrané J. Isolation and Culture of Neurons and Astrocytes from the Mouse Brain Cortex. In: Manfredi G, Kawamata H, editors. Molecular Neurodegeneration [Internet]. Totowa, NJ: Humana Press; 2011. p. 63–75. (Methods in Molecular Biology; vol. 793). Available from: http://www.pubmedcentral.nih.gov/articlerender.fcgi?artid=3035023&tool=pmcentrez&rendertype=abstract

Chapter 3
Nanoparticles conjugation of with CPP and CNS drugs

3.1. Introduction

So far intracellular delivery of therapeutic molecules has been one of the major challenges to achieving successful treatment. The biological cell membrane acts as a barrier to proteins and specific compounds unless an active transport mechanism is involved. Certain pharmaceutical nanocarriers have been designed to facilitate the drug delivery inside cells and increase the stability of the administered drug. Among all delivery vectors, CPPs and NP present the greatest potential, however, some limitations are still associated with this. The conjugation of CPPs with NP has been analyzed in order to fulfil the gap between both molecules, and to potentiate the development of a new compound/conjugate that possesses enhanced efficiency, accuracy and therapeutic activity (Figure 3.1). Many studies have demonstrated successful results in this conjugation to treat variety of diseases, such as dermatological disorders (topical application) (1), cancer (2,3), as imaging probes, inflammation (4) and CNS disorders.

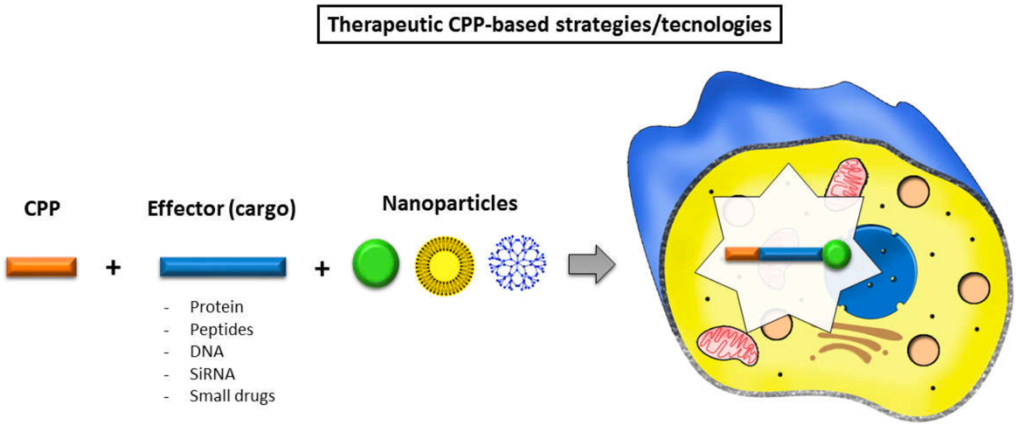


Figure 3.1 - Schematic representation of recent CPP-based strategies. This dual conjugation of CPP, nanoparticle and effector (cargo) can further potentiate the therapeutic effectiveness and enhance stability.

3.1.1. Neurodegenerative diseases

3.1.1.1. Alzheimer Disease

AD was first described by Alois Alzheimer in 1907. Nowadays around 50–75% cases of dementia worldwide are originated by AD and affects almost 6% of the population (5). AD is a progressive neurodegenerative disease and about 95% of AD cases are sporadic and the familiar AD is associated with different genetic mutations resulting in the same phenotypic expression. The mutations more prevalent are associated with gene precursor amyloid protein, presenilin 1, and presenilin 2 (6,7). Normally in cases of familiar disease the symptoms developed more early mainly in the late 30 and 50 years old. On the other hand, late outset AD is characterized by a group of factors such as environmental, epigenetic, and genetic modifications. Around 20% of genetic factors that are associated with the disease are well known. Mutations on the Apo 2 gene are linked with high risk of development sporadic AD, which is crucial for the balance between clearance and deposition of beta amyloid peptide (aβ) (8,9). So far, many studies were conducted to propose different mechanisms involved in the complexity of AD pathology, such as amyloid cascade hypothesis where plaques of amyloid composed of aβ accumulate in the extracellular compartment of neurons leading to synaptic and cell death (10). In this case, there is an imbalance between production, clearance and aggregation of aβ (11) (Figure 3.2). Another hypothesis is hyperphosphorylation of Tau which is a protein component of microtubules. In AD cases, there is a dysfunction of Tau resulting on the formation of neurofibrillary tangles that accumulate inside neurons which limits the transport of nutrients and mitochondria and causes disruption of growing neurons (12). All of these default mechanisms create excitotoxicity in the brain leading to neurotoxicity and neuron dysfunction and death (13) (Figure 3.2).

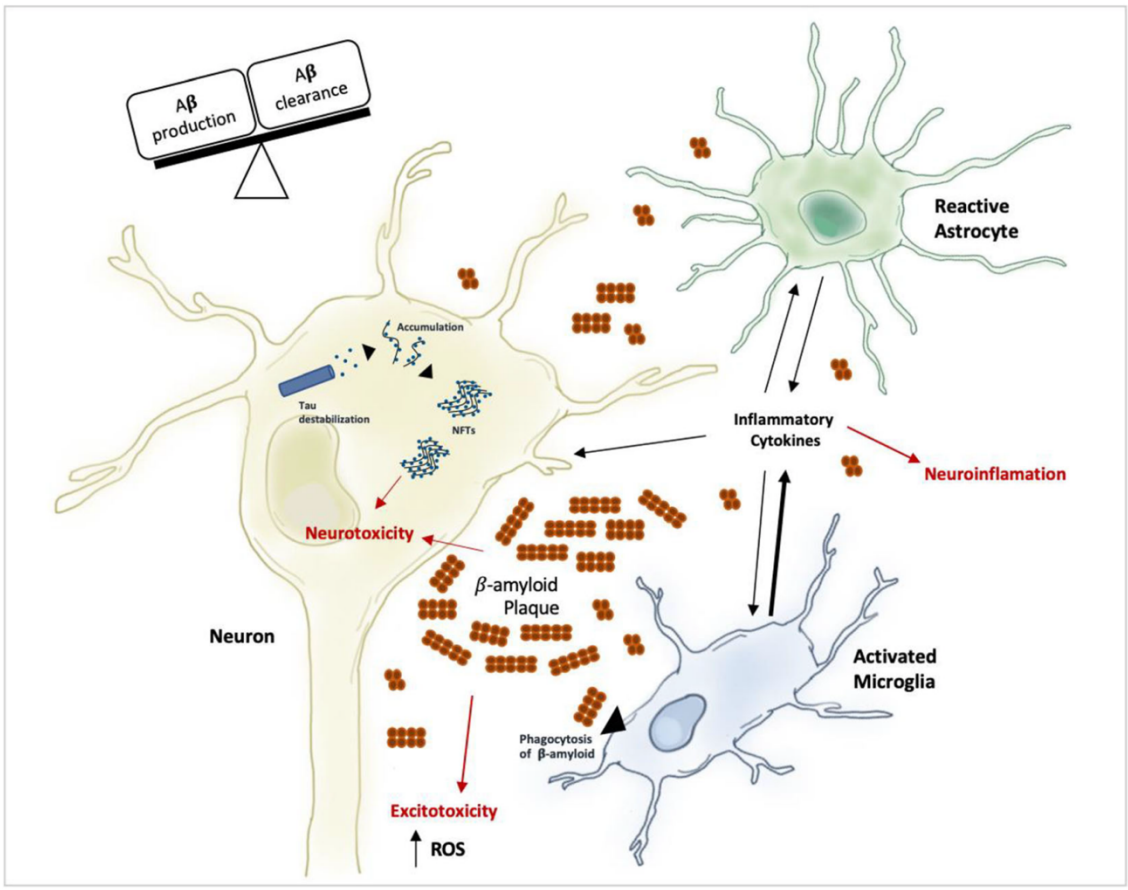


Figure 3.2 - An overview of the major hallmark events leading to AD such as amyloid hypothesis, Tau hyperphosphorylation, neuroinflammation, and excitotoxicity. Amyloid hypothesis begins with an imbalance between aβ production and clearance which leads to an increase of aβ production. Gradual accumulation of aβ leads to the formation of aβ oligomers followed by the formation of aβ plaque with direct impairment of neuronal, synaptic function (neurotoxicity), microglia and astrocyte activation with release of cytokines (neuro- inflammation), increase of reactive oxygen species (excitotoxicity), and induce Tau hyperphosphorylation.

In recent years, other factors and neuronal responses are being linked with aggravation of the disease onset as vascular diseases, diabetes, and neuroinflammation with incorporation of oxidative stress and astrocyte impairment (5,13–17). AD is a neurodegenerative disease characterized by the progressive loss cholinergic neurons in the hippocampus and cortex which are crucial for memory development and cognitive behavior. So, the patients over time exhibit progressive loss of memory and exacerbate neuropsychiatric symptoms such as aphasia, apraxia, agnosia, and confusion (14,18). Although AD molecular pathogenesis is becoming more explicit, there is still a lack of effective disease- modifying treatments. The current therapeutic approach is based on alleviate symptomatic expression and delays the progression of the disease. The main treatment strategy now is the use of acetylcholinesterase inhibitors (AChEI) in order to

improve acetylcholine availability and decrease the effects of the cholinergic loss (Figure 3.3). The current AchEI drugs approved by the FDA to treat AD are donepezil (commercial brand name Aricept®), rivastigmine (Exelon®), and galantamine (Razadyne®) (18) (Figure 3.3). Another approved drug is memantine (Namenda®) which acts on N-methyl-D-aspartate (NMDA) receptor inhibiting glutamate-mediated excitotoxicity. Still, the efficacy of this drugs shows modest positive effects on the memory recovery, cognitive behavior, and in elapse of the disease (18). Furthermore, in long-term treatments, these drugs are associated with several side effects and pharmacokinetics limitations.

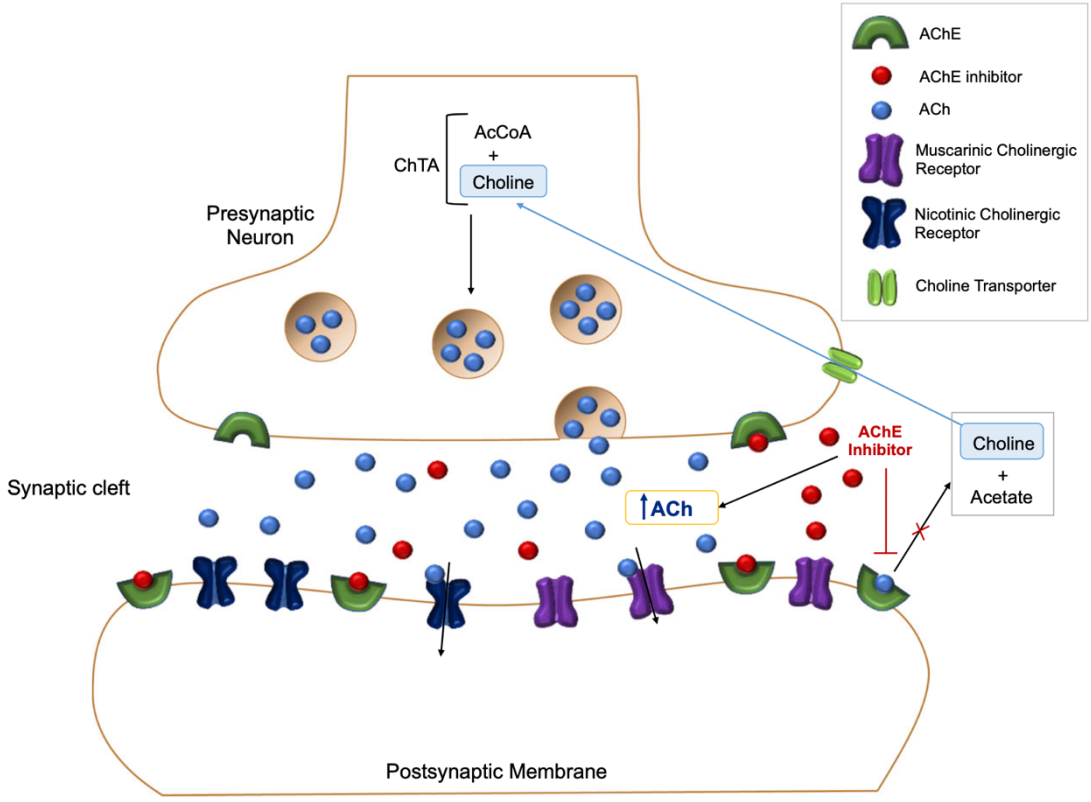


Figure 3.3 - Overview of acetylcholinesterase inhibitors mechanisms of action and respective molecular structure of AD drugs referred in the present review; ACh, acetylcholine; AChE, acetylcholinesterase; ChTA, choline acetyltransferase; AcCoA, acetyl–ScoA (derived from mitochondria)

In order to decrease adverse effects and enhance targeting potential with lower doses, the use of NP has been studied to deliver these pharmaceutical compounds. These nanostructures are considered to be safe, capable to mimic, and modifying biological

processes (19) and demonstrated potential as delivery vectors to treat a wide range of diseases including neurodegenerative diseases (20).

3.1.1.2. Parkinson Disease

Over the years with increases of life expectancy, neurodegenerative diseases have become common causes of mortality and morbidity worldwide, affecting more the elderly population. Neurodegenerative diseases are characterized by a heterogenous clinical presentation, and successful diagnosis is crucial to ensure good treatment (21). For instance, PD is the second most prevalent neurodegenerative disease after AD. It is estimated that PD affects around ten million people worldwide, with an incidence of 3% of the population over 80 years old (22–24). PD was first described by James Parkinson in 1817 (23). Clinical manifestations of PD are characterized by motor and non-motor symptoms (cognitive changes, behavior/neuropsychiatric changes, and autonomic dysfunctions). Motor symptoms includes resting tremors, rigidity, postural instability, and bradykinesia (the inability of PD patients to do fine motor tasks). Non-motor symptoms comprise sleep disturbances, anosmia (loss of sense of smell), constipation, and speech changes. In addition, around 60% of PD patients develop dementia, and around 50% are affected by depression (22,25,26). In the early stages of PD, it is usually a challenge to determine an accurate diagnose due to the variety of parkinsonism forms that exist with similar symptoms of PD. Some examples include infectious disease (encephalitis, prion disease, neurosyphilis, and toxoplasmosis), drug-induced parkinsonism, Lewy bodies disease, progressive supranuclear palsy, corticobasal degeneration, and multiple system atrophy (27). In clinical practice, PD is diagnosed from an evaluation of a patient's symptoms, genetic tests, a drug challenge test with levodopa (dopaminergic response), autonomic function testing, olfactory testing or neuroimaging (magnetic resonance imaging, positron emission tomography) and midbrain sonography) (27). After diagnosis, expected life span of PD is around 6.9–14.3 years, the main cause of death is not directly linked to the disease, and the progression of the disease varies in each individual (28). The pathology of PD is characterized by a loss of dopaminergic neurons within the substantia nigra pars compacta and the development of lewy bodies that are eosinophilic cytoplasmatic inclusions composed of aggregated proteins, mainly α-syn (29). These α-syn aggregates interfere with microtubule-based subcellular transport, thus contributing to synaptic dysfunction and the destabilization of neuronal homeostasis. Moreover, several studies had demonstrated that these toxic α-syn aggregates are able to propagate throughout the brain, similar to prion virus disease. Even though these PD hallmarks are present in post-mortem PD patient autopsies, the primary cause of the

early stage of the disease is still unclear (30). Several studies conducted so far have proposed multiple pathogenic and epigenetic mechanisms that must underlie the development of the disease, such as mitochondrial dysfunction, lysosomal and proteasome dysfunction, neuroinflammation (microglia and astrocyte impairment), and oxidative stress (31–34). All of these correlated pathologic events lead to imbalance of brain homeostasis, dopamine depletion, synaptic dysfunction, and neuronal loss (35), as shown in Figure 3.4.

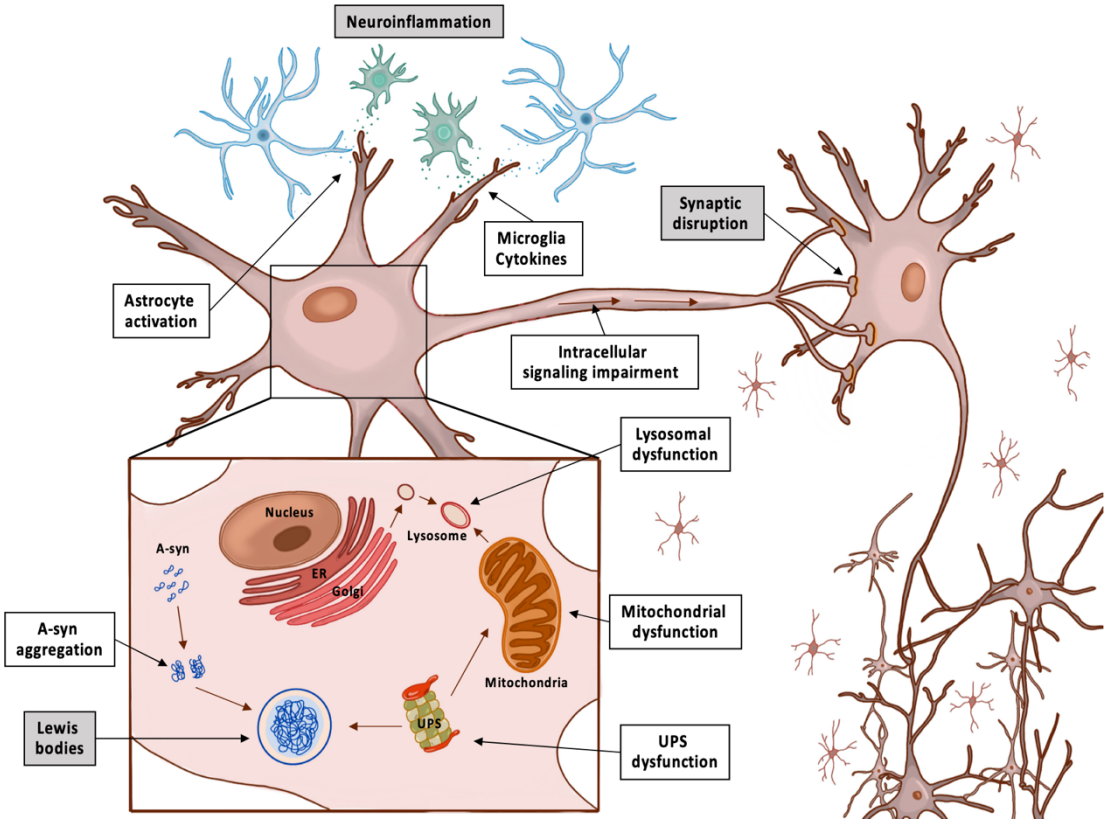


Figure 3.4 - Schematic representation of the major hallmark events leading to Parkinson's disease with the formation of Lewis bodies, ubiquitin proteosome system (UPS) dysfunction, neuroinflammation, and synaptic disruption with neurodegeneration. Endoplasmic reticulum (ER); alfa-synuclein (α-syn).

Several risks factors could potentiate the development of PD such as age, genetic factors, environmental factors, and lifestyle behaviors (reviewed in more depth in (36)). The majority of PD patients have an idiopathic disease, around 15% have a family history, and 5–10% present a monogenic form of the disease. Recent research collected at least 23 loci and 19 disease-causing genes for PD, including 10 autosomal-dominant genes and 9 autosomal-recessive genes (37). Depending on the type of gene mutation, the pathophysiological hallmarks and clinical manifestations are different. Some gene

mutations are directly linked with the disruption of α-syn function and the accumulation of, e.g., PARK 1, PARK 4, and LRRK2 are directly linked with disruption of α-syn function and accumulation (38). In addition, gene mutations such as PINK 1, PARKIN, UCHL 1 are linked with malfunction of the ubiquitin–proteasome system and the autophagy system. These systems enable the efficient clear of misfolded proteins and remotion of disrupted mitochondria in neurons. Dysfunction of these regulatory mechanisms facilitated accumulation of misfolded proteins such as α-syn and consequently leads to the formation of Lewy bodies. Moreover, the impairment of lysosomal function has been linked with PD and alterations to the ATP13 A2 gene (34). Several environmental factors have been related as well with increased risk of developing PD such as exposure to certain toxins, insecticides (paraquat and rotenone), narcotic drugs, and some solvents (36). The treatment of PD starts when motor signs are developed. Current treatments include pharmacologic therapy, physical therapy, rehabilitating therapy and surgery (Figure 3.5).

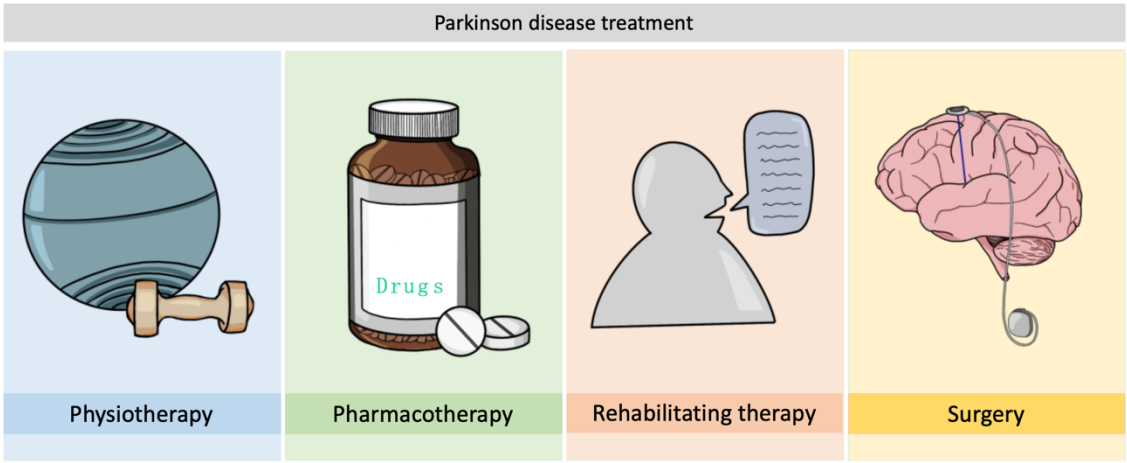


Figure 3.5 - The current Parkinson's disease treatment introduced to recently diagnosed patients.

Physical therapy and exercise are beneficial in PD patients for both motor and non-motor symptoms. The activities include speech therapy, nutrition, physiotherapy, and support groups. The current pharmacologic therapy is based on the symptomatic relief of motor and non-motor symptoms (just reported in (28)). Today, the main strategy for motor symptom treatments is based on an increase of dopamine levels, mimic dopamine effect or decrease dopamine metabolization and storage. There are seven types of drugs that clinicians use to treat PD: levodopa/carbidopa, dopamine agonists, MAO-B inhibitors,

injectable dopamine agonists, NMDA inhibitors, and anticholinergic drugs (Figure 3.6) (28). For initial therapy, levodopa, non-ergot dopamine agonists, and MAO-B inhibitors can be used. Even though levodopa is the most effective treatment so far, early use is associated with the early development of dyskinesia (involuntary muscles movements). Levodopa alternative drugs can be used for PD treatment but with the progression of the disease the therapy starts to fail, and motor dysfunction starts to develop. Eventually, levodopa has to be included in the treatment in order to ensure adequate motor symptom relief (39). Moreover, there are some clinicians that start levodopa treatment at the beginning and only use adjunctive and combination therapy when motor fluctuations (‘’on-time” and “off-time”) and dyskinesia appear. All of these adjunctive compounds are able to improve the pharmacokinetics of levodopa (40) (Figure 3.6).

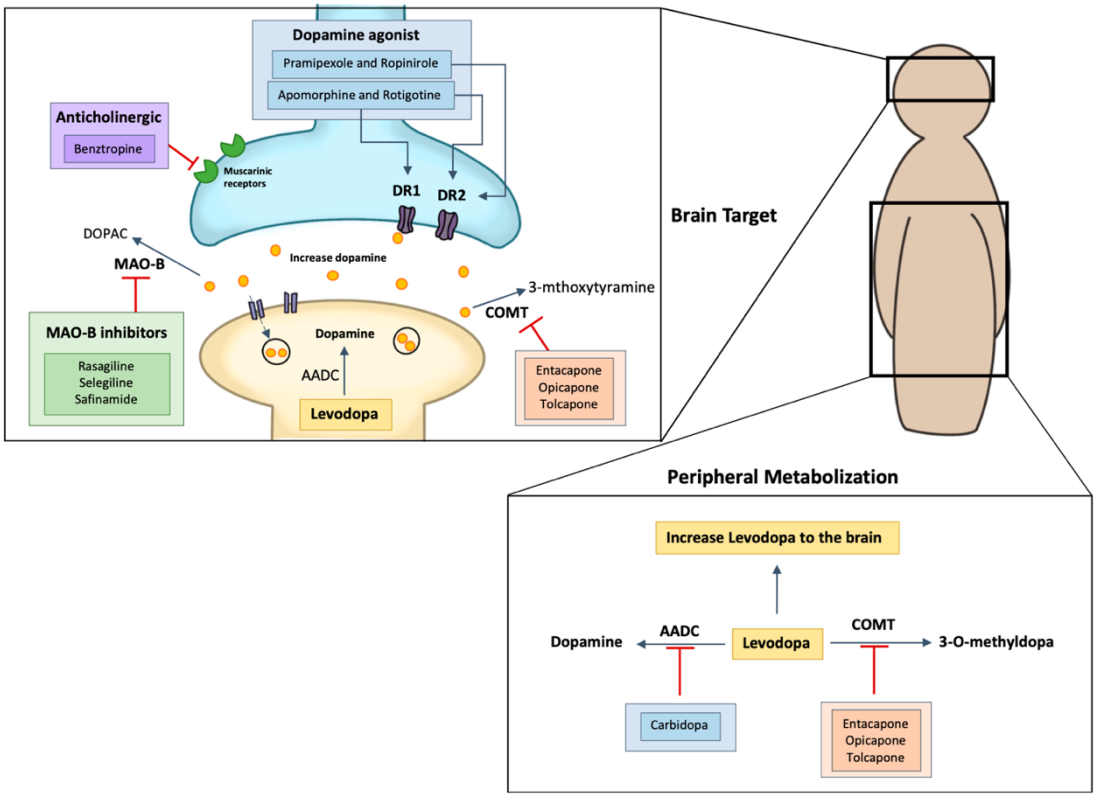


Figure 3.6 - PD pharmacotherapy mechanism and sites of action. COMT: Catechol o-methyltransferase; MAO-B: mono-amide oxidase B. Aromatic L-amino acid decarboxylase (AADC); Catechol o-methyltransferase (COMT); mono-amide oxidase B (MAO-B); Dopamine receptors (DR); dihydroxyphenyl acetic acid (DOPAC).

Though current PD therapy with dopamine replacement is effective in reducing motor symptoms, the long-term drug treatment and progression of PD pathology consequently leads to a loss of drug effectiveness and an increase of side-effects (41). In addition, and

as mentioned above, some of the available drugs used to treat PD present a poor pharmacokinetic profile, low diffusion through the BBB, and limited bioavailability. Therefore, there is a need to develop new strategies that are able to extend and control the release of drugs. An increasing number of studies have demonstrated that nanoparticles can enhance drug delivery through both conventional and unconventional administration routes, which is crucial to explore alternatives in progressively debilitating diseases such as PD. In the next section, we review some already developed nanosystems to deliver PD-available drugs through different modes of administration that could be applied in future therapeutic approaches.

3.1.1.3. CPP and NPs in CNS

Currently, there is no cure for neurodegenerative diseases and current therapeutics were developed to address symptoms and not the mechanisms underlying the disease. Kesselheim's work demonstrated that the development of CNS drugs has slowed down since 1990 for both early and late stages of clinical trials. So, it is important to refocus attention on these diseases and develop new, effective compounds (42). The CPP-derived peptide therapeutics were also designed and developed for the treatment of neurodegenerative disorders (43). Insulin has an important role in neurodegenerative diseases such as dementia, autism and AD's and is responsible for improving cognitive function, learning and memory. Yan and his team developed a Tat mediated PLGA nanoparticle to deliver insulin to the brain via a non-invasive pathway (nose-to-brain route) (44). This approach resulted in a 4.5-fold increase in intracellular accumulation of insulin (44). Another work of Huang and his team used the same Angiopept-2/nanoparticle strategy but studied its potential to deliver a therapeutic gene in Parkinson disease models (45). The authors prepared Angiopep-2 conjugated with dendrigraft poly-L-Lysine (DGL) PEG and concluded that long term administration of the compound improved locomotor activity and recovery of dopaminergic neurons in behavioral studies (45). Another study demonstrated the importance of K16ApoE CPP incorporation in NP. The CPP K16ApoE improved permeability across BBB and brain accumulation of the construct up to 8–10 times higher than formulations without CPP (46).

3.1.2. Cancer

In 2020, Cancer has recorded 19.3 million new cases and is responsible for around 10 million deaths worldwide. Breast cancer is considered the most diagnosed cancer followed by lung and colorectal cancer. In addition, lung cancer is associated with the highest mortality rate followed by colorectal and liver cancers (47,48). For several years the treatment of cancer has been based on tumor surgical removal (whenever possible), radiotherapy and pharmacotherapy. The treatment of cancer with chemotherapy drugs lacks specificity and often results in toxicity and many side-effects for patients. Conventional chemotherapy shows poor water solubility, low tumor specificity, high toxicity and rapid blood clearance. Another limitation that can be added to the list is the emergence of multi-drug resistance, making cancer one of the most concerning health problems, and life-threatening diseases worldwide (49). One example with a poor prognosis is glioblastoma; to the presence of the blood–brain barrier (BBB) limits the amount of chemotherapy and makes it difficult to conduct radiotherapy and some cases surgical approaches (50). Cancer is characterized as a complex disease with tumor heterogeneity between cancers and among individuals. In order to achieve more successful treatment and reduce side effects, chemotherapy has been conjugated with NP as delivery systems (51). However, limitations continue to persist, and tumor penetration is required. Therefore, new strategies and the addition of new moieties can enhance anti-tumor efficacy and promote tumor penetration.

3.1.2.1. CPPs and NPs in Cancer

The CPP/NP-cargo delivery can enable targeted treatment and eradication of tumors without affecting healthy tissues. Several studies have exploited this CPP/NP potential as delivery systems in cancer cell-lines and cancer animal models. One of the most challenging barriers to cross is the BBB, which is crucial for maintenance of brain homeostasis and protection against organisms and toxins and translocation of molecules is limited. The work of and his team demonstrated the potential of a 12-mer peptide that targets the brain—TGN. Conjugation of TGN and PEG-PGLA NP were able to deliver coumarin-6 as a probe into the brain at 3.6-fold times higher than NP alone (52). Using the same brain peptide sequence, Gao and his team analyzed the potential of TGN peptide and A5411 aptamer conjugated with PEG-poly(ε-caprolactone) (PEG-PCL) NP to deliver docetaxel in brain glioma bearing mice (53). Aptamers are short sequences of RNA or DNA that enables the complex to bind to a specific protein. In this work, aptamers A5411 was able to bind necleotin, which is highly expressed protein in plasma membrane

cancer promoting dual selectivity with TGN peptide. The authors demonstrated the success of the treatment, which was reflected in increased survival rates in treated mice and improvements in anti-tumor activity compared to saline and drug-free treated mice (53). Glioblastoma multiform is a primary central nervous system tumor and the second cause of death in patients less than 35 years old. The pathogenesis of the tumor is characterized by an increase diffusion rate, which makes it almost impossible to remove completely with surgery, and chemotherapy cannot reach the tumor at the desirable concentration (54). Therefore, Xin and his team studied the potential of CPP/NP conjugation to target CNS multiform glioblastoma tumors (55). In this work, the authors engineered a new multifunctional carrier with CPP Angiopep-2 and NPPEG-PCL loaded with placlitaxel. The CPP angiopep-2 targets BBB and glioma tumor cell because it binds to the low-density lipoprotein receptor-related protein that is highly expressed in human glioma cell and BBB. The authors demonstrated that the dual-targeting drug delivery system promoted inhibition and apoptosis against U87M6 glioma cells in a monolayer model and accumulated in the glioma site *in vivo* (55). Due to the target selectivity of Angiopep-2, this sequence was further used in other constructs involving glioblastoma targeted delivery. The work of Mei and his team demonstrated the potential of this Angiopep-2 combined with NP and the addition of an activable CPP (ACPP) in the construct (56). The ACPP takes advantage of target site microenvironment differences such as pH, redox potential, and up regulated protein to turn inactive molecules into active ones (57). The stimulus-sensitive drug delivery system is able to specifically target tumors. Mei's work used an ACPP with PLGGLAG sequence which is the subtract of metalloproteinase 2 (MMP2) that is over expressed in tumor cells. The authors demonstrated that dual functionalization further improves the tumor target efficiency *in vivo* (56). In another interesting publication, this construct was further investigated to deliver DTX as a drug model to evaluate glioma-targeting ability and treatment efficiency. The authors demonstrated through ex vivo imaging the target selectivity of the dual construct to the brain and into the tumor site after 24 h. In addition, the conjugate angiopep-2 and ACPP dual-modified NPs (AnACNPs) showed a high anti-tumor effect, reflected by higher survival rates in treated mice over the control (58). The dual-functionalization of NP was further tested in the work of Zhu and his team, which designed crosslinks of tandem nanomicelles with both Angiopep-2 and a TAT shield with PEG6000 for anti- glioma chemotherapy. *In vivo* results with the treatment with DTX/ANG20/TAT10-MS demonstrated inhibition of tumor growth and longest survival time of 53 days compared to 29 days for free DTX (59). Kadari and his team introduced Angiopep-2 into solid lipid nanoparticles (SLN) to deliver DTX (A-SLN) against U87MG human glioma (60). The A-SLN demonstrated strong inhibition of cell proliferation after

24 h of treatment compared to controls, a percentage of apoptosis of 45.9% and observed the presence of apoptotic bodies. *In vivo* studies demonstrated an increased rate survival of about 39 days and no side effects associated with A-SLN treatment (60); as chemotherapy causes severe side effects due to lack of selectivity. Another strategy proposes the utilization of other pharmaceutical alternatives, as siRNA, that are capable of silencing the expression of the defined gene, that in cancer, could be crucial to cellular growth. Kanazawa and his team developed a system for intranasal delivery of siRNA loaded in methoxy-PEG (MPEG)-PCL)-TAT micelles (61). The results demonstrated that this conjugation accelerated transport along olfactory and trigeminal nerves and enabled the delivery in the brain (61). Subsequently, the construct was loaded with camptothecin to target glioblastoma through intranasal delivery. The authors demonstrated that non-invasive routes by intranasal administration were more efficient for drug delivery than intravenous infusion. Nose- to-brain delivery resulted in reduction of tumor size and prolonged survival time for 28 days compared to 16.6 days in control mice (62). This CPP/NP conjugation as a delivery system, enhanced circulation time, BBB permeability, improved glioma targeting and selectivity and anti-tumor activity. The idea of CPP/NP conjugation was translated to other types and different cancers in order to achieve better treatment and development of new alternatives. For instance, breast cancer affects over 2 million women in 2018 and is considered the most frequent cause of death among women worldwide. The current major challenge in breast cancer treatment is the ability to predict therapeutic resistance and how to select the ideal drug for each individual (63,64). Therefore, Hossain and his team monitored time-dependent anticancer drug delivery kinetics through surface-enhanced Raman spectroscopy (SERS) (65). For this purpose, they constructed a biohybrid nanoparticle composed of gold NP, TAT and breast cancer antibody (anti-HER2) and analyzed the release rate of doxubicin (DOX). SERS map images showed higher signals from the biohybrid constructed in SK-BR-3 cell line (breast cancer) when compared to SH-SY5Y (neuroblastoma), and DOX intracellular release rate was more pronounced up to 12h after treatment (65). In another study, CPP TAT was conjugated with gold NP platform to carry DOX against brain metastatic breast cancer (66). The authors demonstrated that DOX was able to accumulate in intracranial brain metastasis *in vivo* and continuous treatment resulted in an increase life-span of 21.9% compared to PBS treatment (66). Furthermore, Farkhani and her team evaluated the effect of CPP RW incorporated in silver NP (AgNP) against MCF-7 cell-lines (67). The results demonstrated that AgNP were able to reduce growth of MCF-7 in a dose dependent manner. In addition, RW conjugation was essential for a 10-fold increase in anti-tumor activity (AgNP-RW cytotoxicity at 10.2 μg/mL and AgNP at 104.1 μg/mL) (67). This conjugation was further explored in skin cancer for topical

administration due to the potential of CPPs to permeate into skin layers and deliver the desire compounds (68). Patlolla and his team formulated skin permeation of CPPs coated NP into the skin and demonstrated that NP functionalized with TAT showed a 3-fold increase in skin penetration compared to NP alone to a depth of 120 μM (68). In other work by Asai and his team, siRNA molecules were incorporated into a CPP derived from protamine-decorated lipid NP (CPP-LNP-siRNA) against melanoma and fibrosarcoma cell-line (69). The authors observed that CPP incorporation led to a significant enhancement of the interaction with both cell-lines. In addition, through confocal microscopy the authors demonstrated the cytoplasmatic distribution of siRNAs inside the cells and efficient silencing of 70% with no toxicity associated (69).

In the area of hepatocarcinomas, some studies with CPP/NP conjugation have shown good results and nanocarriers have been widely developed in this field. Zhang's work validated the capacity of TAT incorporation into poly PLGA NP to efficiently delivery epirubicin against hepatic cancer and neuroblastoma cell-lines (70). The construct demonstrated a sustainable release of about 38.3% in 48 h and intravenous administration of 4 μg/mL resulted in inhibition of tumor growth after 15 days of treatment (70). Jin and his team further modified their CPP/NP/drug conjugated with the addition of a target moiety—HAb18F(ab specific antibody—that interacts with HAb186 over expressed in hepatocarcinoma tumors (71). The authors demonstrated PTX-loaded NP and polyarginine peptide conjugation was successful to target liver tumor cells and showed significant anticancer activity among all formulations tested. After 3 days of treatment, tumors growth was about 77.3% and mice presented a long life-span of 35.2 days compared to control (71). Using a different approach, Kapur and his team decided to test gold NP (AuNP) as a toxic compound and made AuNP selective with the conjugation of SVS-1 CPP specially designed as an anticancer peptide to facilitate efficiently delivery. Results demonstrated that SVS-1 incorporation promoted intracellular delivery of Au NP through direct translocation (72).

Other studies have proposed the utilization of this CPP/NP strategy in the area of lung cancer. Gao and his team used a RLW CPP anchored to PEG-PCL NP (RNP) to target and deliver DTX in a lung cancer cell model (A549) (73). The results of cellular uptake showed a 4.5-fold increase in apoptosis percentage in RNP complexes. In addition, the results of RNP-DTX treatment in A549 spheroid tumors resulted in enhanced core penetration when compared to periphery distribution by NP alone (73). Furthermore, Zhu and his team used an ACPP cleavable by MMP that is over expressed in many malignant tumors to enhance selectivity of the conjugate (74). The authors synthesized a self-

assembly drug-polymer prodrug consisting of: MMP2 cleavable peptide, TAT protected with PEG and loaded with PTX. Interestingly, nano preparations accumulated in tumor. sites and cleavable MMP2 peptide was broken, which allowed the exposure of TAT promoting cell internalization and drug release (74).

In a recent study, Carnevale and his team designed and tested CPP/NP conjugates against drug resistant cancer cell-lines. The first phase of this study demonstrated CPPs differences in cell selectivity attached to quantum dots in resistant cell lines versus naive (75). The authors observed that different CPPs exhibit selective uptake profiles for each cell-line. Although prominent uptake profiles were observed for the hCT (9–32), Ku-70 and HSV1-VP22 in resistant melanoma and rat glioblastoma cells (75).

3.2. Overview

In this Chapter 3 the presentation of the work was divided into 2 phases. Phase 1 is regarding MAP activity towards cancer cell lines (SH-SY5Y and MCF-7). Phase 2 is the preparation of optimized NLC with conjugates and evaluation of it's toxicity against two cancer cell lines (Caco-2 and SH-SY5Y)

3.3. Material and Methods

3.3.1. Materials

TAC (9-amino-1,2,3,4-tetrahydroacridine hydrochloride hydrate). TCP ((±)-trans-2-Phenylcyclopropylamine) and RAS (N-Propargyl-1(R)-aminoindan methanesulfonate) were acquired from Sigma Al-drich (St Louis, MO, USA). Diethylene glycol monoethyl ether (Transcutol® HP) and glyceryl dibehenate (Compritol® 888 ATO) were a kind gift from Gattefossé (France). T80 was purchased from J. Vaz Pereira S.A. (Portugal). From Sigma-Aldrich (St Louis, MO, USA) were purchased MTT, SRB and phosphate buffer solution (PBS - pH 7.4). Caprylic/capric triglycerides (Miglyol® 812) were a gift from Sasol Olefins & Surfactants GmbH (Hamburg, Germany). DMSO was adquired from Millipore-Sigma. Fluorescamine was purchased from Acros organics. For the viability studies, neuroblastoma cell line (SH-SY5Y, ATCC® CRL-2266TM) and colorectal adenocarcinoma cell line (Caco-2, ATCC® HTB-37™) were used. Cell culture medium and penicillin-streptomycin solution were acquired from Sigma-Aldrich and the rest of the cell culture supplies were acquired from Millipore Sigma.

3.3.2. Preparation of NLC

TCP-loaded, TCP+MAP loaded and TCP-MAP loaded NLC were prepared using a modification of a hot HSH method previously described in (76,77). Briefly, 300 mg of Compritol® 888 ATO were melted at a temperature 10 °C above its melting point (80 °C). TCP, TAC, RAS, Drug MAP conjugates and Lys-(N_3)-MAP were dissolved in the liquid lipid Transcutol® HP (at theoretical concentrations of 25% w/w), which was added to the molten Compritol® 888 ATO. A hot aqueous phase consisting of 10 mL ultra-purified water with 3% of T80 was added to the lipid phase under high-shear homogenization at 12,300 rpm for 10 min on a Silverson SL2 (UK), in a water bath to maintain the temperature. The NLC dispersion was then cool in an ice bath with gentle stirring for 5 min. Each formulation was carried out in triplicates (n=3). The final dispersion was sealed and stored at 4 °C until further use.

3.3.3. Characterization of NLC

3.3.3.1. Particle size and surface charge

Particle size distribution was analyzed by photon correlation spectroscopy using Zetasizer Nano S (Malvern Instruments, UK). Samples were placed in polystyrene cuvettes, and their size was measured at a 173° scattering angle at 25.0 ± 0.1 °C. All the results were expressed as average particle size and PI. Through nanoparticle electrophoretic mobility (previously diluted with filtered purified water) ZP was calculated using a Zetasizer Nano Z (Malvern Instruments, UK). For all measurements, at least three replicates' samples were determined.

3.3.3.2. Encapsulation efficiency

EE and DL for all the NLC formulations prepared were determined using one indirect and two direct methods. First, the free drug, i.e. unassociated to the NLC, was separated from the particles using centrifugation (Amicon ultra centrifugal filter units; ultra-15, MWCO 100 Kda, Sigma-Aldrich). Briefly, 1 mL of the sample was kept in the upper chamber compartment of the ultra-centrifuge tube and centrifugated at 12,000 rpm for 15 min. The collected sample in the lower chamber was and was quantified using high-pressure liquid chromatography (HPLC). The second, unencapsulated with drug and peptide was separated from the NLC by size exclusion chromatography using Sephadex G-25/ PD-10 columns. Encapsulated drug and peptide to NLC was calculated after

dissolving the NLC with acetonitrile (1:1) followed by a centrifugation (30 min at 12,300 rpm) step (Hettich Universal 320R, Germany), promoting the lipid phase precipitation. After centrifugation, the encapsulated compounds remained in the supernatant, and the drugs were first attempt to be measured by UV–visible spectrophotometry, at l_{max} of 320nm, in a microplate spectrophotometer reader (FLUOstar Omega, BMGLabtech, Germany) and the supernatant of non-loaded NLC was used as basic correction (see detail information in section 3 in the Supplementary information regarding this experiment). After those results HPLC method was used, and the peptide conjugates were measured by a fluorometric assay. Briefly, 50 µL of fluorescamine (3 mg/mL) were added to 150 µL solution with 50 µL of aliquot supernatant and 100 µL of PBS at pH 10 in a black 96-well plate. The fluorescent intensity was measured using a fluorescent plate reader equipped with a 390 nm excitation filter and a 475 nm absorption filter. The concentration of the samples was calculated through each peptide calibration curve. In addition, entrapment efficiency and drug loading were determined using the following equations:

$$Encapsulation\ efficiency\ (\%\ w/w) = \frac{(w1 - w2)}{w1} \times\ 100$$

$$Drug\ loading\ (\%\ w/w) = \frac{w1 - w2}{w3} \times 100$$

where w1 is the amount of drug added in the NLCs, w2 is the amount of free drug and w3 is the amount of lipid.

3.3.4. *In vitro* cell viability studies

The cytotoxicity of all NLC formulations against SH-SY5Y and Caco-2 cell lines were assessed by MTT, SRB and microscope visualization.

3.3.4.1. MTT assay

The MTT assay was conducted for viability assay evaluation. Cells were maintained in culture DMEM supplemented with 10% of heat-inactivated FBS and 1% penicillin and

streptomycin at 37 °C in a controlled atmosphere of 5% CO2, according to the ATCC recommendations. Before the experiment, SH-SY5Y cells and Caco-2 cell line were seeded in sterile flat bottom 96-well plate at the density of 18,000 cells per well and 6,000 cells per well, respectively, and incubated for 24 h. In the next day, the medium was replaced with increasing concentrations of free TAC, free RAS, free TCP, free TAC-MAP, free RAS-MAP, free TCP-MAP and drug and peptide loaded NLCs. Then the cells were incubated for 24 h and both negative and positive controls were included with incubation with culture media and sterilized water (5:1) and DMSO 10% to promote the cell lyses, respectively. After incubation, all media was aspirated and replaced with 100 µL of MTT solution (at 0.5 mg/mL). The cells were further incubated for 3 h in the dark. After this, the medium was aspirated and 100 µL DMSO was added to dissolve the formazan crystals and the absorbance was measured at 570 nm in a microplate reader (Synergy HT, Biotech Instruments inc., USA and Tecan Infinite M200, Tecan group Ltd, Switzerland). All experiments were performed in triplicates and the relative cell viability (%) was compared to control cells and calculated using the following equation:

$$Cell\ viability\ (\%\ of\ sample) = \frac{Abs\ sample}{Abs\ control} \times 100$$

3.3.4.2. SRB assay

Cell viability assay of all formulations was also determined by SRB assay. For this, the same conditions and methods described above for MTT assay were used. After cells were treated with all NLC formulations and respective controls, the cells were fixed with 100 µL of ice-cold 10% TCA per well for 1 h at 4 °C. Then TCA was aspirated and allowed to dry before adding 100 µL of 0.4% SRB solution. After 1 h the plates were washed with running tap water and air-dried. The incorporated dye was solubilized by the addition of 200 µL of 10 mM tris buffer per well. The absorbance was measured at 510 nm in a microplate reader (Synergy HT, Biotech Instruments inc., USA and Tecan Infinite M200, Tecan group Ltd, Switzerland). All experiments were performed in triplicates.

3.3.4.3. Cell morphology visualization

After the treatments, cell morphology and growth were assessed by contrast phase microscope Lionheart FX (Biotech, USA) with use of Gen5 software (Biotech, USA) and Leica DMI 6000B microscope equipped with a Leica DFC350 FX camera and then analyzed with the Leica LAS X imaging software (v3.7.4).

3.3.5. Analysis of Drug Interactions

To quantify the interaction of TAC and MAP in the conjugate, the dose-effect curves were estimated by the unified theory, introduced by Chou and Talalay (78) using CompuSyn software (ComboSyn, Inc., New York, NY, USA). The dose was plotted on the y-axis as a function of effect level (Fa) on the x-axis to assess the drugs' behavior. Experiments were conducted in triplicate (n = 3) with three replications.

3.3.6. Statistical analysis

Statistical analysis of the experimental data was performed using a one-way analysis of variance (one-way ANOVA) and differences between groups were tested by a two-way ANOVA with GraphPad Prism version 9.0 (GraphPad Software, San Diego, CA). Data were expressed as mean ±SD or 95% confidence interval. A $p < 0.05$ value was considered significant.

3.4. Results

PHASE 1

3.4.1. Toxicity of TAC and Its MAP Conjugate to MCF-7 and SH-SY5Y Cells

The toxicity of TAC and TAC-MAP towards MCF-7 (breast cancer) and SH-SY5Y (neuroblastoma) cells was tested at four different concentrations (1, 2.5, 5, and 10 μM), using the MTT reduction assay after a 24 h-incubation period. Results show no significant differences in MTT reduction by TAC alone, when compared to control, for both cell lines (Figure 3.7). On the other hand, the TAC-MAP conjugate caused a significant mitochondrial dysfunction for the three higher concentrations, as reflected by the decrease in the ability to metabolize MTT both by MCF-7 (2.5, 5 and 10 μM (73.1 ± 4.4), (46.6 ± 2.4) and (37.7 ± 4.5)% of control cells, respectively) and, more

pronouncedly, SH-SY5Y (2.5, 5 and 10 μM (42.4 ± 5.2), (15.5 ± 3.4) and (8.7 ± 4.4)% of control cells, respectively) cells (Figure 3.7).

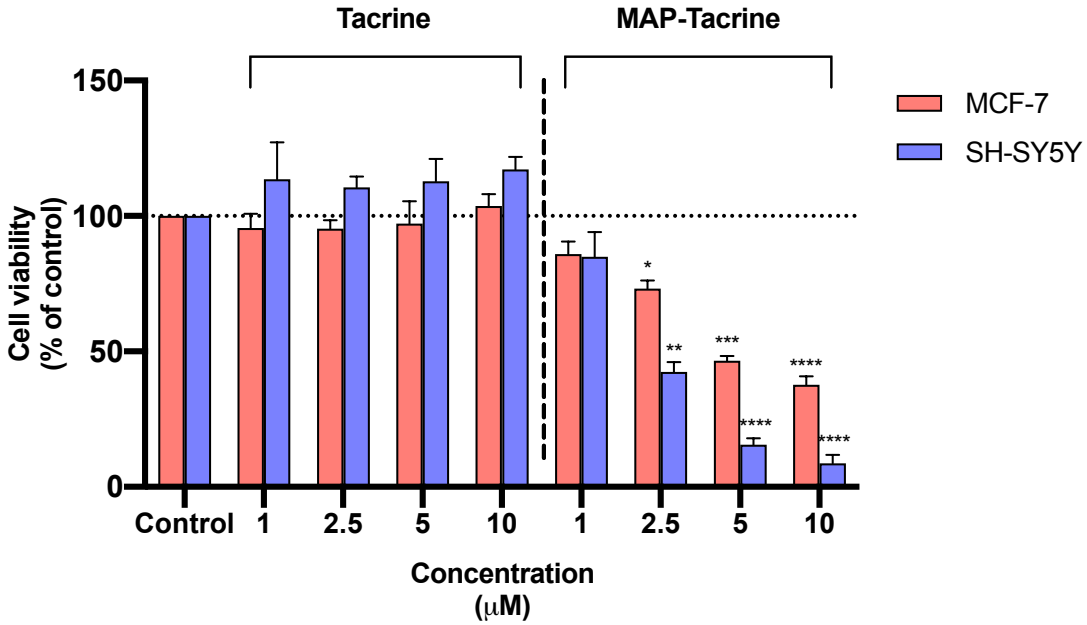


Figure 3.7 - MCF-7 breast cancer and SH-SY5Y cell line cytotoxic effects of increasing concentrations of TAC, and TAC-MAP after a 24 h incubation. H_2O was used in control. Significant differences (ANOVA test, followed by the with Dunnett's post hoc test): * $p < 0.05$, ** $p < 0.01$, *** $p < 0.001$ and **** $p < 0.0001$ vs. Control. The values represent mean ± SEM (n = 3).

A cell count analysis was also conducted and corroborated data from MTT assays for both cell lines. Hence, it was confirmed that, while Tacrine did not affect the number of cells in culture up to 10 μM, the TAC-MAP conjugate significantly decreased cell count (Figure 3.8), thus displaying strong toxicity to both types of cancer cells.

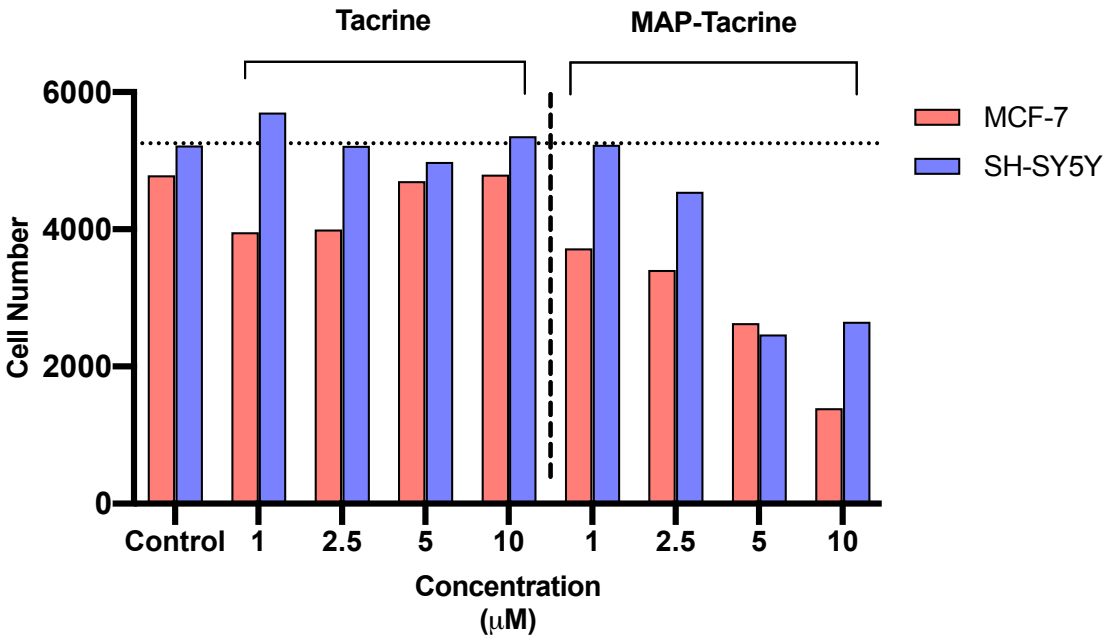


Figure 3.8 - Cell count through Lionheart FX treatment of MCF-7 and SH-SY5Y cell lines with TAC and TAC-MAP (1, 2.5, 5, and 10 μM) after 24h incubation (*n* = 1). 2.5. Determination of IC_{50} and cell count analysis of TAC, MAP, and TAC-MAP against MCF-7.

3.4.2. Determination of IC_{50} and Cell Count Analysis of TAC, MAP, and TAC-MAP against MCF-7.

The effect of coupling MAP to TAC on the intrinsic cytotoxic activity of the parent peptide was also assessed on MCF-7 cells. Dose-response curves are depicted in Figure 3.9 and show similar IC_{50} values of 2.721 μM and 2.732 μM for both MAP and TAC-MAP, respectively. Moreover, cell count analysis after treatment with increasing concentrations of TAC, MAP, and TAC-MAP, show that while TAC has no significant effects, both MAP and its conjugate cause a severe drop in cell count at 20 and 25 μM (Figure 3.10).

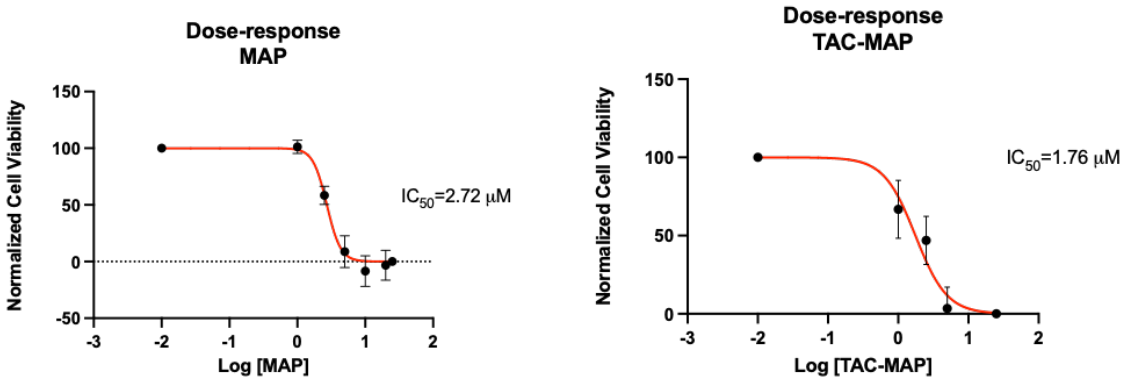


Figure 3.9 - Dose-response curves (from triplicates) of MCF-7 cells viability with increasing concentrations of MAP (left plot) and TAC-MAP (right plot). IC_{50} values thus determined are shown next to the respective curves. The values represent mean ± SD (n = 3).

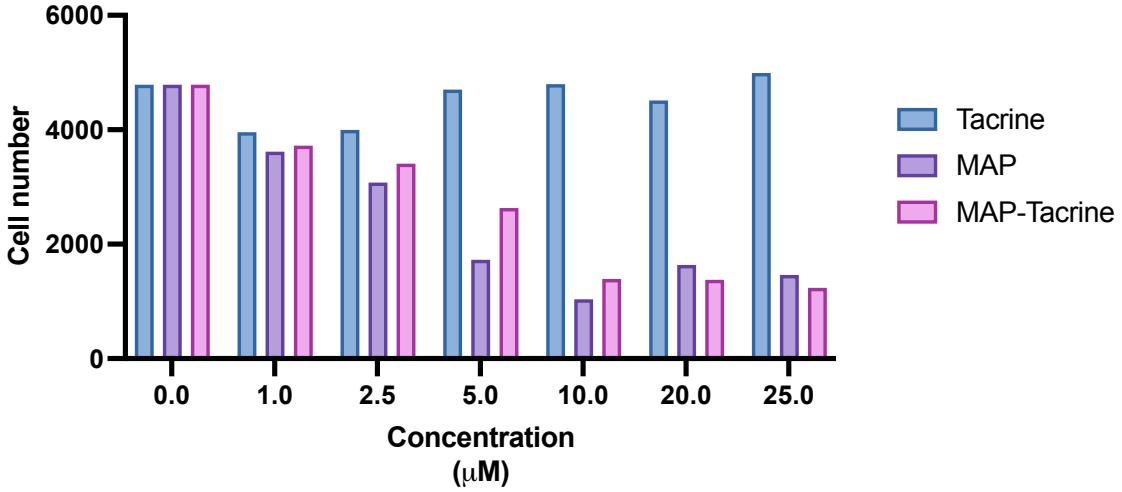


Figure 3.10 - Cell count through Lionheart FX treatment of MCF-7 lines with TAC, MAP, and TAC-MAP (1-25 μM) after 24 h incubation (n = 1).

3.4.3. Morphological Changes Caused by TAC, MAP, and TAC-MAP on MCF-7 Cells

Morphological changes in MCF-7 cells after 24 h incubation with TAC, MAP, TAC-MAP at different concentrations were evaluated by Lionheart FX (Figure 3.11). No significant differences in cell morphology were observed between the control and TAC at all concentrations tested, as expected. In turn, MAP was confirmed to exert toxic effects on

the cells, as significant differences are observed when comparing the effects of the peptide at 5, 10, 20, and 25 μM to control, including an increase of cells in suspension, loss of morphological features and cell death. Even at 2.5 μM, a slight increase of cells in suspension is already observed when compared to control. In the case of the TAC-MAP conjugate, cell damage observed was similar to that caused by MAP alone, with substantial morphological changes and an increased level of cell death at higher concentrations (Figure 3.11).

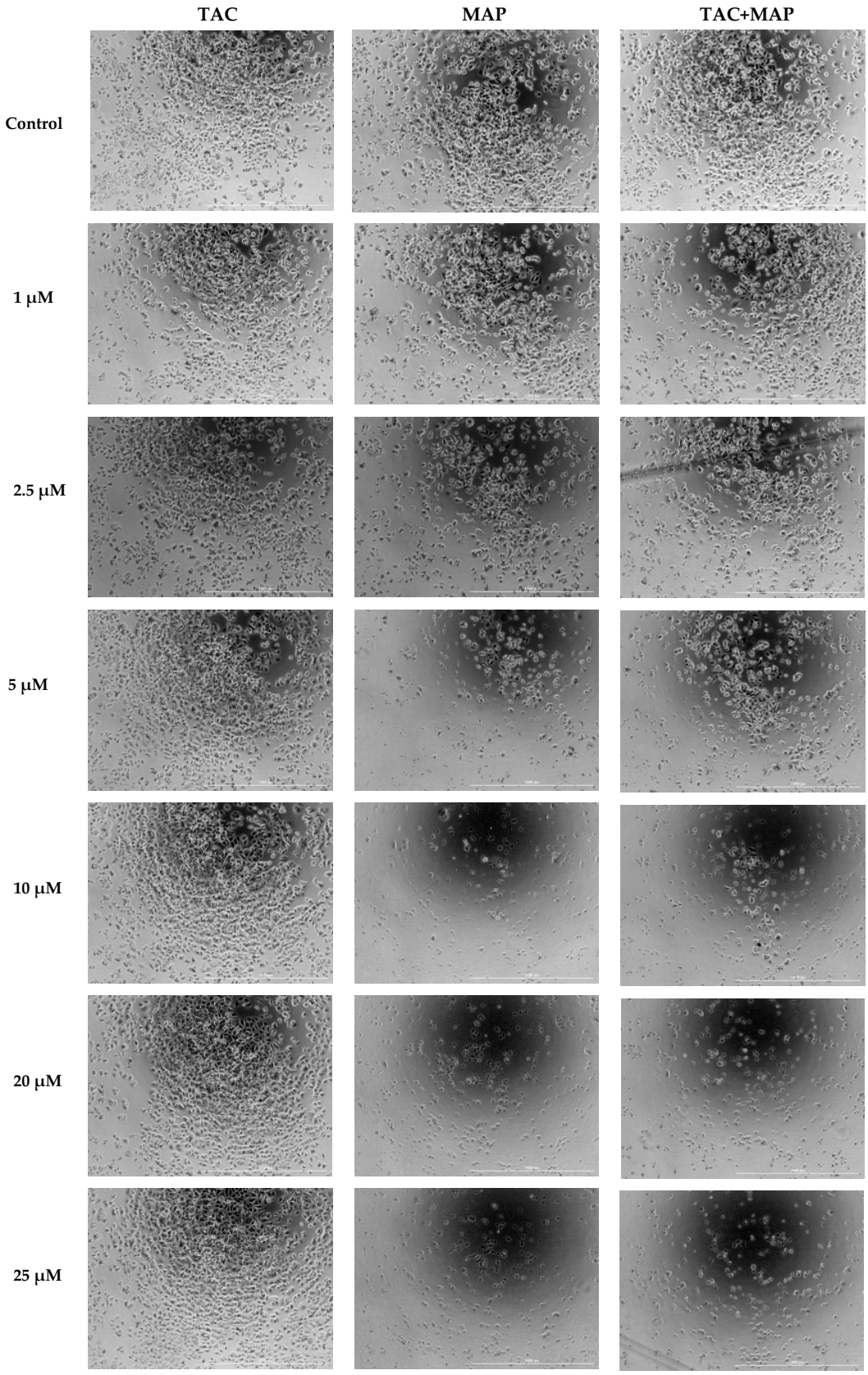


Figure 3.11 - Micrographs (Lionheart FX of phase-contrast images) obtained for MCF-7 cells after a 24 h period of incubation with TAC, MAP, and TAC-MAP conjugate at different concentrations.

3.4.4. Drug Interactions between TAC and MAP in the Conjugate

In Figure 3.12, we can observe the impact of synergism and antagonism in the MAP combination with TAC. Using our data, it is possible to confirm that we have a synergistic effect in decreasing cell viability for lower doses of drug and peptide and, an additive effect for higher doses. The fact that we observe synergism only in smaller concentrations, allows us to think that any secondary effects associated with peptides can be minimized in conjugates such as the one we report. In addition, the effect of MAP and TAC can be considered super-additive and demonstrate action that is above what is expected from their individual potencies and efficacies at a lower concentration

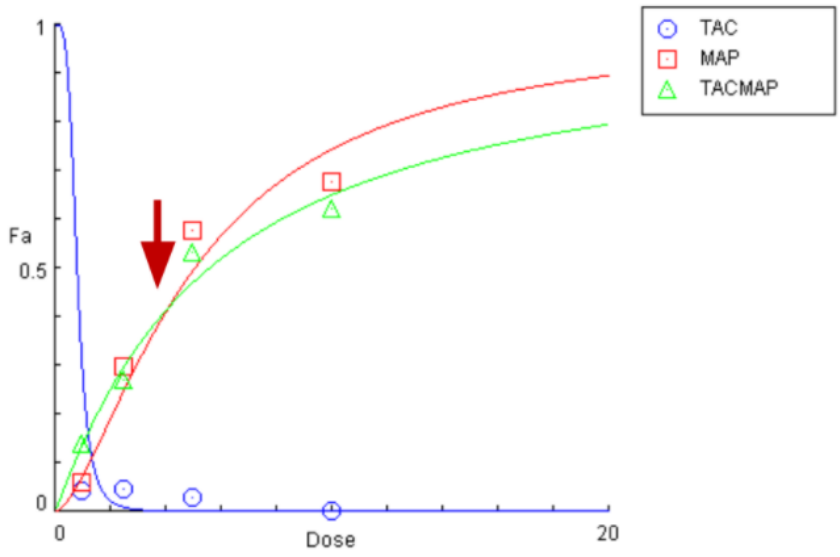


Figure 3.12 - Dose-effect curves of TAC, MAP, and TAC-MAP estimated by the unified theory using CompuSyn software. The dose was plotted on the y-axis as a function of effect level (Fa) on the x-axis to assess each drug behavior. Doses below the red arrow indicate better activity of TAC-MAP conjugate than MAP and TAC alone. Experiments were conducted in triplicate (n = 3).

3.4.5. Discussion

The development of novel drugs for cancer therapy can be challenging, time-consuming, and expensive. As such, in order to overcome these hurdles, the combination and repurposing of drugs have been gaining prominence recently. Both strategies allow reducing overall costs and offer a fast-testing track for new therapeutic indications other than the original ones. In view of this and based on the previously reported anticancer

potential of TAC, we explored how such potential might be enhanced by coupling this neuroactive drug to a CPP. To this end, we successfully synthesized both the selected CPP, MAP, and its TAC conjugate, formed via the well-known CuAAC click reaction. Both the conjugate and its parent building blocks were characterized by a toolbox of *in vitro* techniques, which allowed us to conclude that despite the conjugate no longer retaining the ability of the parent drug to cross the BBB or inhibit AChE, it displays significant cytotoxic action against two cancer cell lines, namely breast (MCF-7) and neuroblastoma (SH-SY5Y) cells. This cytotoxic action was coherently observed in different types of assays, including the assessment of cell counts and morphological changes. Relevantly, this same cytotoxic effect was observed for the MAP peptide alone, which, on the one hand, puts into question if TAC is important for the effects observed, and on the other, highlights a cell destructive rather than a cell-penetrating role for the peptide. This highlights the potential use of MAP not as a classic CPP, but more as an antimicrobial peptide (AMP), able to destroy cell membranes even at low concentration levels, leading to fast cell death. Indeed, the behavior observed for both MAP and its TAC conjugate in this work closely resemble those reported in previous works focused on AMP, including examples where these AMP were found to exert selective membrane toxicity against malignant cells (79–83). The observation of alterations on membrane integrity caused by MAP or its TAC conjugate has no precedent in the literature but, interestingly, comes into agreement with very recent reports highlighting the lytic character of CPP-drug conjugates comprising heterocyclic drug moieties (83,84).

PHASE 2

3.4.6. NLC formulation and characterization

The composition of each prepared NLC is described in Table 3.1. Physicochemical properties of the prepared NLC were analyzed and the overall results are also expressed in Table 3.1. The analysis of all NLC prepared formulations showed particle size distributions below 160 nm and a PI below 0.3. The ZP analysis demonstrated that all NLC had negative values of -4.13 to -0.38 mV. The EE determined for NLC-loaded with TAC, RAS and TCP was 35.49%, 63.10% and 26.02%, respectively. The DL for CT25TAC was 1.57%, CT2RAS was 0.33% and CT25TCP was 1.57% (Table 3.1). The data obtained for the peptide encapsulation demonstrated an EE of 12.58%, 18.21%, 14.21% and 58.34% for CT25 Lys(N_3)-MAP, CT25TAC-MAP, CT25TCP-MAP and CT25RAS-MAP, respectively. Furthermore, co-encapsulation of CNS drug and peptide

Lys(N_3)-MAP demonstrated a peptide EE of 2.70% for CT25TAC + Lys(N_3)-MAP, 18.70% for CT25TCP + Lys(N_3)-MAP and 35.38% for CT25 RAS + Lys(N_3)-MAP (see table 3.1). For instance, we observed a DL increase with the encapsulation of peptides and peptide-drug conjugates.

Table 3.1 - Physicochemical properties of all NLCs formulated freshly (mean SD, n = 4 or 6).

NLC	NLC composition	PS (nm)	PI	ZP (mV)	EE %	DL %
CT25 B	Lipids: 75 % C and 25 % TE Surfactant: 3 % T80	122.0 ± 31.5	0.305 ± 0.07	-4.1 ± 3.6	n.d.	n.d.
CT25 Lys(N_3)-MAP	Lipids: 75 % C and 25 % TE Surfactant: 3 % T80	112.1 ± 9.5	0.277 ± 0.09	-2.0 ± 0.1	12.6 ± 59.3	2.0 ± 7.1
CT25TAC	Lipids: 75 % C and 25 % TE Surfactant: 3 % T80	117.2 ± 55.0	0.290 ± 0.06	-4.4 ± 5.3	35.5 ± 22.6	1.6 ± 0.3
CT25TAC-MAP	Lipids: 75 % C and 25 % TE Surfactant: 3 % T80	98.0 ± 11.6	0.251 ± 0.03	-4.3 ± 3.9	18.2 ± 2.3	3.7 ± 0.9
CT25 TAC+ Lys(N_3)-MAP	Lipids: 75 % C and 25 % TE Surfactant: 3 % T80	122.0 ± 1.1	0.236 ± 0.02	-1.0 ± 0.3	2.7 ± 50.9	2.0 ± 10.1
CT25 TCP	Lipids: 75 % C and 25 % TE Surfactant: 3 % T80	164.1 ± 43.0	0.362 ± 0.05	-3.5 ± 5.6	26.0 ± 8.0	1.6 ± 0.7
CT25 TCP-MAP	Lipids: 75 % C and 25 % TE Surfactant: 3 % T80	92.1 ± 3.2	0.272 ± 0.03	-1.7 ± 0.4	14.2 ± 1.4	1.7 ± 0.2
CT25TCP + Lys(N_3)-MAP	Lipids: 75 % C and 25 % TE Surfactant: 3 % T80	128.3 ± 6.5	0.247 ± 0	-0.4 ± 0.1	18.7 ± 0.0	1.9 ± 0.7
CT25 RAS	Lipids: 75 % C and 25 % TE Surfactant: 3 % T80	114.8 ± 0.0	0.274 ± 0.04	-3.6 ± 3.6	63.1 ± 26.0	0.3 ± 0.3

CT25 RAS-MAP	Lipids: 75 % C and 25 % TE Surfactant: 3 % T80	129.0 ± 3.1	0.281 ± 0.03	-1.1 ± 0.1	58.3 ± 39.2	5.2 ± 1.4
CT25 RAS Lys(N_3)-MAP	Lipids: 75 % C and 25 % TE Surfactant: 3 % T80	88.0 ± 5.3	0.233 ± 0	-2.0 ± 0.3	35.4 ± 29.8	3.8 ± 2.8

PS: Mean particle size; PI: polydispersity index; ZP: Zeta Potential; EE: encapsulation efficiency; DL: drug loading; C: Compritol® ATO 888; TE: Transcutol® HP; T80: polisorbato 80; B: Blank.

3.4.7. *In vitro* cytotoxicity assays against Caco-2 cell line

3.4.7.1. Toxicity of MAP, Lys(N_3)-MAP and drug-MAP conjugate

The MTT assay conducted on Caco-2 cells with the treatment of MAP and TAC-MAP demonstrated a significant decrease of cell viability for 20 % at 10 µM. On the other hand, Lys(N_3)-MAP, TCP-MAP and RAS-MAP demonstrated more toxicity reflected on the decrease of cell viability of 70%, 40% and 60 % at 5 µM, respectively (Figure 3.13). The SRB results corroborate with MTT analysis even not reflecting the same values of toxicity (Supplementary Figure S3.5). The IC_{50} values determine demonstrated very close IC_{50} for free MAP and Lys(N_3)-MAP of 5.56 µM and 5.11 µM, respectively (Figure 3.14).

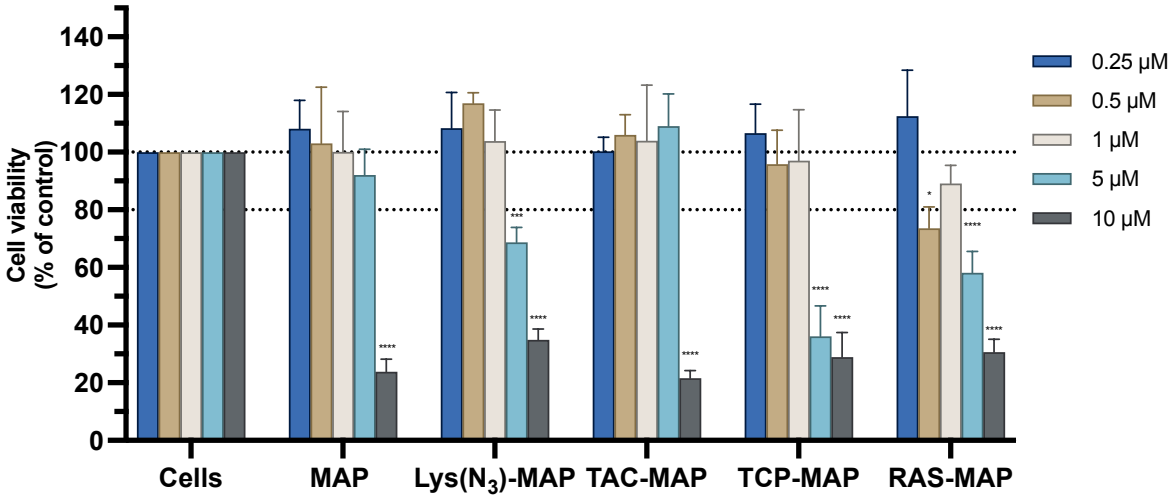


Figure 3.13 - Relative cell viability of Caco-2 cell line measured by the MTT reduction after 24 h incubation. Treatment with free MAP, Lys(N_3)-MAP, TAC-MAP, TCP-MAP and RAS-MAP (0.25 µM-10 µM). Results are expressed as mean ±SD (n = 3 or 6). Statistical analysis between the control groups was performed using two-way ANOVA with Tukey's multiple comparisons test (* p <0.05; *** p <0.001; **** p <0.0001).

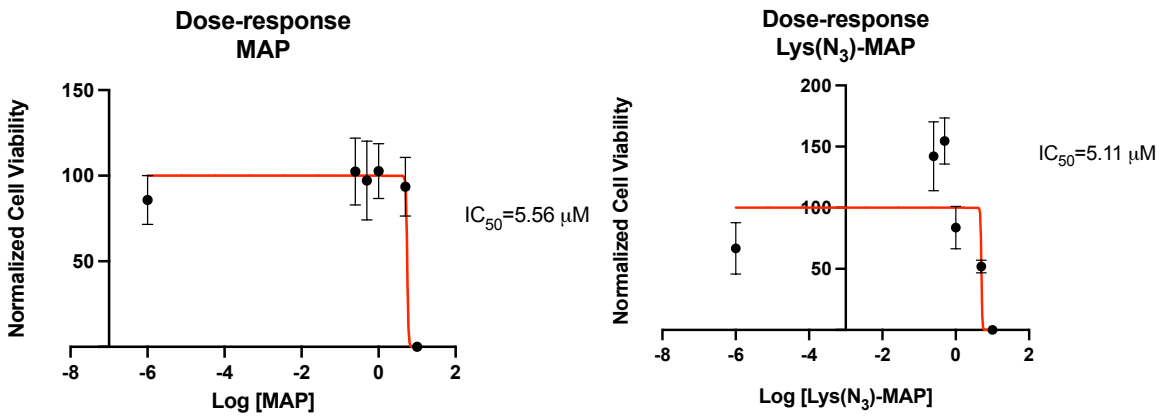


Figure 3.14 - The effect of MAP and Lys(N_3)-MAP on Caco-2 cell line dose-response curve. Each point is the average of at least three independent experiments.

The morphology of the Caco-2 cell line was evaluated after 24 h incubation with all formulations (Figure 3.15). The analysis conducted through microscope visualization was able to demonstrate and corroborate the results obtain from MTT and SRB assays. Treatment with MAP at 10 μM and Lys(N_3)-MAP at 5 μM and 10 μM showed a decrease of cell viability and substantial morphologic changes, supporting *in vitro* cytotoxicity data. On the other hand, the conjugates demonstrated higher toxicity at 10 μM with decreased cell viability and a decrease of normal cellular Caco-2 growth in clusters (Figure 3.15).

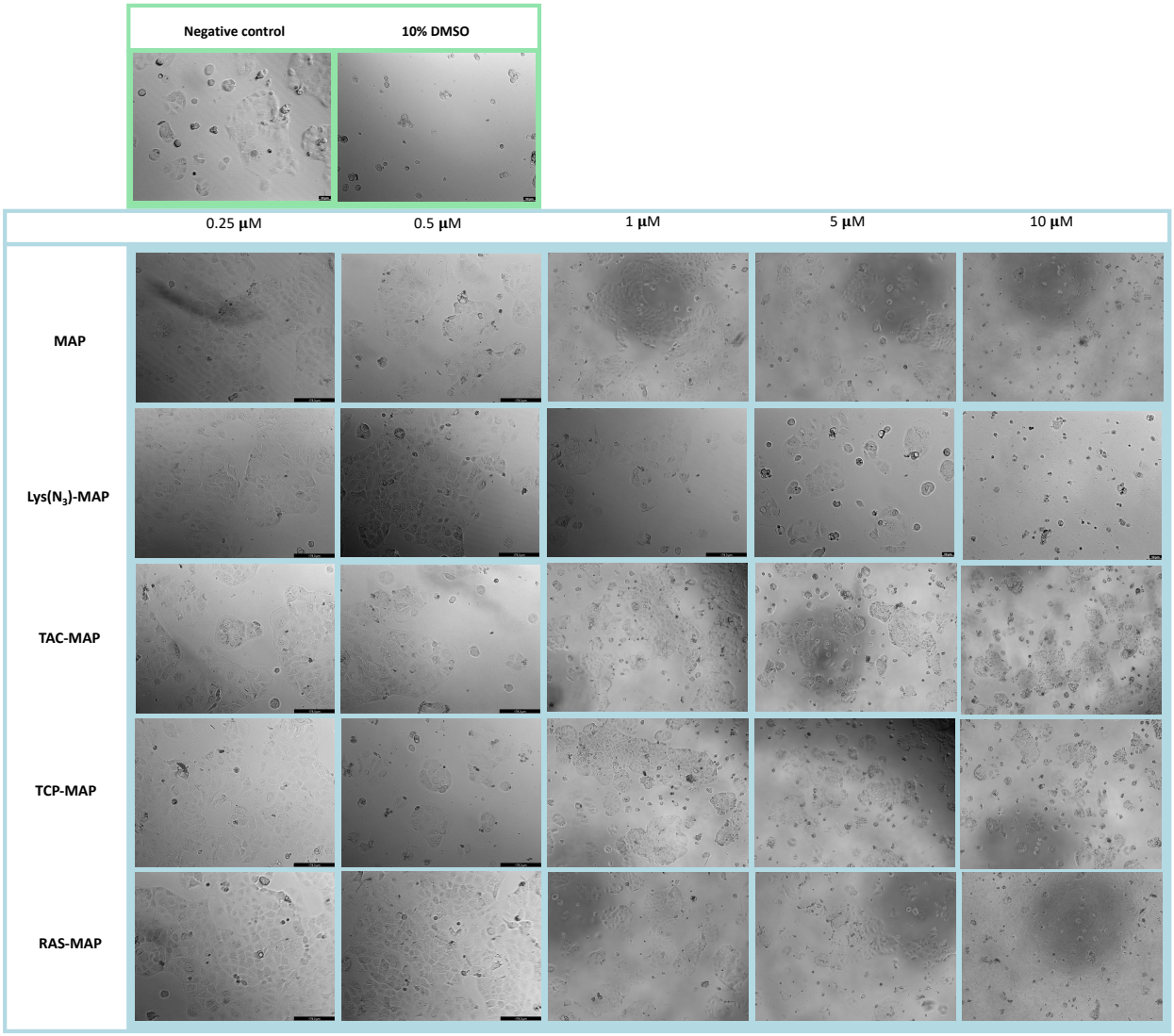


Figure 3.15 - Microscope cellular visualization through Lionheart FX and Leica DFC350 FX of treatment with negative control (ultra-purified H_2O), positive control (10% DMSO), free peptides and conjugates on Caco-2 cell line at a concentration of 0.25, 0.5, 1, 5 and 10 µM.

3.4.7.2. Toxicity of NLC loaded with TCP, Lys(N_3)-MAP and TCP-MAP

The data from the MTT assay in Figure 3.16A demonstrates that CT25B and CT25TCP treatment resulted in a decrease of around 20% on cell viability on all concentrations tested. In Figure 3.16B the data demonstrated a significant cell viability decrease of 50 to 80% on NLC loaded TCP-MAP when compared to free TCP-MAP upon administration in the Caco-2 cell line. In addition, co-administration of TCP or TCP-MAP with CT25 Blank NLC did not contribute to enhance of cell toxicity when compared with loaded formulations (Figure 3.16). In Figure 3.16 D, we conducted an assay to address co-encapsulation toxicity and the results demonstrated that TCP-MAP promotes significantly more toxicity on the Caco-2 cell line compared to the two compounds TCP and Lys(N_3)-MAP co-encapsulated on lower concentrations of 0.5 µM and 1 µM and cell viability decreased to around 30% for CT25 TCP-MAP and 50% for CT25 TCP+ Lys(N_3)-MAP. On the supplementary information, the SRB results corroborate with MTT analysis (Figure S3.6).

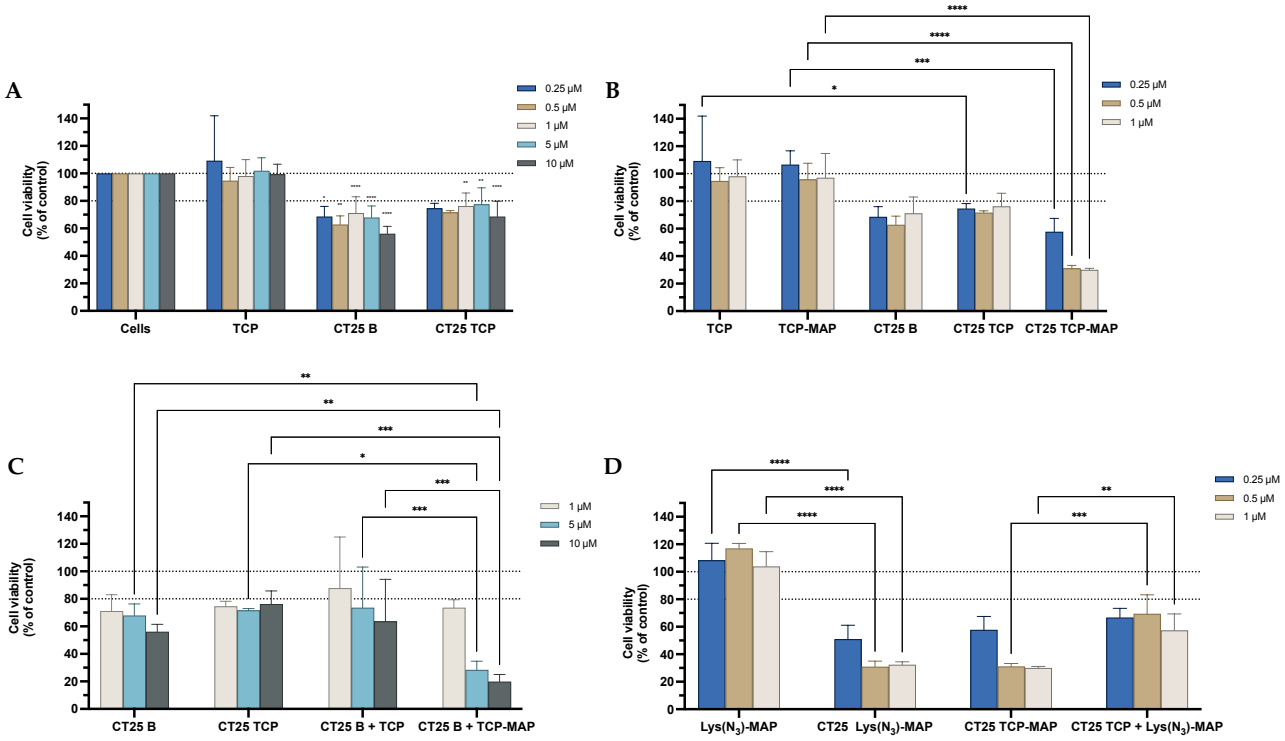


Figure 3.16 - Relative cell viability of Caco-2 cell line measured by the MTT reduction after 24h incubation. (A) represents NLC safety test with the treatment of free TCP, blank CT25 and TCP loaded CT25 (0.25-10 µM). (B) Represents differences in the cell viability of treatment with free TCP, TCP-MAP, blank CT25, TCP loaded CT25, MAP, TCP-MAP loaded CT25 (0.25-10 µM). (C)

Represents co-administration of TCP and TCP-MAP with blank CT25 (1-10 μM). (D) Represents the data obtained from the encapsulation of Lys(N_3)-MAP and co-encapsulation of TCP and Lys(N_3)-MAP in the NLC compared to peptide conjugate. Results are expressed as mean ±SD (n = 4). Statistical analysis between the groups was performed using two-way ANOVA with Tukey's multiple comparisons test (* p <0.05; ** p <0.01; *** p <0.001; **** p <0.0001).

Dose response analysis demonstrated a decrease on IC_{50} value of 0.23 μM for CT25TCP-MAP when compared to IC_{50} of 2.70 μM of free TCP (Figure 3.17). On the other hand, treatment with Lys(N_3)-MAP or CT25 TCP Lys(N_3)-MAP resulted on IC_{50} values of 0.23 μM and 0.18 μM (Figure 3.17).

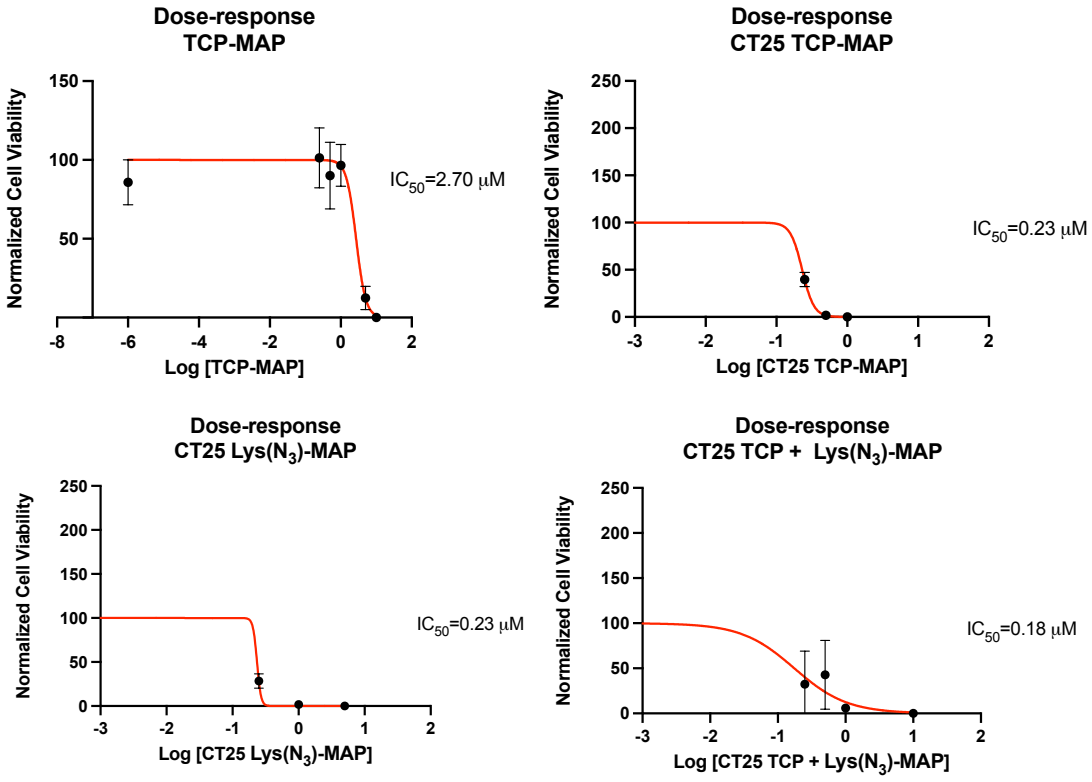


Figure 3.17 - The effect of TCP-MAP, CT25TCP-MAP, CT25 Lys(N_3)-MAP and CT25 TCP + Lys(N_3)-MAP on Caco-2 cell line dose-response curve. Each point is the average of at least three independent experiments.

Microscope visualization showed that treatment with CT25TCP did not result in a decrease of cell viability, neither morphological change in Caco-2 cells when compared to the free TCP (Figure 3.18). Co-administration of TCP and TCP-MAP with CT25 blank microscope images showed corroboration with MTT assay (Figure S3.9). On the other

hand, similar to the MTT data, CT25TCP-MAP treatment resulted in a decrease of cell viability and severe morphological changes represented in Figure 3.18 at all concentrations tested, at only 0.25 µM we observed cytoplasmatic granulation inside the Caco-2. Once again, co-encapsulation of the TCP and Lys(N_3)-MAP showed a decrease of cell viability but no morphological changes at 1 µM concentration.

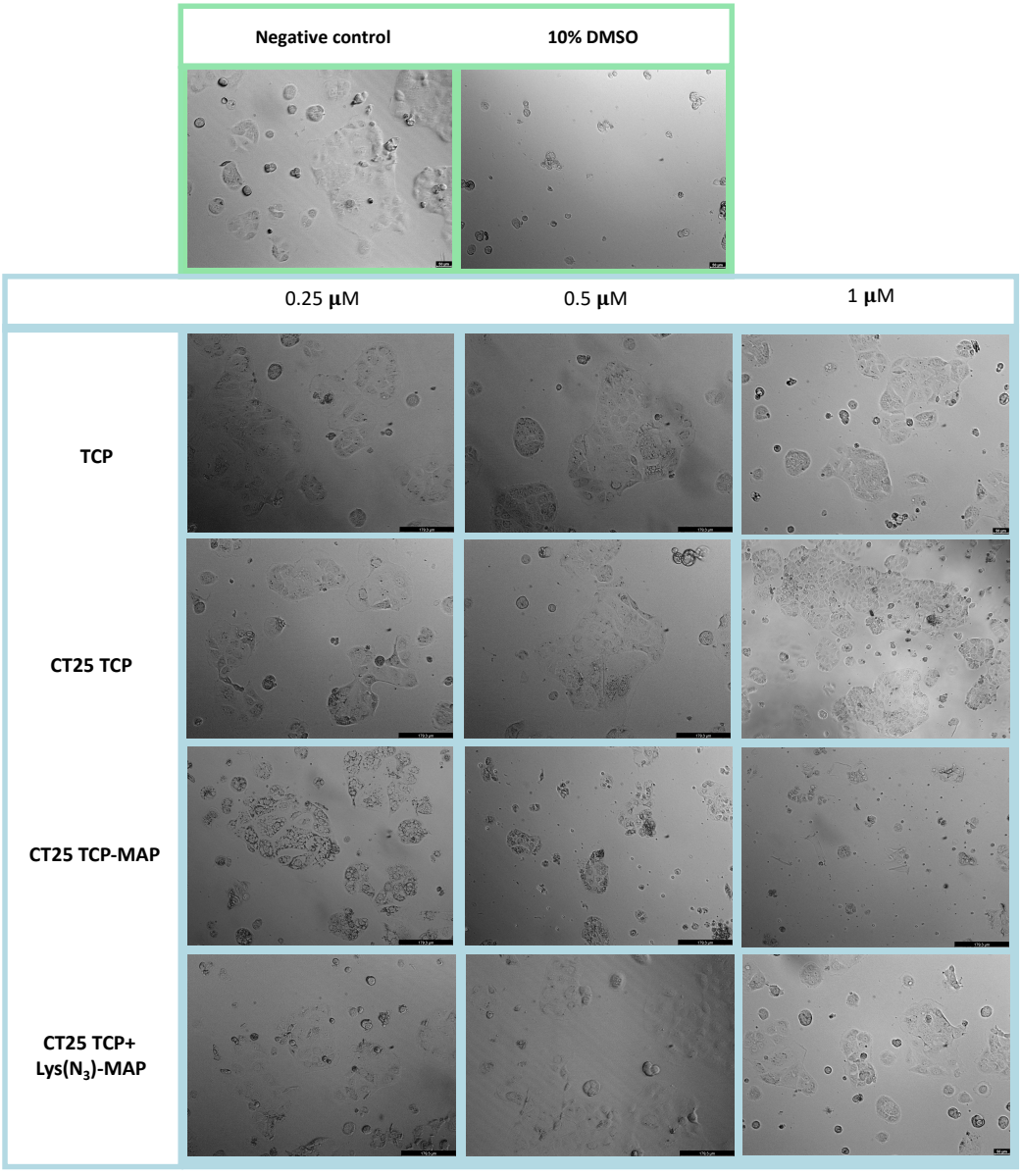


Figure 3.18 - Microscope cellular visualization through Leica DFC350 FX of treatment with negative control (ultra-purified H_2O), positive control (10% DMSO), free drug and NLC loaded formulations on Caco-2 cell line at a concentration of 0.25, 0.5 and 1 µM.

3.4.7.3. Toxicity of NLC loaded with RAS, Lys(N_3)-MAP and RAS-MAP

The results obtain from the MTT assay showed in Figure 3.19A that CT25B and CT25RAS treatment resulted in a decrease of around 20% on cell viability on all concentrations tested. The cell viability showed a significant decrease to 30% on NLC loaded RAS-MAP when compared to free RAS-MAP at the concentration of 1 μM (Figure 3.19 B). Furthermore, co-administration of RAS or RAS-MAP with CT25 Blank NLC did not contribute to a significant enhancement of cell toxicity when compared with loaded formulations (Figure 3.19 C). The co-encapsulation of RAS and Lys(N_3)-MAP in the NLC showed that RAS-MAP promote significant more toxicity on the Caco-2 cell line when compared to the two compounds RAS and Lys(N_3)-MAP co-encapsulated at all concentrations study. Cell viability decreased to around 60%, 50% and 30% on CT25 RAS-MAP and 80%, 78% and 65% for CT25 RAS + Lys(N_3)-MAP at 0.25 μM, 0.5 μM and 1 μM, respectively (Figure 3.19 D). On the supplementary material, the SRB results corroborate with MTT analysis (Figure S3.7).

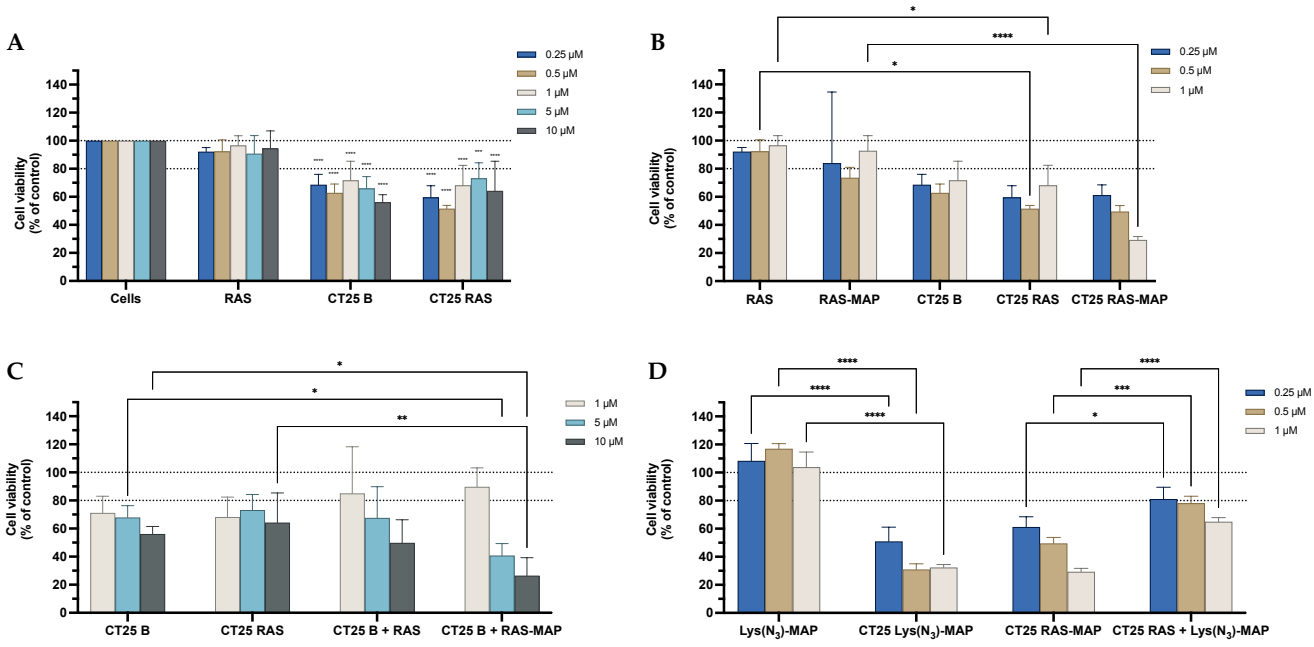


Figure 3.19 - Relative cell viability of Caco-2 cell line measured by the MTT reduction after 24h incubation. (A) represents NLC safety test with the treatment of free RAS, blank CT25 and RAS loaded CT25 (0.25-10 μM). (B) Represents differences in the cell viability of treatment with free RAS, RAS-MAP, blank CT25, RAS loaded CT25, MAP, RAS-MAP loaded CT25 (0.25-10 μM). (C) Represents co-administration of RAS and RAS-MAP with blank CT25 (1-10 μM). (D) Represents the data obtained from the encapsulation of Lys(N_3)-MAP and co-encapsulation of RAS and Lys(N_3)-MAP in the NLC compared to peptide conjugate. Results are expressed as mean ±SD (n = 4 or 6). Statistical analysis between the groups was performed using two-way

ANOVA with Tukey's multiple comparisons test (* p <0.05; ** p <0.01; *** p <0.001; **** p <0.0001).

Dose-response analysis of RAS-MAP, CT25 RAS-MAP demonstrated similar profile and a decrease on IC_{50} from 4.91 μM to 0.23 μM was obtain (Figure 3.20). The data for CT25Lys(N_3)-MAP determine an IC_{50} of 0.26 μM close to the CT25Lys(N_3)-MAP (Figure 3.20).

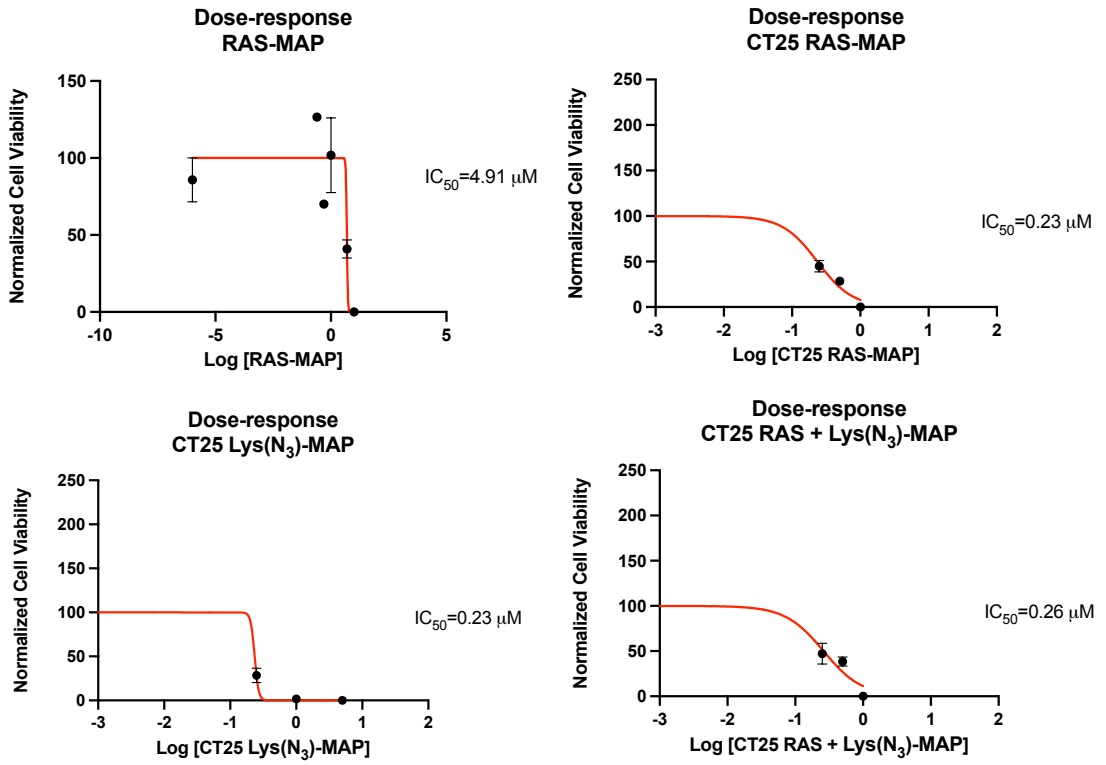


Figure 3.20 - The effect of RAS-MAP, CT25RAS-MAP, CT25 Lys(N_3)-MAP and CT25 RAS + Lys(N_3)-MAP on Caco-2 cell line dose-response curve. Each point is the average of at least three independent experiments.

The morphological evaluation of the Caco-2 cell line showed that treatment with CT25RAS did not result in a decrease in cell viability neither morphological change when compared to the free TCP and negative control (Figure 3.21). Co-administration of RAS and RAS-MAP with CT25 blank microscope images showed corroboration with MTT assay (Figure S3.9). With the data obtained from the MTT assay, CT2RAS-MAP

treatment showed a decrease of cell viability and severe morphological changes represented in Figure 3.21 at all concentrations tested. Once again, co-encapsulation of the RAS and Lys(N_3)-MAP showed less decrease in cell viability, but we can observe some morphological changes at 0.5 and 1 µM concentrations with cytoplasmatic granulation.

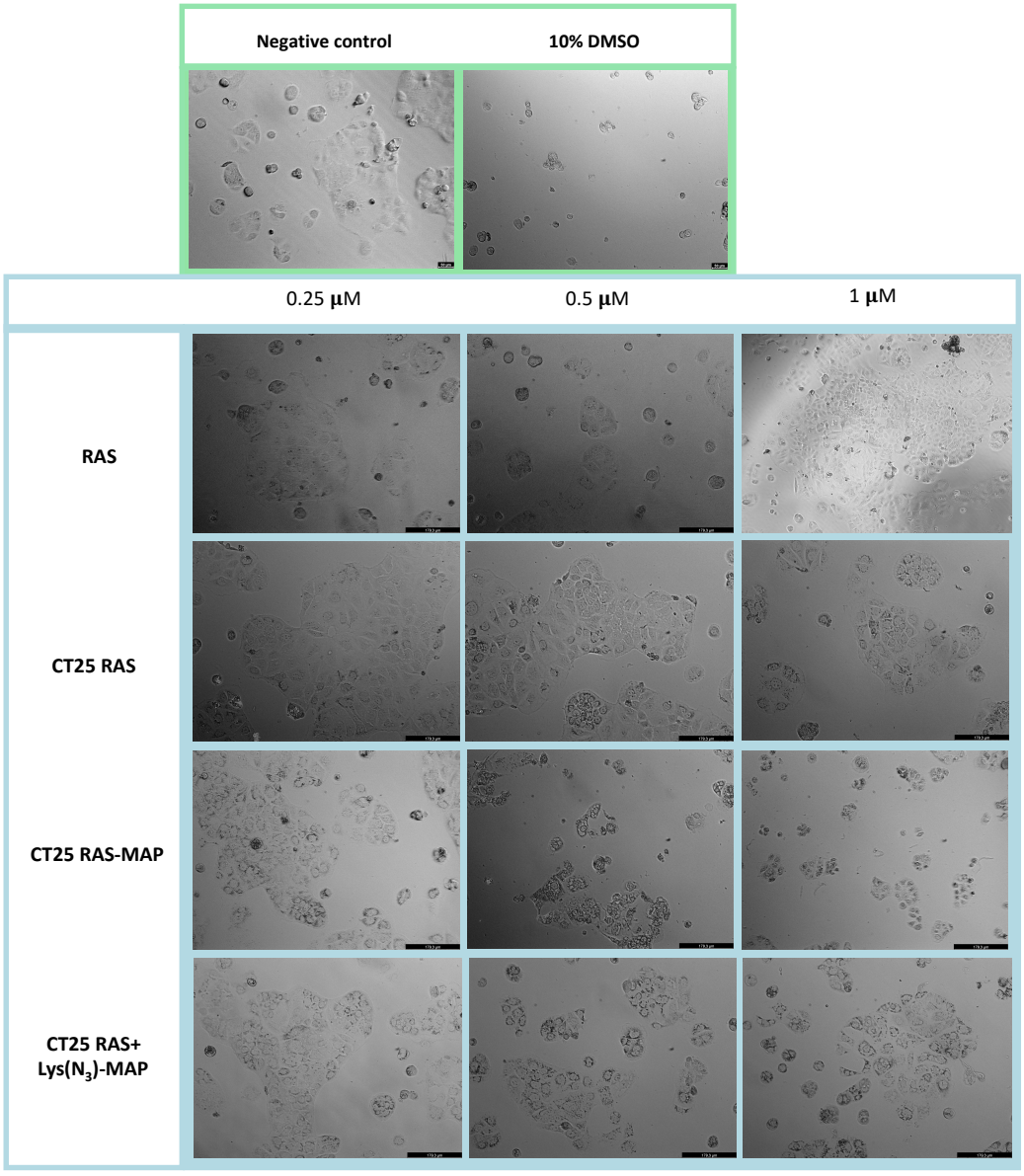


Figure 3.21 - Microscope cellular visualization through Leica DFC350 FX of treatment with negative control (ultra-purified H_2O), positive control (10% DMSO), free drug and NLC loaded formulations on Caco-2 cell line at a concentration of 0.25, 0.5 and 1 µM.

3.4.7.4. Toxicity of NLC loaded with TAC, Lys(N_3)-MAP and TAC-MAP

The MTT assays shown in Figure 3.22 A demonstrate that CT25B and CT25TAC treatment results in a significant decrease of around 30% on cell viability at all concentrations tested. For instance, in Figure 3.22 B the data demonstrated a significant cell viability decrease on NLC loaded TAC-MAP when compared to free TAC-MAP on all concentrations tested. Moreover, no differences were observed on co-administration of TAC or TAC-MAP with CT25 Blank NLC test when compared with loaded formulations (Figure 3.22 C). On Figure 3.22 D we analyzed the difference of co-encapsulation toxicity on the Caco-2 cell line and the results demonstrated that CT25TAC-MAP promotes significant more toxicity when compared to the two compounds TAC and Lys(N_3)-MAP co-encapsulated at concentrations of 0.5, 1 and 5 μM with and cell viability decreases to around 30% CT25 TAC-MAP. The SRB results corroborate with MTT analysis (Figure S3.8).

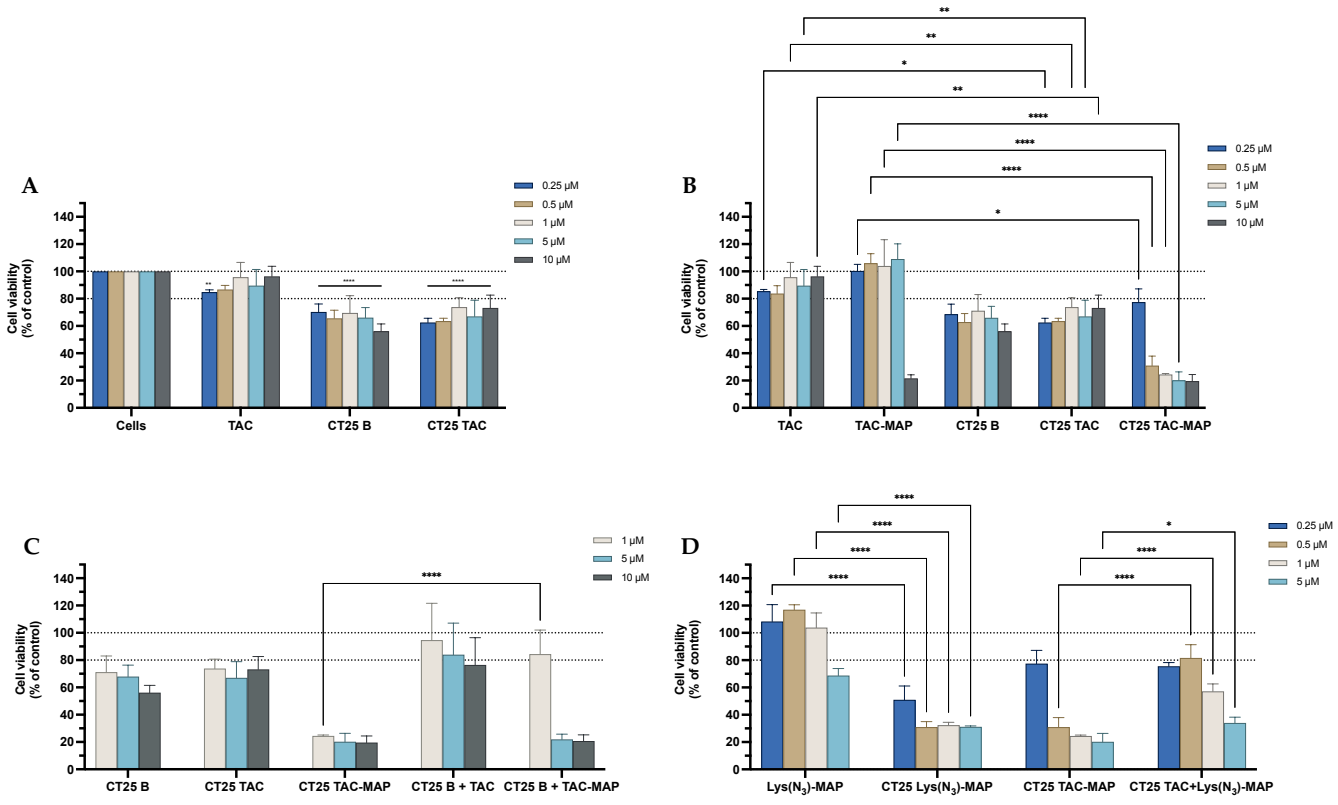


Figure 3.22 - Relative cell viability of Caco-2 cell line measured by the MTT reduction after 24h incubation. (A) represents NLC safety test with the treatment of free TAC, blank CT25 and TAC loaded CT25 (0.25-10 μM). (B) Represents differences in the cell viability of treatment with free TAC, TAC-MAP, blank CT25, TAC loaded CT25, MAP, TAC-MAP loaded CT25 (0.25-10 μM). (C)

Represents co-administration of TAC and TAC-MAP with blank CT25 (1-10 μM). (D) Represents the data obtained from the encapsulation of Lys(N_3)-MAP and co-encapsulation of TAC and Lys(N_3)-MAP in the NLC compared to peptide conjugate. Results are expressed as mean ±SD (n = 4). Statistical analysis between the groups was performed using two-way ANOVA with Tukey's multiple comparisons test (* p <0.05; ** p <0.01; *** p <0.001; **** p <0.0001).

The IC_{50} determine for TAC-MAP was 8.02 μM and for CT25TAC-MAP was 0.32 μM as shown in the graphics represented in Figure 3.23. In addition, treatment of Caco-2 cell line with CT25TAC + Lys(N_3)-MAP show an IC_{50} of 0.87 μM.

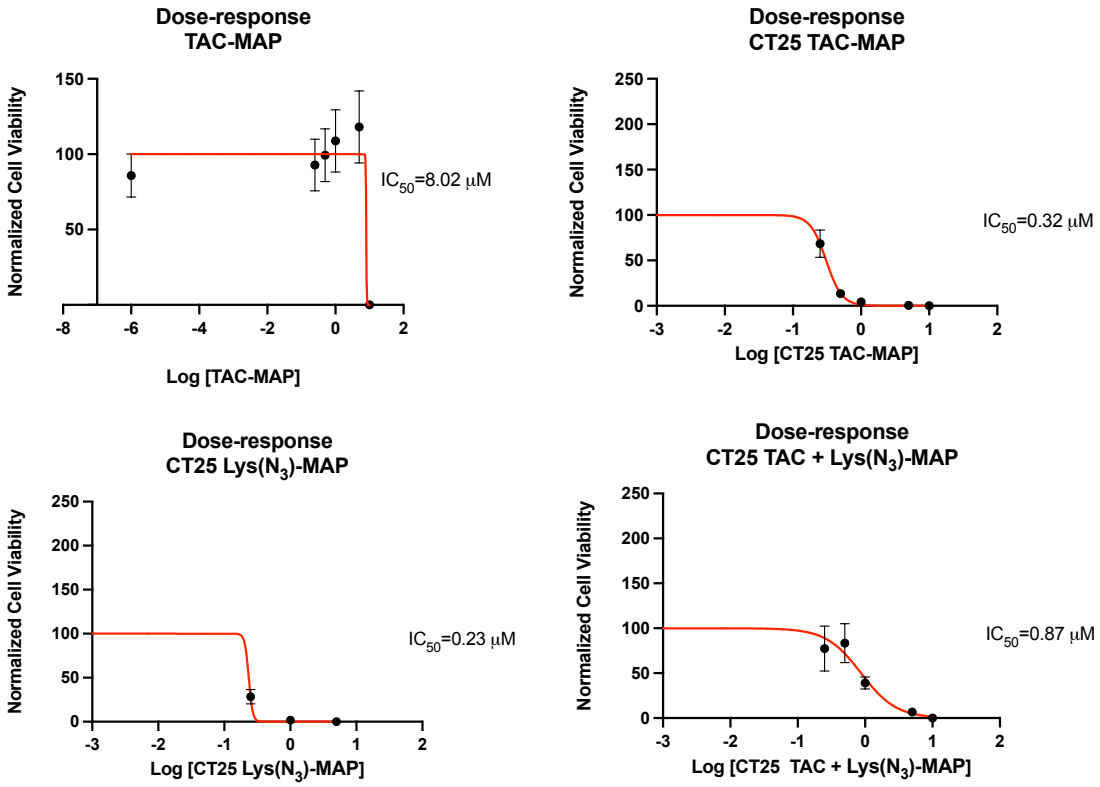


Figure 3.23 - The effect of TAC-MAP, CT25TAC-MAP, CT25 Lys(N_3)-MAP and CT25TAC + Lys(N_3)-MAP on Caco-2 cell line dose-response curve. Each point is the average of at least three independent experiments.

Microscope visualization of the treatment with CT25TAC showed no apparent decrease in cell viability and no morphological changes at all concentrations tested when

compared to negative control and free TAC (Figure 3.24). The co-administration test of TAC and TAC-MAP with CT25 blank microscope images showed corroboration with MTT assay with a decrease in cell viability and severe morphological changes on cell structure (Figure S3.9). The microscope images obtained after CT25TAC-MAP treatment showed a decrease in cell viability and severe morphological changes, as represented in Figure 3.24 in the concentration of 0.5 µM. In this case, co-encapsulation of the TAC and Lys(N_3)-MAP showed a decrease in cell viability and observed morphological changes at of 1, 5 and 10 µM concentration with complete loss of cell structure and decrease cellular size.

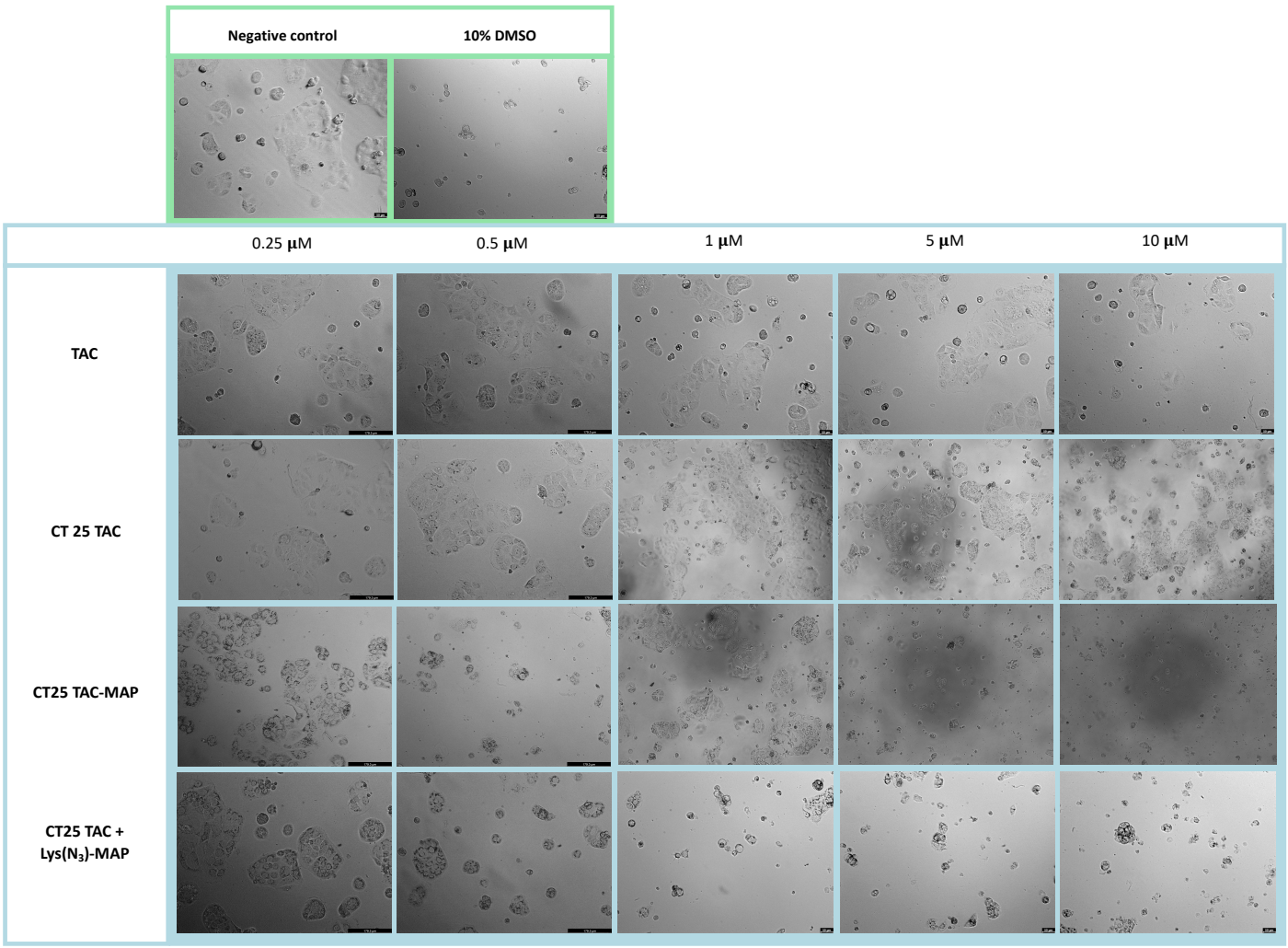


Figure 3.24 - Microscope cellular visualization through Lionheart FX and Leica DFC350 FX of treatment with negative control (ultra-purified H_2O), positive control (10% DMSO), free drug and NLC loaded formulations on Caco-2 cell line at a concentration of 0.25, 0.5, 1, 5 and 10 µM.

3.4.8. *In vitro* cytotoxicity assays against SH-SY5Y

3.4.8.1. Toxicity of MAP, Lys(N_3)-MAP and drug-MAP conjugates.

The MTT assay conducted on SH-SY5Y cells with the treatment of MAP and TAC-MAP demonstrated a significant decrease of cell viability at 5 μM. On the other hand, Lys(N_3)-MAP didn't promote decrease on cell viability. The treatment with free TCP-MAP and RAS-MAP demonstrated toxicity reflected on the decrease of cell viability of around 75% and 60 % at 5 μM, respectively (Figure 3.25). The SRB results corroborate with MTT analysis even not reflecting the same values of toxicity (Supplementary Figure S3.11). The IC_{50} of MAP free calculated was 1.05 μM (Figure 3.26).

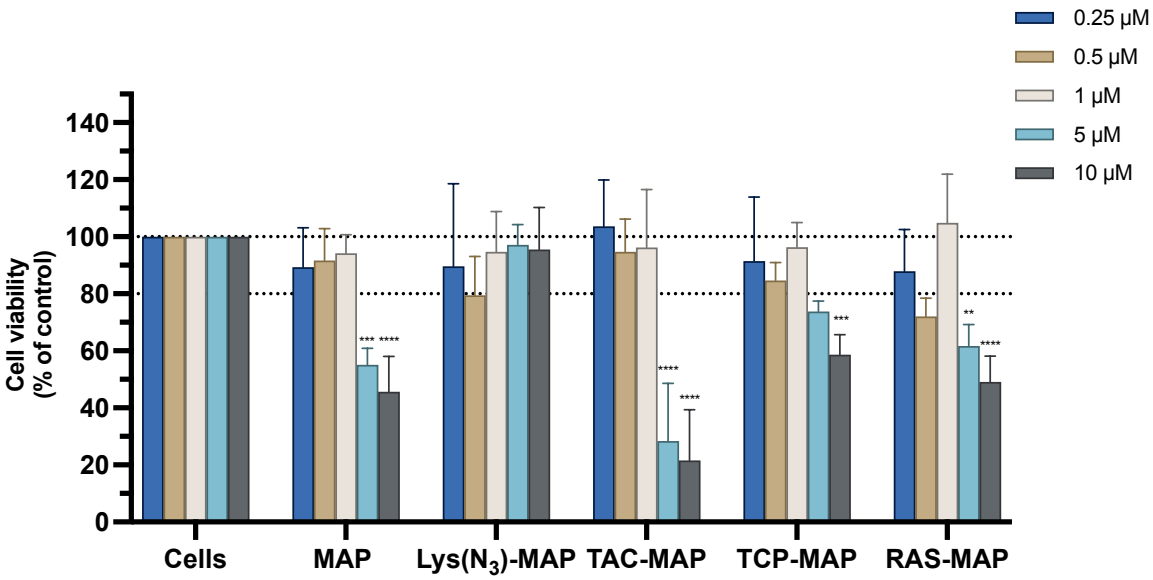


Figure 3.25 - Relative cell viability of SH-SY5Y cell line measured by the MTT reduction after 24 h incubation. Treatment with free MAP, Lys(N_3)-MAP, TAC-MAP, TCP-MAP and RAS-MAP (0,25 μM-10 μM). Results are expressed as mean ±SD (n = 3 or 6). Statistical analysis between the control groups was performed using two-way ANOVA with Tukey's multiple comparisons test (* p <0.05; *** p <0.001; **** p <0.0001).

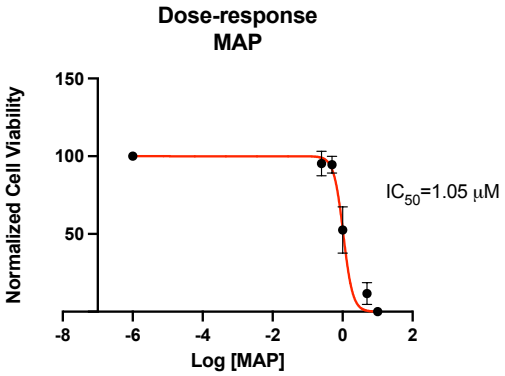


Figure 3.26 - The effect of MAP SH-S5Y5 cell line dose-response curve. Each point is the average of at least three independent experiments.

The morphology of SH-SY5Y was evaluated after 24 h incubation with all formulations (Figure 3.27). The analysis conducted through microscope visualization showed that treatment with MAP at 1 μM and Lys(N_3)-MAP at 5 μM decrease substantial cell viability and showed some morphologic change with loss of normal cellular structure and round aspect. Moreover, treatment with free TCP-MAP, RAS-MAP and TAC-MAP resulted in a decrease of cell density at 1 μM and severe morphological changes with loss of cell structure at 5 μM and 10 μM (Figure 3.27). The IC_{50} values determine demonstrated very close IC_{50} for free MAP and Lys(N_3)-MAP of 1.05 μM and 1.02 μM, respectively.

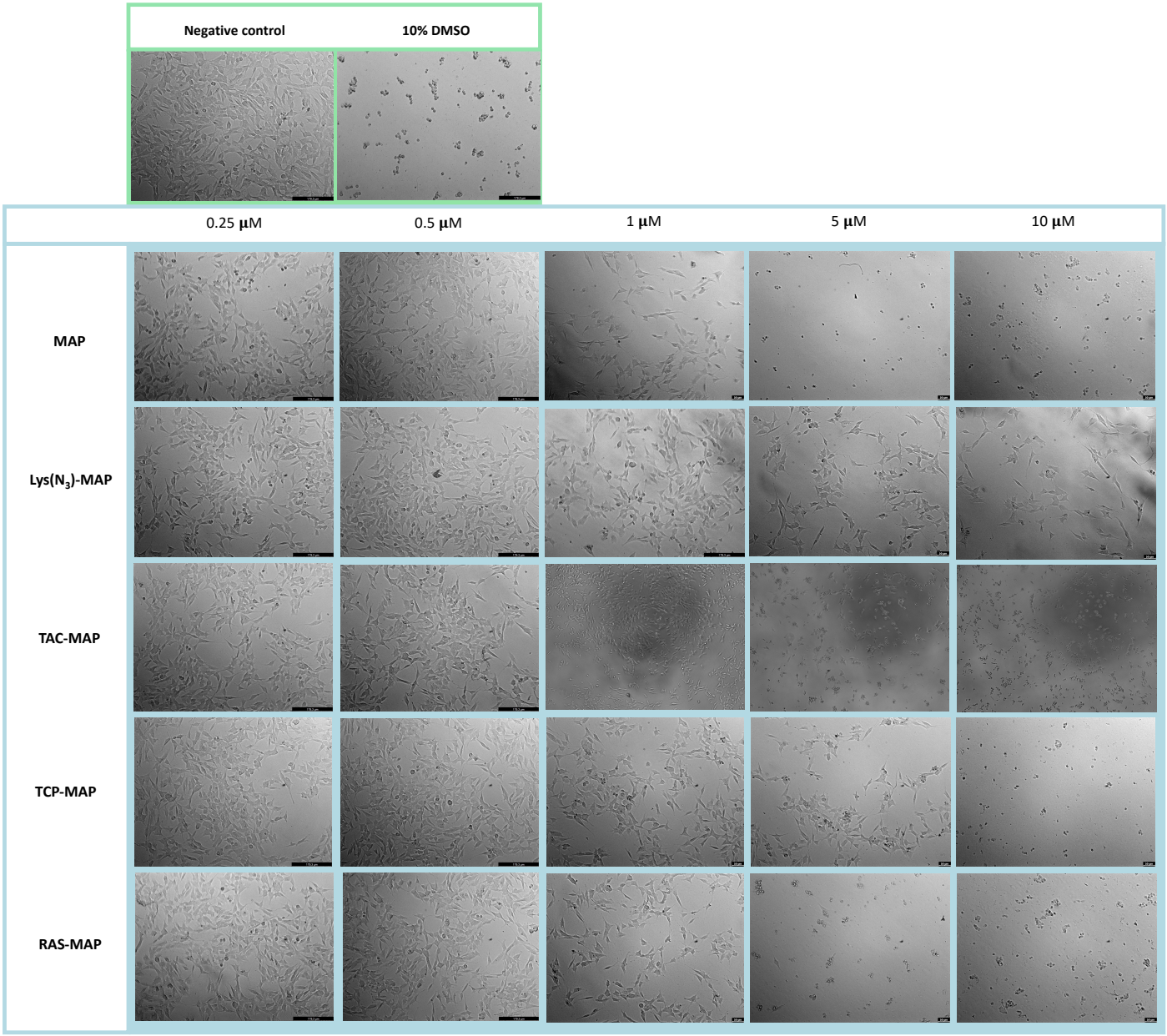


Figure 3.27 - Microscope cellular visualization through Lionheart FX and Leica DFC350 FX of treatment with negative control (ultra-purified H_2O), positive control (10% DMSO), free peptides and conjugates on SH-SY5Y cell line at a concentration of 0.25, 0.5, 1, 5 and 10 µM

3.4.8.2. Toxicity of NLC loaded with TCP, Lys(N_3)-MAP and TCP-MAP.

The data from the MTT assay in Figure 3.28 A shows that CT25B and CT25TCP treatment results in a decrease of around 25% on cell viability on all concentrations tested against neuroblastoma cell line SH-SY5Y. In Figure 3.28 B the data demonstrated a significant cell viability decrease of around 70% on NLC loaded TCP-MAP when compared to free TCP-MAP. In addition, co-administration of TCP or TCP-MAP with CT25 Blank NLC lead to similar cell toxicity profiles when compared with loaded formulations and free compound administration (Figure 3.28 C). Moreover, Figure 3.28 D demonstrated that co-encapsulation of TCP and Lys(N_3)-MAP does not promote significant toxicity on the SH-SY5Y cell line when compared to the CT25TCP-MAP on all concentrations tested. The results demonstrated a cell viability decrease to around 30% on CT25 TCP-MAP treatment and to around 65% for CT25 TCP+ Lys(N_3)-MAP. The SRB results show the same toxic profile off MTT analysis (Figure S3.12).

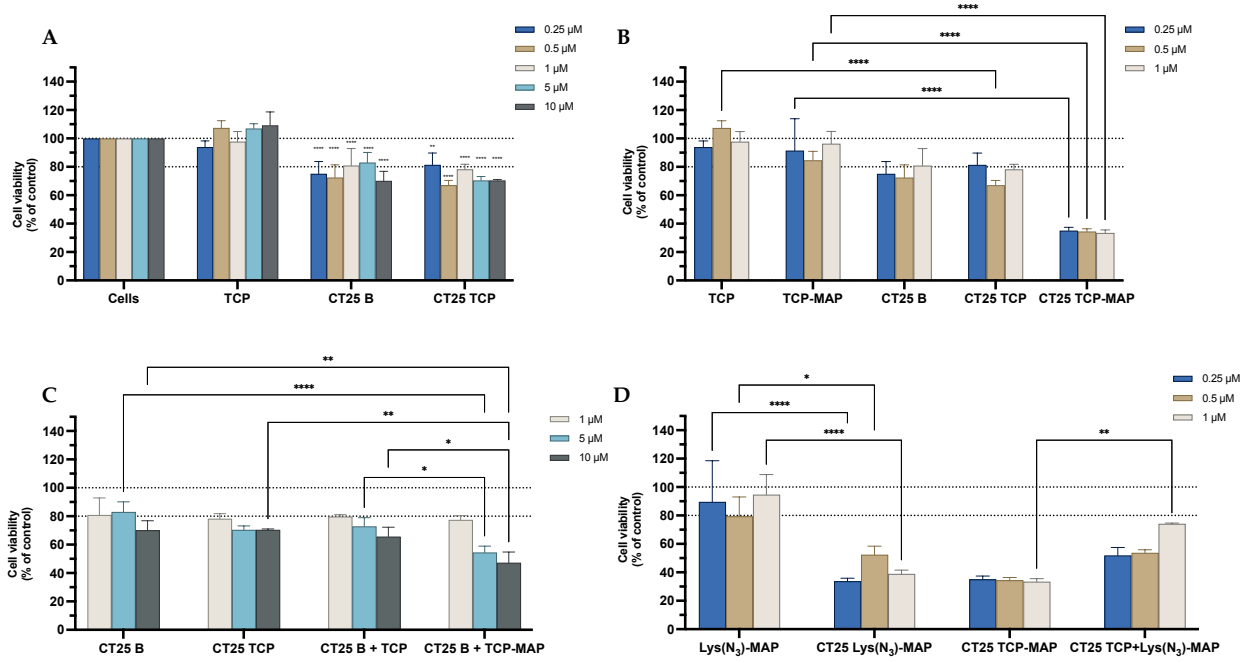


Figure 3.28 - Relative cell viability of SH-SY5Y cell line measured by the MTT reduction after 24 h incubation. (A) represents NLC safety test with the treatment of free TCP, blank CT25 and TCP loaded CT25 (0.25-10 µM). (B) Represents differences in the cell viability of treatment with free TCP, TCP-MAP, blank CT25, TCP loaded CT25, MAP, TCP-MAP loaded CT25 (0.25-10 µM). (C) Represents co-administration of TCP and TCP-MAP with blank CT25 (1-10 µM). (D) Represents the data obtained from the encapsulation of Lys(N_3)-MAP and co-encapsulation of TCP and Lys(N_3)-MAP in the NLC compared to peptide conjugate. Results are expressed as mean ±SD (n

= 4). Statistical analysis between the groups was performed using two-way ANOVA with Tukey's multiple comparisons test (* p <0.05; ** p <0.01; **** p <0.0001).

Dose response analysis demonstrated a decrease on IC_{50} value of 0.23 μM for CT25TCP-MAP when compared to IC_{50} of 0.68 μM of free TCP-MAP (Figure 3.29). On the other hand, treatment with Lys(N_3)-MAP or CT25 TCP + Lys(N_3)-MAP resulted on IC_{50} values of 0.23 μM and 0.18 μM (Figure 3.29).

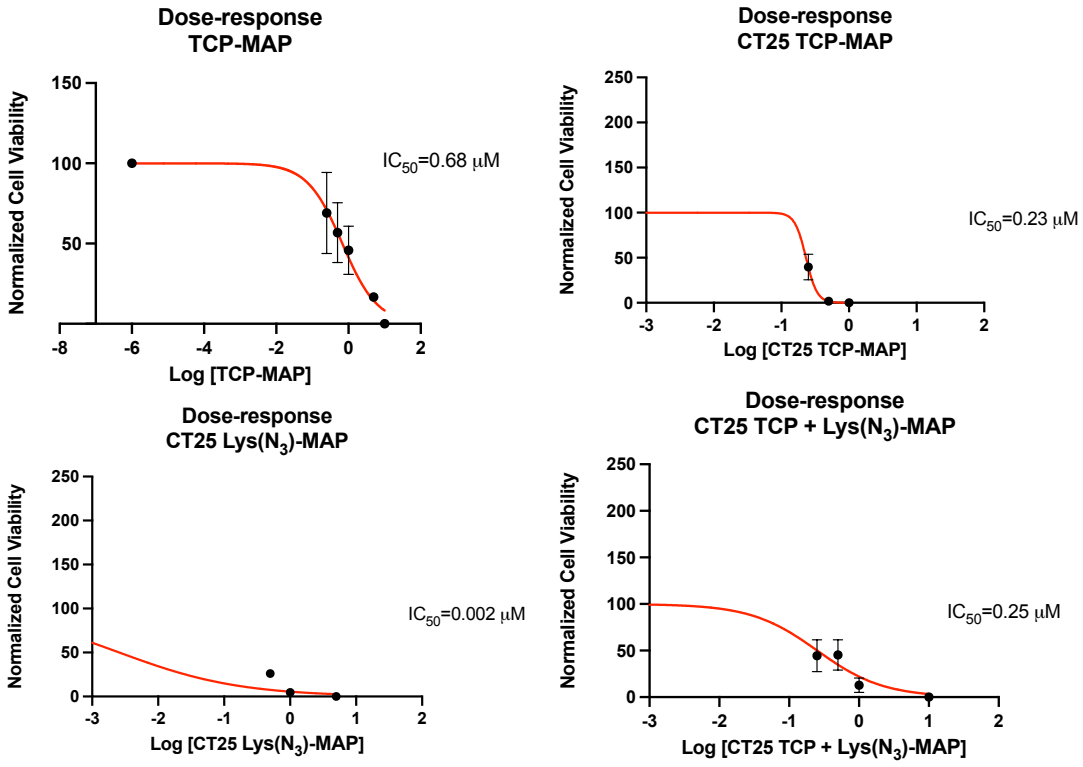


Figure 3.29 - The effect of TCP-MAP, CT25TCP-MAP, CT25 Lys(N_3)-MAP and CT25 TCP + Lys(N_3)-MAP on SH-S5Y5 cell line dose-response curve. Each point is the average of at least three independent experiments.

Microscope visualization showed that treatment with CT25TCP showed no alteration on cell viability and no morphological changes on SH-SY5Y when compared to negative control and free TCP (Figure 3.30). MTT assay showed no differences on co-administration of TCP and TCP-MAP with CT25 blank and the microscope images showed similar results with decreased cell viability at all concentrations tested (Figure

S3.15). Furthermore, CT25TCP-MAP treatment showed a high decrease in cell viability and severe morphological changes with loss of cell structure at all concentrations represented in Figure 3.30. The co-encapsulation treatment of the TCP and Lys(N_3)-MAP showed a decrease in cell viability at 0.5 µM but no morphological changes at all concentrations.

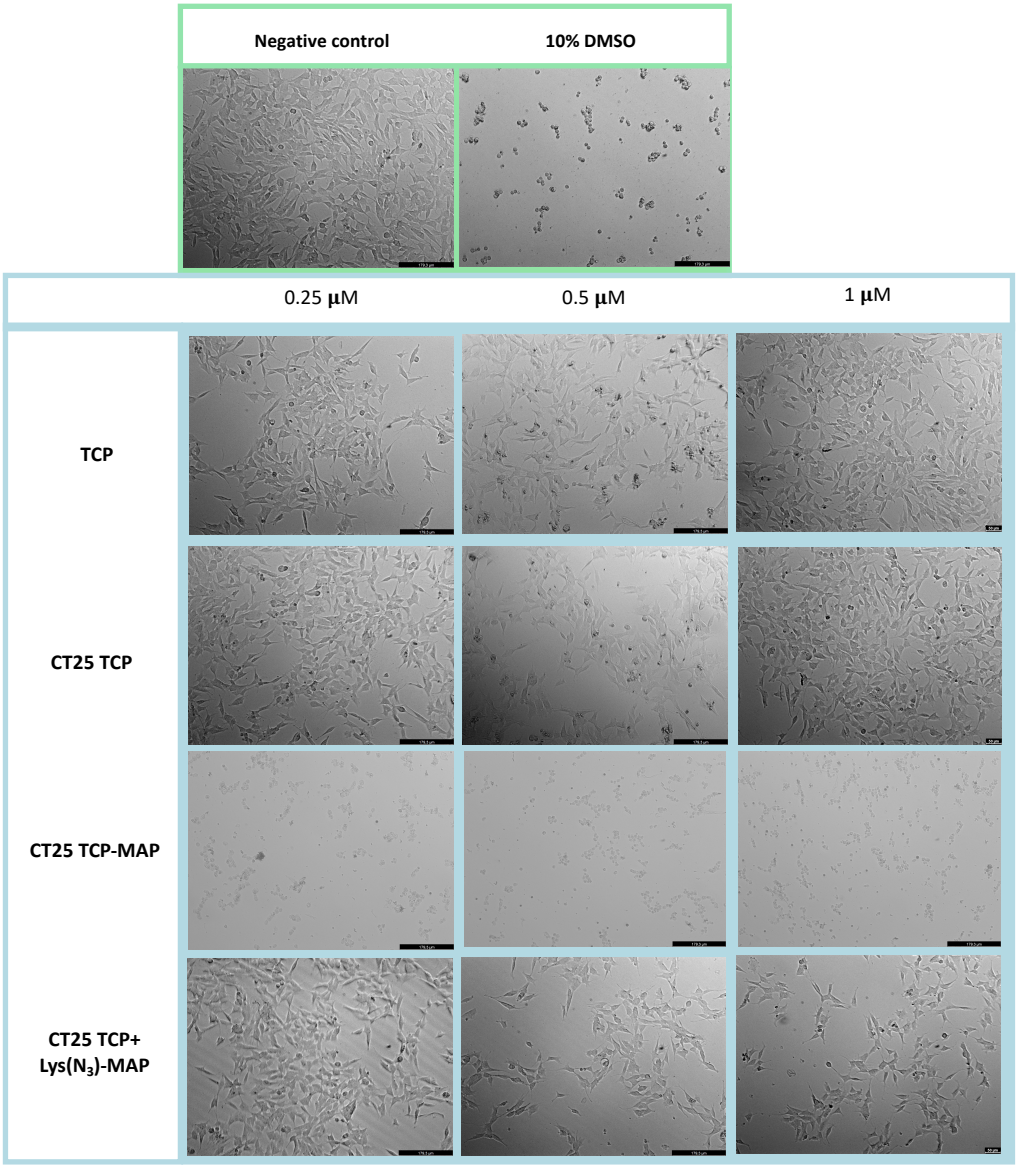


Figure 3.30 - Microscope cellular visualization through Leica DFC350 FX of treatment with negative control (ultra-purified H_2O), positive control (10% DMSO), free drug and NLC loaded formulations on SH-SY5Y cell line at a concentration of 0.25, 0.5 and 1 µM.

3.4.8.3. Toxicity of NLC loaded with RAS, Lys(N_3)-MAP and RAS-MAP

The results obtained from the MTT assay shown in Figure 3.31 A demonstrate that CT25B and CT25RAS treatment result in a decrease of around 25% on cell viability on all concentrations tested. The cell viability showed a significant decrease on NLC loaded RAS-MAP treatments when compared to free RAS-MAP at all concentrations (Figure 3.31 B). Furthermore, co-administration of RAS or RAS-MAP with CT25 Blank NLC did not contribute to a significant decrease in cell viability when compared with loaded formulations (Figure 3.31 C). Figure 3.31 D showed that CT25RAS-MAP promote slightly more toxicity on the SH-SY5Y cell line when compared to the two compounds RAS and Lys(N_3)-MAP co-encapsulated at all concentrations studied. Cell viability decreased to around 50%, 30% and 30% on CT25 RAS-MAP and 75%, 40% and 45% for CT25 RAS + Lys(N_3)-MAP at 0.25 µM, 0.5 µM and 1 µM, respectively (Figure 3.31 D). The SRB results corroborate with MTT analysis conducted (Figure S3.13).

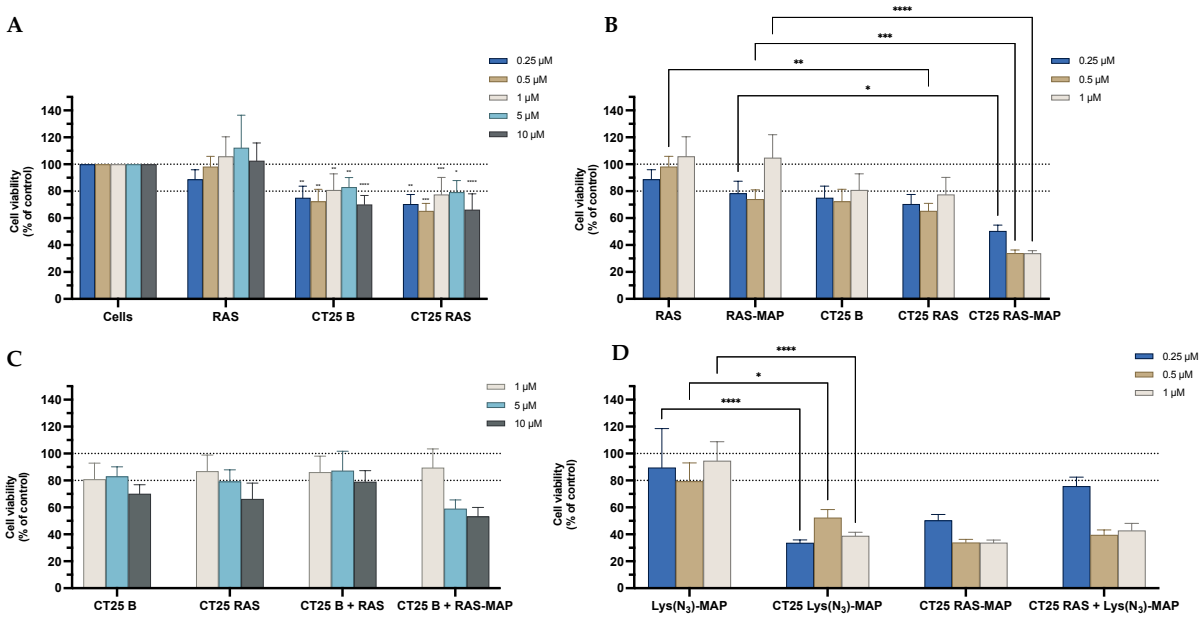


Figure 3.31 - Relative cell viability of SH-SY5Y cell line measured by the MTT reduction after 24 h incubation. (A) represents NLC safety test with the treatment of free RAS, blank CT25 and RAS loaded CT25 (0.25-10 µM). (B) Represents differences in the cell viability of treatment with free RAS, RAS-MAP, blank CT25, RAS loaded CT25, MAP, RAS-MAP loaded CT25 (0.25-10 µM). (C) Represents co-administration of RAS and RAS-MAP with blank CT25 (1-10 µM). (D) Represents the data obtained from the encapsulation of Lys(N_3)-MAP and co-encapsulation of RAS and Lys(N_3)-MAP in the NLC compared to peptide conjugate. Results are expressed as mean ±SD (n = 4). Statistical analysis between the groups was performed using two-way ANOVA with Tukey's multiple comparisons test (* p <0.05; ** p <0.01; *** p <0.001; **** p <0.0001).

Dose-response analysis of RAS-MAP, CT25 RAS-MAP demonstrated similar profile and a decrease on IC_{50} from 0.40 μM to 0.22 μM was obtain (Figure 3.32). The data for CT25RAS + Lys(N_3)-MAP determine an IC_{50} of 0.25 μM slight increase when compared with IC_{50} of 1.11 μM CT25Lys(N_3)-MAP (Figure 3.32).

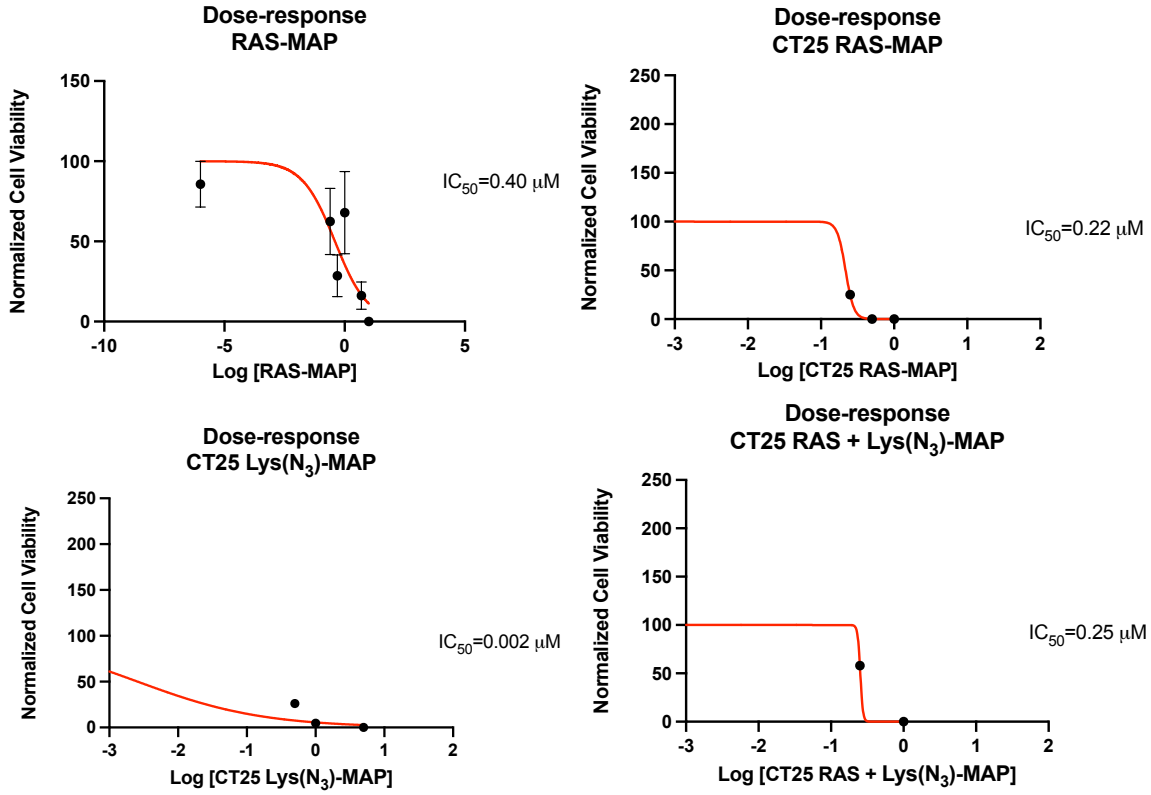


Figure 3.32 - The effect of RAS-MAP, CT25RAS-MAP, CT25 Lys(N_3)-MAP and CT25 RAS + Lys(N_3)-MAP on SH-S5Y5 cell line dose-response curve. Each point is the average of at least three independent experiments.

The morphological evaluation of neuroblastoma SH-SY5Y cell line showed that treatment with CT25RAS results in similar cell viability and no morphologic change compared to the negative control and free RAS (Figure 3.33). Co-administration of RAS and RAS-MAP with CT25 blank microscope images showed corroboration with MTT assay with decreased cellular viability at 5 μM (Figure S3.15). The treatment of CT25RAS-MAP showed a severe decrease in cell viability and loss of normal cellular structure at 0.5 μM. The co-encapsulation of the RAS and Lys(N_3)-MAP treatment showed a decrease in cell viability, but we only observe some morphological changes at the concentration of 1 μM.

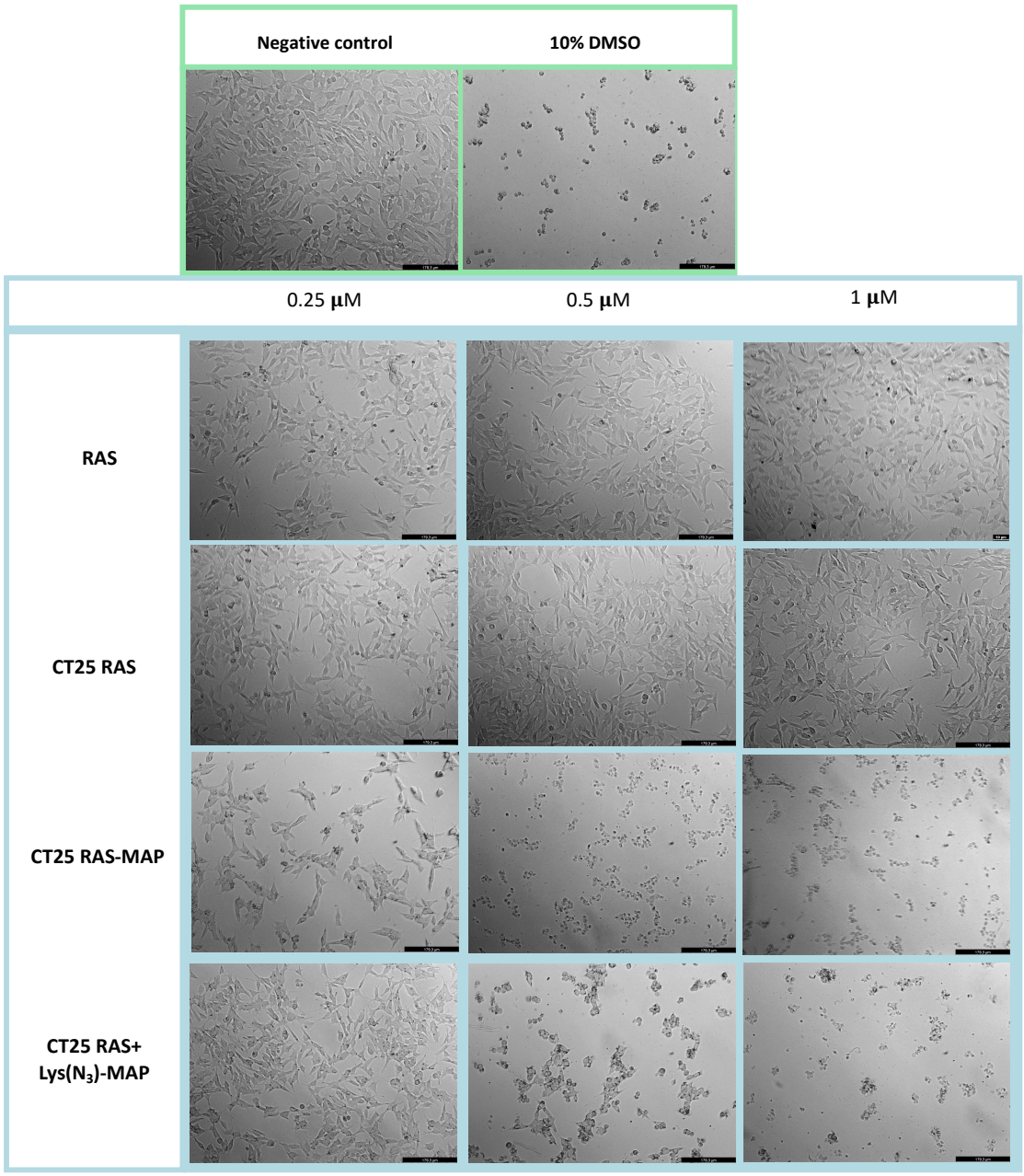


Figure 3.33 - Microscope cellular visualization through Leica DFC350 FX of treatment with negative control (ultra-purified H_2O), positive control (10% DMSO), free drug and NLC loaded formulations on SH-SY5Y cell line at a concentration of 0.25, 0.5 and 1 µM.

3.4.8.4. Toxicity of NLC loaded with TAC, Lys(N_3)-MAP and TAC-MAP

The MTT assays performed on the SH-SY5Y cell line shown in Figure 3.34 A demonstrate that CT25B and CT25TAC treatments result in a significant decrease of

around 28% on cell viability on all concentrations tested (Figure 3.34A). For instance, in Figure 3.34B the data demonstrated a significant cell viability decrease on NLC loaded TAC-MAP when compared to free TAC-MAP, more pronounced on lower concentrations of 0.25 μM and 0.5 μM. Furthermore, no differences were observed on co-administration of TAC or TAC-MAP with CT25 Blank NLC test when compared with loaded formulations CT25TAC and CT25TAC-MAP (Figure 3.34 C). In Figure 3.34 D we analyzed the difference of co-encapsulation toxicity and the results demonstrated that CT25TAC-MAP promotes more toxicity than the two compounds TAC and Lys(N_3)-MAP co-encapsulated at all concentrations. The SRB results corroborate with MTT analysis (Figure S3.14).

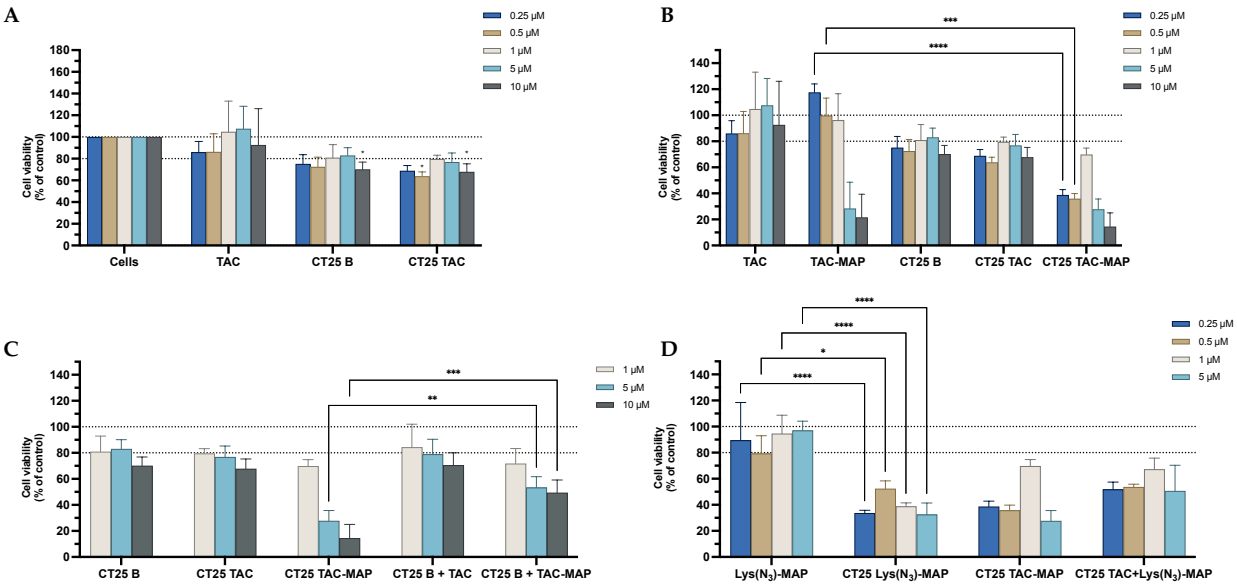


Figure 3.34 - Relative cell viability of SH-SY5Y cell line measured by the MTT reduction after 24 h incubation. (A) represents NLC safety test with the treatment of free TAC, blank CT25 and TAC loaded CT25 (0.25-10 μM). (B) Represents differences in the cell viability of treatment with free TAC, TAC-MAP, blank CT25, TAC loaded CT25, MAP, TAC-MAP loaded CT25 (0.25-10 μM). (C) Represents co-administration of TAC and TAC-MAP with blank CT25 (1-10 μM). (D) Represents the data obtained from the encapsulation of Lys(N_3)-MAP and co-encapsulation of TAC and Lys(N_3)-MAP in the NLC compared to peptide conjugate. Results are expressed as mean ±SD (n = 4). Statistical analysis between the groups was performed using two-way ANOVA with Tukey's multiple comparisons test (* p <0.05; ** p <0.01; *** p <0.001; **** p <0.0001).

The IC_{50} determine for TAC-MAP was 1.95 μM and for CT25TAC-MAP was 1.43 μM as shown in the graphics represented in figure 3.25. In addition, treatment of SH-SY5Y cell line with CT25Lys(N_3)-MAP + TAC show an IC_{50} of 0.91 μM.

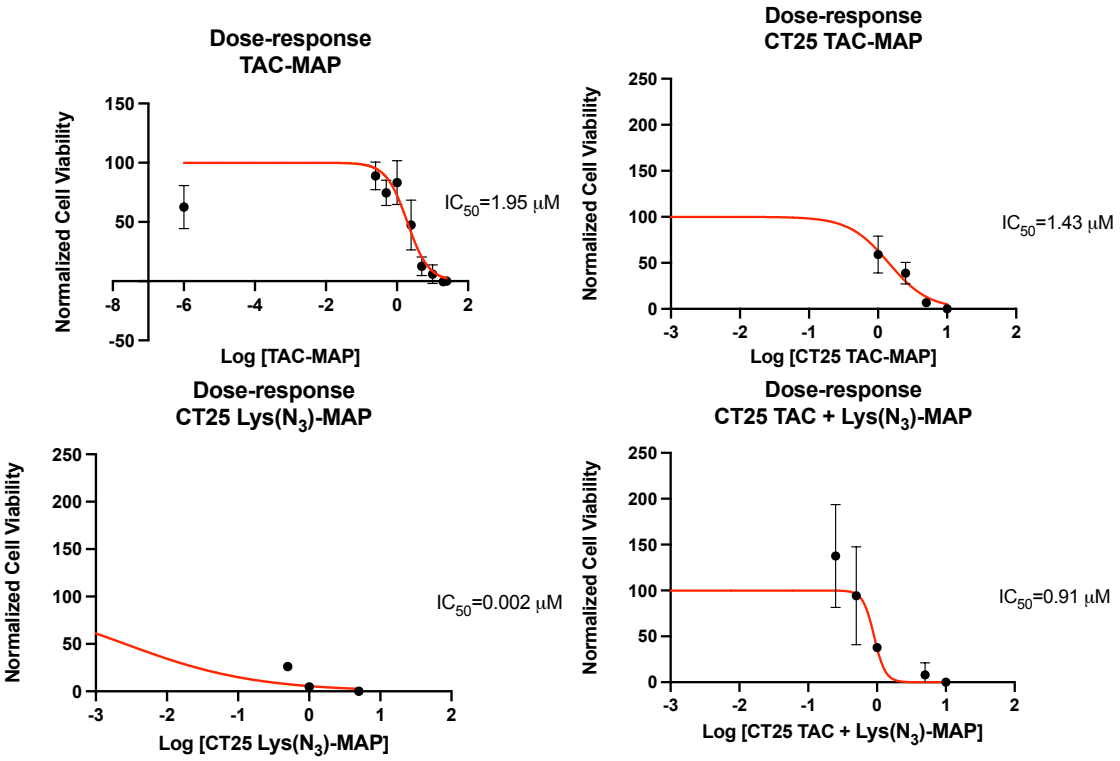


Figure 3.35 - The effect of TAC-MAP, CT25TAC-MAP, CT25 Lys(N_3)-MAP and CT25 TAC + Lys(N_3)-MAP on SH-S5Y5 cell line dose-response curve. Each point is the average of at least three independent experiments.

Microscope visualization of the treatment with CT25TAC showed a decrease in cell viability and no morphological changes at 1, 5 and 10 μM when compared to negative control and free TAC (Figure 3.36). The co-administration assay of TAC and TAC-MAP with CT25 blank microscope images showed corroboration with MTT assay with a decrease in cell viability at 1 μM and severe morphological changes on cell structure at 5 μM and 10 μM (Figure S3.15). The microscope images obtained with CT2TAC-MAP treatment showed a decrease of cell viability and severe morphological changes represented in Figure 3.36 in 0.5 μM, 5 and 10 μM. Moreover, co-encapsulation of the TAC and Lys(N_3)-MAP showed a decrease in cell viability and observed morphological changes at of 1, 5 and 10 μM concentration, with complete loss of cell structure and decrease of cellular size at 5 and 10 μM.

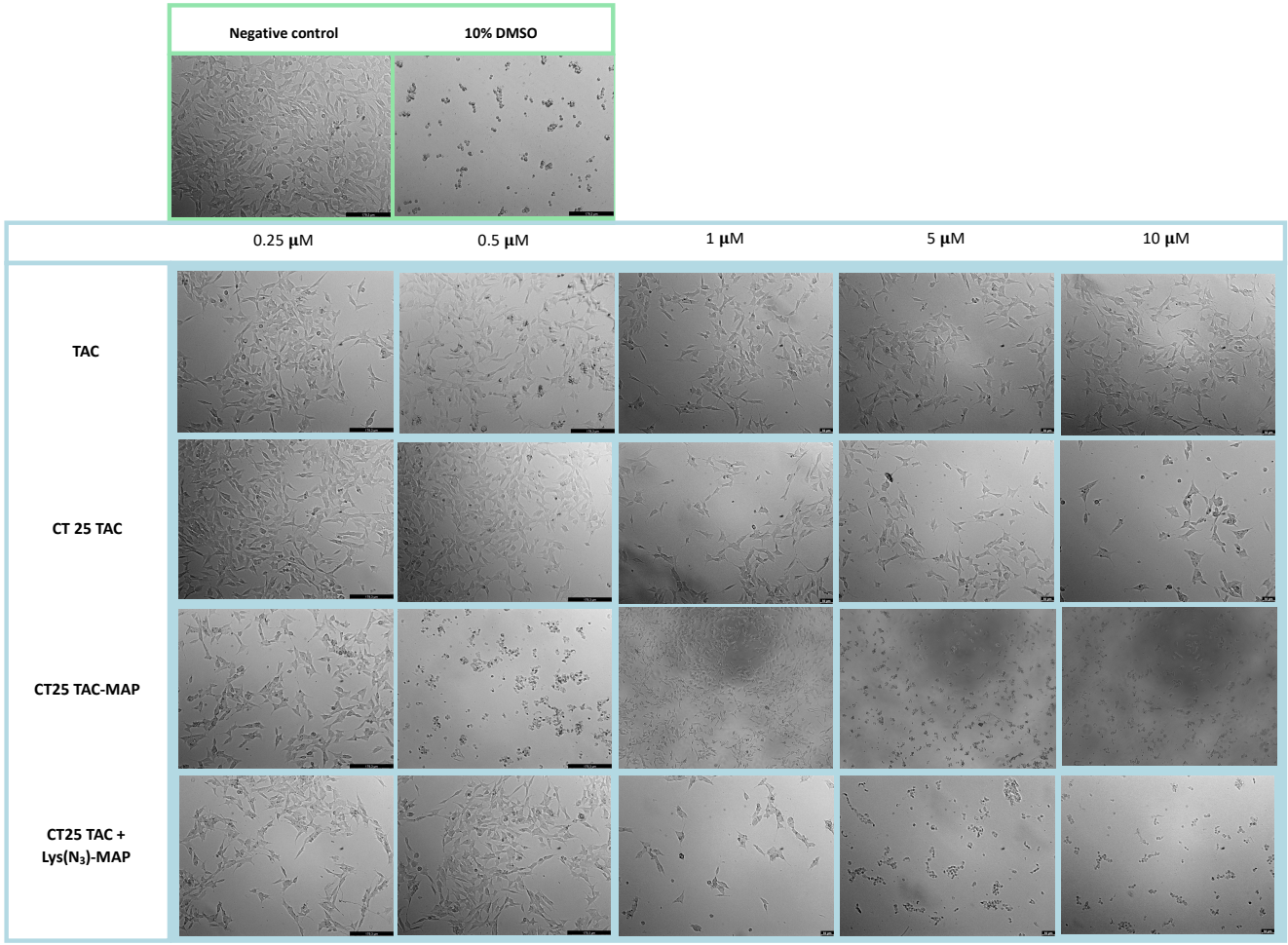


Figure 3.36 - Microscope cellular visualization through Lionheart FX and Leica DFC350 FX of treatment with negative control (H_2O), positive control (10% DMSO), free drug and NLC loaded formulations on SH-SY5Y cell line at a concentration of 0.25, 0.5, 1, 5 and 10 µM.

3.4.9. Discussion

The use of nanotechnology in this type of concept aims to overcome current free drug limitations by increasing drug bioavailability, circulation stability, decrease peripheral metabolization and toxicity. Taking this into consideration, different optimized NLC formulations were prepared loaded with the respective CNS drugs (TAC, TCP or RAS), Lys(N_3)-MAP, CNS-MAP conjugates (TAC-MAP, TCP-MAP, RAS-MAP) and dual encapsulation of Lys(N_3)-MAP and CNS drugs. The main NLC composition used Compritol® 888 ATO as solid lipid component, 25% of Transcutol® HP as liquid lipid component and 3% of T80 as surfactant. All NLC formulations prepared demonstrated a particle size distribution below 160 nm and a PI below 0.3 (Table 3.1). Particle size

analysis showed that incorporation of drug-MAP conjugates and co-encapsulation of CNS drugs and Lys(N_3)-MAP did not contribute to particle size increase on NLC formulations when compared to CT25 blank (Table 3.1). A similar outcome was observed on all NLC ZP. Preliminary solubility studies conducted prior to the NLC formulation demonstrated that TAC, TCP and RAS had a maximum solubility level in liquid lipid Transcutol® HP when compared to the other lipid tested. This will contribute to ensure an enhanced EE of the drug inside the NLC which is crucial for enhancing drug efficacy. The overall EE and DL demonstrated higher levels on RAS related NLC formulations than for the others CNS drugs used, most likely to be related to lower water solubility associated with RAS. Even though extensive NLC analysis was evaluated is important that in future studies with an *in vivo* model that a more in-depth analysis should be conducted on NLC such as, particle morphology and particle-particle interactions using other available techniques (85,86).

To assess and validate the enhanced drug-MAP conjugates efficacy on tumor cell toxicity with the use of nanoparticles, we conducted two cytotoxicity studies (MTT and SRB assays) and microscope cellular visualization. In the first part of the thesis, we confirm the toxic activity against two cell lines (Caco-2 and SH-SY5Y) of chosen peptides and the new synthesized drug-peptide conjugates. Then we evaluated the differences in their cytotoxic activity when encapsulated in NLC, co-administrated and co-encapsulated in the NLC. The results of free peptide administration demonstrated, as expected, a high cytotoxic activity and strong membrane lytic proprieties of peptide MAP against both cell lines at 10 μM, a result similar to the value already described in the literature (87). The treatment with lysine modified MAP (Lys(N_3)-MAP) demonstrated higher toxicity than MAP against the Caco-2 cell line at 5 μM (Figure 3.13). In addition, all synthesized drug-MAP conjugates demonstrated that membrane lytic proprieties of MAP were maintained even when conjugated to CNS drug and its respective toxic activity was observed at the same concentrations. Furthermore, the data collected from cytotoxicity assays demonstrated that CT25 B, CT25 TAC, CT25 TCP and CT25 RAS were relatively safe to both cell lines used. Even though some toxicity was observed with a decrease of around 20% of cell viability, this was already expected, from our previous studies and its related to the use of T80 as a surfactant in the NLC formulation (77,88,89). After encapsulation of drug-MAP conjugates and Lys(N_3)-MAP, the cytotoxic assays and microscope evaluation demonstrated a significant decrease in cell viability in both cell lines and severe cell morphological changes after treatment when compared to free drug-MAP and free Lys(N_3)-MAP at the lowest concentration. To ensure that nanoparticles were more efficient to deliver the toxic compound and thus contributing to

enhancement of cytotoxic activity, we conducted a co-administration assay with the treatment of both CT25 B and free drug-MAP on the tumoral cells. The results only demonstrated toxicity at higher concentrations. This study showed that encapsulation of drug-conjugates did not compromise their toxic effect and showed that was crucial to ensure higher drug efficacy at lower concentrations. The IC_{50} values show that conjugate encapsulation into NLC led to a decrease on cell viability and promote cell death with less required amount of conjugate. It's important to notice through IC_{50} evaluation that Caco-2 cell line were less susceptible to MAP and Lys(N_3)-MAP when compared to SH-SY5Y. This might be related with MAP strong TJ interaction that might promote cell endocytosis (90,91). In addition, we also prepared a co-encapsulated NLC to evaluate the toxic capability of CNS drug and Lys(N_3)-MAP combined but not covalently bound. The cytotoxic assays and microscope analysis showed less toxic activity when compared to NLC encapsulated with drug-MAP conjugate.

In conclusion, was possible to successfully synthesize a TCP-MAP conjugate and demonstrate its antiproliferative activity against two distinct cancer cell lines, Caco-2 and SH-SY5Y. Moreover, with this work we were able to encapsulate CNS drugs such as RAS, TAC and TCP; drug-MAP conjugates; amphipathic peptide Lys(N_3)-MAP and co-encapsulate both CNS drug and Lys(N_3)-MAP into NLC matrix. The overall cytotoxic assays confirmed the potential use of nanoparticles as carrier systems to successfully deliver therapeutic compounds not only against cancer but also potential in neurodegenerative diseases. In the future is important to evaluate the mechanisms behind drug-MAP conjugates anticancer activity with cells.

3.5. References

1. Park D, Lee JY, Cho HK, Hong WJ, Kim J, Seo H, et al. Cell-Penetrating Peptide-Patchy Deformable Polymeric Nanovehicles with Enhanced Cellular Uptake and Transdermal Delivery. Biomacromolecules [Internet]. 2018 Jul 9;19(7):2682–90. Available from: https://pubs.acs.org/doi/10.1021/acs.biomac.8b00292

2. Jiang T, Zhang Z, Zhang Y, Lv H, Zhou J, Li C, et al. Dual-functional liposomes based on pH-responsive cell-penetrating peptide and hyaluronic acid for tumor-targeted anticancer drug delivery. Biomaterials [Internet]. 2012;33(36):9246–58. Available from: http://dx.doi.org/10.1016/j.biomaterials.2012.09.027

3. Wei G, Wang Y, Huang X, Hou H, Zhou S. Peptide-Based Nanocarriers for Cancer Therapy. 2018;1700358:1–16. Available from: https://onlinelibrary.wiley.com/doi/10.1002/smtd.201700358

4. Bartlett RL, Sharma S, Panitch A. Cell-penetrating peptides released from thermosensitive nanoparticles suppress pro-inflammatory cytokine response by specifically targeting inflamed cartilage explants. Nanomedicine Nanotechnology, Biol Med. 2013;9(3):419–27.

5. Lane CA, Hardy J, Schott JM. Alzheimer's disease. Eur J Neurol. 2018;25(1):59–70.

6. Hansen D V, Hanson JE, Sheng M. Microglia in Alzheimer's disease. J Cell Biol [Internet]. 2018 Feb 5;217(2):459–72. Available from: https://rupress.org/jcb/article/217/2/459/52543/Microglia-in-Alzheimers-diseaseAlzheimers-disease

7. Selkoe DJ, Hardy J. The amyloid hypothesis of Alzheimer's disease at 25 years. EMBO Mol Med. 2016; Available from: https://onlinelibrary.wiley.com/doi/10.15252/emmm.201606210

8. Bales KR, Verina T, Dodel RC, Du Y, Altstiel L, Bender M, et al. Lack of apolipoprotein E dramatically reduces amyloid β-peptide deposition. Nat Genet [Internet]. 1997 Nov;17(3):263–4. Available from: http://www.nature.com/articles/ng1197-263

9. Bales KR, Verina T, Cummins DJ, Du Y, Dodel RC, Saura J, et al. Apolipoprotein E is essential for amyloid deposition in the APP(V717F) transgenic mouse model of Alzheimer's disease. Proc Natl Acad Sci U S A. 1999; Available from:

https://pnas.org/doi/full/10.1073/pnas.96.26.15233

10. Hardy J, Higgins G. Alzheimer's disease: the amyloid cascade hypothesis. Science (80-) [Internet]. 1992 Apr 10;256(5054):184–5. Available from: https://www.sciencemag.org/lookup/doi/10.1126/science.1566067

11. Querfurth HW, LaFerla FM. Mechanisms of Disease Alzheimer's Disease. N Engl J Med. 2010; Available from: http://www.ncbi.nlm.nih.gov/pubmed/21391318

12. Galimberti D, Scarpini E. Progress in Alzheimer's disease. J Neurol. 2012;259(2):201–11. Available from: http://link.springer.com/10.1007/s00415-011-6145-3

13. Briggs R, Kennelly SP, O'Neill D. Drug treatments in Alzheimer's disease. Clin Med (Northfield Il) [Internet]. 2016 Jun 1;16(3):247–53. Available from: https://www.rcpjournals.org/lookup/doi/10.7861/clinmedicine.16-3-247

14. Cole L, Kramer PR. Alzheimer's Disease. In: Human Physiology, Biochemistry and Basic Medicine [Internet]. Elsevier; 2016. p. 215–7. Available from: https://linkinghub.elsevier.com/retrieve/pii/B9780128036990000451

15. Santello M, Toni N, Volterra A. Astrocyte function from information processing to cognition and cognitive impairment. Nat Neurosci [Internet]. 2019;22(2):154–66. Available from: http://dx.doi.org/10.1038/s41593-018-0325-8

16. Butterfield DA, Halliwell B. Oxidative stress, dysfunctional glucose metabolism and Alzheimer disease. Nat Rev Neurosci [Internet]. 2019;20(3):148–60. Available from: http://dx.doi.org/10.1038/s41583-019-0132-6

17. Heneka MT, Carson MJ, Khoury J El, Landreth GE, Brosseron F, Feinstein DL, et al. Neuroinflammation in Alzheimer's disease. Lancet Neurol. 2015;14(4):388–405. Available from: https://linkinghub.elsevier.com/retrieve/pii/S1474442215700165

18. Blennow K, de Leon MJ, Zetterberg H. Alzheimer's disease. Lancet. 2006;368(9533):387–403.

19. Singh R, Lillard JW. Nanoparticle-based targeted drug delivery. Exp Mol Pathol [Internet]. 2009 Jun;86(3):215–23. Available from: https://linkinghub.elsevier.com/retrieve/pii/S001448000800141X

20. Alonso M, Couvreur P. Chapter 1:Historical View of the Design and Development

of Nanocarriers for Overcoming Biological Barriers. In 2012. Available from: http://dx.doi.org/10.1039/9781849735292-00003

21. Erkkinen MG, Kim M-O, Geschwind MD. Clinical Neurology and Epidemiology of the Major Neurodegenerative Diseases. Cold Spring Harb Perspect Biol [Internet]. 2018 Apr;10(4):a033118. Available from: http://cshperspectives.cshlp.org/lookup/doi/10.1101/cshperspect.a033118

22. Beitz JM. Parkinson s disease a review. Front Biosci [Internet]. 2014;S6(1):S415. Available from: https://www.bioscience.org/2014/v6s/af/S415/list.htm Available from: http://dx.doi.org/10.1016/S0140-6736(14)61393-3

23. Hayes MT. Parkinson's Disease and Parkinsonism. Am J Med [Internet]. 2019 Jul;132(7):802–7. Available from: https://doi.org/10.1016/j.amjmed.2019.03.001

24. Dorsey ER, Elbaz A, Nichols E, Abd-Allah F, Abdelalim A, Adsuar JC, et al. Global, regional, and national burden of Parkinson's disease, 1990–2016: a systematic analysis for the Global Burden of Disease Study 2016. Lancet Neurol [Internet]. 2018 Nov;17(11):939–53. Available from: https://linkinghub.elsevier.com/retrieve/pii/S1474442218302953

25. Samii A, Nutt JG, Ransom BR. Parkinson's disease. In: Lancet. 2004.

26. Sherer TB, Chowdhury S, Peabody K, Brooks DW. Overcoming obstacles in Parkinson's disease. Mov Disord [Internet]. 2012 Nov;27(13):1606–11. Available from: http://doi.wiley.com/10.1002/mds.25260

27. Tolosa E, Wenning G, Poewe W. The diagnosis of Parkinson's disease. Lancet Neurol [Internet]. 2006 Jan;5(1):75–86. Available from: https://linkinghub.elsevier.com/retrieve/pii/S1474442205702854

28. Armstrong MJ, Okun MS. Diagnosis and Treatment of Parkinson Disease: A Review. JAMA - J Am Med Assoc. 2020;323(6):548–60. Available from: https://jamanetwork.com/journals/jama/fullarticle/2760741

29. Cavaliere F, Cerf L, Dehay B, Ramos-Gonzalez P, De Giorgi F, Bourdenx M, et al. *In vitro* α-synuclein neurotoxicity and spreading among neurons and astrocytes using Lewy body extracts from Parkinson disease brains. Neurobiol Dis [Internet]. 2017;103:101–12. Available from: http://dx.doi.org/10.1016/j.nbd.2017.04.011

30. Antony PMA, Diederich NJ, Krüger R, Balling R. The hallmarks of Parkinson's

disease. FEBS J [Internet]. 2013 Dec;280(23):5981–93. Available from: http://doi.wiley.com/10.1111/febs.12335

31. Ceccatelli S. Mechanisms of neurotoxicity and implications for neurological disorders. J Intern Med [Internet]. 2013 May;273(5):426–8. Available from: http://doi.wiley.com/10.1111/joim.12053

32. Poewe W, Seppi K, Tanner CM, Halliday GM, Brundin P, Volkmann J, et al. Parkinson disease. Nat Rev Dis Prim [Internet]. 2017 Dec 21;3(1):17013. Available from: http://www.nature.com/articles/nrdp201713

33. Kam T-I, Hinkle JT, Dawson TM, Dawson VL. Microglia and astrocyte dysfunction in parkinson's disease. Neurobiol Dis [Internet]. 2020 Oct;144(July):105028. Available from: https://doi.org/10.1016/j.nbd.2020.105028

34. Dehay B, Martinez-Vicente M, Ramirez A, Perier C, Klein C, Vila M, et al. Lysosomal dysfunction in Parkinson disease. Autophagy [Internet]. 2012 Sep 14;8(9):1389–91. Available from: http://www.tandfonline.com/doi/abs/10.4161/auto.21011

35. Kalia L V., Lang AE. Parkinson's disease. Lancet [Internet]. 2015 Aug;386(9996):896–912. Available from: http://dx.doi.org/10.1016/S0140-6736(14)61393-3

36. Ascherio A, Schwarzschild MA. The epidemiology of Parkinson's disease: risk factors and prevention. Lancet Neurol [Internet]. 2016;15(12):1257–72. Available from: http://dx.doi.org/10.1016/S1474-4422(16)30230-7

37. Deng H, Wang P, Jankovic J. The genetics of Parkinson disease. Ageing Res Rev [Internet]. 2018 Mar;42(December 2017):72–85. Available from: https://doi.org/10.1016/j.arr.2017.12.007

38. Rui Q, Ni H, Li D, Gao R, Chen G. The Role of LRRK2 in Neurodegeneration of Parkinson Disease. Curr Neuropharmacol [Internet]. 2018 Oct 5;16(9):1348–57. Available from: http://www.eurekaselect.com/160051/article

39. Reich SG, Savitt JM. Parkinson's Disease. Med Clin North Am [Internet]. 2019 Mar;103(2):337–50. Available from: https://doi.org/10.1016/j.mcna.2018.10.014

40. Gazewood JD, Richards DR, Clebak K. Parkinson disease: An update. Am Fam Physician. 2013;87(4):267–73. Available from:

https://journals.lww.com/00127893-200407000-00002

41. Olanow CW, Schapira AHV. Therapeutic prospects for parkinson disease. Ann Neurol. 2013; Available from: https://onlinelibrary.wiley.com/doi/10.1002/ana.24011

42. Gulati N, Nagaich U, Saraf S. Fabrication and *in vitro* characterization of polymeric nanoparticles for Parkinson's therapy: A novel approach. Brazilian J Pharm Sci. 2014;50(4):869–76. Available from: http://www.scielo.br/scielo.php?script=sci_arttext&pid=S1984-82502014000400869&lng=en&tlng=en

43. Jafarieh O, Md S, Ali M, Baboota S, Sahni JK, Kumari B, et al. Design, characterization, and evaluation of intranasal delivery of ropinirole-loaded mucoadhesive nanoparticles for brain targeting. Drug Dev Ind Pharm [Internet]. 2015 Oct 3;41(10):1674–81. Available from: http://www.tandfonline.com/doi/full/10.3109/03639045.2014.991400

44. Mustafa G, Ahuja A, Al Rohaimi AH, Muslim S, Hassan AA, Baboota S, et al. Nano-ropinirole for the management of Parkinsonism: blood–brain pharmacokinetics and carrier localization. Expert Rev Neurother [Internet]. 2015 Jun 3;15(6):695–710. Available from: http://www.tandfonline.com/doi/full/10.1586/14737175.2015.1036743

45. Raj R, Wairkar S, Sridhar V, Gaud R. Pramipexole dihydrochloride loaded chitosan nanoparticles for nose to brain delivery: Development, characterization and *in vivo* anti-Parkinson activity. Int J Biol Macromol [Internet]. 2018;109:27–35. Available from: http://dx.doi.org/10.1016/j.ijbiomac.2017.12.056

46. Sridhar V, Wairkar S, Gaud R, Bajaj A, Meshram P. Brain targeted delivery of mucoadhesive thermosensitive nasal gel of selegiline hydrochloride for treatment of Parkinson's disease. J Drug Target [Internet]. 2018;26(2):150–61. Available from: http://dx.doi.org/10.1080/1061186X.2017.1350858

47. Sung H, Ferlay J, Siegel RL, Laversanne M, Soerjomataram I, Jemal A, et al. Global Cancer Statistics 2020: GLOBOCAN Estimates of Incidence and Mortality Worldwide for 36 Cancers in 185 Countries. CA Cancer J Clin [Internet]. 2021 May 4;71(3):209–49. Available from: https://onlinelibrary.wiley.com/doi/10.3322/caac.21660

48. Ferlay J, Colombet M, Soerjomataram I, Parkin DM, Piñeros M, Znaor A, et al.

Cancer statistics for the year 2020: An overview. Int J Cancer [Internet]. 2021 Aug 15;149(4):778–89. Available from: https://onlinelibrary.wiley.com/doi/10.1002/ijc.33588

49. Tata A, Zheng J, Ginsberg HJ, Jaffray DA, Ifa DR, Zarrine-Afsar A. Contrast Agent Mass Spectrometry Imaging Reveals Tumor Heterogeneity. Anal Chem. 2015;87(15):7683–9. Available from: https://pubs.acs.org/doi/10.1021/acs.analchem.5b01992

50. Haumann R, Videira JC, Kaspers GJL, van Vuurden DG, Hulleman E. Overview of Current Drug Delivery Methods Across the Blood–Brain Barrier for the Treatment of Primary Brain Tumors. CNS Drugs [Internet]. 2020 Nov 23;34(11):1121–31. Available from: https://doi.org/10.1007/s40263-020-00766-w

51. Biswas S, Kumari P, Lakhani PM, Ghosh B. Recent advances in polymeric micelles for anti-cancer drug delivery. Vol. 83, European Journal of Pharmaceutical Sciences. 2016. p. 184–202. Available from: https://linkinghub.elsevier.com/retrieve/pii/S0928098715301056

52. Li J, Feng L, Fan L, Zha Y, Guo L, Zhang Q, et al. Targeting the brain with PEG-PLGA nanoparticles modified with phage-displayed peptides. Biomaterials. 2011;32(21):4943–50. Available from: https://linkinghub.elsevier.com/retrieve/pii/S0142961211002870

53. Gao H, Qian J, Cao S, Yang Z, Pang Z, Pan S, et al. Precise glioma targeting of and penetration by aptamer and peptide dual-functioned nanoparticles. Biomaterials [Internet]. 2012;33(20):5115–23. Available from: http://dx.doi.org/10.1016/j.biomaterials.2012.03.058

54. Davis M. Glioblastoma: Overview of Disease and Treatment. Clin J Oncol Nurs [Internet]. 2016 Oct 1;20(5):S2–8. Available from: https://www.ncbi.nlm.nih.gov/pubmed/27668386

55. Xin H, Jiang X, Gu J, Sha X, Chen L, Law K, et al. Angiopep-conjugated poly(ethylene glycol)-co-poly(ε-caprolactone) nanoparticles as dual-targeting drug delivery system for brain glioma. Biomaterials [Internet]. 2011;32(18):4293–305. Available from: http://dx.doi.org/10.1016/j.biomaterials.2011.02.044

56. Mei L, Zhang Q, Yang Y, He Q, Gao H. Angiopep-2 and activatable cell penetrating peptide dual modified nanoparticles for enhanced tumor targeting and penetrating. Int J Pharm [Internet]. 2014;474(1–2):95–102. Available from:

http://dx.doi.org/10.1016/j.ijpharm.2014.08.020

57. Aguilera TA, Timmers MM, Olson ES, Jiang T, Roger Y, Timmers MM, et al. Systemic *in vivo* distribution of activatable cell penetrating peptides is superior to that of cell penetrating peptides. Integr Biol [Internet]. 2009;1(5–6):371. Available from: http://xlink.rsc.org/?DOI=b904878b

58. Gao H, Zhang S, Cao S, Yang Z, Pang Z, Jiang X. Angiopep-2 and activatable cell-penetrating peptide dual-functionalized nanoparticles for systemic glioma-targeting delivery. Mol Pharm. 2014;11(8):2755–63. Available from: https://pubs.acs.org/doi/10.1021/mp500113p

59. Zhu Y, Jiang Y, Meng F, Deng C, Cheng R, Zhang J, et al. Highly efficacious and specific anti-glioma chemotherapy by tandem nanomicelles co-functionalized with brain tumor-targeting and cell-penetrating peptides. J Control Release. 2018;278(March):1–8.

60. Kadari A, Pooja D, Gora RH, Gudem S, Kolapalli VRM, Kulhari H, et al. Design of multifunctional peptide collaborated and docetaxel loaded lipid nanoparticles for antiglioma therapy. Eur J Pharm Biopharm [Internet]. 2018;132(September):168–79. Available from: https://doi.org/10.1016/j.ejpb.2018.09.012

61. Kanazawa T, Akiyama F, Kakizaki S, Takashima Y, Seta Y. Delivery of siRNA to the brain using a combination of nose-to-brain delivery and cell-penetrating peptide-modified nano-micelles. Biomaterials [Internet]. 2013;34(36):9220–6. Available from: http://dx.doi.org/10.1016/j.biomaterials.2013.08.036

62. Kanazawa T, Morisaki K, Suzuki S, Takashima Y. Prolongation of life in rats with malignant glioma by intranasal siRNA/drug codelivery to the brain with cell-penetrating peptide-modified micelles. Mol Pharm. 2014;11(5):1471–8. Available from: https://pubs.acs.org/doi/10.1021/mp400644e

63. Redig AJ, Mcallister SS. Breast cancer as a systemic disease: A view of metastasis. Vol. 274, Journal of Internal Medicine. 2013. p. 113–26.

64. Cedolini C, Bertozzi S, Londero AP, Bernardi S, Seriau L, Concina S, et al. Type of breast cancer diagnosis, screening, and survival. Clin Breast Cancer [Internet]. 2014;14(4):235–40. Available from: http://dx.doi.org/10.1016/j.clbc.2014.02.004

65. Hossain MK, Cho HY, Kim KJ, Choi JW. In situ monitoring of doxorubicin release from biohybrid nanoparticles modified with antibody and cell-penetrating peptides

in breast cancer cells using surface-enhanced Raman spectroscopy. Biosens Bioelectron [Internet]. 2015;71:300–5. Available from: http://dx.doi.org/10.1016/j.bios.2015.04.053

66. Morshed RA, Muroski ME, Dai Q, Wegscheid ML, Auffinger B, Yu D, et al. Cell-Penetrating Peptide-Modified Gold Nanoparticles for the Delivery of Doxorubicin to Brain Metastatic Breast Cancer. Mol Pharm. 2016;13(6):1843–54. Available from: https://pubs.acs.org/doi/10.1021/acs.molpharmaceut.6b00004

67. Mussa Farkhani S, Asoudeh Fard A, Zakeri-Milani P, Shahbazi Mojarrad J, Valizadeh H. Enhancing antitumor activity of silver nanoparticles by modification with cell-penetrating peptides. Artif Cells, Nanomedicine Biotechnol. 2017;45(5):1029–35.

68. Patlolla RR, Desai PR, Belay K, Singh MS. Translocation of cell penetrating peptide engrafted nanoparticles across skin layers. Biomaterials. 2010;31(21):5598–607. Available from: https://linkinghub.elsevier.com/retrieve/pii/S0142961210003522

69. Asai T, Tsuzuku T, Takahashi S, Okamoto A, Dewa T, Nango M, et al. Cell-penetrating peptide-conjugated lipid nanoparticles for siRNA delivery. Biochem Biophys Res Commun [Internet]. 2014;444(4):599–604. Available from: http://dx.doi.org/10.1016/j.bbrc.2014.01.107

70. Zhang L, Liu F, Li G, Zhou Y, Yang Y. Twin-Arginine Translocation Peptide Conjugated Epirubicin-Loaded Nanoparticles for Enhanced Tumor Penetrating and Targeting. J Pharm Sci [Internet]. 2015;104(12):4185–96. Available from: http://dx.doi.org/10.1002/jps.24649

71. Jin C, Bai L, Lin L, Wang S, Yin X. Paclitaxel-loaded nanoparticles decorated with bivalent fragment HAb18 F(ab')2 and cell penetrating peptide for improved therapeutic effect on hepatocellular carcinoma. Artif Cells, Nanomedicine Biotechnol [Internet]. 2018;46(5):1076–84. Available from: https://doi.org/10.1080/21691401.2017.1360325

72. Kapur A, Medina SH, Wang W, Palui G, Schneider JP, Mattoussi H. Intracellular Delivery of Gold Nanocolloids Promoted by a Chemically Conjugated Anticancer Peptide. ACS Omega [Internet]. 2018;3(10):12754–62. Available from: http://pubs.acs.org/doi/10.1021/acsomega.8b02276

73. Gao H, Zhang Q, Yang Y, Jiang X, He Q. Tumor homing cell penetrating peptide

decorated nanoparticles used for enhancing tumor targeting delivery and therapy. Int J Pharm [Internet]. 2015;478(1):240–50. Available from: http://dx.doi.org/10.1016/j.ijpharm.2014.11.029

74. Zhu L, Wang T, Perche F, Taigind A, Torchilin VP. Enhanced anticancer activity of nanopreparation containing an MMP2-sensitive PEG-drug conjugate and cell-penetrating moiety. Proc Natl Acad Sci [Internet]. 2013;110(42):17047–52. Available from: http://www.pnas.org/cgi/doi/10.1073/pnas.1304987110

75. Carnevale KJF, Muroski ME, Vakil PN, Foley ME, Laufersky G, Kenworthy R, et al. Selective Uptake Into Drug Resistant Mammalian Cancer By Cell Penetrating Peptide-Mediated Delivery. Bioconjug Chem [Internet]. 2018;acs.bioconjchem.8b00429. Available from: http://pubs.acs.org/doi/10.1021/acs.bioconjchem.8b00429

76. Silva S, Marto J, Gonçalves L, Almeida AJ, Vale N. Formulation, characterization and evaluation against sh-sy5y cells of new tacrine and tacrine-map loaded with lipid nanoparticles. Nanomaterials. 2020;10(10). Available from: https://www.mdpi.com/2079-4991/10/10/2089

77. Gaspar DP, Faria V, Gonçalves LMD, Taboada P, Remuñán-López C, Almeida AJ. Rifabutin-loaded solid lipid nanoparticles for inhaled antitubercular therapy: Physicochemical and *in vitro* studies. Int J Pharm [Internet]. 2016 Jan;497(1–2):199–209. Available from: http://dx.doi.org/10.1016/j.ijpharm.2015.11.050

78. Chou TC. Drug combination studies and their synergy quantification using the chou-talalay method. Cancer Res. 2010 Jan;70(2):440–6. Available from: https://aacrjournals.org/cancerres/article/70/2/440/559704/Drug-Combination-Studies-and-Their-Synergy

79. Hällbrink M, Florén A, Elmquist A, Pooga M, Bartfai T, Langel Ü. Cargo delivery kinetics of cell-penetrating peptides. Biochim Biophys Acta - Biomembr. 2001;1515(2):101–9. Available from: https://linkinghub.elsevier.com/retrieve/pii/S0005273601003984

80. Palm-Apergi C, Lorents A, Padari K, Pooga M. The membrane repair response masks membrane disturbances caused by cell-penetrating peptide uptake. FASEB J. 2009;23(1):214–23. Available from: https://onlinelibrary.wiley.com/doi/10.1096/fj.08-110254

81. Saar K, Lindgren M, Hansen M, Eiríksdóttir E, Jiang Y. Cell-penetrating peptides : A comparative membrane toxicity study. 2005;345:55–65. Available from: https://linkinghub.elsevier.com/retrieve/pii/S0003269705005439

82. Pannecouque C, Daelemans D, De Clercq E. Tetrazolium-based colorimetric assay for the detection of HIV replication inhibitors: Revisited 20 years later. Nat Protoc. 2008; Available from: http://www.nature.com/articles/nprot.2007.517

83. Mao F, Chen J, Zhou Q, Luo Z, Huang L, Li X. Novel tacrine-ebselen hybrids with improved cholinesterase inhibitory, hydrogen peroxide and peroxynitrite scavenging activity. Bioorganic Med Chem Lett. 2013; Available from: https://linkinghub.elsevier.com/retrieve/pii/S0960894X13012407

84. Ellman GL, Courtney KD, Andres V, Featherstone RM. A new and rapid colorimetric determination of acetylcholinesterase activity. Biochem Pharmacol. 1961; Available from: https://linkinghub.elsevier.com/retrieve/pii/0006295261901459

85. Rostami E, Kashanian S, Azandaryani AH. Preparation of solid lipid nanoparticles as drug carriers for levothyroxine sodium with *in vitro* drug delivery kinetic characterization. Mol Biol Rep [Internet]. 2014;41(5):3521–7. Available from: https://doi.org/10.1007/s11033-014-3216-4

86. de Souza ALR, Andreani T, Nunes FM, Cassimiro DL, de Almeida AE, Ribeiro CA, et al. Loading of praziquantel in the crystal lattice of solid lipid nanoparticles: Studies by DSC and SAXS. J Therm Anal Calorim J Therm Anal Calorim [Internet]. 2012;108(1):353–60. Available from: https://akjournals.com/view/journals/10973/108/1/article-p353.xml

87. Oehlke J, Scheller A, Wiesner B, Krause E, Beyermann M, Klauschenz E, et al. Cellular uptake of an α-helical amphipathic model peptide with the potential to deliver polar compounds into the cell interior non-endocytically. Biochim Biophys Acta - Biomembr. 1998;1414(1–2):127–39. Available from: https://www.sciencedirect.com/science/article/pii/S0005273698001618

88. Silva S, Marto J, Gonçalves L, Almeida AJ, Vale N. Formulation, Characterization and Evaluation against SH-SY5Y Cells of New Tacrine and Tacrine-MAP Loaded with Lipid Nanoparticles. Nanomaterials [Internet]. 2020 Oct 21;10(10):2089. Available from: https://www.mdpi.com/2079-4991/10/10/2089

89. Doktorovova S, Souto EB, Silva AM. Nanotoxicology applied to solid lipid

nanoparticles and nanostructured lipid carriers - A systematic review of *in vitro* data. Eur J Pharm Biopharm [Internet]. 2014;87(1):1–18. Available from: http://dx.doi.org/10.1016/j.ejpb.2014.02.005

90. Bocsik A, Gróf I, Kiss L, Ötvös F, Zsíros O, Daruka L, et al. Dual action of the PN159/KLAL/MAP peptide: Increase of drug penetration across caco-2 intestinal barrier model by modulation of tight junctions and plasma membrane permeability. Pharmaceutics. 2019;11(2). Available from: http://www.mdpi.com/1999-4923/11/2/73

91. Bocsik A, Walter FR, Gyebrovszki A, Fülöp L, Blasig I, Dabrowski S, et al. Reversible Opening of Intercellular Junctions of Intestinal Epithelial and Brain Endothelial Cells with Tight Junction Modulator Peptides. J Pharm Sci. 2016;105(2):754–65. Available from: https://linkinghub.elsevier.com/retrieve/pii/S0022354915001331

Chapter 4
Nanoparticle surface Functionalization

4.1. Introduction

Functionalization of NPs surface can be a useful technique to enhance the potential of the nanosystem in development. These surface modifications include conjugation of different molecules of interest such as chemicals, active biomolecules, oligonucleotides, peptides, antibodies, aptamers, and more (1). This strategy enables linkage of diagnostic, therapeutic, and theragnostic molecules that promote targeting, cellular delivery, and avoid degradation (2). Conjugation of molecules on NPs surface can occur through physical absorption with non-covalent interactions or by direct binding through covalent conjugation. Focusing on physical adsorption, the molecule of interest is linked to the surface by weak interactions which includes electrostatic interactions, hydrogen binding, hydrophobic, and Van der Waals attractive forces (3). This method is simple, less time-consuming, and do not require NPs or molecules modifications (3). For instance, there are some peptides that can be used to improve transport across membranes through energy-independent pathways (4), also known as CPP. CPP are characterized as short peptides with less than 30 amino acid residues with the ability to interact with cellular membrane promoting endocytosis. Furthermore, CPP can form CPP/cargo complexes and successfully deliver to the cell's different types of drugs, biomolecules, NPs, and liposomes against a variety of diseases (5). MAP, a model amphipathic peptide, was developed with special design to ensure amphipathic structure and high membrane cellular interaction (6,7). The CPP MAP, under the right conditions, demonstrates high cellular penetration through multiple mechanisms (non-endocytic and endocytic) (7,8) and delivers different cargo into cell compartments (9–12). And other that can be used such has Neuropeptide Y (NPY).

NPY is a 36-amino-acid neuropeptide that is synthetized, processed, and stored in neurons (13). NPY is highly expressed on central and peripheral neurons but is more prevalent in cortical areas, limbic system, amygdala, hippocampus, hypothalamus, and more (14,15). In addition, NPY can act as a neurotransmitter or neuromodulator and displays multiple functions including balance of food intake (16), energy metabolism, blood pressure, regulate smooth muscle tone, balance with cognitive functions, and more (17–19). Different peptide fragments can arise from NPY mRNA sequence and its

expression of NPY can be affected by classic neurotransmitters, steroid hormones, and growth factors (19,20) and is mainly found in GABA neurons. For instance, C-terminal amphipathic end as the most structural importance, α-helix is important for receptor binding selectivity and its biological effect and polyproline type II helix is linked with secondary and tertiary structure stability (17). At molecular level, NPY exerts its functions through binding and activation of different receptors such as Y1, Y2, Y4, Y5, and Y6 that are coupled with G-proteins (18). Although NPY has been described with the main functions in recent research papers, it has become clearer that NPY can exert a wide range of molecular functions crucial to neuronal protection and proliferation (15). Several studies have demonstrated a close relationship of NPY with inhibition of noradrenaline release and inhibition of voltage-dependent Ca^{2+} channel resulting in a decrease in Ca^{2+} intracellular influx (21). Moreover, NPY can modulate neurogenesis and neurotrophins (22,23), decrease excitotoxicity (24), regulate calcium homeostasis (21), and attenuate neuroinflammation (25), making a good candidate as a therapeutic molecule against central nervous systems disorders (anxiety, epilepsy, depression, ischemia), and neurodegenerative diseases. The increase of world population life-spam neurodegenerative diseases is becoming more prevalent. Several studies have shown that NPY is a key neurological biomarker demonstrating NPY mRNA expression, and NPY binding sites are affected in different ways for each neurological disease. For instance, in AD, researchers observed decreased NPY levels and NPY receptors in patients' brain (cerebral cortex and hippocampus), decreased NPY levels in cerebrospinal fluid (CSF), and decreased NPY levels in peripheral plasma. This decrease is associated with the neurodegeneration progress. In PD patients, the opposite was observed; that is an increase in NPY mRNA expression levels on striatum and this phenom its related with an endogenous protective response mechanism to neurodegeneration occurring (26). In a study conducted by Croce and his team, a close link between neurotrophins expression and NPY treatment was demonstrated. The authors exposed both neuroblastoma cell line and primary neuron cells to toxic concentrations of amyloid beta peptide and NPY treatment leading to neuroprotection, increased neurotrofins expression, and promoted cell survival (22,23). Another study demonstrated that NPY delivery to the brain of AD model mice resulted in a decrease of neurodegeneration and improvement in memory (27). Furthermore, Decressac and his team demonstrated that NPY injection led to neuroprotection of nigral dopamine neurons through Y2 activation in PD mice models (28). The authors also modified the disease course of Huntington's disease transgenic mice (29).

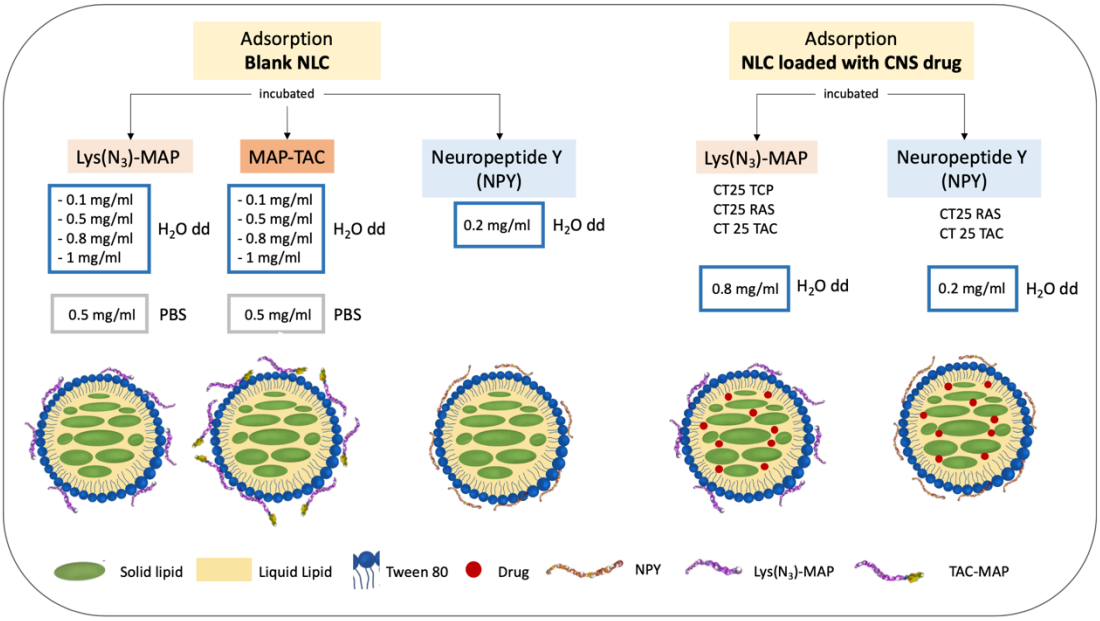


Figure 4.1 - Graphical representation of adsorption method applied with the three peptides, NLCs, different concentrations, and medium conditions conducted in this project.

4.2. Overview

In this Chapter 4, was applied an adsorption method to functionalize three different peptides onto NLC surface and conduct an initial NP characterization to determine some evidence of peptide absorption (Figure 4.1). We demonstrated how adsorption of NPY, an CPP lysine-modified MAP (Lys(N_3)-MAP) and CPP/cargo complex (TAC-MAP) can affect particle size, PI, and ZP.

4.3. Materials and Methods

4.3.1. Materials

TAC (9-amino-1,2,3,4-tetrahydroacridine hydrochloride hydrate), TCP ((±)-trans-2-Phenylcyclopropylamine), RAS (N-Propargyl-1(R)-aminoindan methanesulfonate), and buffer solution (PBS—pH 7.4) were acquired from Sigma-Merck (Merck Life Science S.L.U., Algés, Portugal). Diethylene glycol monoethyl ether (Transcutol® HP®) and glyceryl dibehenate (Compritol® 888 ATO) were a kind gift from Gattefossé (Neuilly-Sur-Seine, France). T80 was purchased from J. Vaz Pereira S.A. (Sintra, Portugal). Neuropeptide Y was Sigma- Merck (Merck Life Science S.L.U., Algés, Portugal).

Peptides MAP and Lys(N_3)-MAP, TAC-MAP, and RAS-MAP. Briefly, MAP was synthetized through Fmoc/tBu SPPS methodologies assisted with microwave (MW) energy, using a Liberty Microwave Peptide Synthesizer. Conjugation with TAC or RAS was achieved through “click chemistry” −a CuAAC reaction.

4.3.2. Nanoparticle Preparation

Blank, RAS-loaded, TAC-loaded, and TCP-loaded NLC were already prepared in a previous work with modification of a hot HSH method. Around 300 mg of Compritol® 888 ATO was melted at a temperature of 80 ◦C. RAS, TAC, and TCP were dissolved in the liquid lipid Transcutol® HP (at theoretical concentrations of 25% w/w), and then added to the molten solid lipid. A hot aqueous phase consisting of 10 mL ultra-purified water with 3% of T80 was added to the lipid phase under high-shear homogenization at 12,300 rpm for 10 min on a Silverson SL2 (UK), in a water bath to maintain 80 ◦C. Afterwards, the NLC dispersion was cooled in an ice bath with gentle stirring for 5 min. Each formulation was carried out in triplicates (n = 3). The final dispersion was sealed and stored at 4 ◦C until further use.

4.3.3. Peptide and Peptide Conjugate Adsorption Method

NPY, Lys(N_3)-MAP, and TAC-MAP conjugate adsorbed onto NLC. The method was carried out with the incubation of 150 µL and 300 µL of NLC formulation (Blank and/or drug encapsulated) with different peptide solution: NPY (0.2 mg/mL) in ultra-purified water; Lys(N_3)-MAP (0.1–1 mg/mL) in ultra-purified water and (0.5 mg/mL) in PBS pH 7.4; TAC-MAP (0.1–1 mg/mL) in ultra-purified water and (0.5 mg/mL) in PBS pH 7.4, at 37 ◦C, overnight with gentle horizontal shaking (300 rpm).

4.3.4. Nanoparticle Size and Surface Charge

The average particle size of NLC formulations before and after peptide adsorption was analyzed by photon correlation spectroscopy using a Zetasizer Nano S (Malvern Instruments, UK). Measurements were made at a scattering angle of 173◦, at 25 ◦C after appropriate dilution (1:5) in filtered purified water. All results obtained were expressed as average particle size and PI. Furthermore, ZP determination was performed by anemometry using a Zetasizer Nano Z (Malvern Instruments, Malvern, UK). For that purpose, samples were placed in a specific cuvette where a potential of 150 mV was established after appropriate dilution (1:5) of the samples in filtered purified water. For all the measurements, three replicate samples were determined.

4.3.5. Statistical Analysis

Statistical analysis of the experimental data was performed using a two-way analysis of variance (two-way ANOVA) and differences between groups were tested by a two-way ANOVA with GraphPad Prism version 9.0 (GraphPad Software, San Diego, CA, USA). Data were expressed as mean SD or 95% confidence interval. A $p < 0.05$ value was considered significant. All data are shown as mean SD.

4.4. Results

4.4.1. CPP and CPP/Drug Complex Adsorption onto NLC Surface

4.4.1.1. Influence of Different Lys(N_3)-MAP Concentrations

After Lys(N_3)-MAP incubation with increased concentrations, we can observe some gradual increased changes to the particle size and ZP Figure 4.2 and Table 4.1). The data show after Lys(N_3)-MAP incubation the CT25 Blank (CT25 B) NLC formulation significantly increased the size from 140 nm to up to 170 nm at a higher concentration of 1 mg/mL. The graphic shows a sustained increase of CT25 B size depending on the amount of Lys(N_3)-MAP use. On the other hand, PI results in a slight increase after peptide incubation. For instance, the ZP values demonstrated significant differences dependent on concentration. CT25 B incubation with 0.1 mg/mL, 0.5 mg/mL, 0.8 mg/mL, and 1 mg/mL resulted in a ZP change from −7.88 mV to −1.89 mV, −0.05 mV, 0.85 mV, and 1.27 mV, respectively.

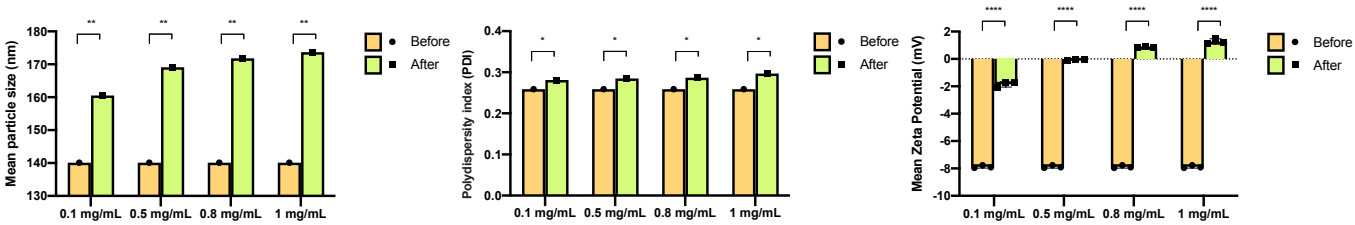


Figure 4.2 - Particle size, polydispersity index, and zeta potential of blank CT25 NLC before and after adsorption experiments with different peptide concentrations of Lys(N_3)-MAP at 37 °C with incubation in ultra-purified double distilled water (H_2O dd); mean ± SD, *n* = 3. Statistical analysis between the control groups was performed using two-way ANOVA with Tukey's multiple comparisons test (* $p < 0.05$; ** $p < 0.01$; **** $p < 0.0001$).

Table 4.1 - Resume data analysis from all the adsorption experiments conducted in this article.

NLC	Incubation conditions	PS (nm)	PI	ZP (mV)
CT25 B	H_2O dd	140.1	0.259	-7.88
CT25 B (300 µL)	H_2O dd	146.5	0.265	-8.53
CT25 B	Lys(N_3)-MAP 0.1 mg/mL in H_2O dd	160.5	0.281	-1.89
CT25 B	Lys(N_3)-MAP 0.5 mg/mL in H_2O dd	169.1	0.285	-0.05
CT25 B	Lys(N_3)-MAP 0.8 mg/mL in H_2O dd	171.8	0.287	0.85
CT25 B	Lys(N_3)-MAP 1 mg/mL in H_2O dd	173.7	0.297	1.27
CT25 TAC	H_2O dd	159.5	0.258	-9.73
CT25 RAS	H_2O dd	104.8	0.210	-9.39
CT25 TCP	H_2O dd	144.5	0.254	-9
CT25 TAC	Lys(N_3)-MAP 0.8 mg/mL in H_2O dd	200.5	0.305	1.28
CT25 RAS	Lys(N_3)-MAP 0.8 mg/mL in H_2O dd	112.6	0.251	1.23
CT25 TCP	Lys(N_3)-MAP 0.8 mg/mL in H_2O dd	177.3	0.287	1.85
CT25 B	TAC-MAP 0.1 mg/mL in H_2O dd	158.3	0.288	-1.65
CT25 B	TAC-MAP 0.5 mg/mL in H_2O dd	164.6	0.270	0.16
CT25 B	TAC-MAP 0.8 mg/mL in H_2O dd	167.6	0.272	0.3
CT25 B	TAC-MAP 1 mg/mL in H_2O dd	165.9	0.287	0.55
CT25 B (300 µL)	TAC-MAP 0.5 mg/mL in H_2O dd	164.9	0.296	-0.54
CT25 B	PBS (pH 7.4)	141.2	0.264	-7.82

CT25 B	Lys(N_3)-MAP 0.5 mg/mL in PBS PBS (pH 7.4)	267.8	0.887	2.83
CT25 B	TAC-MAP 0.5 mg/mL in PBS PBS (pH 7.4)	217.6	0.350	-2.16
CT25 B	NPY 0.2 mg/mL in H_2O dd	143.1	0.269	-23.27
CT25 TAC	NPY 0.2 mg/mL in H_2O dd	160.4	0.261	-25.20
CT25 RAS	NPY 0.2 mg/mL in H_2O dd	105.3	0.222	-21.73

* H_2O dd – Double distilled ultra-purified water; TAC – tacrine; RAS – rasagiline; TCP – tranyl-cypromine; B – Blank; PBS – phosphate buffered saline; PS – particle size; PI – polydispersity index; ZP – zeta potential;

4.4.1.2. Influence of Lys(N_3)-MAP Adsorbed into Drug Loaded NLC

When analyzing the influence of different drug-loaded NLC formulations with the fixed concentration of 0.8 mg/mL of Lys(N_3)-MAP, the results showed similar changes before and after incubation (Figure 4.3 and Table 4.2). There was no significant increase in the NLC particle size, and a significant increase in PI values was found. For CT25 loaded with TAC (CT25TAC) before incubation particle size and PI were 159.5 nm and 0.258, respectively and after Lys(N_3)-MAP incubation the values were 200.5 nm and 0.305. The CT25 loaded with RAS (CT25RAS) before incubation particle size and PI were 104.8 nm and 0.210 and after Lys(N_3)-MAP incubation the values were 112.6 nm and 0.251, respectively. TCP loaded CT25 (CT25TCP) before incubation particle size and PI were 146.5 nm and 0.254 and after Lys(N_3)-MAP incubation the values were 158.3 nm and 0.288, respectively. As expected, the ZP after incubation switched from negative to positive in all CT25 drug-loaded NLC formulations.

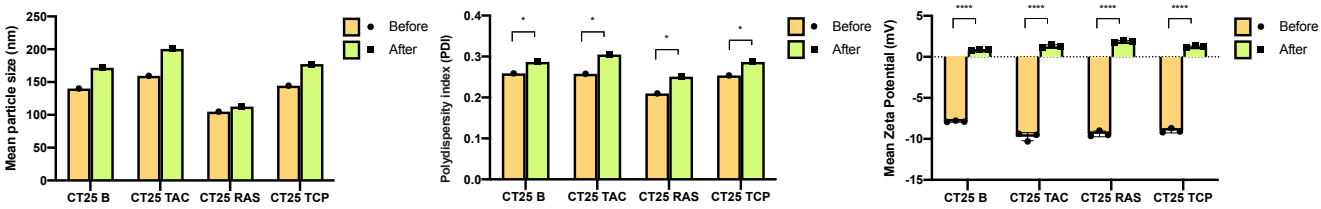


Figure 4.3 - Particle size, polydispersity index and zeta potential of CT25 B and drug load CT25 NLC before and after adsorption experiments with 0.8 mg/mL Lys(N_3)-MAP at 37 °C with incubation in H_2O dd; mean ± SD, n = 3. Statistical analysis between the control groups was performed using two-way ANOVA with Tukey's multiple comparisons test (* $p < 0.05$; **** $p < 0.0001$).

4.4.1.3. Influence of Different TAC-MAP Concentrations

This analysis was conducted to evaluate the influence of crescent concentration of TAC-MAP on CT25 B physicochemical parameters. The data showed a significant increase in CT25 B particle size after incubation, values ranging from 140 nm before incubation to up to 165.9 nm after TAC-MAP incubation (Figure 4.4). PI values indicate no significant change in CT25 B formulation after TAC-MAP incubation independent of the concentration used. The mean ZP analysis demonstrated significant increase in CT25 B surface charge after TAC-MAP incubation dependent on concentration applied. Control CT25 B showed a ZP of −7.88 mV, whereas 0.1 mg/mL resulted in an increase to −1.65 mV; 0.5 mg/mL to 0.16 mV; 0.8 mg/mL to 0.30 mV; and 1 mg/mL to 0.55 mV.

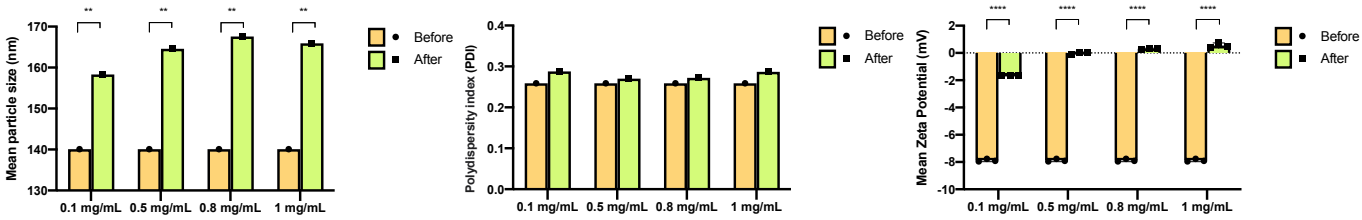


Figure 4.4 - Particle size, polydispersity index and zeta potential of blank CT25 NLC before and after adsorption experiments with different TAC-MAP concentrations at 37 °C with incubation in H_2O dd; mean ± SD, n = 3. Statistical analysis between the control groups was performed using two-way ANOVA with Tukey's multiple comparisons test (** $p < 0.01$; **** $p < 0.0001$).

4.4.1.4. Influence of CT25 B Amount on TAC-MAP Adsorption

Another parameter was assessed to determine the influence of the quantity of CT25 B NLC in solution when the same concentration of TAC-MAP was applied. The data showed that the increase in the amount of CT25 B in solution lead to the same differences in characterization values before and after TAC-MAP incubation (Figure 4.5).

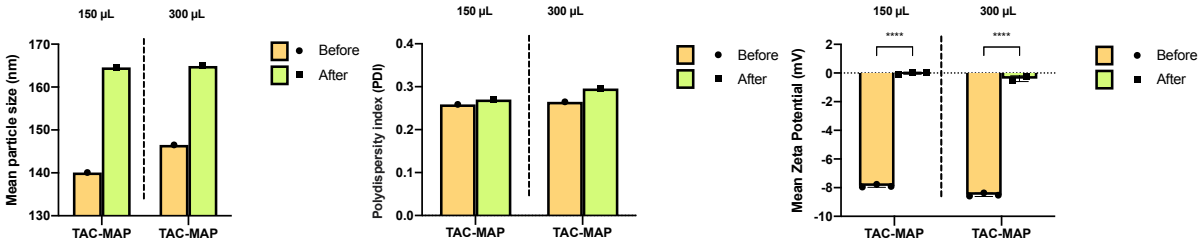


Figure 4.5 - Particle size, polydispersity index and zeta potential of different initial amount of blank CT25 NLC before and after adsorption experiments with 0.5 mg/mL TAC-MAP at 37 °C with incubation in H_2O dd; mean ± SD, n = 3. Statistical analysis between the control groups was performed using two-way ANOVA with Tukey's multiple comparisons test (**** $p < 0.0001$).

4.4.1.5. Influence of Incubation Medium H_2O vs. PBS on Peptide Adsorption

In order to predict a more physiological context, we compared the differences obtain from incubation of CT25 B with 0.5 mg/mL of Lys(N_3)-MAP and TAC-MAP in phosphate buffered solution (PBS pH 7.4). From this analysis, the results demonstrated some differences between the two incubation mediums (Figure 4.6). For instance, particle size increases substantially in both peptides when incubated with PBS medium. After Lys(N_3)-MAP was incubated with CT25 B in H_2O dd medium, the particle size increased around 20%, on the other hand, PBS medium incubation resulted in 90% particle size increase. For the PI and ZP the increase was higher, after Lys(N_3)-MAP incubation on PBS the values increased around 236% and 10.65 mV, respectively (Figure 4.6). After TAC-MAP was incubated with CT25 B in H_2O dd medium the particle size increased around 18%, on the other hand, PBS medium incubation resulted in 54% particle size increase. For the PI and ZP the same increase was observed, after TAC-MAP incubation on PBS the values increased around 33% and 5.66 mV, respectively (Figure 4.6).

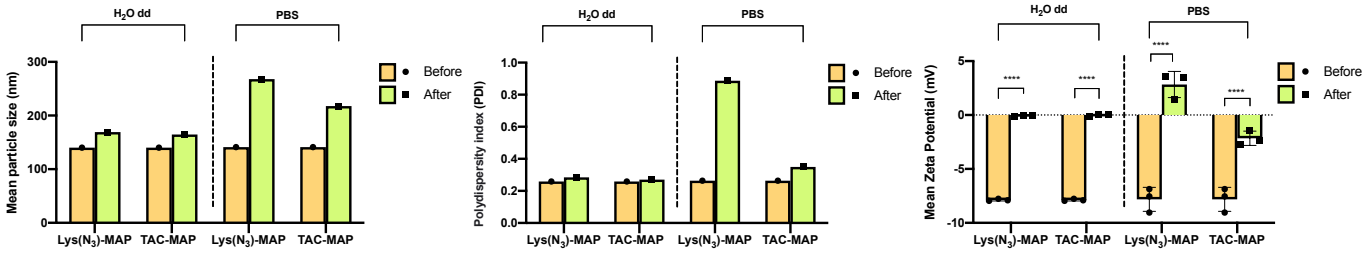


Figure 4.6 - Particle size, polydispersity index, and zeta potential of blank CT25 NLC before and after adsorption experiments with 0.5 mg/mL Lys(N_3)-MAP and 0.5 mg/mL TAC-MAP at 37 °C with different incubation medium H_2O dd and PBS; mean ± SD, *n* = 3. Statistical analysis between the control groups was performed using two-way ANOVA with Tukey's multiple comparisons test (**** $p < 0.0001$).

4.4.1.6. Neuropeptide Y Adsorption onto NLC Surface

Potential therapeutic peptide NPY was incubated with CT25 B and drug-loaded CT25 NLC. The characterization on its particle size, PI, and ZP is expressed in Figure 4.7 and Table 4.1. The results showed similar particle size and PI values before and after NPY incubation. Although, ZP analysis after NPY incubation resulted in a decrease in all NLC tested, independent of the type of drug encapsulated. For the CT25 B there was a decrease in ZP from −7.88 mV to −23.27 mV; for CT25TAC the ZP decreased from −9.73 mV to −25.2 mV; and for CT25RAS from −9.39 mV to −21.73 mV.

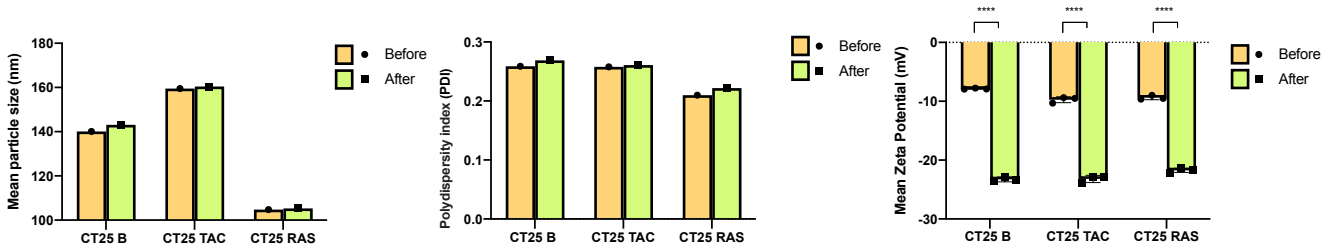


Figure 4.7 - Particle size, polydispersity index, and zeta potential of CT25 B and drug load CT25 NLC before and after adsorption experiments with NPY at 37 °C with incubation in H_2O dd; mean ± SD, *n* = 3. Statistical analysis between the control groups was performed using two-way ANOVA with Tukey's multiple comparisons test (**** $p < 0.0001$).

4.5. Discussion

Molecular interactions are important to understand and determined certain biological phenomena such as peptide adsorption, cell adhesion, and biological membrane interaction. Adsorption methods have been widely applied to functionalize different NPs with a variety of molecules. Some of them have been coated with PEG, T80, antibodies, peptides, and even drugs for different purposes such as disease diagnostic, treatment, and delivery (30–35). In this project, we conducted three peptide adsorption experiments onto NLC surface and observed the physicochemical changes occurring on NLC suspension in terms of particle size, PI, and ZP through dynamic light scattering analyses and anemometry. ZP analysis is crucial for the characterization of NP-based drug delivery systems. From the data, we can deduce the stability of NPs in suspension. A high value of ZP ±30 mV is linked with repulsive electrostatic forces between NPs which is related with higher stability and decreased NP aggregation in suspension (35). The ZP can also vary depending on pH of the suspension medium. The influence of pH can be determined by calculation of the isoelectric point. Moreover, ZP can be a powerful indicator for the characterization of NPs surface overall charge and indicates a possible molecule adsorption (36). In this article several parameters were evaluated to ensure a protocol optimization and determine the differences that can occur in different method conditions. The data obtain from increased peptide concentrations in NLC incubation demonstrated a concentration-dependent increase in particle size, PI, and ZP for both Lys(N_3)-MAP and TAC-MAP. The increase of particle size could indicate the formation of a multilayer peptide on CT25 B surface (Figure 4.8—multilayer hypothesis), already observed in other similar articles (37,38). The results from ZP analysis showed a concentration-dependent increase in mean ZP where at higher concentration of 1 mg/mL peptide the CT25 B surface charge changes to positive. This ZP increase could result in enhanced destabilization of CT25 B formulation due to a decrease in repulsion forces leading to the observed increase of PI values. In addition to this, this surface charge increase corroborates with peptide adsorption in a concentration-dependent manner. Both peptides are characterized to have a positive net charge which could explain this increased surface charge. On the other hand, incubation of Lys(N_3)-MAP and NPY on loaded drug NLC did not change the overall values when compared to the values obtain for CT25 B. ZP confirmed peptide adsorption in all NLCs irrespective of the drug being associated or not.

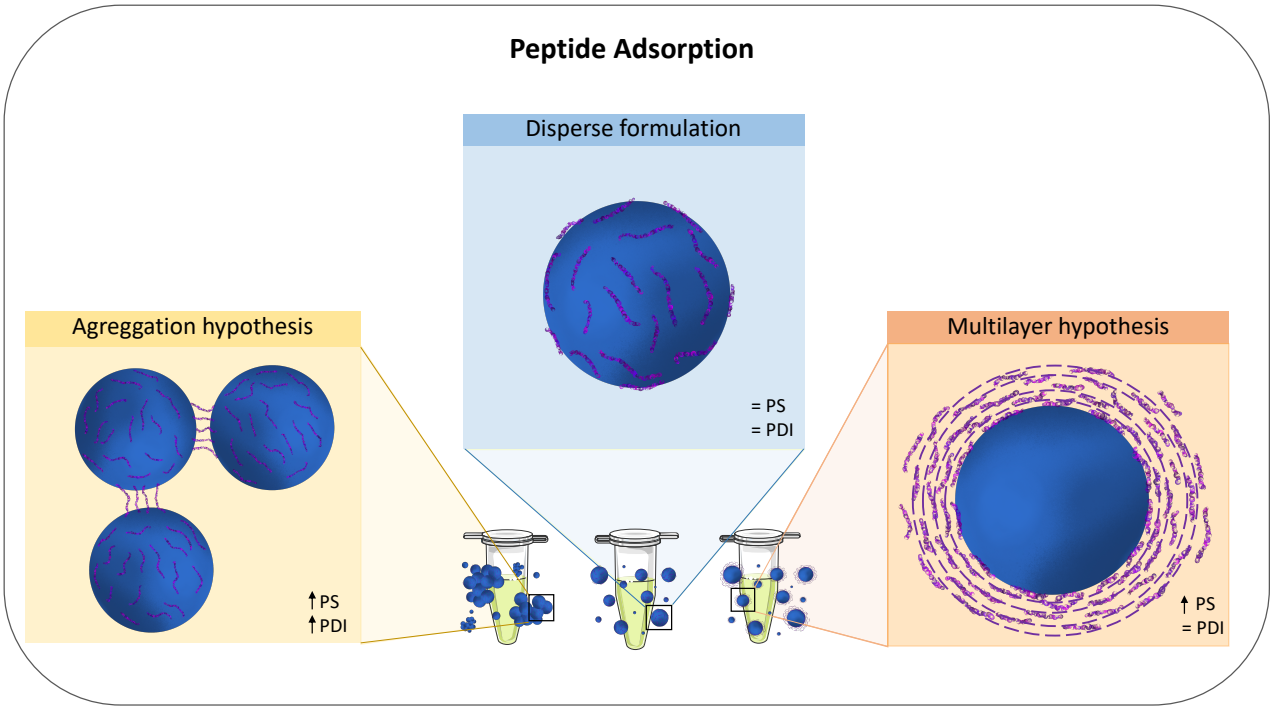


Figure 4.8 - Schematic representation of three hypotheses occurring through the data obtain in this project to explain the differences on particle size and PDI observed.

The use of different incubation medium was also evaluated, and results demonstrated high differences between H_2O dd and PBS incubation. In the physiological state with PBS after peptide incubation we observed a significant increase in particle size allied with increase in PI values. This data suggests that in PBS, Lys(N_3)-MAP adsorption led to NLC aggregation in suspension (Figure 4.8 - aggregation hypothesis). Several studies demonstrated that MAP tends to aggregate in monomers when close to lipidic cell membranes (8,39,40); similar mechanism might be involve due to lipidic proprieties of the NLC formulation. The data resulted from ZP analysis showed some differences from PBS incubation when compared to H_2O dd incubation. Indicating that this functionalized NPs have different physicochemical proprieties in physiologic conditions which will result in different behavior in a possible systemic administration. These results demonstrated the importance to test formulations in different physiologic conditions which is crucial to understand and predict the type of behavior our NPs delivery systems will have when administrated *in vivo*. Furthermore, with this method, ZP shows that NPY was successfully adsorbed into CT25 B and drug loaded CT25. The ZP values indicated the NPY surface adsorption led to more stable NLC formulations due to higher mean ZP

value obtained (Figure 4.8 - disperse formulation). This initial analysis demonstrated promising results with successful adsorption of these three peptides onto NLC surface. Still, more experiments are needed to be conducted to better understand the types of interactions that are occurring. By analyzing the proprieties and structure of both peptides and NLC components we can propose two ways of adsorption that might be happening. First, the polyethylene oxide chains-exposed hydrogen groups can interact with amine groups present in the peptide sequences leading to the formation of hydrogen bonds. The second hypothesis is the interaction of NLC lipophilic part with peptides by the formation of hydrophobic bonds or through van der Waals attractive forces. Taking in consideration the isoelectric points, net charge, and average hydrophilicity of Lys(N_3)-MAP and NPY proprieties we could predict that adsorption occur on the negatively charged NLC surface. Furthermore, several studies have demonstrated the use of T80 in the NLC formulation has an important role in adsorption of human plasma proteins in particular apolipoprotein E that can promote transport across BBB through low density receptor (41–43).

4.6. References

1. Gaspar DP, Faria V, Quintas JP, Almeida AJ. Targeted Delivery of Lipid Nanoparticles by Means of Surface Chemical Modification. Curr Org Chem [Internet]. 2017 Nov 28;21(23):2360–75. Available from: http://www.eurekaselect.com/146869/article

2. Avvakumova S, Colombo M, Tortora P, Prosperi D. Biotechnological approaches toward nanoparticle biofunctionalization. Trends Biotechnol [Internet]. 2014 Jan;32(1):11–20. Available from: http://dx.doi.org/10.1016/j.tibtech.2013.09.

3. Cagliani R, Gatto F, Bardi G. Protein Adsorption: A Feasible Method for Nanoparticle Functionalization? Materials (Basel) [Internet]. 2019 Jun 21;12(12):1991. Available from: https://www.mdpi.com/1996-1944/12/12/1991

4. Gupta B, Levchenko TS, Torchilin VP. Intracellular delivery of large molecules and small particles by cell-penetrating proteins and peptides. Adv Drug Deliv Rev [Internet]. 2005;57(4):637–51. Available from: https://www.sciencedirect.com/science/article/pii/S0169409X04002716

5. Xie J, Bi Y, Zhang H, Dong S, Teng L, Lee RJ, et al. Cell-Penetrating Peptides in Diagnosis and Treatment of Human Diseases: From Preclinical Research to Clinical Application. Front Pharmacol [Internet]. 2020 May 20;11:697. Available from: https://www.frontiersin.org/article/10.3389/fphar.2020.00697

6. Steiner V, Schär M, Börnsen KO, Mutter M. Retention behaviour of a template-assembled synthetic protein and its amphiphilic building blocks on reversed-phase columns. J Chromatogr A. 1991 Nov 8;586(1):43–50. Available from: https://linkinghub.elsevier.com/retrieve/pii/002196739180023A

7. Oehlke J, Scheller A, Wiesner B, Krause E, Beyermann M, Klauschenz E, et al. Cellular uptake of an α-helical amphipathic model peptide with the potential to deliver polar compounds into the cell interior non-endocytically. Biochim Biophys Acta - Biomembr. 1998;1414(1–2):127–39. Available from: https://www.sciencedirect.com/science/article/pii/S0005273698001618

8. Scheller A, Wiesner B, Melzig M, Bienert M, Oehlke J. Evidence for an amphipathicity independent cellular uptake of amphipathic cell-penetrating peptides. Eur J Biochem [Internet]. 2000 Oct;267(19):6043–50. Available from: http://doi.wiley.com/10.1046/j.1432-1327.2000.01681.x

9. Oehlke J, Wallukat G, Wolf Y, Ehrlich A, Wiesner B, Berger H, et al. Enhancement of intracellular concentration and biological activity of PNA after conjugation with a cell-penetrating synthetic model peptide. Eur J Biochem. 2004;271(14):3043–9. Available from: https://onlinelibrary.wiley.com/doi/10.1111/j.1432-1033.2004.04236.x

10. Oehlke J, Lorenz D, Wiesner B, Bienert M. Studies on the cellular uptake of substance P and lysine-rich, KLA-derived model peptides. J Mol Recognit [Internet]. 2005 Jan;18(1):50–9. Available from: https://onlinelibrary.wiley.com/doi/10.1002/jmr.691

11. Kenien R, Zaro JL, Shen W-C. MAP-mediated nuclear delivery of a cargo protein. J Drug Target [Internet]. 2012 May 1;20(4):329–37. Available from: https://doi.org/10.3109/1061186X.2011.649481

12. Kenien R, Shen WC, Zaro JL. Vesicle-to-cytosol transport of disulfide-linked cargo mediated by an amphipathic cell-penetrating peptide. J Drug Target. 2012; Available from: http://www.tandfonline.com/doi/full/10.3109/1061186X.2012.719899

13. Tatemoto K, Carlquist M, Mutt V. Neuropeptide Y - A novel brain peptide with structural similarities to peptide YY and pancreatic polypeptide. Nature. 1982;296(5858). Available from: http://www.nature.com/articles/296659a0

14. Adrian TE, Allen JM, Bloom SR, Ghatei MA, Rossor MN, Roberts GW, et al. Neuropeptide Y distribution in human brain. Nature. 1983;306(5943).

15. Hansel DE, Eipper BA, Ronnett G V. Neuropeptide Y functions as a neuroproliferative factor [Internet]. 2001. Available from: www.nature.com

16. Kalra SP, Kalra PS. Neuropeptide Y: A Physiological Orexigen Modulated by the Feedback Action of Ghrelin and Leptin [Internet]. Vol. 22, Endocrine. 2003. p. 49–55. Available from: http://link.springer.com/10.1385/ENDO:22:1:49

17. Dumont Y, Martel J, Fournier A, Stpierre S, Quirion R. Neuropeptide Y and neuropeptide Y receptor subtypes in brain and peripheral tissues. Prog Neurobiol [Internet]. 1992;38(2):125–67. Available from: https://www.sciencedirect.com/science/article/pii/030100829290038G

18. Sheikh SP, Williams JA. Structural characterization of Y1 and Y2 receptors for neuropeptide Y and peptide YY by affinity cross-linking. J Biol Chem [Internet].

1990 Jun 25;265(14):8304–10. Available from: https://linkinghub.elsevier.com/retrieve/pii/S0021925819390726

19. Magni P, Beretta E, Scaccianoce E, Motta M. Retinoic acid negatively regulates neuropeptide Y expression in human neuroblastoma cells [Internet]. Vol. 39, Neuropharmacology. 2000. Available from: www.elsevier.com/locate/neuropharm

20. Wernersson J, Johansson I, Larsson U, Minth-Worby C, Påhlman S, Andersson G. Activated transcription of the human neuropeptide Y gene in differentiating SH-SY5Y neuroblastoma cells is dependent on transcription factors AP-1, AP-2α, and NGFI. J Neurochem. 1998;70(5). Available from: http://doi.wiley.com/10.1046/j.1471-4159.1998.70051887.x

21. McDonald RL, Vaughan PFT, Beck-Sickinger AG, Peers C. Inhibition of Ca2+channel currents in human neuroblastoma (SH-SY5Y) cells by neuropeptide Y and a novel cyclic neuropeptide Y analogue. Neuropharmacology. 1995;34(11).

22. Croce N, Dinallo V, Ricci V, Federici G, Caltagirone C, Bernardini S, et al. Neuroprotective effect of neuropeptide Y against beta-amyloid 25-35 toxicity in SH-SY5Y neuroblastoma cells is associated with increased neurotrophin production. Neurodegener Dis. 2011 Jun;8(5):300–9.

23. Croce N, Ciotti MT, Gelfo F, Cortelli S, Federici G, Caltagirone C, et al. Neuropeptide Y protects rat cortical neurons against β-amyloid toxicity and re-establishes synthesis and release of nerve growth factor. ACS Chem Neurosci. 2012 Apr 18;3(4):312–8. Available from: https://pubs.acs.org/doi/10.1021/cn200127e

24. Pain S, Vergote J, Gulhan Z, Bodard S, Chalon S, Gaillard A. Inflammatory process in Parkinson disease: neuroprotection by neuropeptide Y. Fundam Clin Pharmacol [Internet]. 2019 Oct;33(5):544–8. Available from: https://onlinelibrary.wiley.com/doi/10.1111/fcp.12464

25. Ferreira R, Santos T, Bernardino L. Novel role of neuropeptide y in the modulation of microglia activity. Adv Neuroimmune Biol. 2013;4(3):167–76.

26. Duarte-Neves J, Pereira de Almeida L, Cavadas C. Neuropeptide Y (NPY) as a therapeutic target for neurodegenerative diseases. Neurobiol Dis [Internet]. 2016 Nov 1;95:210–24. Available from: https://linkinghub.elsevier.com/retrieve/pii/S0969996116301802

27. Spencer B, Potkar R, Metcalf J, Thrin I, Adame A, Rockenstein E, et al. Systemic central nervous system (CNS)-targeted delivery of neuropeptide y (NPY) reduces neurodegeneration and increases neural precursor cell proliferation in a mouse model of Alzheimer disease. J Biol Chem. 2016 Jan 22;291(4):1905–20. Available from: http://dx.doi.org/10.1074/jbc.M115.678185

28. Decressac M, Barker RA. Neuropeptide Y and its role in CNS disease and repair. Exp Neurol [Internet]. 2012 Dec;238(2):265–72. Available from: http://dx.doi.org/10.1016/j.expneurol.2012.09.004

29. Decressac M, Wright B, Tyers P, Gaillard A, Barker RA. Neuropeptide Y modifies the disease course in the R6/2 transgenic model of Huntington's disease. Exp Neurol [Internet]. 2010 Nov;226(1):24–32. Available from: http://dx.doi.org/10.1016/j.expneurol.2010.07.022

30. Curry D, Cameron A, MacDonald B, Nganou C, Scheller H, Marsh J, et al. Adsorption of doxorubicin on citrate-capped gold nanoparticles: Insights into engineering potent chemotherapeutic delivery systems. Nanoscale. 2015;7(46):19611–9. Available from: http://xlink.rsc.org/?DOI=C5NR05826K

31. Perera YR, Xu JX, Amarasekara DL, Hughes AC, Abbood I, Fitzkee NC. Understanding the adsorption of peptides and proteins onto pegylated gold nanoparticles. Molecules. 2021 Oct 1;26(19). Available from: https://www.mdpi.com/1420-3049/26/19/5788

32. Zhang F, Liu J. Label-Free Colorimetric Biosensors Based on Aptamers and Gold Nanoparticles: A Critical Review. Anal Sens. 2021;1(1). Available from: https://onlinelibrary.wiley.com/doi/10.1002/anse.202000023

33. Tonigold M, Simon J, Estupiñán D, Kokkinopoulou M, Reinholz J, Kintzel U, et al. Pre-adsorption of antibodies enables targeting of nanocarriers despite a biomolecular corona. Nat Nanotechnol [Internet]. 2018;13(9):862–9. Available from: https://doi.org/10.1038/s41565-018-0171-6

34. Ruiz G, Ryan N, Rutschke K, Awotunde O, Driskell JD. Antibodies Irreversibly Adsorb to Gold Nanoparticles and Resist Displacement by Common Blood Proteins. Langmuir [Internet]. 2019 Aug 13;35(32):10601–9. Available from: https://doi.org/10.1021/acs.langmuir.9b01900

35. Mahmood S, Mandal UK, Chatterjee B, Taher M. Advanced characterizations of nanoparticles for drug delivery: investigating their properties through the

techniques used in their evaluations. Nanotechnol Rev [Internet]. 2017;6(4):355–72. Available from: https://doi.org/10.1515/ntrev-2016-0050

36. Ferraris S, Cazzola M, Peretti V, Stella B, Spriano S. Zeta Potential Measurements on Solid Surfaces for *in Vitro* Biomaterials Testing: Surface Charge, Reactivity Upon Contact With Fluids and Protein Absorption. Front Bioeng Biotechnol [Internet]. 2018;6. Available from: https://www.frontiersin.org/article/10.3389/fbioe.2018.00060

37. Puddu V, Perry CC. Peptide adsorption on silica nanoparticles: Evidence of hydrophobic interactions. ACS Nano. 2012 Jul 24;6(7):6356–63.

38. Daifullah AAM, Girgis BS, Gad HMH. A study of the factors affecting the removal of humic acid by activated carbon prepared from biomass material. Colloids Surfaces A Physicochem Eng Asp. 2004;235(1–3). Available from: https://linkinghub.elsevier.com/retrieve/pii/S0927775704000196

39. Blondelle SE, Houghten RA. Design of Model Amphipathic Peptides Having Potent Antimicrobial Activities. Biochemistry. 1992;31(50):12688–94.

40. Wadhwani P, Bürck J, Strandberg E, Mink C, Afonin S, Ulrich AS. Using a Sterically Restrictive Amino Acid as a 19 F NMR label To Monitor and To Control Peptide Aggregation in Membranes. J Am Chem Soc [Internet]. 2008 Dec 10;130(49):16515–7. Available from: https://pubs.acs.org/doi/10.1021/ja804928q

41. Göppert TM, Müller RH. Polysorbate-stabilized solid lipid nanoparticles as colloidal carriers for intravenous targeting of drugs to the brain: Comparison of plasma protein adsorption patterns. J Drug Target. 2005;13(3):179–87. Available from: http://www.tandfonline.com/doi/full/10.1080/10611860500071292

42. Aggarwal P, Hall JB, McLeland CB, Dobrovolskaia MA, McNeil SE. Nanoparticle interaction with plasma proteins as it relates to particle biodistribution, biocompatibility and therapeutic efficacy. Adv Drug Deliv Rev [Internet]. 2009/04/17. 2009 Jun 21;61(6):428–37. Available from: https://pubmed.ncbi.nlm.nih.gov/19376175

43. Alyautdin RN, Tezikov EB, Ramge P, Kharkevich DA, Begley DJ, Kreuter J. Significant entry of tubocurarine into the brain of rats by adsorption to polysorbate 80–coated polybutylcyanoacrylate nanoparticles: An in situ brain perfusion study. J Microencapsul [Internet]. 1998 Jan 1;15(1):67–74. Available from: https://doi.org/10.3109/02652049809006836

Chapter 5
Preliminary In-Silico approach

5.1. Introduction

Molecular docking is becoming a crucial tool in drug discovery to find and optimize lead compounds and can also be applied to predict in-silico experimental binding mode and affinity of a selective molecule to a binding site of the receptor of interest (1). During computational docking experiment, the computer generates several poses and compares scoring to the target molecule. The poses can be accepted or rejected based on the score obtain (2). Moreover, different programs can be employed for high throughput docking of a large database of molecules such as AutoDock Vina, DOCK, FlexX, GOLD, ICM (2). Another interaction observed was MAP had the ability to interact with cellular TJ and modulate TJ to enhance systemic delivery (3). TJ are composed by 3 main proteins (occluding, claudins and junctional adhesion molecules) and are important to promote integrity of cell barrier and its dynamic structure regulates endocytic processes (3). In recent years, this capability of MAP was further study by Bocsik and her team and several experiments were conducted in order to understand which TJ specific target is involved. The authors demonstrated that 10 μM for 1 h didn't cause significant change in metabolic activity of Caco-2 cell line or brain endothelial cells and show an increase molecular permeability through both barriers after MAP incubation (4). The authors based on affinity-binding measurements discovered that MAP was most effective as modulator of junctional permeability acting via claudin-1 and 5 (4). In addition, in a more recent study was demonstrated that MAP was successful to interact with TJ, promote enhance permeability of different compounds (such as quinidine and verapamil). The authors also showed a concentration-dependent effect of MAP with 3 μM resulting on significant changes in the Claudin-1 pattern and the actin cytoskeleton organization. These results allow the understanding that MAP can act on claudins 1, 4 and 7 and open cell-cell junctions. Through dock analysis the authors observed that Q44 and V55 residues of Claudin 1 and 7 can form a binding pocket for L11 of the peptide and lysine K1 and K5 and Leucine L6 and L17 interact with all three claudins tested (5).

5.2. Overview

In Chapter 5, was explored an in-silico receptor molecular docking assay to evaluate possible MAP interaction with NPY Y1 receptor and better understand a possible future interaction in cells with this membrane receptor.

5.3. Methods

5.3.1. Receptor Molecular Docking Assays

5.3.1.1. Model Preparation for Human Neuropeptide Y Y1 Receptor

A model for the human neuropeptide Y receptor type 1 (NPY1R) was prepared, starting from the 5ZBQ (6) crystallographic structure available on the Protein Data Bank (7) with a resolution of 2.70 Å. This structure represents NPY1R complexed with T4 Lysozyme and with the selective antagonist ligand UR-MK299 (6). In preparing the NPY1R model, the T4 lysozyme was removed, while UR-MK299 was extracted to be used as reference ligand for docking validation. Missing amino acid residue position (241 to 256) were modelled upon alignment with the Alphafold Model for this receptor (8).

CHARMM-GUI Membrane Builder (9) was used to position NPY1R into a 100 × 100 Å membrane bilayer, comprised of 145 cholesterol molecules, 149 1-palmitoyl-2-oleoyl-sn-glycero-3-phosphoethanolamine (POPE), and 135 palmitoylsphingomyelin (PSM) molecules, in agreement with the GPI-Anchored CD59 in human plasma membrane described by Lee and his team (10).

5.3.1.2. Preparation of MAP and NPY

Structures for MAP and NPY were prepared with AMBER21 software (11) using the xleap module and GaussView 5.0. Structures were placed in TIP3P periodic water boxes with a minimum distance of 12 Å of waters to the box edges. Periodic boundaries were applied, and the long-range electrostatic interactions were calculated using the particle mesh Ewald summation method. The cut-off value for the short-range electrostatic and Lennard–Jones interactions were set at 10.0 Å. The hydrogen bonds were constrained using the SHAKE algorithm. A time step of 2 fs was used.

Four minimization steps were performed to remove clashes and applied in the following order: 1. water molecule (2500 steps); 2. hydrogens atoms (2500 steps); 3. side chains of all the amino acid residues (2500 steps); and 4. full systems (10,000 steps). After minimization, a molecular dynamics equilibration procedure was performed for 50 ps, in which the systems were gradually heated to 310 K using a Langevin thermostat at constant volume (NVT ensemble). Finally, the production phase was run for a total of 1000 ps in an NPT ensemble at a pressure of 1 bar and a temperature of 310 K. This protocol is described in more detail in the literature (12–14). Stabilized conformations of MAP and NPY in water were taken from the equilibrated stage of both MD simulations and were used as starting point for flexible peptide docking calculation.

5.3.2. Docking

UR-MK299 antagonist was used as a reference to evaluate the accuracy of the docking protocol and to optimize it. The conformation of this ligand was randomized, and the ligand was redocked against the NPY1R-membrane model structure using the GOLD software (15) with the PLP scoring function (16). The binding pocket was defined as centered on the initial cavity defined by UR-MK299, plus a radius of 30 Å, encompassing the NPY1R amino acid residues in the outer membrane leaflet. The optimized protocol was later extended to enable the docking of MAP and NPY models.

5.4. Results and Discussion

5.4.1. Receptor Molecular Docking Assays

Figure 5.1 illustrates the comparison of the pose predicted using the optimized docking protocol in redocking UR-MK299 antagonist against the experimental NPY1R/UR-MK299 complex (PDB structure 5ZBQ). As can be seen, the optimized docking protocol is able to accurately reproduce the experimental structure, with a root-mean-square deviation (RMSD) of 0.86 Å, demonstrating its robustness.

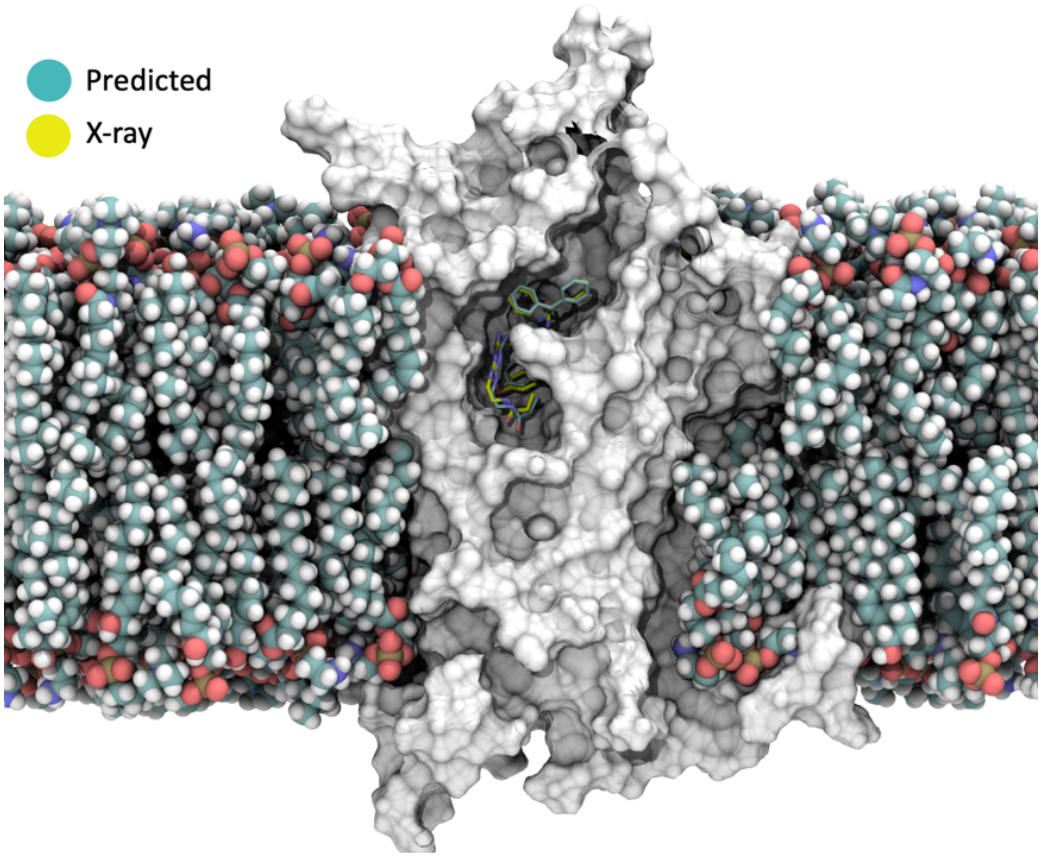


Figure 5.1 - Validation of the docking protocol by redocking UR-MK299 against NPY1R. In cyan, the conformation predicted from docking. In yellow the X-ray crystallography conformation. Slab-view representation, showing the plane of the interior binding pocket.

Table 5.1 presents the docking scores obtained with GOLD/PLP in docking MAP and NPY against NPY1R. The value obtained for the reference ligand, the UR-MK299 antagonist, is presented for comparison. The GOLD/PLP scoring function is dimensionless and scores higher values to molecules with the highest affinity (16). Values above 60 are normally considered to be indicative of strong association (17).

Table 5.1 - Docking scores of UR-MK299, MAP and NPY on NPY1R.

	UR-MK299	MAP	NPY
GOLD/PLP Score	107.70	101.29	95.12

The values presented in table 5.1 for MAP and NPY suggest that both peptides are able to strongly interact with the NPY1R receptor, with scores of 101.29 and 95.12, respectively. These values are very high and close to the docking score obtained for the reference antagonist ligand UR-MK299, reinforcing their potential as NPY1R binders.

The results suggest that MAP is able to bind with higher affinity to NPYR1 than NPY. Figure 5.2 shows the predicted dominant binding modes of MAP and NPY. As can be seen in figure 5.2, MAP is able to insert tightly inside NPYR1, occupying the binding pocket that was initially occupied by UR-MK299, and filling the most important interactions established by this antagonist.

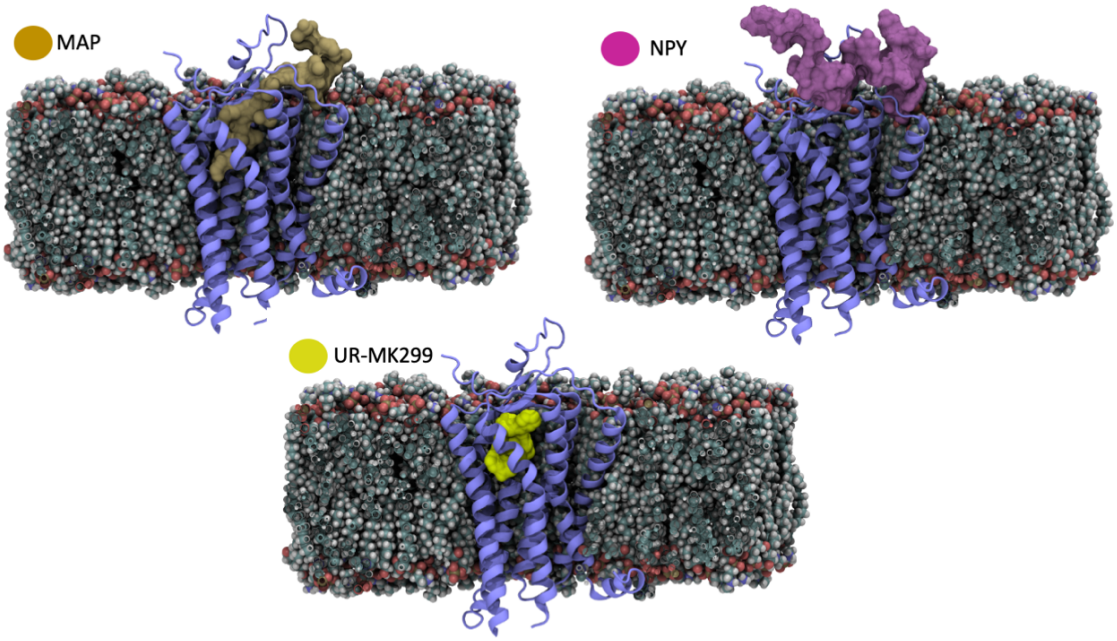


Figure 5.2 - Representation of the volume occupied by MAP, NPY and antagonist UR-MK299 when complexed with NPY1R, illustrating the different binding modes predicted for the two peptides and the one observed in the x-Ray of the complex formed with the antagonist molecule.

For NPY a similar binding mode was not identified. Nevertheless, the results show that NPY has the ability to establish strong interactions with the outer loops of NPY1R.

Figure 5.3 represents the main interactions established between MAP and NPY1R. MAP interacts preferentially through its N-terminal amino acid residues, with its Lys1-Lys9 portion inserting deep into the NPYR1 inside cavity. It forms important interactions with Gln219, Asn283 and Asp287, and Gln177. In addition, it establishes hydrophobic contacts with Leu26, Ile124, Phe173, and Phe302. Other relevant interactions were observed with Tyr100, Met103, Asp104, Leu215, and Asn299, near the cavity exit.

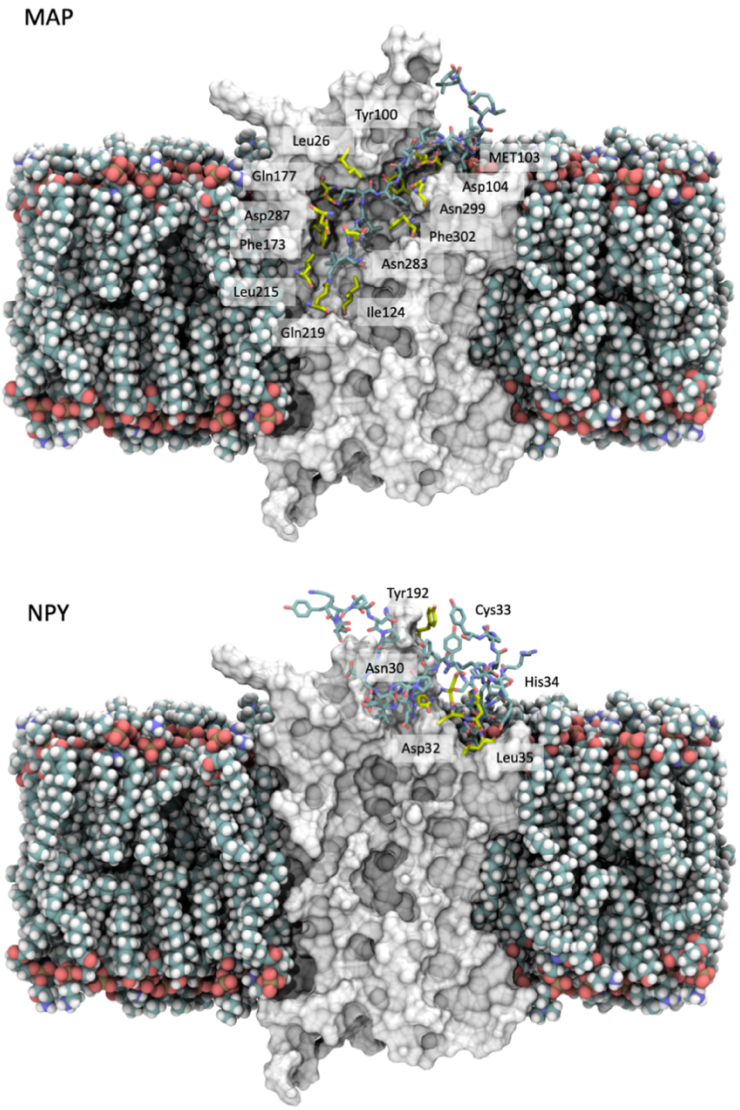


Figure 5.3 - Slab-view representation of the interaction of MAP and NPY with NPY1R, illustrating the most important interactions established.

5.5. Discussion

In the second part of the work, we evaluate the possible advantages from functionalization of the NLC surface with in-silico evaluation of interaction between NPY Y1 receptor and MAP. The structural information of the results obtained from the complex docking in-silico experience allows to clarify the mechanism of molecular recognition and a possible mode of interaction that could reflect the observed *in vitro* results in cells. Biochemical effects of an agonist and antagonist differ and produce different responses in the cells. Usually, agonists stabilize the receptor conformation in the active form whereas antagonists stabilize the receptor conformation in the inactive form and interfere with the binding of agonists (18). The overall results demonstrated strong association between MAP and NPY Y1 receptor when compared to both UR-ML299 antagonist and NPY. Moreover, docking assays demonstrated that MAP interacts through N-terminal amino acid residues with deep insertion into NPYR1 inside cavity such as the UR-ML299 antagonist. More studies must be included to better understand the possible cellular outcome that can arise from this MAP interaction with the NPY 1 receptor and important to evaluate if MAP has the capability to interact to other NPY receptors. These studies can be crucial to determining the advantage of this adsorption in the NLC surface.

5.6. References

1. Guedes IA, de Magalhães CS, Dardenne LE. Receptor-ligand molecular docking. Biophys Rev. 2014;6(1):75–87. Available from: http://link.springer.com/10.1007/s12551-013-0130-2

2. Mohan V, Gibbs A, Cummings M, Jaeger E, DesJarlais R. Docking: Successes and Challenges. Curr Pharm Des. 2005;11(3):323–33. Available from: http://link.springer.com/10.1007/s12551-013-0130-2

3. Johnson PH, Quay SC. Advances in nasal drug delivery through tight junction technology. Expert Opin Drug Deliv [Internet]. 2005 Mar 12;2(2):281–98. Available from: https://www.tandfonline.com/doi/full/10.1517/17425247.2.2.281

4. Bocsik A, Walter FR, Gyebrovszki A, Fülöp L, Blasig I, Dabrowski S, et al. Reversible Opening of Intercellular Junctions of Intestinal Epithelial and Brain Endothelial Cells with Tight Junction Modulator Peptides. J Pharm Sci. 2016;105(2):754–65. Available from: https://linkinghub.elsevier.com/retrieve/pii/S0022354915001331

5. Bocsik A, Gróf I, Kiss L, Ötvös F, Zsíros O, Daruka L, et al. Dual action of the PN159/KLAL/MAP peptide: Increase of drug penetration across caco-2 intestinal barrier model by modulation of tight junctions and plasma membrane permeability. Pharmaceutics. 2019;11(2). Available from: http://www.mdpi.com/1999-4923/11/2/73

6. Yang Z, Han S, Keller M, Kaiser A, Bender BJ, Bosse M, et al. Structural basis of ligand binding modes at the neuropeptide Y Y1 receptor. Nature [Internet]. 2018;556(7702):520–4. Available from: https://doi.org/10.1038/s41586-018-0046-x

7. Berman HM, Westbrook J, Feng Z, Gilliland G, Bhat TN, Weissig H, et al. The Protein Data Bank. Nucleic Acids Res. 2000 Jan;28(1):235–42.

8. Jumper J, Evans R, Pritzel A, Green T, Figurnov M, Ronneberger O, et al. Highly accurate protein structure prediction with AlphaFold. Nature [Internet]. 2021;596(7873):583–9. Available from: https://doi.org/10.1038/s41586-021-03819-2

9. Wu EL, Cheng X, Jo S, Rui H, Song KC, Dávila-Contreras EM, et al. CHARMM-GUI Membrane Builder toward realistic biological membrane simulations. J Comput Chem [Internet]. 2014 Oct 15;35(27):1997–2004. Available from: https://doi.org/10.1002/jcc.23702

10. Lee J, Patel DS, Ståhle J, Park S-J, Kern NR, Kim S, et al. CHARMM-GUI Membrane Builder for Complex Biological Membrane Simulations with Glycolipids and Lipoglycans. J Chem Theory Comput [Internet]. 2019 Jan 8;15(1):775–86. Available from: https://doi.org/10.1021/acs.jctc.8b01066

11. Case DA, Cheatham TE, Darden T, Gohlke H, Luo R, Merz KM, et al. The Amber biomolecular simulation programs. J Comput Chem [Internet]. 2005 Dec 1;26(16):1668–88. Available from: https://doi.org/10.1002/jcc.20290

12. Vieira TF, Magalhães RP, Simões M, Sousa SF. Drug Repurposing Targeting Pseudomonas aeruginosa MvfR Using Docking, Virtual Screening, Molecular Dynamics, and Free-Energy Calculations. Antibiotics [Internet]. 2022 Jan 31;11(2):185. Available from: https://www.mdpi.com/2079-6382/11/2/185

13. Quelhas D, Carneiro J, Lopes-Marques M, Jaeken J, Martins E, Rocha JF, et al. Assessing the effects of PMM2 variants on protein stability. Mol Genet Metab [Internet]. 2021 Dec;134(4):344–52. Available from: https://www.sciencedirect.com/science/article/pii/S1096719221008209

14. Vieira TF, Martins FG, Moreira JP, Barbosa T, Sousa SF. In Silico Identification of Possible Inhibitors for Protein Kinase B (PknB) of Mycobacterium tuberculosis. Molecules [Internet]. 2021 Oct 12;26(20):6162. Available from: https://www.mdpi.com/1420-3049/26/20/6162

15. Jones G, Willett P, Glen RC, Leach AR, Taylor R. Development and validation of a genetic algorithm for flexible docking11Edited by F. E. Cohen. J Mol Biol [Internet]. 1997;267(3):727–48. Available from: https://www.sciencedirect.com/science/article/pii/S0022283696908979

16. Korb O, Stützle T, Exner TE. Empirical Scoring Functions for Advanced Protein−Ligand Docking with plants. J Chem Inf Model [Internet]. 2009 Jan 26;49(1):84–96. Available from: https://doi.org/10.1021/ci800298z

17. Martins FG, Melo A, Sousa SF. Identification of New Potential Inhibitors of Quorum Sensing through a Specialized Multi-Level Computational Approach. Molecules [Internet]. 2021 Apr 29;26(9):2600. Available from: https://www.mdpi.com/1420-3049/26/9/2600

18. Gentilucci L, Tolomelli A, De Marco R, Artali R. Molecular Docking of Opiates and Opioid Peptides, a Tool for the Design of Selective Agonists and Antagonists, and for the Investigation of Atypical Ligand-Receptor Interactions. Curr Med Chem. 2012;19(11):1587–601. Available from: http://www.eurekaselect.com/openurl/content.php?genre=article&issn=0929-8673&volume=19&issue=11&spage=1587

Conclusions and Future Perspectives

The present Thesis includes the successful peptide synthesis of MAP and integration of three CNS drugs selected for their ability to conjugate linkage moieties to be further added into the MAP sequence. In Chapter 2, after extensive characterization and toxicity evaluation, the NLC formulation was achieved, comprising two main lipids (Compritol® 888 ATO and 25 % of Transcutol® HP), and the surfactant T80 at 3% (CT25 B). Even though, around 20 % cell viability was always observed in blank NLC, which was expected due to the presence of T80. Still, T80 is one of the few surfactants that are allowed to be parenteral administered in humans. In present study, toxicity is significant due to small working volumes of media used in the *in vitro* microenvironment approach. Moreover, this formulation resulted on high EE and DL values, high stability, less toxicity when compared with other formulations tested. Then, the dual activity of MAP, MAP derivates and MAP conjugates was observed in a concentration-depending manner with concentrations above 5 μM resulting on lytic activity against 3 relevant cell lines (Caco-2, MCF-7 and SH-SY5Y). In addition, NP encapsulation of peptide-drug conjugates led to an increase anti-proliferative activity at lower concentrations, resulting in decreased IC_{50} values.

The advantages of a possible surface modification with the successful adsorption of three peptides into NLC surface should also be noticed. This result can potentiate the development of NPs with the right peptide concentration on the surface, to increase drug delivery capabilities and enhance barrier and cellular uptake. Results suggest that MAP dual effect (penetration ability or cellular lytic effect) observed is influence by the concentration administered to the cells *in vitro*. The in-silico results indicated a third possible function of MAP, with strong interaction with neuronal receptor, thus might have some potential use on treatment of neurodegenerative diseases or promoting neuroprotective effects.

In conclusion the overall results lead to the validation of the potential use of NPs to enhance drug therapeutic efficacy requiring lower doses to exert the same effect as the free drug. This therapeutic efficacy can be study with more complex models, as in vivo models. For instances is important to address the advantages with the use of this NPs on BBB translocation through nasal administration versus parental injection.

Future perspectives rely on three main features: a) understanding MAP receptor activity interaction with neuronal receptors evaluating it's possible cellular mechanism; b) evaluating possible anti-cancer activity of the conjugates, in normal cells, 3D tumors spheroids and *in vivo* studies; c) after deeper NP physicochemical analysis with the evaluation of pH, viscosity and sterilization process we can introduce this NP systems in several *in vivo* models to test the delivery capabilities of the most promising NLC form.

CHAPTER 1

PEPTIDE SYNTHESIS

1.1. RAS-MAP

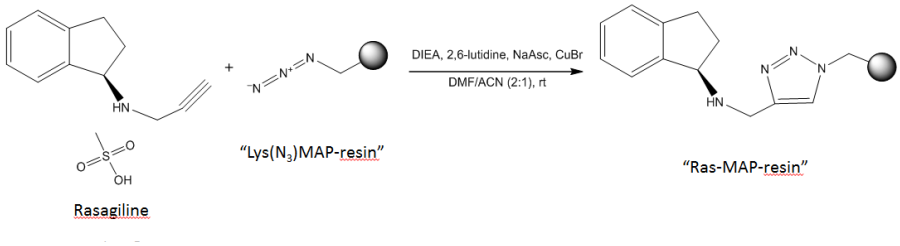


Figure S1.1 - Schematic representation of conjugate Ras-MAP-resin formation through click reaction (CuAAC); Structure of Ras-MAP conjugate.

1.2. Pra-MAP

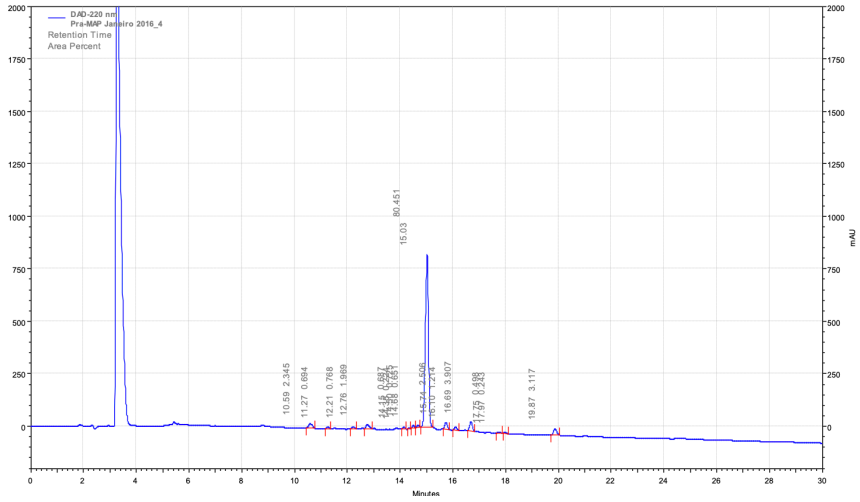


Figure S1.2 - Chromatogram of synthetic crude of Pra-MAP (**2**), acquired with a HPLC system, with a C18 column, using ACN and acidified water (0.05% TFA) as eluent, in gradient mode (0 – 100%), for 30 minutes, at a flow rate of 1 mL/min and detection at λ = 220 nm.

- Solid support: resin Rink Amide (0.38 mmol/g)
- Synthesis scale: 0.2 mmol
- Protection scheme: orthogonal (Fmoc/tBu)
- Pre-activation: 10 eq. DIEA, 5 eq. amino acid in 5 mL DMF
- Coupling agent: 5 eq. HBTU
- Deprotection: 5 mL 20% piperidine in DMF
- Cleavage: 95% TFA + 2.5% H_2O + 2.5% TIS, 1 mL/100 mg of peptidyl-resin, 2 h, room
- Temperature (only a small amount of peptidyl-resin was cleaved to allow HPLC and MS
- Analysis of the functionalized peptide)
- Purification: not done (the Pra-MAP served as a reaction intermediary)
- Purity (crude): 80.4%

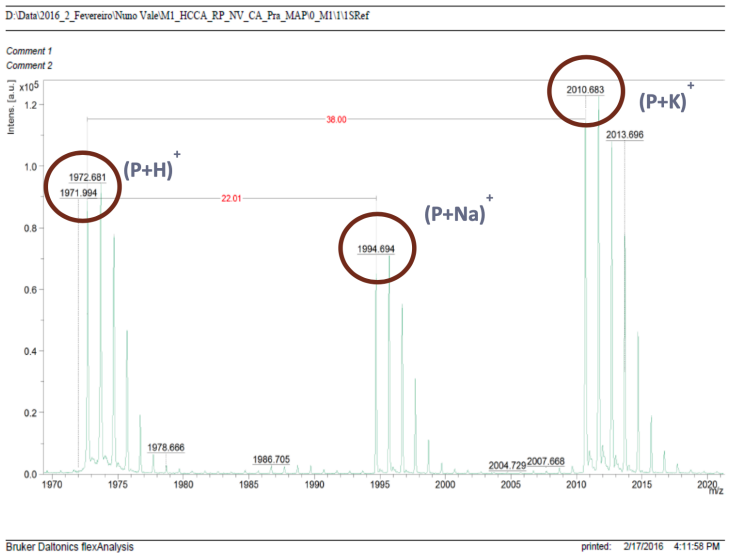


Figure S1.3 - MALDI-TOF mass spectrometry of synthetic crude of Pra-MAP

1.3. TAC-MAP

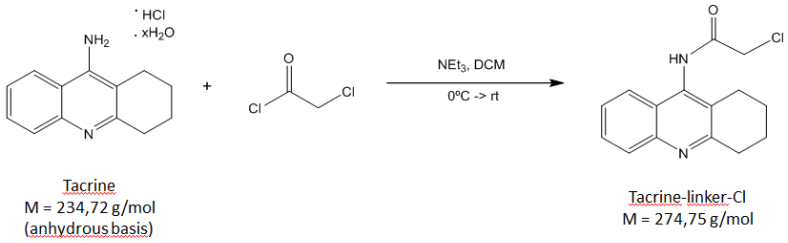


Figure S1. 4 - Schematic representation of synthesis of conjugate TAC-linker-Cl

- TAC pre-activation:
- 20 min stirring with 2 eq. NEt_3, in DCM (ice bath)
- m(TAC)= 200 mg (limitant reagent)
- Addition of 1.25 eq. chloroacethyl chloride (drop wise)
- Solvent: DCM (70 mL)
- Reaction time: 2h30

- Treatment: liquid-liquid extractions with DCM + NaCl (sat.)
- Purification: column in DCM/MeOH 100:1

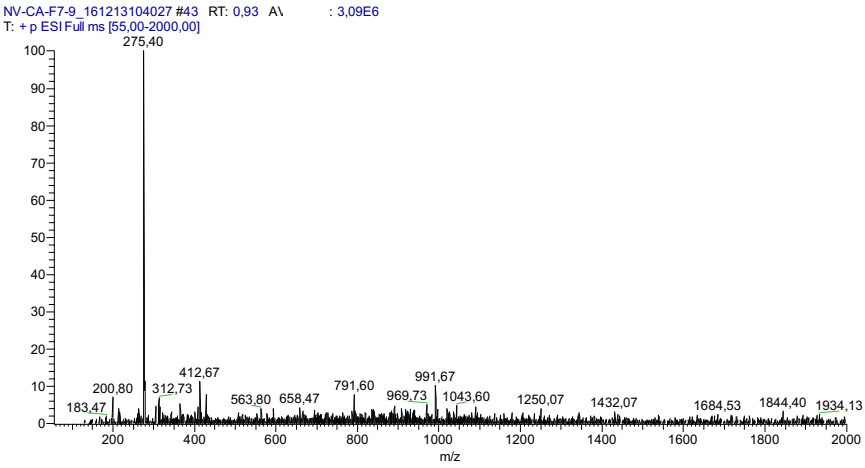


Figure S1.5 - Mass spectrum (LC-ESI/Orbitrap MS, positive mode) of the TAC-linker-Cl.

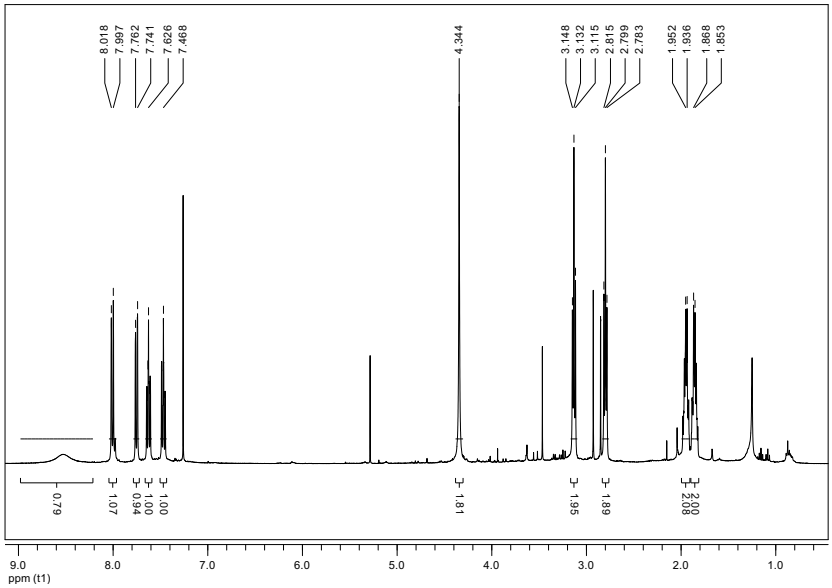


Figure S1.6 - H NMR of TAC-linker-Cl. ^{1}H NMR (400 MHz, $CDCl_3$) δ(ppm) 8.52 (s, 1H), 8.00 (d, *J* = 8.4 Hz, 1H), 7.75 (d, *J* = 8.4 Hz, 1H), 7.67 – 7.57 (m, 1H), 7.51 – 7.41 (m, 1H), 4.34 (s, 2H), 3.13 (t, *J* = 6.5 Hz, 2H), 2.80 (t, *J* = 6.4 Hz, 2H), 2.01 – 1.90 (m, 2H), 1.89 – 1.81 (m, 2H).

- Aspect: brownish solid
- m(product) = 65.4 mg
- η = 27.5 %

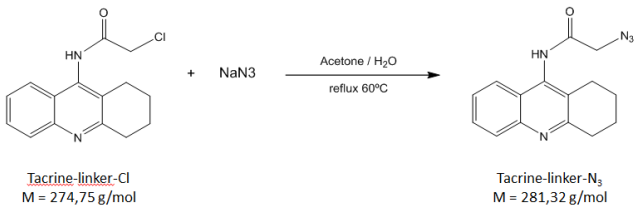


Figure S1.7 - Schematic representation of conjugate TAC-linker-N_3

- m(TAC-linker-Cl)= 18.4 mg (limitant reagent)
- Solvent: Acetone (5 mL) + H_2O (2.5 mL)
- Sodium azide (excess) – 5 eq.
- Reflux 60 °C
- Reaction time: overnight
- Treatment: liquid-liquid extractions with DCM + H_2O

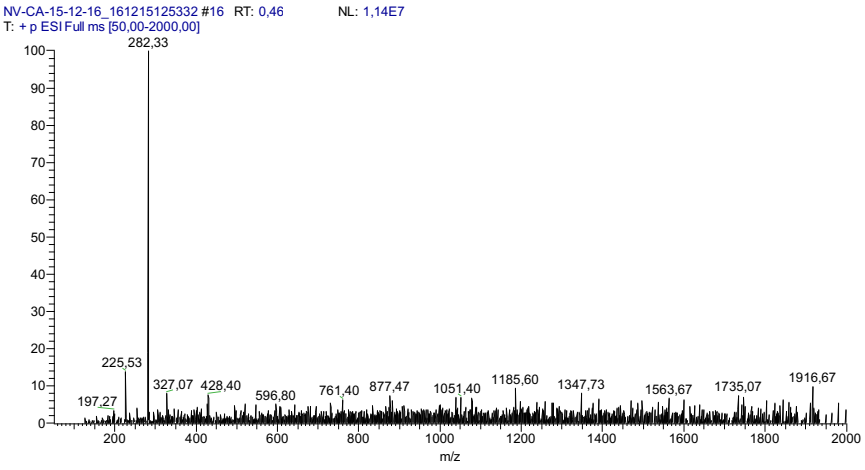


Figure S1.8 - Mass spectrum (LC-ESI/Orbitrap MS, positive mode) of TAC-linker-N_3.

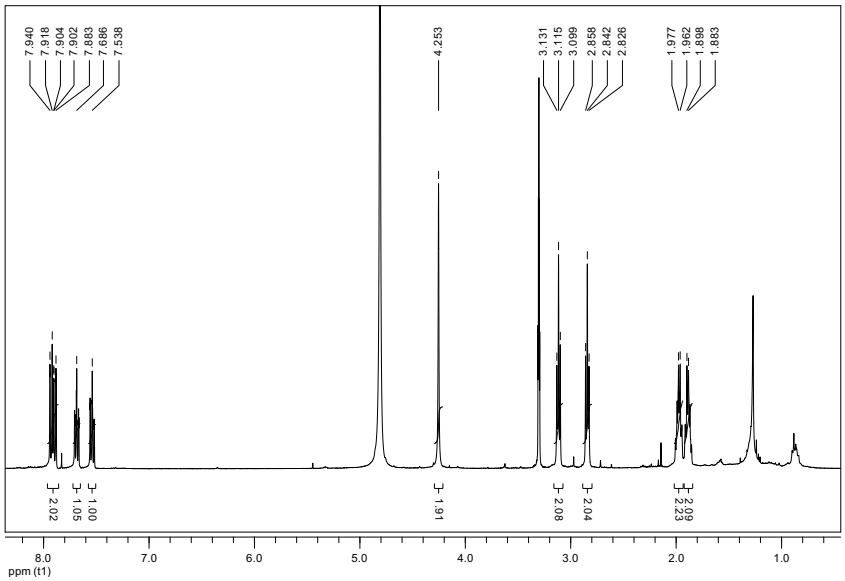


Figure S1.9 - 1H NMR of TAC-linker-N_3. 1H NMR (400 MHz, CD3OD) δ(ppm) 7.92 (dd, J = 14.4, 8.4 Hz, 2H), 7.72 – 7.66 (m, 1H), 7.57 – 7.51 (m, 1H), 4.25 (s, 2H), 3.12 (t, J = 6.5 Hz, 2H), 2.84 (t, J = 6.5 Hz, 2H), 2.01 – 1.94 (m, 2H), 1.92 – 1.84 (m, 2H).

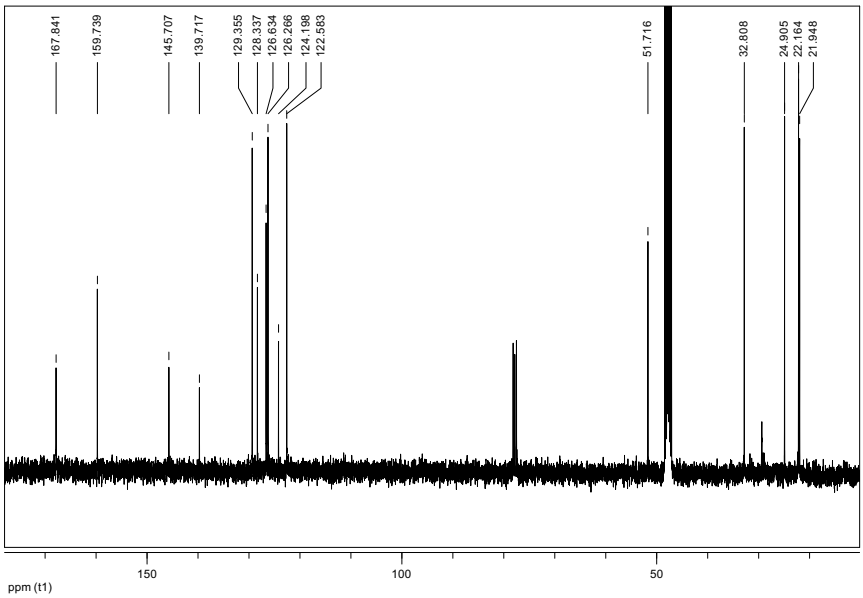


Figure S1.10 - ^{1}H NMR of TAC-linker-N_3. ^{13}C NMR (101 MHz, CD_3OD) δ 169.11 (C=O), 161.01 (C), 146.98 (C), 140.99 (C), 130.63 (CH), 129.61 (CH), 127.91 (CH), 127.54 (CH), 125.47 (CH), 123.85 (CH), 52.99 (CH_2), 34.08 (CH_2), 26.18 (CH_2), 23.43 (CH_2), 23.22 (CH_2).

- Aspect: Orange brownish solid
- m(product) = 20.2 mg
- η = 100 %

1.4. TCP-MAP

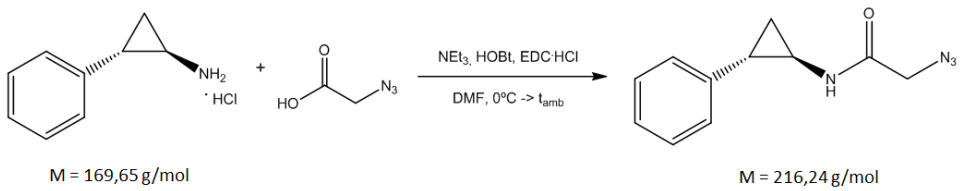


Figure S1.11 - Schematic representation of conjugate TCP-linker-N_3.

- Azidoacetic acid pre-activation (2 eq.);
- 2 h stirring with 2.5 eq. NEt_3, 2 eq. HOBt and 3 eq. EDC.HCl (ice bath)
- m(2-PCPA)= 100 mg (limitant reagent)
- Solvent: DMF (10 mL) - too much volume
- Reaction time: 20h
- Treatment: liquid-liquid extractions with AcOEt + [NaCl (sat.) + $NaHCO_3$ (sat.) + CH_3COOH 5% + H_2O]
- Purification: Filtration with SiO_2 ('Dry Column Vacuum Chromatography'): eluent Hex/AcOEt 1:3 + AcOEt

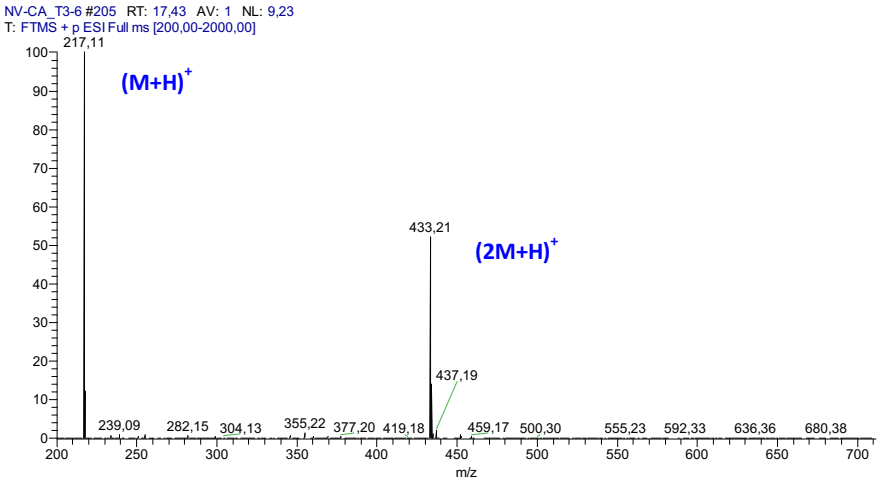


Figure S1.12 - Mass spectrum (LC-ESI/Orbitrap MS, positive mode) of 2-TCP-linker-N_3.

- Aspect: yellow oil (when warm), solidifies when cold
- η = 94.4 %

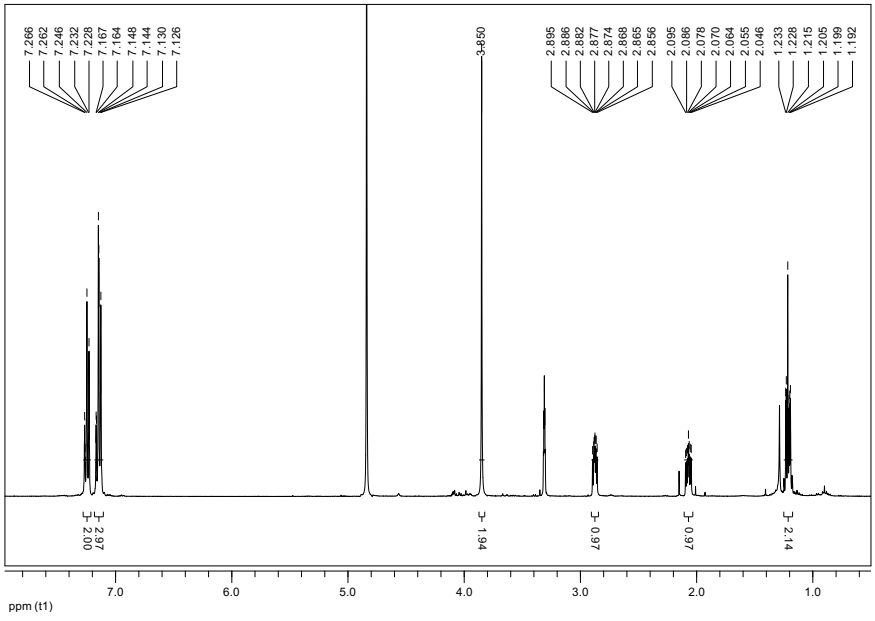


Figure S1.13 - ^{1}H NMR (400 MHz, MeOD) δ(ppm) 7.27 – 7.23 (m, 2H), 7.17 – 7.13 (m, 2H), 3.85 (s, 2H), 2.87 (m, 1H), 2.09 – 2.05 (m, 1H), 1.23 – 1.19 (m, 2H).

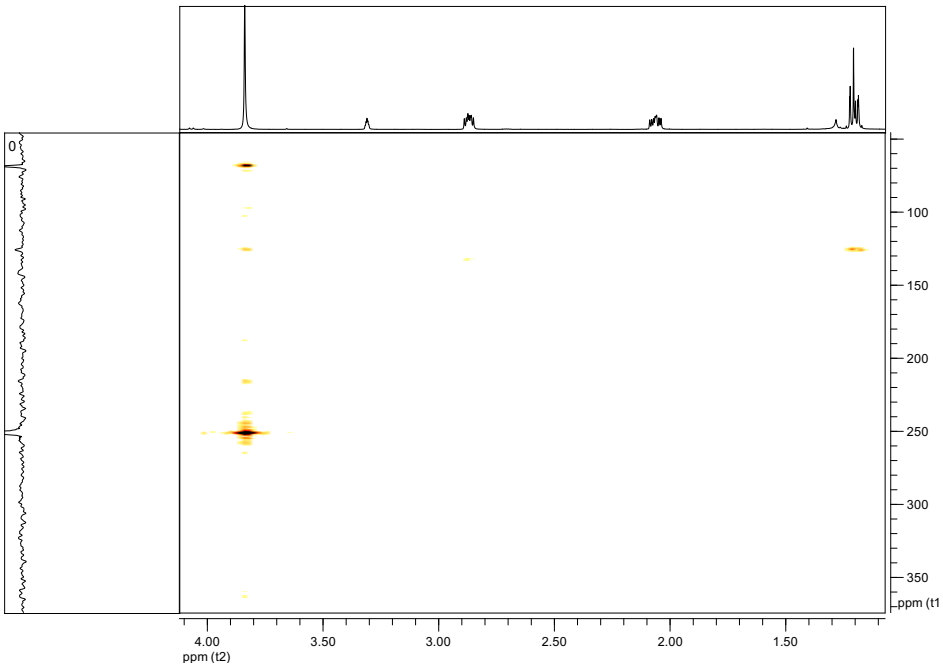


Figure S1.14 - HMBC- ^{15}N (CD_3OD).

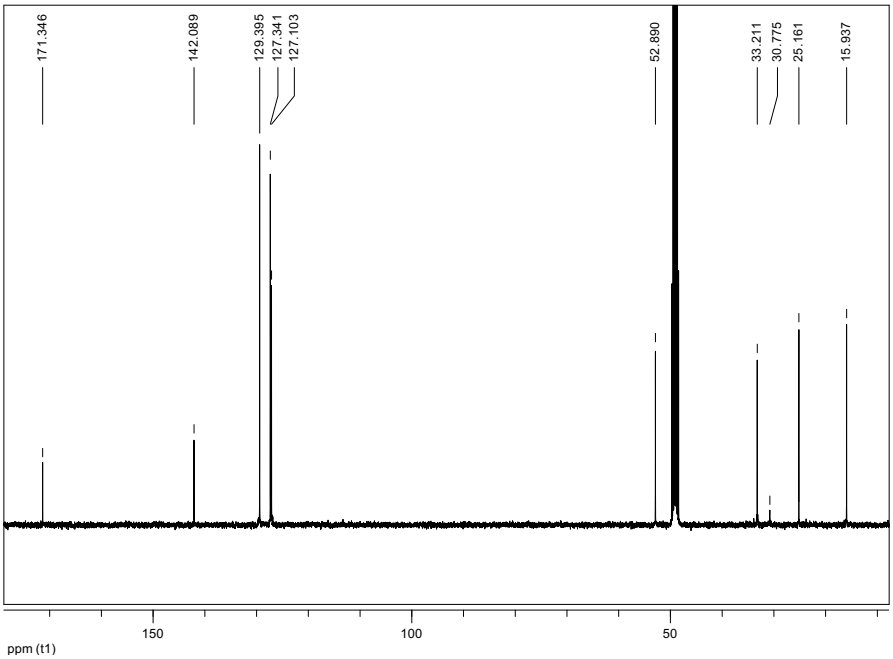


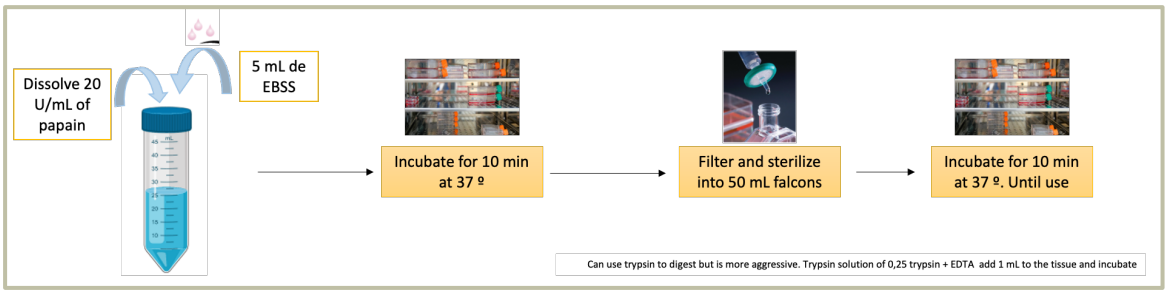
Figure S1.15 - NMR (101 MHz, MeOD) δ(ppm) 171.35 (C=O), 142.09 (C), 129.40 (2xCH), 127.34 (3xCH), 127.10 (CH_2), 52.89 (CH_2), 33.21 (CH), 25.16 (CH), 15.94 (CH_2).

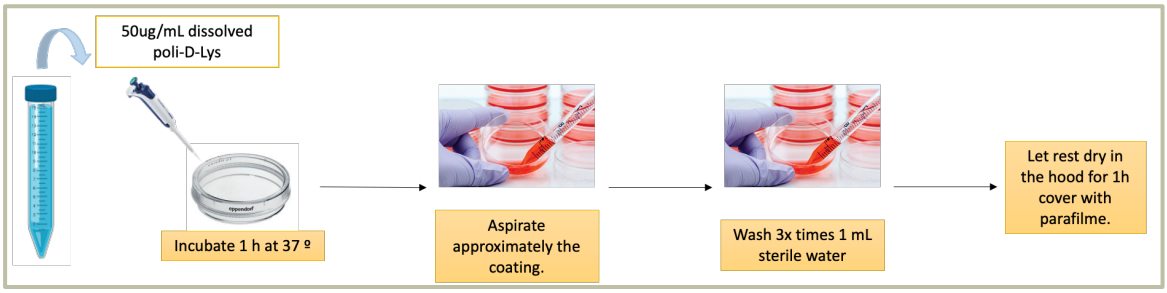
CHAPTER 2

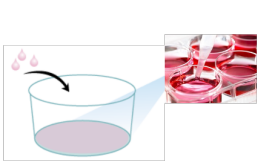
Nanoparticles optimization

2.1. Stablish a primary neuronal cell culture

2.1.1. Protocol design



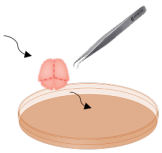




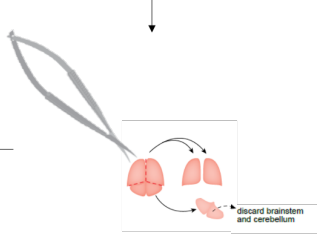
Day 1
Prepared cell culture plates by coating with Poly-D-Lysine or L-Polyornithine. *



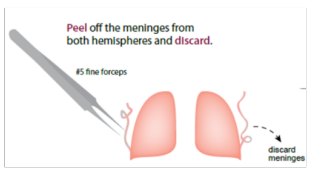
Day 2
Decapitate mice and isolate rat brain

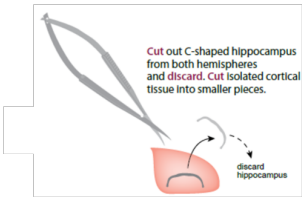


Remove the brains from the heads and place on ice cold hibernate A.



Separate the cortical hemispheres and discard the brainstem and cerebellum





Next page

(Continues in the next page)

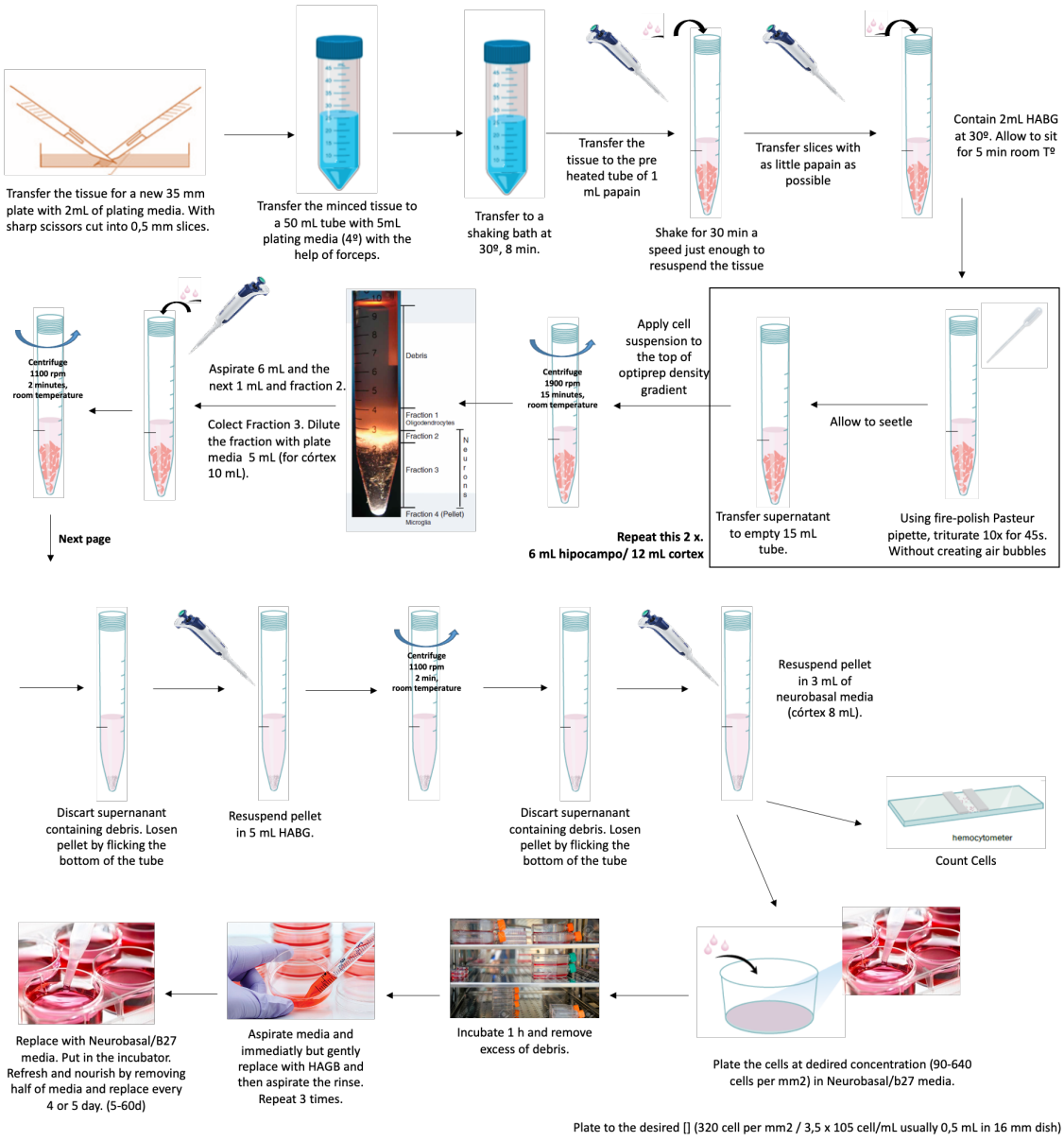
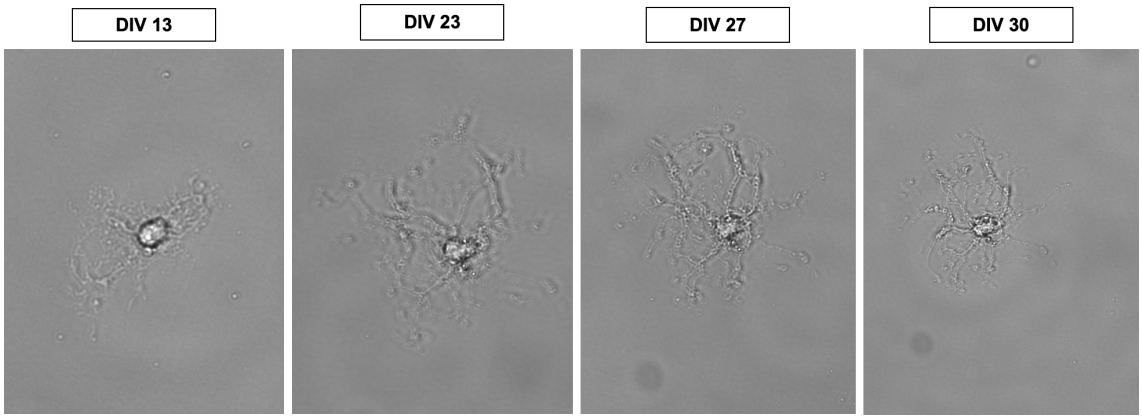


Figure S2.1 - Protocol implemented to establish and isolate a primary neuronal cell line.

2.1.2. Isolation of neurons - Results

The advantages of using primary cellular culture in the experiments are: this cells represent better *in vivo* tissue environment and can mimic the *in vivo* state and retain genetic integrity. To represent better the toxicity assays this protocol was conducted several times and general results obtain are demonstrated in Figure S2.2, S2.3 and S2.4. The Figure S2.2, demonstrated some neurons that were isolated, and its morphologic appearance was observed throughout different DIV. Still, the quantity of neurons isolated was insufficient to conduct any experiment. In Figure S2.3, we can see a group of isolated cells that differ a bit from neurons and could possibly be astrocytes wrongly isolated. One of the experiments conducted also resulted on the development of a contamination and excess tissue debris seen in microscope (Figure S2.4). After evaluation of the results, and demonstration of several of the advantages of using primary cell culture such as a fresh isolation every time, needs optimized culture conditions, present slower cell growth and higher cost. On the other hand, cell lines can be proliferated indefinitely, are more robust and easier to work with well-established protocols. The decision was to stop the isolation of neurons and search for several cell lines that could benefit the work and continuing the toxicity assays.



(Continues in the next page)

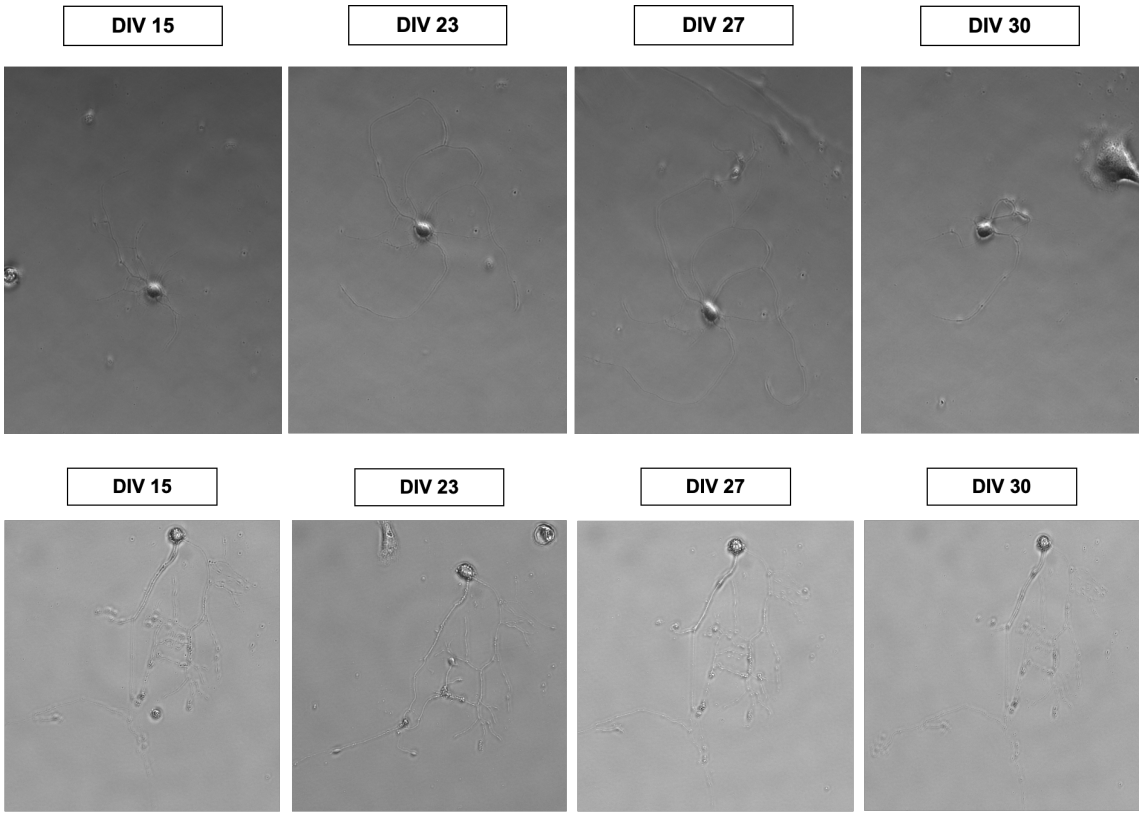


Figure S2.2 - Microscope images of identified neurons isolated from the experiment and protocol applied at different days *in vitro* (DIV).

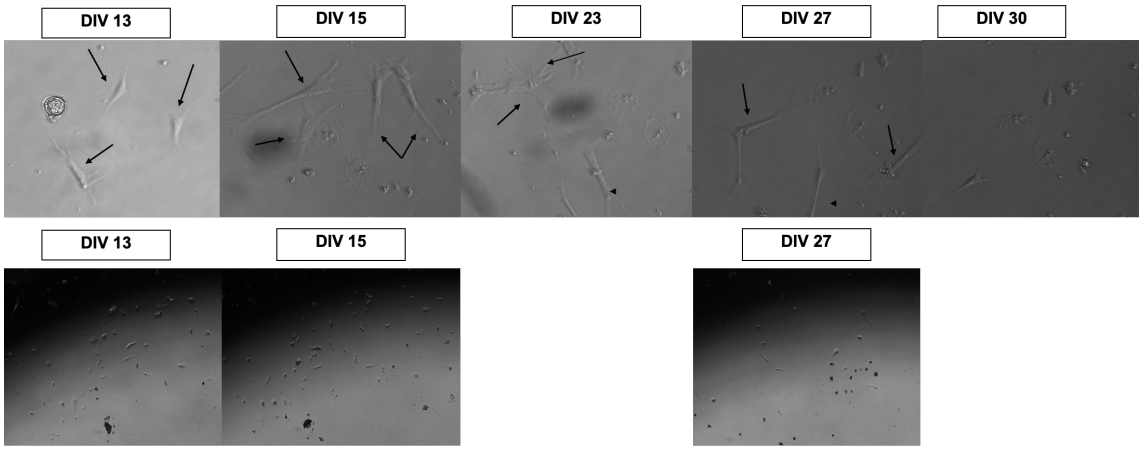


Figure S2.3 - Microscope images of possible astrocytes wrongly isolated from the experiment and protocol applied at different days *in vitro* (DIV).

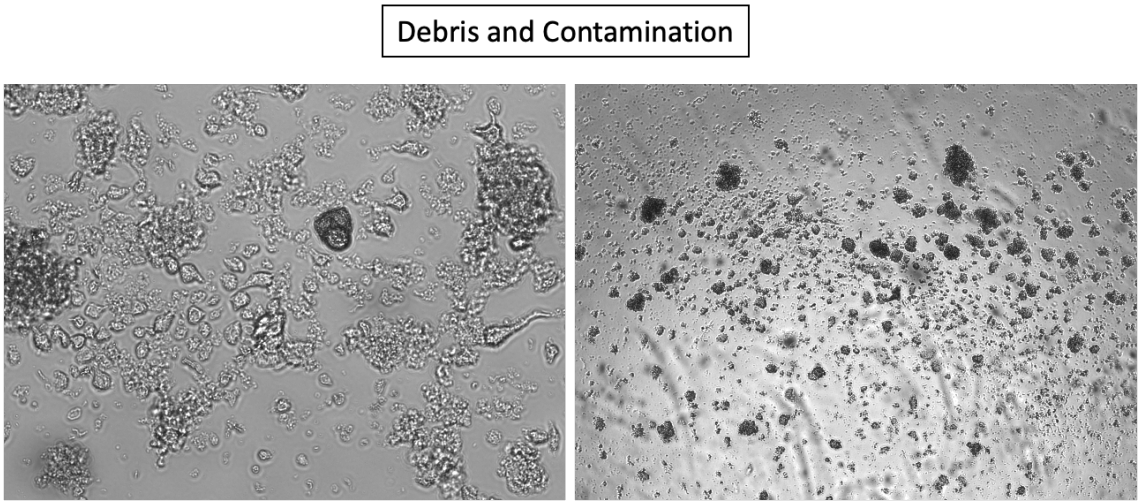


Figure S2.4 - Microscope images of cellular contamination and excess of tissue debris in the experiment conducted.

2.2. Toxicity assays SH-SY5Y

2.1.2. Cell Morphology Visualization

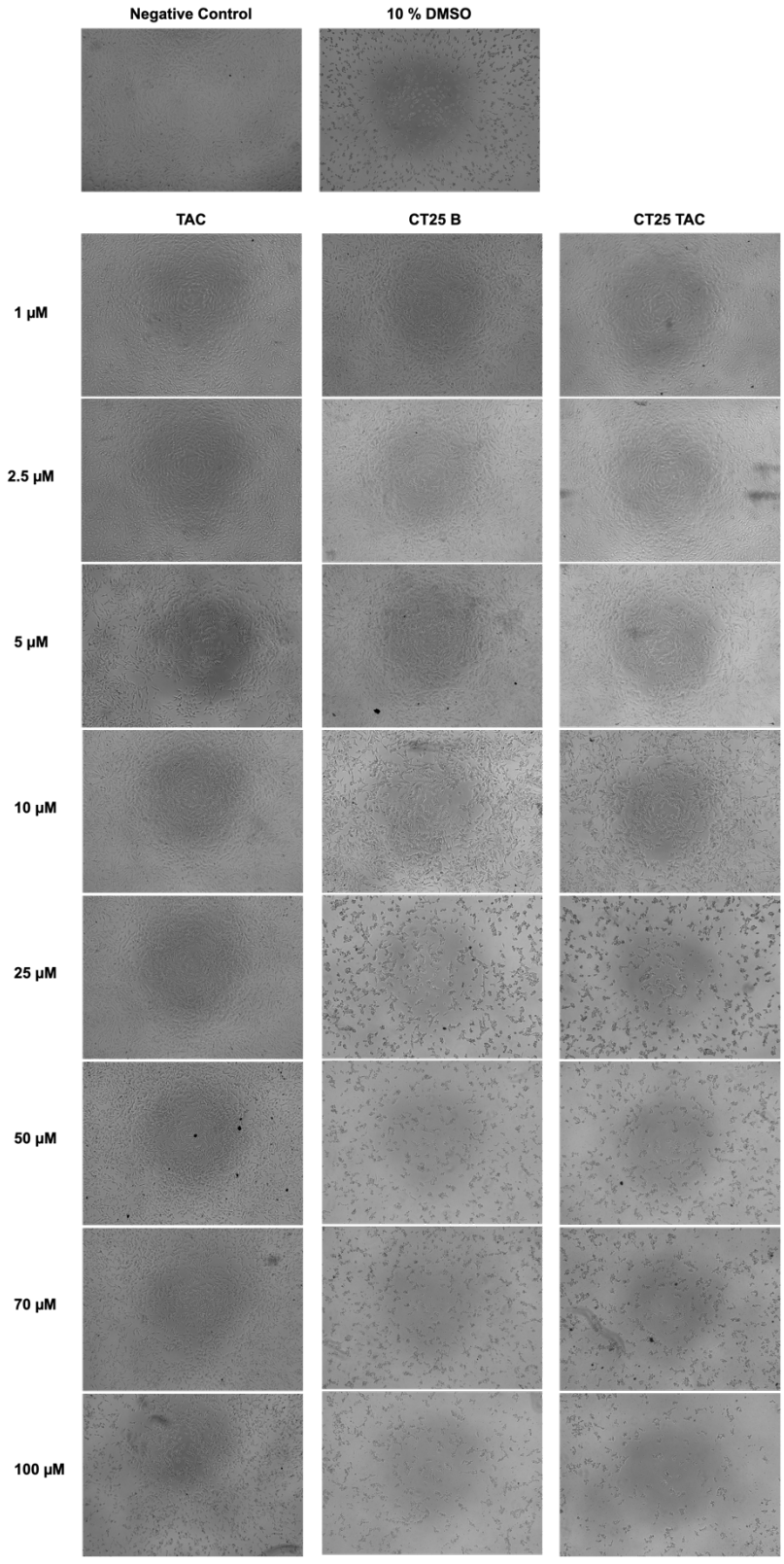


Figure S2.5 - Microscope cellular visualization through Lionheart FX of treatment with negative control (ultra-purified H_2O), positive control (10% DMSO), free TAC, CT25 B and CT25 TAC on SH-SY5Y cell line at a concentration of 1-100 µM.

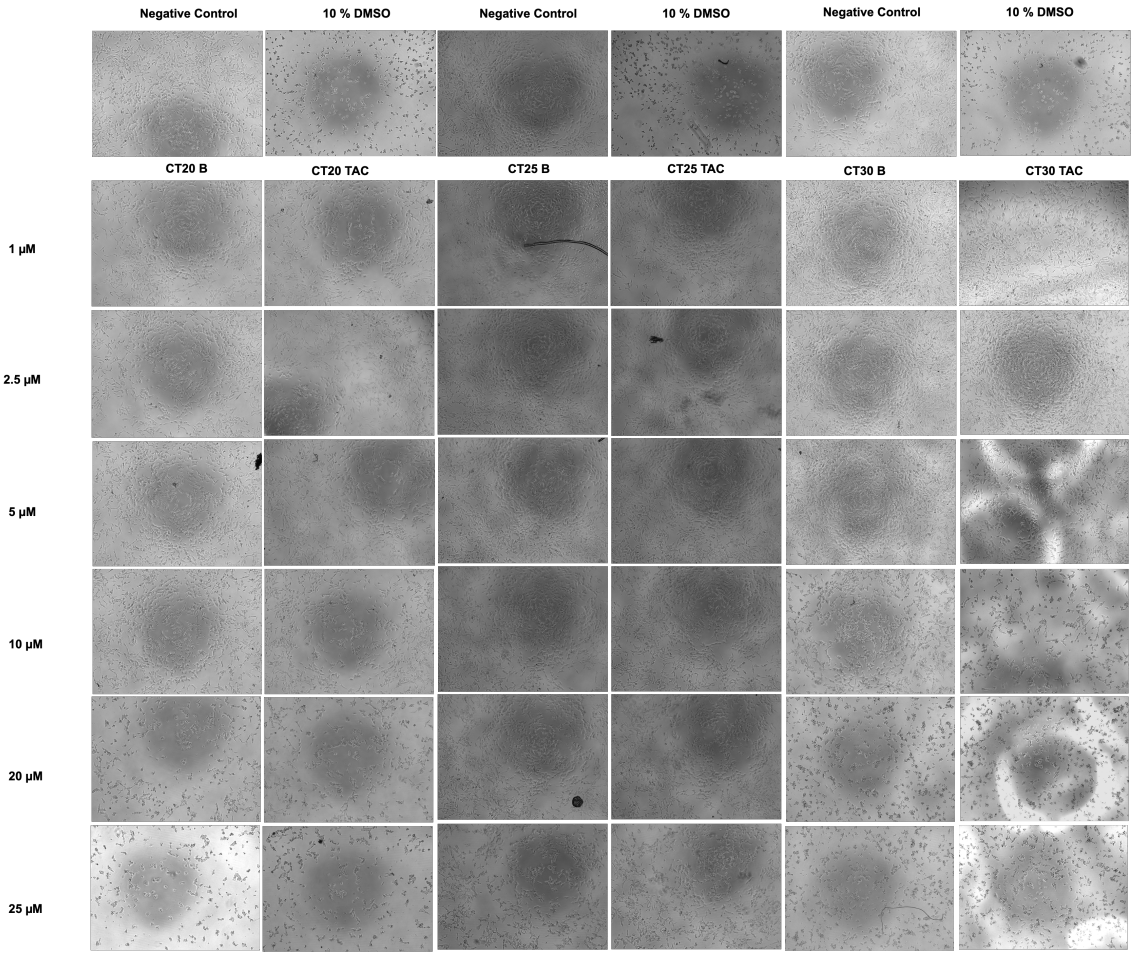


Figure S2.6 - Microscope cellular visualization through Lionheart FX of treatment with negative control (ultra-purified H_2O), positive control (10% DMSO), different blank NLC formulations (CT20 B, CT25 B and CT30 B) and different NLC formulations loaded with TAC on SH-SY5Y cell line at a concentration of 1, 2.5, 5, 10, 20 and 25 µM.

3.1. Encapsulation efficiency – Results

3.1.1. Ultraviolet-visible (UV-Vis) spectroscopy

mM	Abs
0.745	2.37
0.3725	1.609
0.18625	0.923
0.093125	0.498
0.0465625	0.273
0.02328125	0.153
0.01164063	0.094
0.00582031	0.064
0.00291016	0.051
0.00145508	0.045
0	0

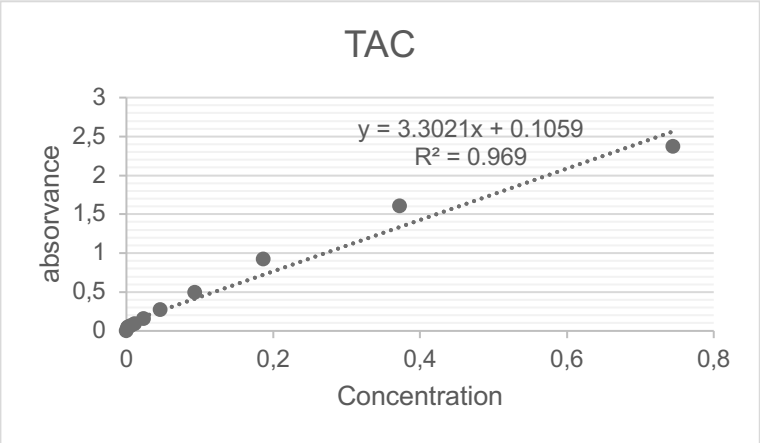


Table 1	Control – CT25 B	CT25 TAC I	CT25 TAC III	CT25 TAC V	CT25 TAC VIII
ABS exp1	0.149	0.207	1.514	0.229	0.479
EE %	---	7.54	74.16	10.28	17.38
ABS exp2	0.182	0.320	0.358	0.451	0.455
EE %	---	15.98	13.25	28.83	16.28

Figure S3.1 - Representation of the results obtain in the UV-Vis analysis of free TAC.

After Chapter 2, nanoparticle optimization freshly new NLCs formulations were prepared, and encapsulation efficiency had to be determined. This method was tried out to see if we could use a more efficient method to determine CNS drugs and peptide conjugated without using HPLC. The overall results shown in Figure S3.1, demonstrated that absorbance needed to detect TAC was very close to the absorbance of the lipids present in the formulation which cause the different values obtain in different NLC batches (CT25 TAC I, III, V and VIII) and same batch two independent analysis (Figure S3.1 – Table 1). This method wasn't further used so HPLC and Fluorescamine assay were applied.

3.1.2. Fluorescamine Protocol optimization

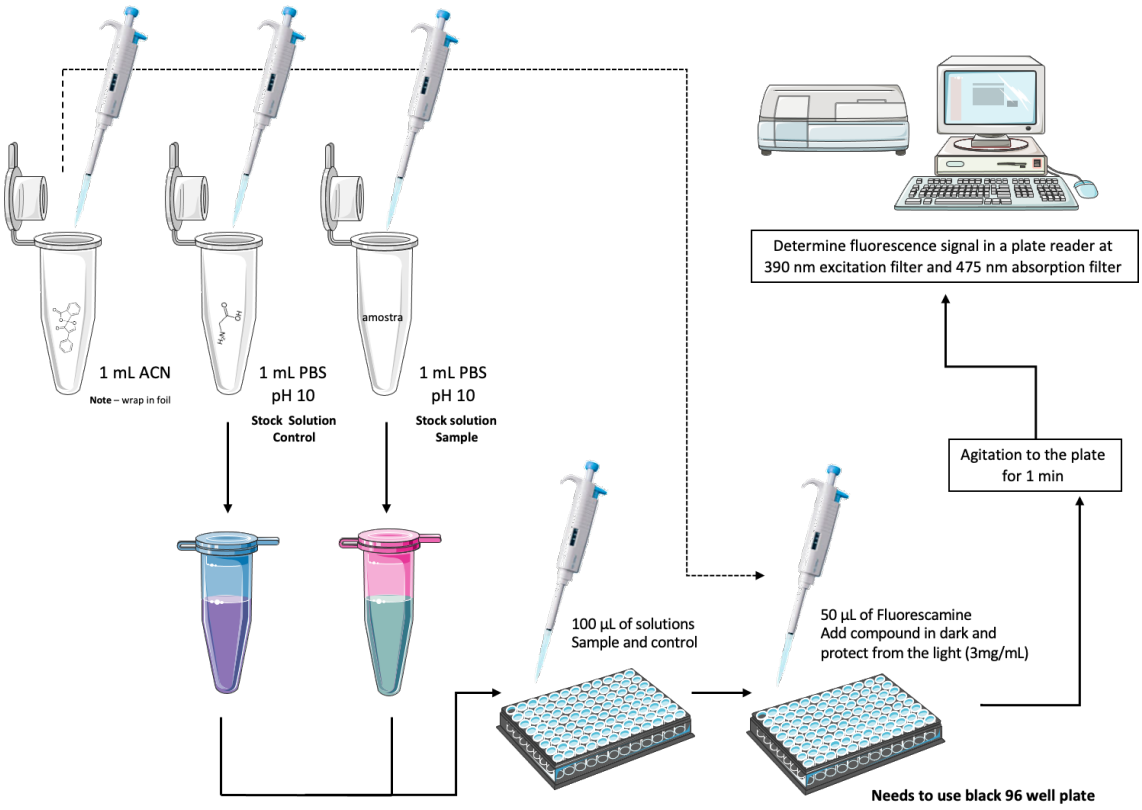


Figure S3.2 - Final protocol implemented to conduct Fluorescamine Assay.

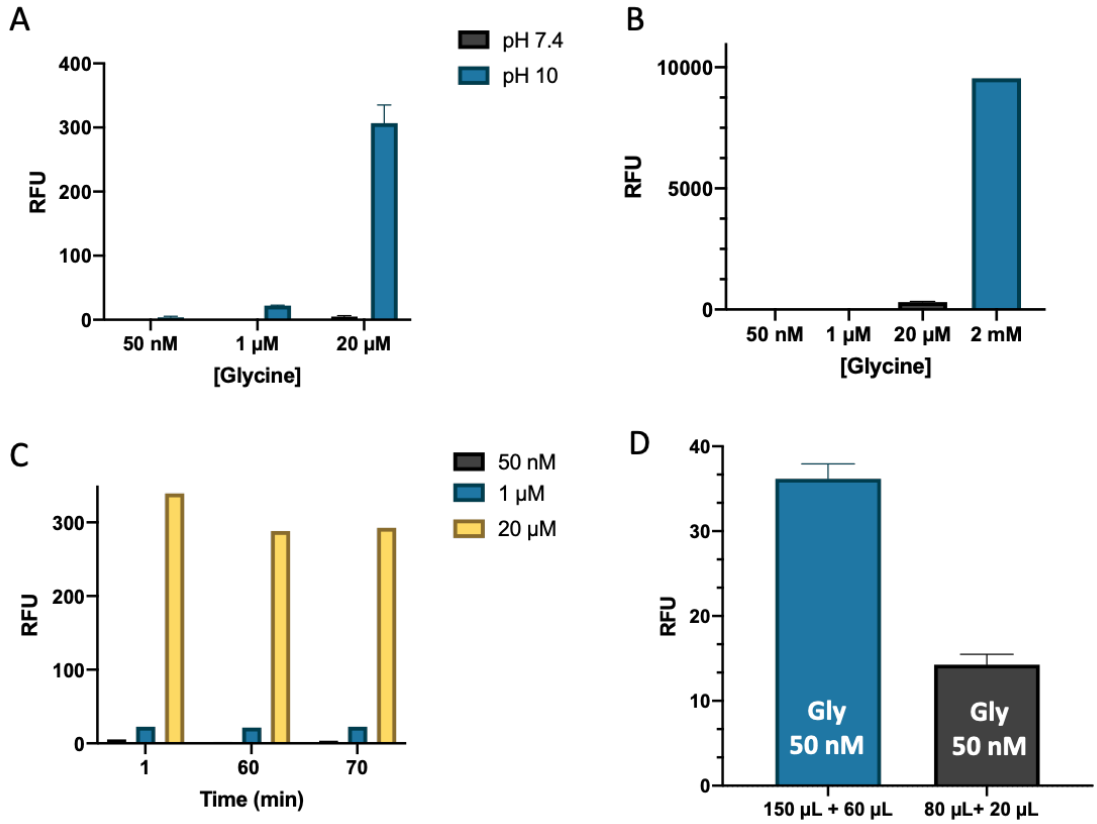


Figure S3.3 - Results obtain from Fluorescamine protocol optimization using Glycine as control. (A) determine the suitable pH needed to conduct the experiment. (B) concentration-dependent graphic; (C) Fluorescamine fluorescent decay at different time; (D) Fluorescamine RFU analysis with different volumes applied.

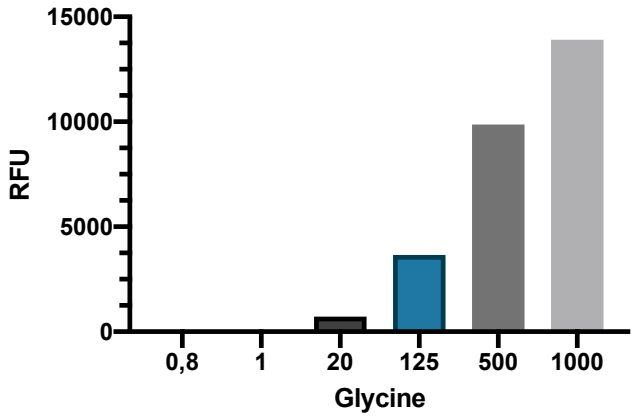


Figure S3.4 - Representation of RFU values in crescent concentrations (µM) of Glycine through fluorescamine assay.

3.2. *In vitro* cytotoxicity assays against Caco-2 cell line

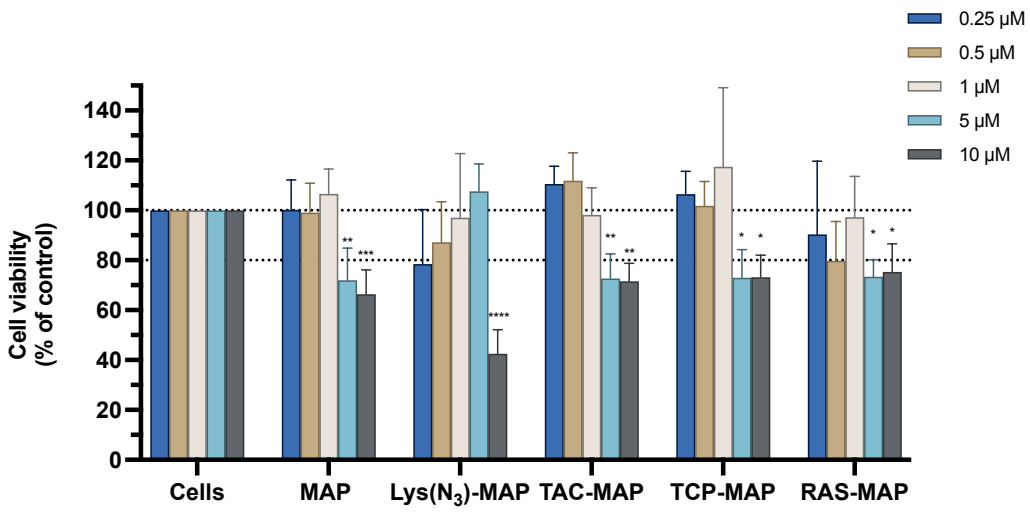


Figure S3.5 - Relative cell viability of Caco-2 cell line measured by the SRB assay after 24 h incubation. Treatment with free MAP, Lys(N_3)-MAP, TAC-MAP, TCP-MAP and RAS-MAP (0.25 µM-10 µM). Results are expressed as mean ± SD (n = 3 or 6). Statistical analysis between the control groups was performed using two-way ANOVA with Tukey's multiple comparisons test (* p <0.05; ** p <0.01; *** p <0.001; **** p <0.0001).

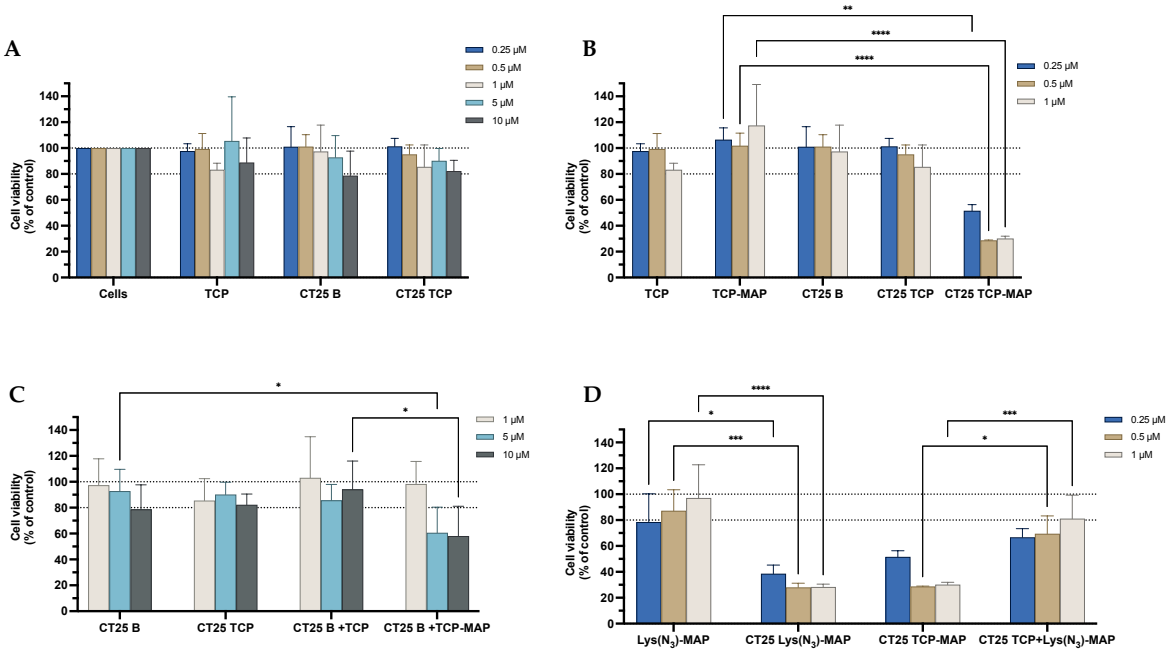


Figure S3.6 - Relative cell viability of Caco-2 cell line measured by the SRB assay after 24 h incubation. (A) represents NLC safety test with the treatment of free TCP, blank CT25 and TCP loaded CT25 (0.25-10 µM). (B) Represents differences in the cell viability of treatment with free TCP, TCP-MAP, blank CT25, TCP loaded CT25, MAP, TCP-MAP loaded CT25 (0.25-10 µM). (C) Represents co-administration of TCP and TCP-MAP with blank CT25 (1-10 µM). (D) Represents the data obtained from the encapsulation of Lys(N_3)-MAP and co-encapsulation of TCP and Lys(N_3)-MAP in the NLC compared to peptide conjugate. Results are expressed as mean ± SD (n = 4). Statistical analysis between the groups was performed using two-way ANOVA with Tukey's multiple comparisons test (* p <0.05; ** p <0.01; *** p <0.001; **** p <0.0001).

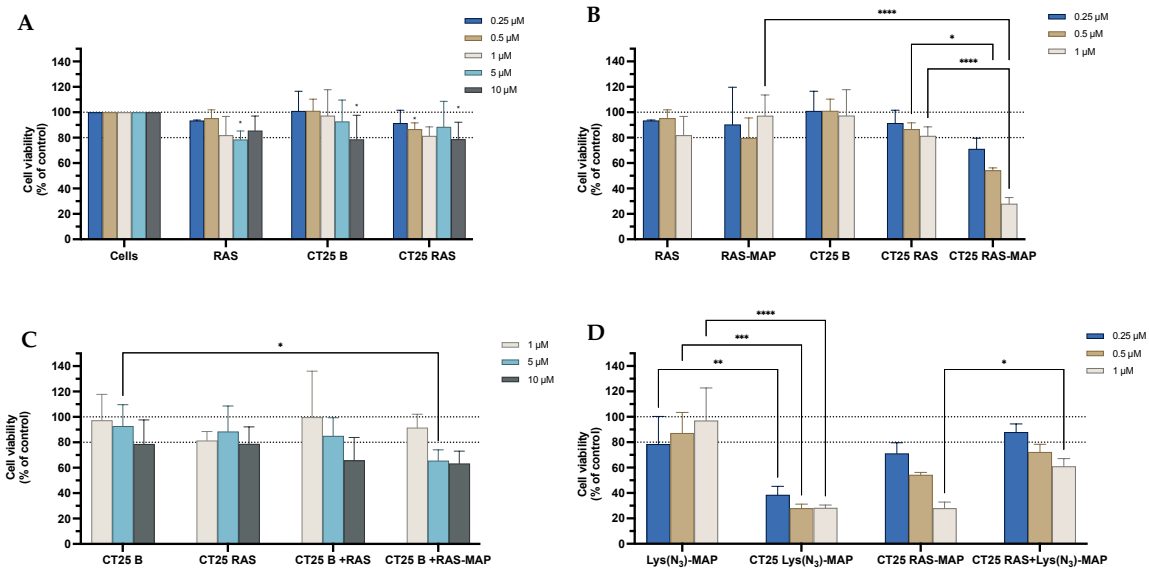


Figure S3.7 - Relative cell viability of Caco-2 cell line measured by the SRB assay after 24 h incubation. (A) represents NLC safety test with the treatment of free RAS, blank CT25 and RAS loaded CT25 (0.25-10 µM). (B) Represents differences in the cell viability of treatment with free RAS, RAS-MAP, blank CT25, RAS loaded CT25, MAP, RAS-MAP loaded CT25 (0.25-10 µM). (C) Represents co-administration of RAS and RAS-MAP with blank CT25 (1-10 µM). (D) Represents the data obtained from the encapsulation of Lys(N_3)-MAP and co-encapsulation of RAS and Lys(N_3)-MAP in the NLC compared to peptide conjugate. Results are expressed as mean ± SD (n = 4). Statistical analysis between the groups was performed using two-way ANOVA with Tukey's multiple comparisons test (* p <0.05; ** p <0.01; *** p <0.001; **** p <0.0001).

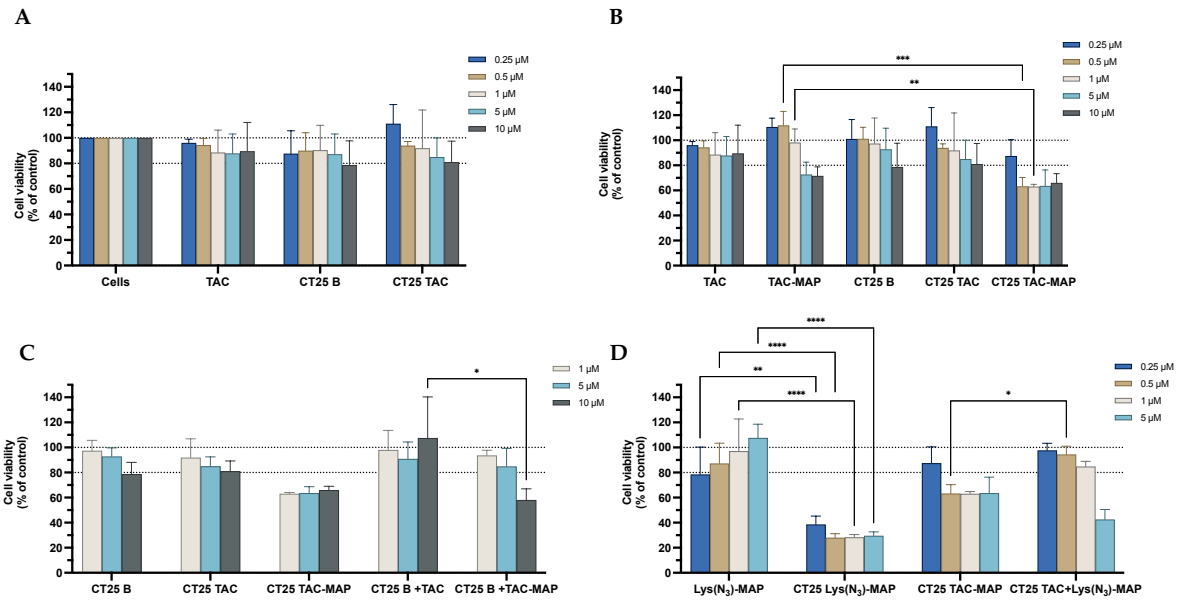


Figure S3.8 - Relative cell viability of Caco-2 cell line measured by the SRB assay after 24 h incubation. (A) represents NLC safety test with the treatment of free TAC, blank CT25 and TAC loaded CT25 (0.25-10 µM). (B) Represents differences in the cell viability of treatment with free TAC, TAC-MAP, blank CT25, TAC loaded CT25, MAP, TAC-MAP loaded CT25 (0.25-10 µM). (C) Represents co-administration of TAC and TAC-MAP with blank CT25 (1-10 µM). (D) Represents the data obtained from the encapsulation of Lys(N_3)-MAP and co-encapsulation of TAC and Lys(N_3)-MAP in the NLC compared to peptide conjugate. Results are expressed as mean ± SD (n = 4). Statistical analysis between the groups was performed using two-way ANOVA with Tukey's multiple comparisons test (* p <0.05; ** p <0.01; *** p <0.001; **** p <0.0001).

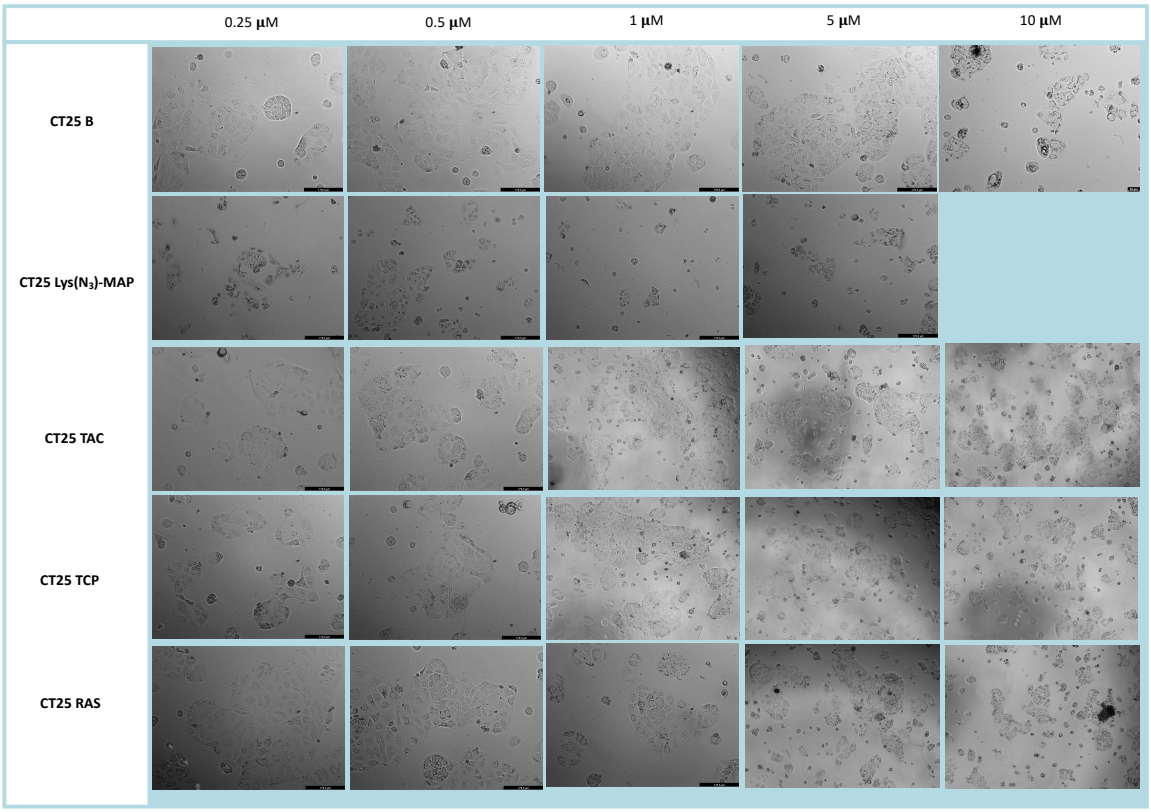


Figure S3.9 - Microscope cellular visualization through Lionheart FX and Leica DFC350 FX of treatment with free drug and NLC loaded formulations on Caco-2 cell line at a concentration of 0.25, 0.5, 1, 5 and 10 µM.

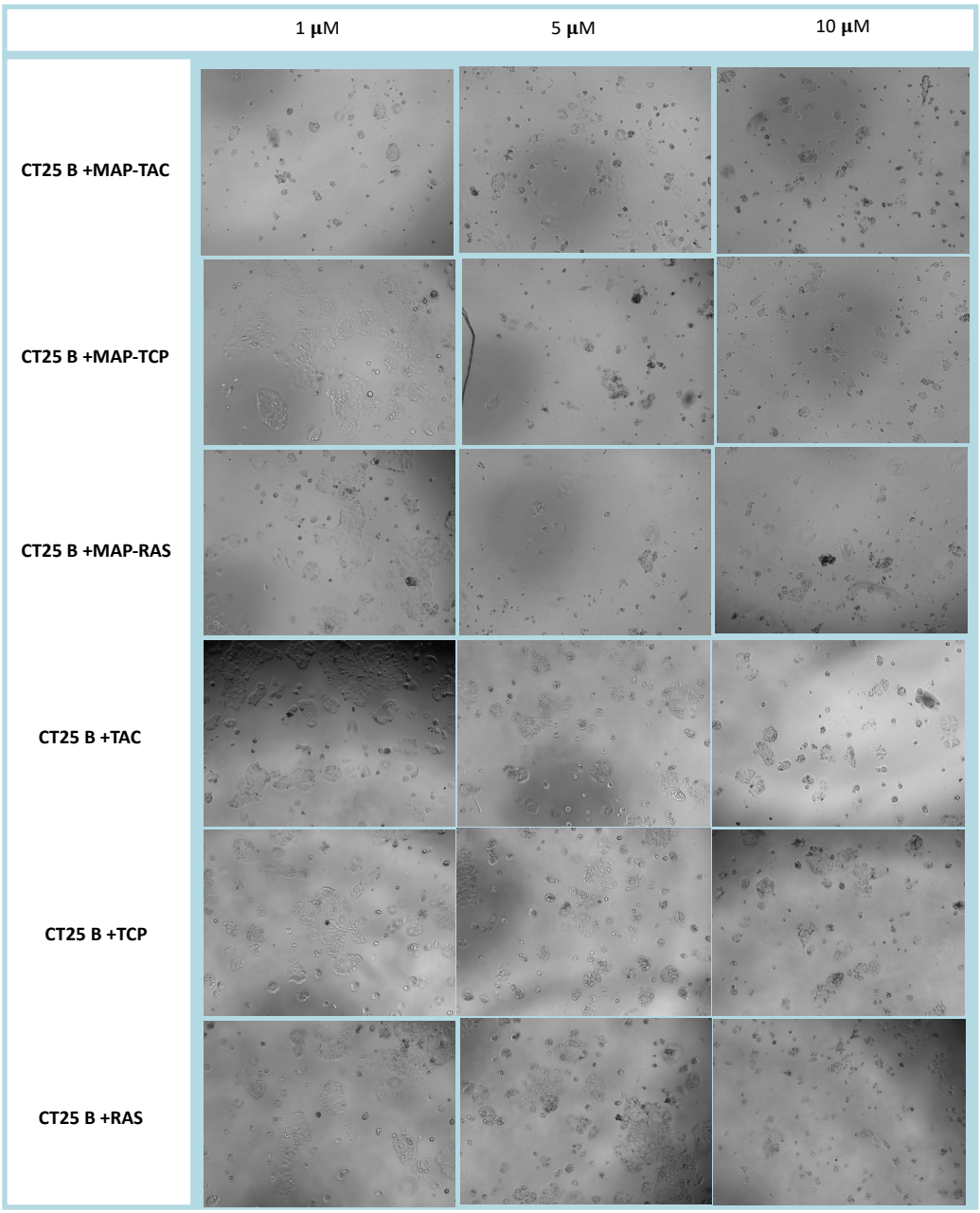


Figure S3.10 - Microscope cellular visualization through Lionheart FX and Leica DFC350 FX of treatment with free drug and NLC loaded formulations on Caco-2 cell line at a concentration of 1, 5 and 10 µM.

3.3. *In vitro* cytotoxicity assays against SH-SY5Y

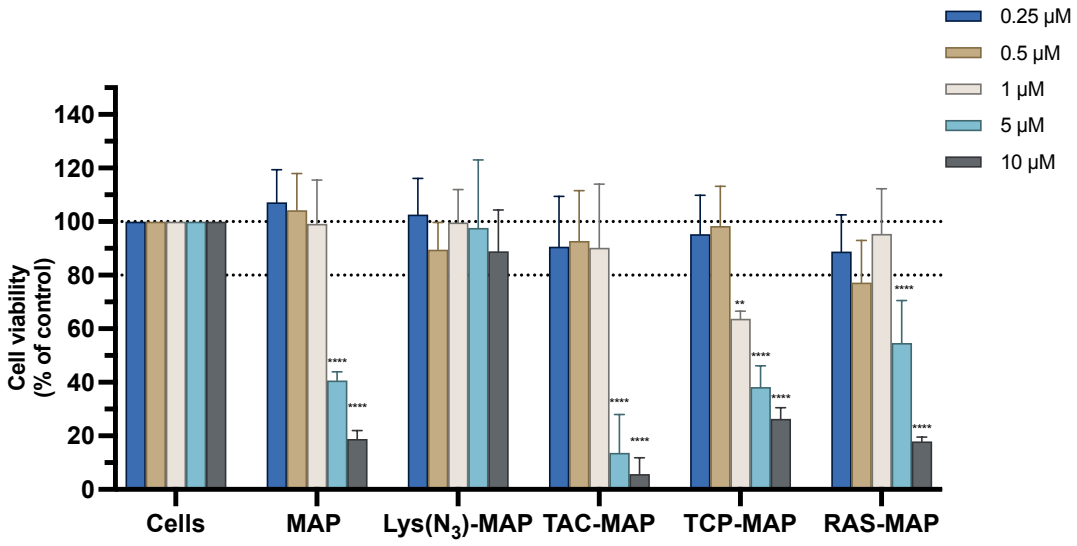


Figure S3.11 - Relative cell viability of SH-SY5Y cell line measured by the SRB assay after 24 h incubation. Treatment with free MAP, Lys(N_3)-MAP, TAC-MAP, TCP-MAP and RAS-MAP (0.25 µM-10 µM). Results are expressed as mean ± SD (n = 3 or 6). Statistical analysis between the control groups was performed using two-way ANOVA with Tukey's multiple comparisons test (** p <0.01; **** p <0.0001).

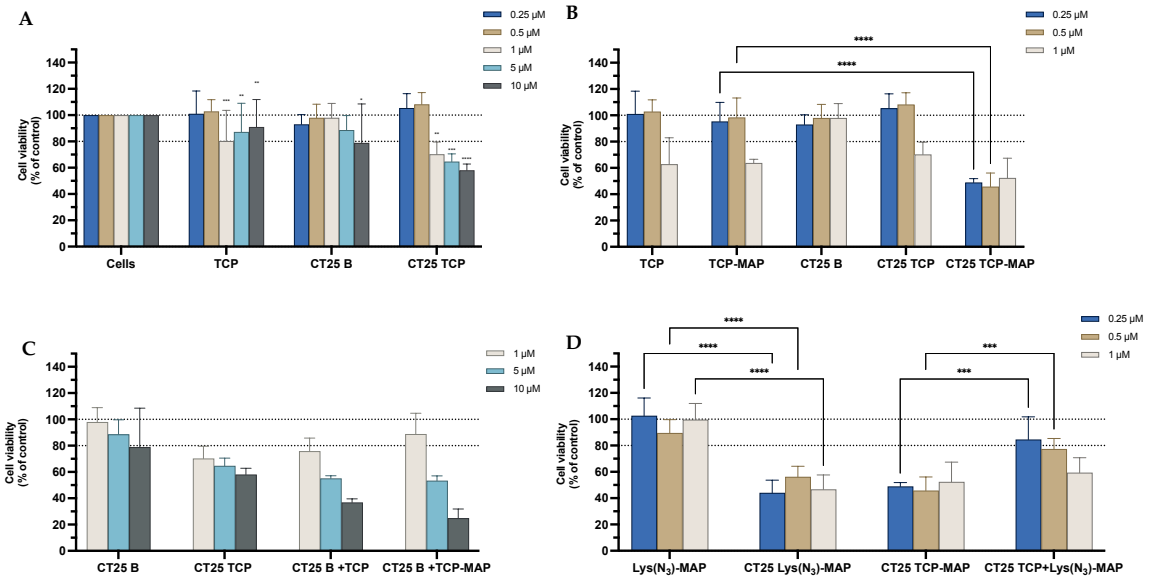


Figure S3.12 - Relative cell viability of SH-SY5Y cell line measured by the SRB assay after 24 h incubation. (A) represents NLC safety test with the treatment of free TCP, blank CT25 and TCP loaded CT25 (0.25-10 µM). (B) Represents differences in the cell viability of treatment with free TCP, TCP-MAP, blank CT25, TCP loaded CT25, MAP, TCP-MAP loaded CT25 (0.25-10 µM). (C) Represents co-administration of TCP and TCP-MAP with blank CT25 (1-10 µM). (D) Represents the data obtained from the encapsulation of Lys(N_3)-MAP and co-encapsulation of TCP and Lys(N_3)-MAP in the NLC compared to peptide conjugate. Results are expressed as mean ± SD (n = 4). Statistical analysis between the groups was performed using two-way ANOVA with Tukey's multiple comparisons test (* p <0.05; ** p <0.01; *** p <0.001; **** p <0.0001).

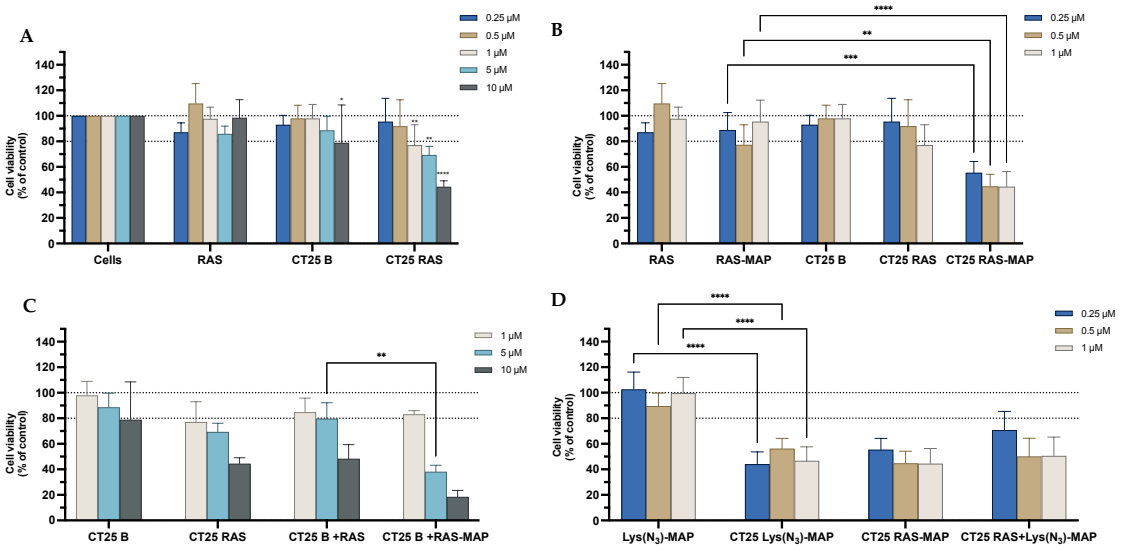


Figure S3.13 - Relative cell viability of SH-SY5Y cell line measured by the SRB assay after 24 h incubation. (A) represents NLC safety test with the treatment of free RAS, blank CT25 and RAS loaded CT25 (0.25-10 µM). (B) Represents differences in the cell viability of treatment with free RAS, RAS-MAP, blank CT25, RAS loaded CT25, MAP, RAS-MAP loaded CT25 (0.25-10 µM). (C) Represents co-administration of RAS and RAS-MAP with blank CT25 (1-10 µM). (D) Represents the data obtained from the encapsulation of Lys(N_3)-MAP and co-encapsulation of RAS and Lys(N_3)-MAP in the NLC compared to peptide conjugate. Results are expressed as mean ± SD (n = 4). Statistical analysis between the groups was performed using two-way ANOVA with Tukey's multiple comparisons test (* p <0.05; ** p <0.01; **** p <0.0001).

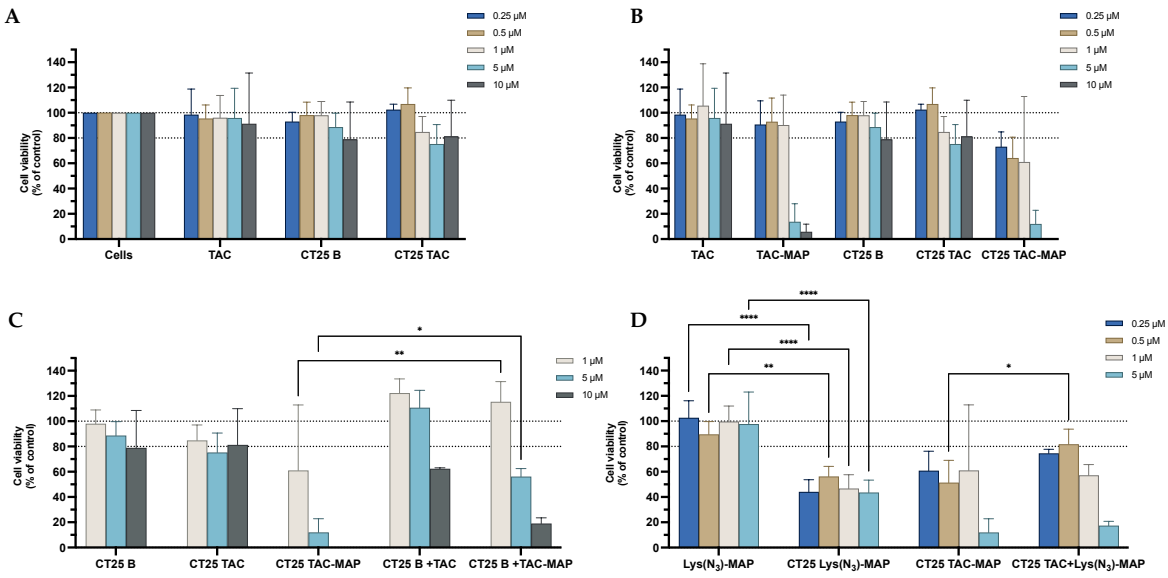


Figure S3.14 - Relative cell viability of SH-SY5Y cell line measured by the SRB assay after 24 h incubation. (A) represents NLC safety test with the treatment of free TAC, blank CT25 and TAC loaded CT25 (0.25-10 µM). (B) Represents differences in the cell viability of treatment with free TAC, TAC-MAP, blank CT25, TAC loaded CT25, MAP, TAC-MAP loaded CT25 (0.25-10 µM). (C) Represents co-administration of TAC and TAC-MAP with blank CT25 (1-10 µM). (D) Represents the data obtained from the encapsulation of Lys(N_3)-MAP and co-encapsulation of TAC and Lys(N_3)-MAP in the NLC compared to peptide conjugate. Results are expressed as mean ± SD (n = 4). Statistical analysis between the groups was performed using two-way ANOVA with Tukey's multiple comparisons test (* p <0.05; ** p <0.01; **** p <0.0001).

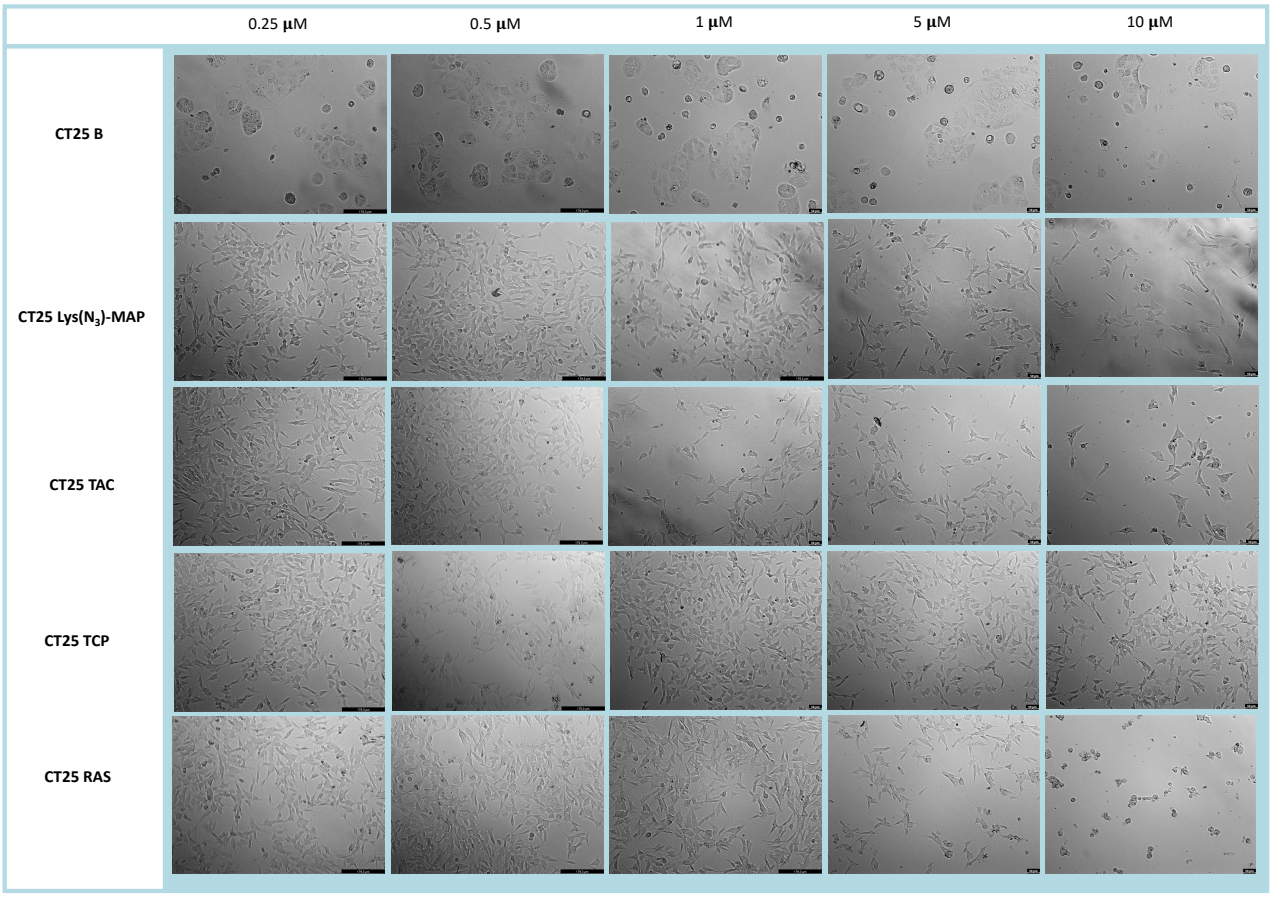


Figure S3.15 - Microscope cellular visualization through Lionheart FX and Leica DFC350 FX of treatment with free drug and NLC loaded formulations on SH-SY5Y cell line at a concentration of 0.25, 0.5, 1, 5 and 10 µM.

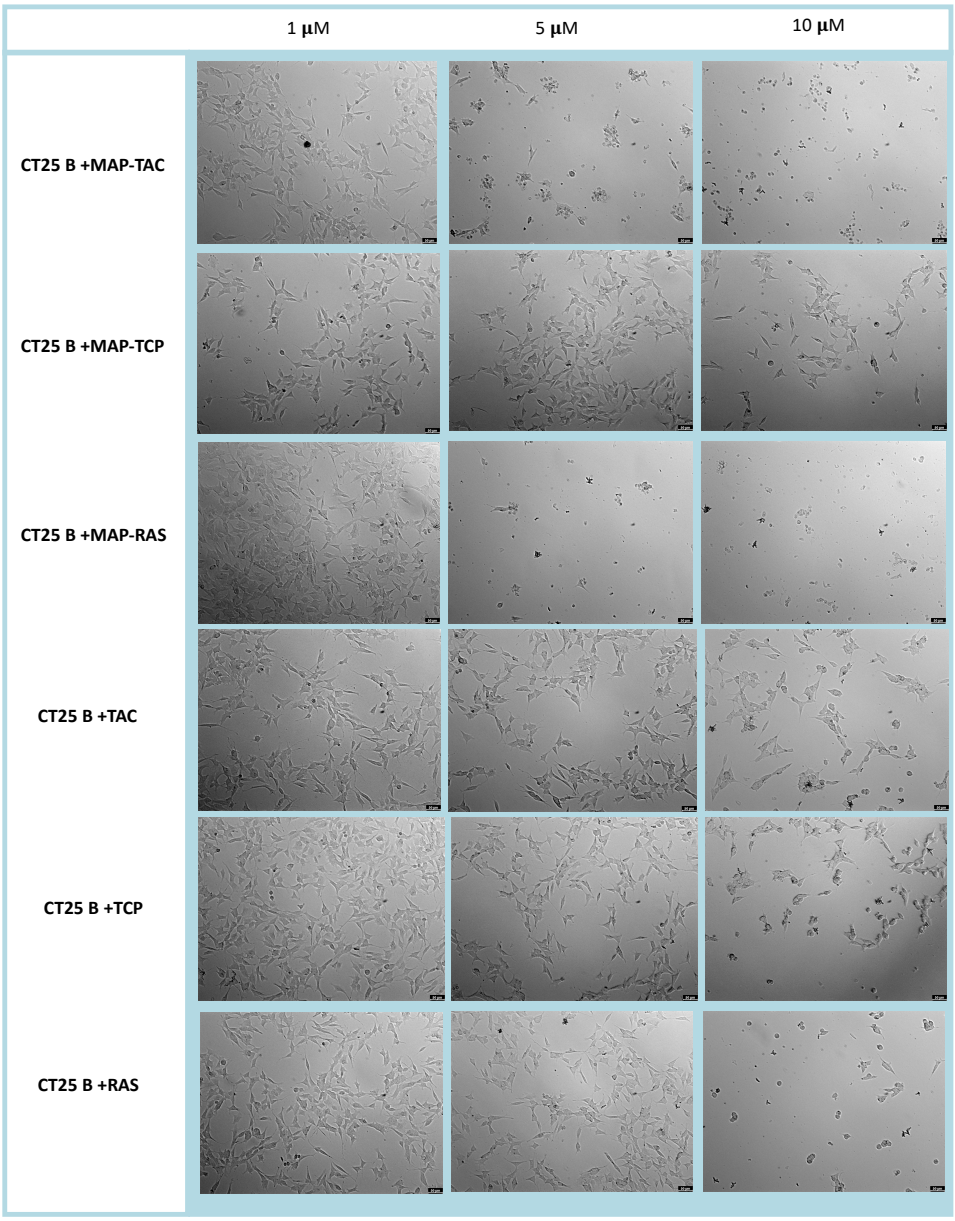


Figure S3.16 - Microscope cellular visualization through Lionheart FX and Leica DFC350 FX of treatment with free drug and NLC loaded formulations on SH-SY5Y cell line at a concentration of 0.25, 0.5, 1, 5 and 10 µM.

List of Publications

First author: Sara Silva

1. Silva, S., Almeida, A., Vale, N., 2019. Combination of Cell-Penetrating Peptides with Nanoparticles for Therapeutic Application: A Review. Biomolecules 9, 22. https://doi.org/10.3390/biom9010022

2. Silva, S., Alves, C., Duarte, D., Costa, A., Sarmento, B., Almeida, A.J., Gomes, P., Vale, N., 2020. Model Amphipathic Peptide Coupled with Tacrine to Improve Its Antiproliferative Activity. Int. J. Mol. Sci. 22, 242. https://doi.org/10.3390/ijms22010242

3. Silva, S., Marto, J., Gonçalves, L., Almeida, A.J., Vale, N., 2020. Formulation, characterization and evaluation against sh-sy5y cells of new tacrine and tacrine-map loaded with lipid nanoparticles. Nanomaterials 10. https://doi.org/10.3390/nano10102089

4. Silva, S., Almeida, A.J., Vale, N., 2021. Acetylcholinesterase inhibitors and nanoparticles on Alzheimer's disease: a review. J. Nanoparticle Res. 23, 9. https://doi.org/10.1007/s11051-020-05118-9

5. Silva, S., Almeida, A.J., Vale, N., 2021. Importance of Nanoparticles for the Delivery of Antiparkinsonian Drugs. Pharmaceutics 13, 508. https://doi.org/10.3390/pharmaceutics13040508

6. Silva, S., Marto, J., Gonçalves, L.M., Duarte, D., Soares, O.S.G.P., Vasques-Nóvoa, F., Almeida, A.J., Vale, N., 2022. New Peptide Functionalized Nanostructured Lipid Carriers with CNS Drugs and Evaluation Anti-proliferative Activity. Int. J. Mol. Sci. 23, 7109. https://doi.org/10.3390/ijms23137109

7. Silva, S., Marto, J., Gonçalves, L.M., Fernandes, H.S., Sousa, S.F., Almeida, A.J., Vale, N., 2022. Development of Neuropeptide Y and Cell-Penetrating Peptide MAP Adsorbed onto Lipid Nanoparticle Surface. Molecules 27, 2734. https://doi.org/10.3390/molecules27092734

8. Silva, S., Kurrikoff, K., Langel, Ü., Almeida, A.J., Vale, N., 2022. A Second Life for MAP, a Model Amphipathic Peptide. Int. J. Mol. Sci. 23, 8322. https://doi.org/10.3390/ijms23158322

Co-author

1. Vale, N., Alves, C., Sharma, V., Lázaro, D.F., Silva, S., Gomes, P., Outeiro, T.F., 2020. A new MAP-Rasagiline conjugate reduces α-synuclein inclusion formation in a cell model. Pharmacol. Reports 72, 456–464. https://doi.org/10.1007/s43440-019-00032-x

2. Vale, N., Duarte, D., Silva, S., Correia, A.S., Costa, B., Gouveia, M.J., Ferreira, A., 2020. Cell-penetrating peptides in oncologic pharmacotherapy: A review. Pharmacol. Res. 162, 105231. https://doi.org/10.1016/j.phrs.2020.105231

U.PORTO

D.FFUP - 2022

NeuroD3S – Dual-Drug Delivery System based on cell-penetrating peptides and nanoparticles for application in biomedicine

Sara Silva

Faculty of Farmacy